Study of a variable geometry radial inflow turbine.

Jasim, Adnan A.

Award date:
1983

Awarding institution:
University of Bath

STUDY OF A VARIABLE GEOMETRY RADIAL INFLOW TURBINE

Submitted by

ADNAN A. JASIM

for the degree of PhD of the University of Bath

1982

A.A. Jasim

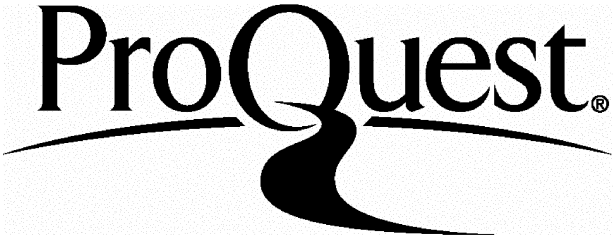

SUMMARY

This study is concerned with a variable geometry inward flow radial turbine for turbocharging Diesel engines.

A detailed theoretical and experimental investigation in both the stator and rotor is presented. The finite element method being applied for the flow analysis.

The finite element procedure was initially developed by applying it to an isolated aerofoil prior to the further application to cover a circular cascade of blades as encountered in the volute-nozzle assembly.

In the rotor, only the hub-shroud analysis was carried out and the results compared with an existing streamline curvature technique. It was shown that the finite element method required less computaional time and was more generally applicable to complex geometric configurations than the streamline curvature technique.

Experimentally, the turbine performance was evaluated with and without exhaust diffusers and with a number of nozzle rings with different restrictions. It was shown that the maximum restriction resulted in high losses due to the flow mismatching at nozzle inlet because of the sudden area change, and relatively low efficiencies resulted.

The effect of swirl, resulting from off-design operation, on the diffusers was analysed with three conical diffusers. The results show that low swirls of the order of 10%, has a beneficial effect on the pressure recovery coefficient for wide angle difuser.

ACKNOWLEDGEMENTS

Throughout this project, I owe a great debt of gratitude to my supervisor, Dr. A. Whitfield. His excellent advice and criticism have been invaluable to me.

I am also indebted to prof. F. J. Wallace for his general interest and detailed advice when I reqired it.

I also would like to thank the Thermodynamic Laboratory technicians Mr. F. Denton, Mr. P. Wyeth, and Mr. A. Coggins for their continues help whenever the rig needed some adjustment or repair.

Finally, I wish to express my gratitude to my wife and children who have accepted many hours of my preoccupation with the subject. I hope the final result will convince them that this was in a good cause.

CONTENTS

1.	**INTRODUCTION**	1
1.1	Survey Of Previous Work	7
1.1.1	The Radial Inflow Turbine	7
1.1.2	The Exhaust Diffuser	15
2.	**THEORETICAL STYDY**	19
2.1	Finite Element Analysis Of The Flow In The Rotor	21
2.1.1	Derivation Of The Equations	21
2.1.2	Derivation Of The Density Equation	26
2.1.3	Formulation Of The Finite Element Equation	29 29
2.2	Finite Element Analysis Of Flow In The Volute Nozzle Assembly	32
2.2.1	Two dimensional Flow About An Isolated Aerofoil	32
2.2.1.1	Choice Of The Field Variable	32
2.2.1.2	Boundary Conditions	34
2.2.1.3	The Solution Domain	35
2.2.1.4	The Solution Procedure	37

2.2.2 Flow Investigation In Volute Nozzle Assembly 38

2.2.2.1 The Choice Of The Dependent Field Variable 39

2.2.2.2 Boundary Conditions 42

2.2.2.3 Solution Procedure 43

3. DESCRIPTION OF APPARATUS AND EXPERIMENTAL INVESTIGATIONS 48

3.1 Turbine Rig 48

3.1.1 The Exhaust Diffuser 50

3.1.2 The Inlet Nozzle 51

3.2 Experimental Procedure 52

3.3 Instrumentations 53

3.3.1 Static Pressure And Scanivalve 53

3.3.2 Five Hole Probe 54

3.4 Analysis Of The Experimental Data 56

3.4.1 Theoretical Method For Static Pressure Calculations 56

3.4.2 Averaging Techniques And Swirl 59

3.4.3 Calculation Of The Rotor Inlet Conditions From Discharge Measurements 64

3.4.4 Calculation Of Radial Distribution Of Losses At Rotor Exit 66

3.4.5 Calculation Of Nozzle Efficiency 67

3.4.6 Calculation Of Turbine Characyeristics From Experimental Data 68

4. PRESENTATION AND DISCUSSION OF RESULTS 71

4.1 Study Of Exhaust Diffuser 71

4.1.1 Detailed Diffuser Performance 73

4.1.1.1 Accuracy Of Measurements 74

4.1.1.2 Diffuser Flow Conditions 75

4.2 Study Of Inlet Nozzle 83

4.2.1 Detailed Volute Nozzle Assembly Investigation 86

4.2.2 Calculated Nozzle Discharge Conditions From Rotor Discharge Measurements 90

4.2.3 Calculated Rotor Loss Coefficient 92

5. PRESENTATION AND DISCUSION OF THE THEORETICAL ANALYSIS RESULTS 94

5.1 Meridional Flow Analysis 94

5.2 Isolated Aerofoil 96

5.3 Volute Nozzle Assembly 97

6. CONCLUSIONS AND SUGESTIONS FOR FURTHER WORK 99

6.1 Conclusions 99

6.2 Suggestions For Further Work 101

APPENDIX "A" DERIVATION OF GALERKIN EQUATION FOR QUADRILATERAL ELEMENT IN ISOPARAMETRIC COORDINATES

APPENDIX "B" DERIVATION OF GALERKIN EQUATION FOR THE MERIDIONAL FLOW ANALYSIS

APPENDIX "C" ASSEMBLING THE GLOBAL MATRIX

APPENDIX "D" CALCULATION OF THE CIRCULATION AS A NODELRSS VARIABLE

APPENDIX "E" GENERAL DIFFUSER THEORY

NOTATIONS

A Area ; Streamline Curvature Equation Coefficient

b Blade Thickness

B Streamline Curcature Equation Coefficient

C Absolute Velocity

CA Area-Averaged Velocity

Cm Mass-Averaged Velocity ; Meridional Velocity

Co Spouting Velocity

Cf Friction Coefficient

Cp Specific Heat At Constant Pressure ; Pressure recovery Coefficient

Cpw Pressure Recovery Coefficient Based On The Wall Static Pressure

F Area

h Static Enthalpy

ho Stagnation Enthalpy

i Angle Of Incidence

k Stream Function Coefficient Which Accounts For Blade Blockage

Ke Kinetic Energy

m Mass Flow Rate

M Mach Number

n Normal Distance

N Ratational Speed ; Interpolation Function

Ns Specific Speed

P Static Pressure

Po Stagnation Pressure

R Gas Constant

q Instantaneous Variable To Be Averaged

Q Volumetric Flow Rate ; Averaged Value Of A Variable

T Static Temperature

To Stagnation Temperature

Tr Temperature Ratio

S Entropy

Sw Swirl Intensity

U Blade Speed

x,y,z Cartesian Coordinates

V Volume

W Relative Velocity

NDM Non-Dimensional Mass Flow Rate

NDS Non-Dimensional Speed

NDT Non-Dimensional Torque

α Absolute Angle; Energy Coefficient Relating Mass Averaged Velocity To The Area Mass Averaging

β Relative Angle; Energy Coefficient Relating Energy Averaged Velocity To The Area Averaging

γ Ratio Of Specific Heats

ω Vorticity; Stagnation Pressure Loss Coefficient

Ω Angular Velocity; Subdomain

ϵ Residual In The Galerkin Equation

ξ Isoparametric coordinate; Loss Coefficient

η Isoparametric coordinate; Efficiency

ρ Density

ν Kinematic Viscosity

λ Prewhirl

τ Torque

Γ Circulation; Domain Boundaries

Ψ Stream Function

Φ Potential Function; Blade Angle In $x-\theta$ Plane

SUBSCRIPTS

is Isentropic

1,x Inlet Station

2,y Exit Station

m Meridional

xy From Inlet To Exit

R Ratio

r relative ; Ratio

0 Tangential Direction

SUPERSCRIPTS

- Approximate

e element

i Instantaneous Variable

CHAPTER -1-
---

1. INTRODUCTION

Turbomachines as a mean of producing mechanical power are superior to reciprocating machines, they are more reliable, free from excessive vibrations, and are able to produce large powers from units of comparatively small size and weight. Generally for a given set of operating requirements there is one type best suited to provide optimum conditions of operation. Wood [1] used the specific speed criterion defined as

$$N_s = N\sqrt{\frac{Q}{\Delta h_{is}^{7.5}}} \qquad 1.1$$

to provide a broad correlation of maximum efficiency for various types of turbines. It can be seen from figure 1.1 that over a limited range of specific speed the best radial inflow turbines match the best efficiency of axial flow machines.

With the added advantage of ease of manufacture and structural strength the radial inflow turbine is preferred in many applications. They are used by NASA in Bryton cycles for space power generation [2,3] and for turbocharging of Diesel engines where they have found wide application in truck vehicles in particular. The evolution of automotive turbochargers over the past decade

demonstrates the superior production cost feature of this type of turbine, since all such units in service are now of this type.

Figure 1.2 shows the general configuration of the IFR-turbine, the rotor blades extending from a radially inward inlet to an axial discharge, the exit part of the blades are curved to minimize the absolute tangential velocity.

Generally, in Diesel engines the instantaneous power is a direct function of the amount of air/fuel available for combustion in the cylinders at a given instant of time. For a turbocharged engine the air flow is a function of the turbocharger's speed. By maintaining high turbocharger speeds at all engine speeds it is possible to increase the air flow and therefore the available power. However, if the turbocharger's speed is maximized at low engine speeds the result will be an over boost to the engine at high engine speeds which will result in either excessive engine loads or overspeeding of the turbocharger. Many solutions have been proposed to overcome this, namely :-

(1) The use of a waste gate in which exhaust energy is bypassed around the turbine at high engine speeds. This is

an inefficient way as large amounts of energy are wasted.

(2) The use of exhaust combusters. This approach was not adequate and also complex. Extra fuel is used in the burners and the necessary fuel control system adds to the cost.

(3) The use of adjustable turbine nozzles to vary the flow area as a function of engine speed. In this way it is possible to maintain high turbine speeds at low engine speeds by closing down the nozzle area. As the engine airflow rate increases with engine speed the nozzle area is opened to prevent overboosting. By this procedure it should be possible to maintain a constant turbocharger speed regardless of engine speed and thereby increase the available power as illustrated by figure 1.3.

Current turbocharger turbine design efforts have concentrated substantially upon the development of variable geometry devices in order to improve overall engine performance. Flaxington [4] gives the potential advantages of variable geometry turbines as :

(1) Increased torque back up

(2) Wider useful speed range.

(3) Improved transient response.

(4) Improved transient smoke emission.

(5) Reduced noise levels.

The variable geometry devices normal considered attempts to provide area control at specific sections in the turbine flow path. Figure 1.4 shows three possible areas for this purpos :

(1) Tongue Area "A1" : This is most suitable for nozzleless casings, simple designs can be considered for cutting off the extra area such as rotating devices or moving side walls.

(2) Volute Exit Area "A2" : This is suitable for nozzled turbines. It can easily be applied to the nozzle area, and it has the advantage that no asymmetric flow is produced around the rotor tip which normally results in vibrations. On the other hand it results in a sudden enlargement losses which affects the overall turbine efficiency.

(3) Rotor Exit Area "A3" : This is in fact a throttling process which can lead to large losses, and it requires complex blade design to minimize these losses.

Balje [5] describes three options for the control area "A2", these are : pivoting nozzle blades, mating plates, and partial admission.

In the case of pivoted nozzle vanes the nozzle angle as well as the throat area are varied simultaneously. The

locations of pivot points if placed as closer as possible to the rotor inlet can avoid excessive losses at small nozzle angles.

The mating plate is mechanically simple. Its main disadvantage is an excessive step in axial width between nozzle exit and rotor inlet which causes a sudden expansion of the flow after the nozzle throat and a mismatch in velocity triangles at rotor inlet. The partial admission concept is suitable for nozzleless turbines and since the losses are a function of the degree of admission, the efficiency drop is dependent on this. Figure 1.5 from ref. [5] compares these different options by plotting the efficiency penalty as a function of nozzle area reduction. It is shown that the pivoted nozzle has a peak efficiency at mid range.

Wallace [6] and his co-workers have concentrated on the mating plate type of variable geometry nozzle arrangement. The restricted nozzled casing used here proved to be successful as at high degrees of restrictions the turbocharger's speed increased sharply within the operating range limits of the engine and this gave rise to an improvement in the air/fuel ratio. This increased fueling resulted in improved torque back up at high engine loads . Hence, the V.G. turbocharger led to a major

improvement in performance. It is, however, shown that at high restrictions the turbine efficiency is reduced. This penalty in efficiency, however, is slight compared to the improvement of the turbocharged engine as a whole.

Controlling the rotor exit area by means of a variable geometry device is not considered by Flaxington [4] to be a good approach. However, if this could be done in conjunction with an efficient exhaust diffuser, the losses could be minimized. The environment downstream of a turbine is extremely hostile for the diffusion process, the flow being unsteady and with a high degree of swirl at off-design conditions. This study has therefore been directed towards an assessment of the exhaust diffuser as a possible candidate for further development into a variable geometry device, and into a detailed study of the mating plate type of variable geometry nozzle as used by Wallace et el [6].

In the present work the fluid dynamic operation of the nozzles both experimentally and theoretically has been investigated in detail. The use of exhaust diffusers with possible V.G. potential has not previously been studied and the present investigation includes a study of overall turbine performance with three exhaust conical diffusers.

CHAPTER -1-

1.1 Survey Of Previous Work

A great deal of research work has been carried out into inward flow radial turbines, and the literature devoted to their analysis, both theoretical and experimental is very extensive. In order to review the work done in this field and to put the present work into its proper context, it has been divided into two parts; (i) The IFR-turbines and (ii) that concerned with the exhaust diffuser.

1.1.1 The Radial Inflow Turbine

The early attempts to analyse the flow within the IFR-turbine were based on isentropic flow considerations at the design point. In a detailed examination of flow conditions in the rotor passage, Wallace [8] derived a force equation for an infinitesimal element, and by integrating radially from the inner to the outer radius and transversely from the leading edge to the trailing edge of the blade passage established the radial and transverse pressure distribution in the passage. Wallace also developed a one-dimensional performance prediction procedure to predict turbine performance at both design and off-design conditiona. At off-design conditions he included a constant pressure incidence loss model to calculate the energy dissipation due to the sudden

deflection of the flow as it entered the rotor.

It is clear that the assessment of losses in the nozzle and rotor play a major role in any prediction method and the study of these losses has been a subject of extensive experimental and theoretical investigations [9,10,11,12, 13,14,15,16,17]. Bridle et el [14] derived a loss coefficient for the rotor based upon the stagnation pressure loss and applied it in their performance prediction procedure. Benson [11,12] also described the losses in the nozzle and rotor. This was based upon two theories, the general theory which was applied in axial turbomachinery and related to the stagnation pressure loss and the shock theory which was related to the constant pressure model developed by Wallace. It was found inconvenient to use the axial turbomachinery model for IFR-turbines as there is a drop in relative stagnation pressure across the rotor due to the difference in blade speed between inlet and outlet.

In the shock theory the loss coefficient introduced had the same value as the loss coefficient at zero incidence, but differed at off-design conditions as it was made a function of the incidence angle. An extensive experimental investigation was carried out by measuring the stagnation pressure and temperature upstream and downstream of the

turbine. The nozzle loss coefficients were calculated according to the general theory while the rotor losses were developed as a function of pressure ratio, torque,mass flow and speed. The variation of these losses were then plotted at different operating conditions.

Benson [15], has reviewed a number of methods for representing the losses for the prediction of the off-design performance of radial turbines. He classified these losses in two categories, the casing and rotor losses. Depending on the experimental results the loss coefficients were correlated to known quantities such as turbine speed and fluid states. As a result of this history of calculations it was found that numerical differences existed between the various methods of calculating the incidence losses, and Benson suggested that the constant pressure model of Wallace be applied.

The constant pressure loss model has yielded quite satisfactory results if the effect of blade blockage is ignored. Whitfield and Wallace [16] showed that when this blockage is significant, as it is in the case of centrifugal compressors and turbines, the constant pressure loss model is not entirely satisfactory. An alternative loss model was therefore developed by using an empirically determined entropy gain multiplier by means of

which the entropy gain at incidence could be varied independently.

Probably, the most comprehensive study of losses and their mathematical modelling was carried out by Ziarati [7]. Here a detailed study of incidence losses with and without blade blockage was considered in addition to all other component loss models.

By applying suitably chosen loss coefficients, the one dimensional prediction procedures were successfully applied to the prediction of the off-design performance of IFR-turbines by many researchers [18,19,20]. It is clear that this simple theory gave good results and it has served as a design tool in turbine developments and for the establishment of performance maps for Diesel engine matching procedures. The most comprehensive one dimensional analysis is the unified approach reported in [7,21,22]. This method compared to previous one dimensional methods is more general and flexible, and has been extended to deal with mixed flow as well as radial flow turbomachines. In this method each component part is modelled as a separate routine which contains the appropriate loss model, the main linking program then specifies the operating point and calls the relevant routines in the required order to perform the calculations

step by step through the turbine. In terms of generality, flexibility, and computational time, the unified approach offers a considerable advance over the previous one dimensional methods.

The one dimensional analysis gives useful information with respect to the operating range of the turbomachine. However, its applicability is limited for design purposes where a more detailed study of the flow in the blade passage is required. A large number of two and three-dimensional flow analysis procedures exist. Wu [23] developed a general theory of three dimensional flow in turbomachines of radial, axial, and mixed flow types where a solution of the three dimensional flow problem was formulated as two dimensional solutions in two flow planes. The equations of continuity were combined with the equations of motion in either the tangential or the radial direction through the use of a stream function defined on the surface.

The streamline curvature procedure is a widely used method. In this approach a first order partial differential equation for the change in velocity along a normal was obtained and then solved in conjunction with the continuity equation for a stream tube width. This is then repeated on successive normals throughout the rotor.

This method was applied by Hamrick and many others [22,24,25,26,27]. Katsanis [28] applied the equations in the hub-shroud plane for the velocity gradient along arbitrary quasi-orthogonals rather than on normals to the stream lines. It was assumed that a mean stream surface was known from hub to shroud between the blades. On this surface a two dimensional solution for the velocity and pressure distribution was obtained, followed by an approximate calculation of the blade surface velocities.

A full three dimensional analysis was reported by Benson [29] for inviscid flow, while Khalil et el [30] used a full compressible and viscous flow analysis for a mixed flow rotor by solving the Navier-Stokes equations over the blade to blade stream channel applying the Alternating Direct Implicit method for numerical integration.

An alternative and relatively new approach is the application of finite element techniques for solving the flow equations within the rotor. This method, originally developed for stress analysis, has been successfully applied to a number of problems in fluid dynamics by solving the simplified Navier-Stokes equations for compressible and incompressible flows [31,32,33,34,35,36,37]. These equations are often

formulated using a single variable, the stream function Ψ or the velocity potential Φ, and are generally reduced to equations of Laplace or Poisson form. By a variational principle or Galerkin method a general finite element equation is derived within specified boundary conditions.

In turbomachines the variational approach was used by Worster [38] in a three dimensional analysis of the flow in a pump impeller using the velocity potential as the dependent variable. While the weighted residual formulation was reported by Lakaris [39] for full three dimensional analysis in turbomachines using the potential flow theory.

Perhaps the most popular finite element technique in meridional flow and blade to blade flow analysis in turbomachines is due to Hirsch and Warzze [40], where the governing equation is of the Poisson type solved by the Galerkin method and is of the form :

$$\frac{\partial}{\partial r}\left(k\,\frac{\partial \psi}{\partial r}\right)+\frac{\partial}{\partial z}\left(k\frac{\partial \psi}{\partial z}\right)-f=0 \qquad 1.2$$

which when the inner product of the residual and the

weight function are integrated by parts gives :

$$\int\left[k\left(\frac{\partial\Psi}{\partial r}\frac{\partial N}{\partial r}-\frac{\partial\Psi}{\partial z}\frac{\partial N}{\partial z}\right)-fN\right]dV=0 \qquad 1.3$$

In this approach the weight function is taken as equal to the trial function N in the finite element process. Then the flow field is divided into a number of non-overlaping elements where in each element the unknown stream function is supposed to have a variation of some specific form (usually polynomials) and is chosen as

$$\Psi=\sum\Psi_j N_j \qquad 1.4$$

which is substituted in equation 1.3 to give the general Galerkin equation :

$$\int\left[k\left(\frac{\partial N_i}{\partial r}\frac{\partial N_j}{\partial r}-\frac{\partial N_i}{\partial z}\frac{\partial N_j}{\partial z}\right)\Psi_i-fN_j\right]dV=0 \qquad 1.5$$

which for one element is of the form :

$$[k]^e\cdot[\Psi]^e=[f]^e \qquad 1.6$$

By assembling all equations for all elements the global form becomes :

$$[K]\cdot[\Psi]=[F] \qquad 1.7$$

In exactly the same way the blade to blade equations can be derived and solved (see Hirsch et el [40]).

A full analysis of the flow in IFR-turbines using the finite element method is given in chapter 2. This includes the hub-sroud, and volute-nozzle assembly analysis.

1.1.2 The Exhaust Diffuser

Diffusers are devices which perform the conversion of kinetic energy into pressure. As a result of this an increase of pressure in the direction of the flow occurs and, if the pressure gradient is large, separation is then a natural effect associated with the diffusion process.

Separation within a diffuser causes losses and reduces the effect flow area both of which affects the performance of the diffuser. Three types of diffusers have extensively been studied in the literature :

(1) Straight walled diffusers

(2) Conical diffusers

(3) Annular diffusers

Some of this work was carried out with uniform flow conditions at inlet, ref. [41], others with swirling flows.

CHAPTER -1-

From examining the literature one can see that there are two types of data concerning diffusers, these are in the form of maps of flow regimes, and performance. The first type of data were obtained from extensive flow visualization tests. Kline et el [42] identified four different flow regimes figure 1.6. The region of no appreciable stall is steady and uniform, the region of transitory stall is unsteady and non-uniform, while the fully developed and jet flow regimes are steady but non-uniform. Howard and Thorton [43] presented the flow regimes for annular diffuser by following the same procedures. Kwan [44] made a visualization study using smoke to investigate the vortex phenomena in conical diffusers with 6 deg. double cone angle and with swirling flow at inlet. He found that there were five flow regimes, figure 1.7, associated with the swirl, namely

(1) laminar one-celled vortex

(2) Transitional one-celled vortex flow from laminar to turbulent

(3) Turbulent one-celled vortex

(4) Transitional phenomenon of break down of two celled vortex to a one celled vortex

(5) Turbulent flow regime two celled vortex

He found that the transitional regimes were a function

of the strength of inlet swirl.

Runstadler et el [41] in extensive experimental work involving conical and rectangular diffusers presented a collection of diffuser characteristics in a form of maps ready to be applied for design purposes. Sovran and Klomp [45] presented procedures for evaluating the diffuser performance using a one dimensional analysis based upon the kinetic energy profile at inlet and discharge for non-swirling flows. Kaiser et el [48] have studied the effect of wake type non-uniform inlet velocity profiles on the first appreciable stall in flat diffusers, and showed that moderate distortion of inlet velocity profiles increased the area ratio at which for first appreciable stall occured. This was reduced, however, as the distortion became severe, and a centreline "pocket" stall developed in the most severe case. They suggested that more experiments were required before any generalizations could be made.

The effect of inlet swirl on the pressure recovery and performance of conical diffusers has been reported by McDonald et el [49] and Senoo et el [50]. Experimentally it has been shown that by imparting a limited amount of swirl at the diffuser inlet a noticeable improvement in pressure recovery resulted. This was particularly so for

large cone angle diffusers as the tendency to flow separation was reduced. From a set of experiments McDonald [49] showed the influence of swirling flow on the performance of conical diffusers. For unstalled diffuser with axial flow the introduction of swirl has little effect, but for stalled diffusers the addition of swirl improves the performance, and there is an optimum swirl for best performance. This has been presented in terms of contour plots for diffuser length versus area ratio AR-1 for cases with and without swirl. This showed, figure 1.8, that the line of optimum performance $\alpha - \alpha$ shifts to the left, which implies that shorter wide angle diffusers could be used. Senoo [50], figure 1.9, showed that swirl intensity up to 0.10 at the inlet of conical diffusers gave improved pressure recovery for wide angle diffusers.

Similar experiments have been carried out with annular diffusers. refs. [51,52,53], and a similar behaviour noticed with the introduction of swirl. There is, however, always a limit to the amount of swirl which can be tolerated beyond which the diffuser performance deteriorates.

FIG 1.1 SPECIFIC SPEED CHARACTERISTICS; REF.[1]

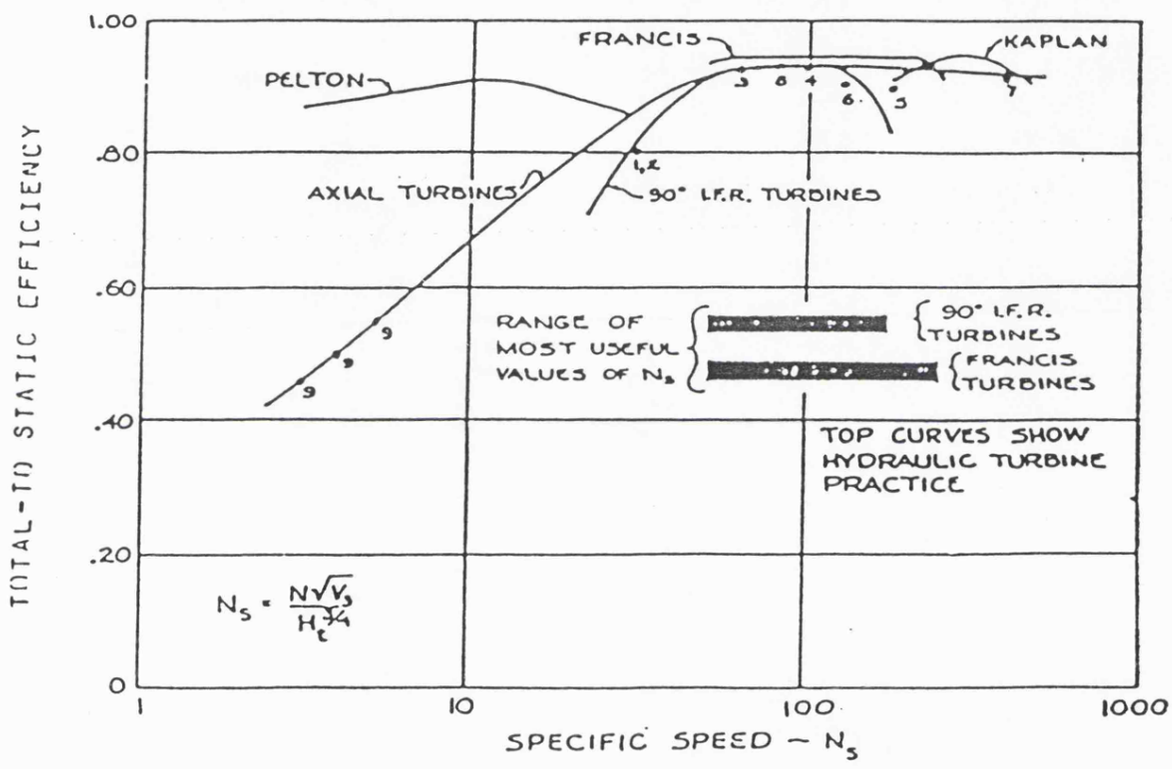

FIG 1.2 INWARD FLOW RADIAL TURBINE ROTOR

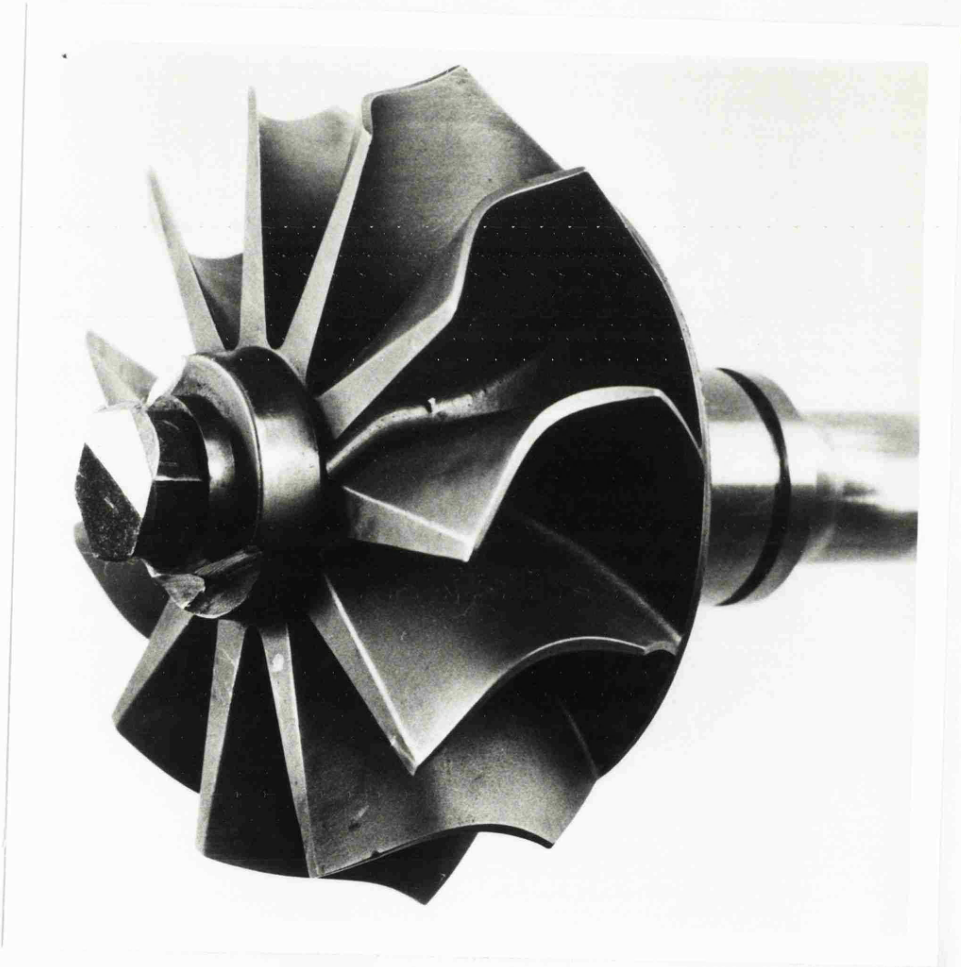

FIG 1.3 PROJECTED TORQUE CURVE WITH VARIABLE AREA TURBINE
REF.[65]

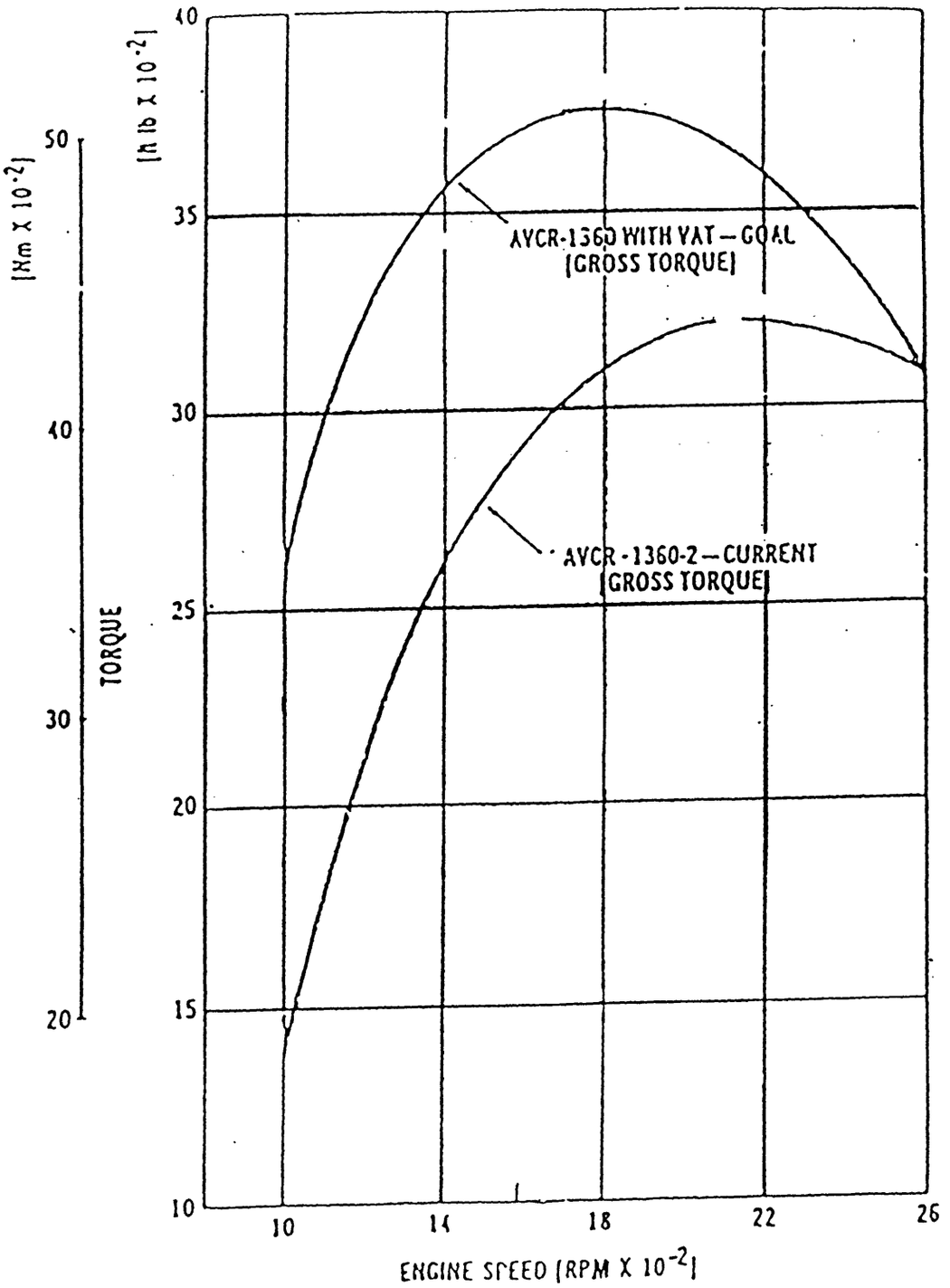

FIG 1.4 POTENTIAL CONTROL AREAS IN THE TURBINE FLOW PATH
REF.[4]

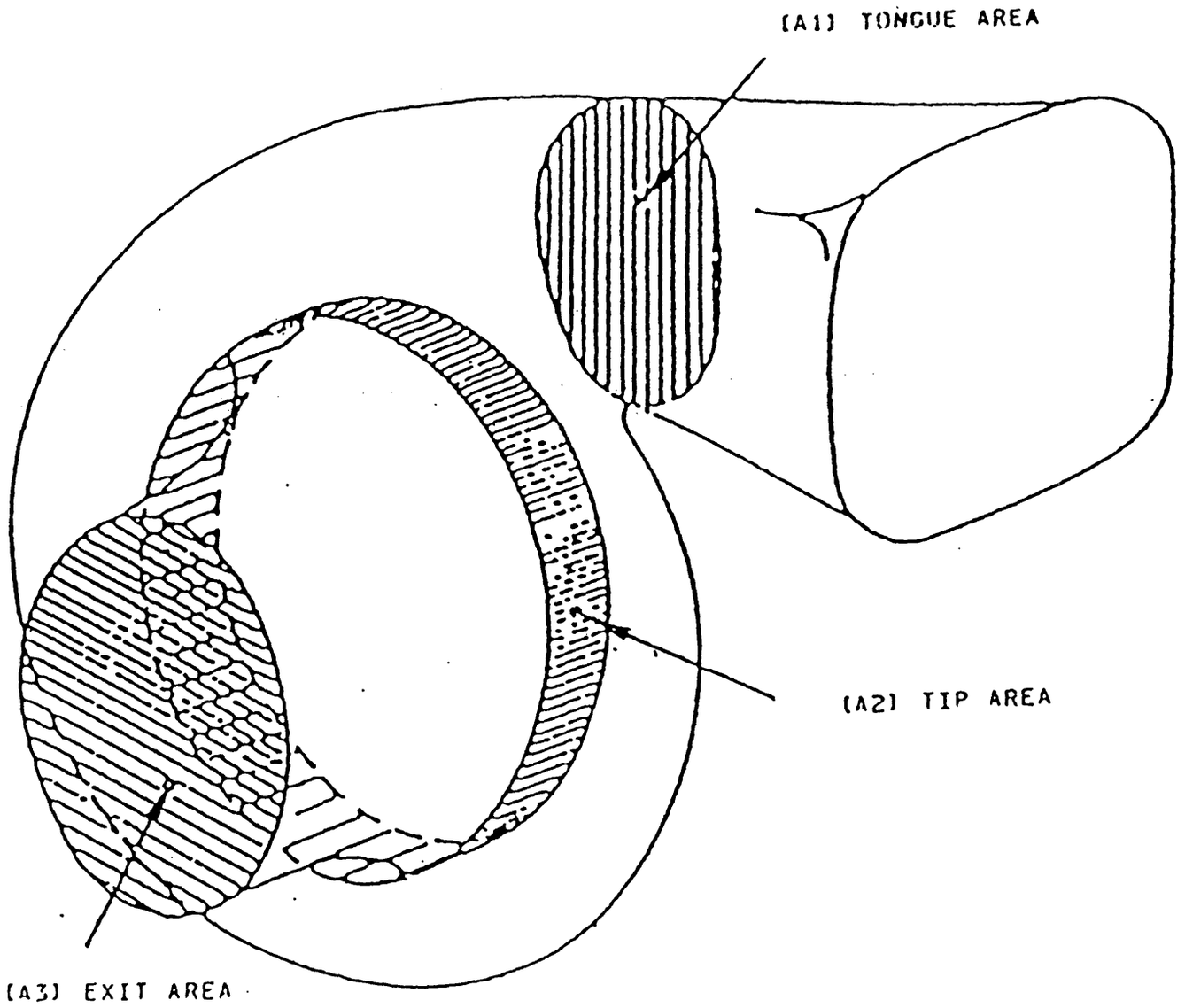

FIG 1.5 VARIABLE NOZZLE EFFECTS IN IFR TURBINES; REF.[5]

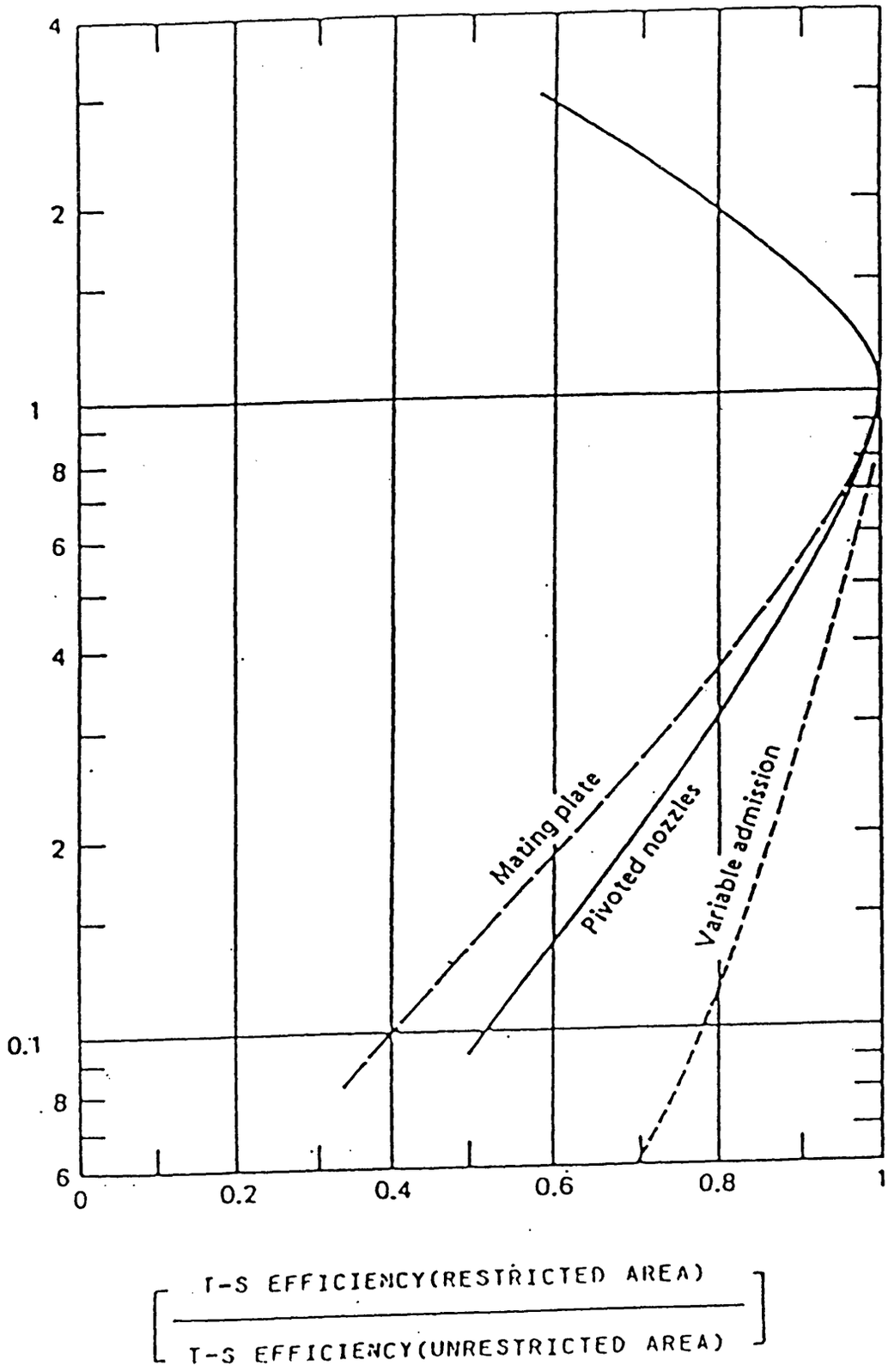

FIG 1.6 FLOW REGIMES IN FLAT DIFFUSERS; REF. [42]

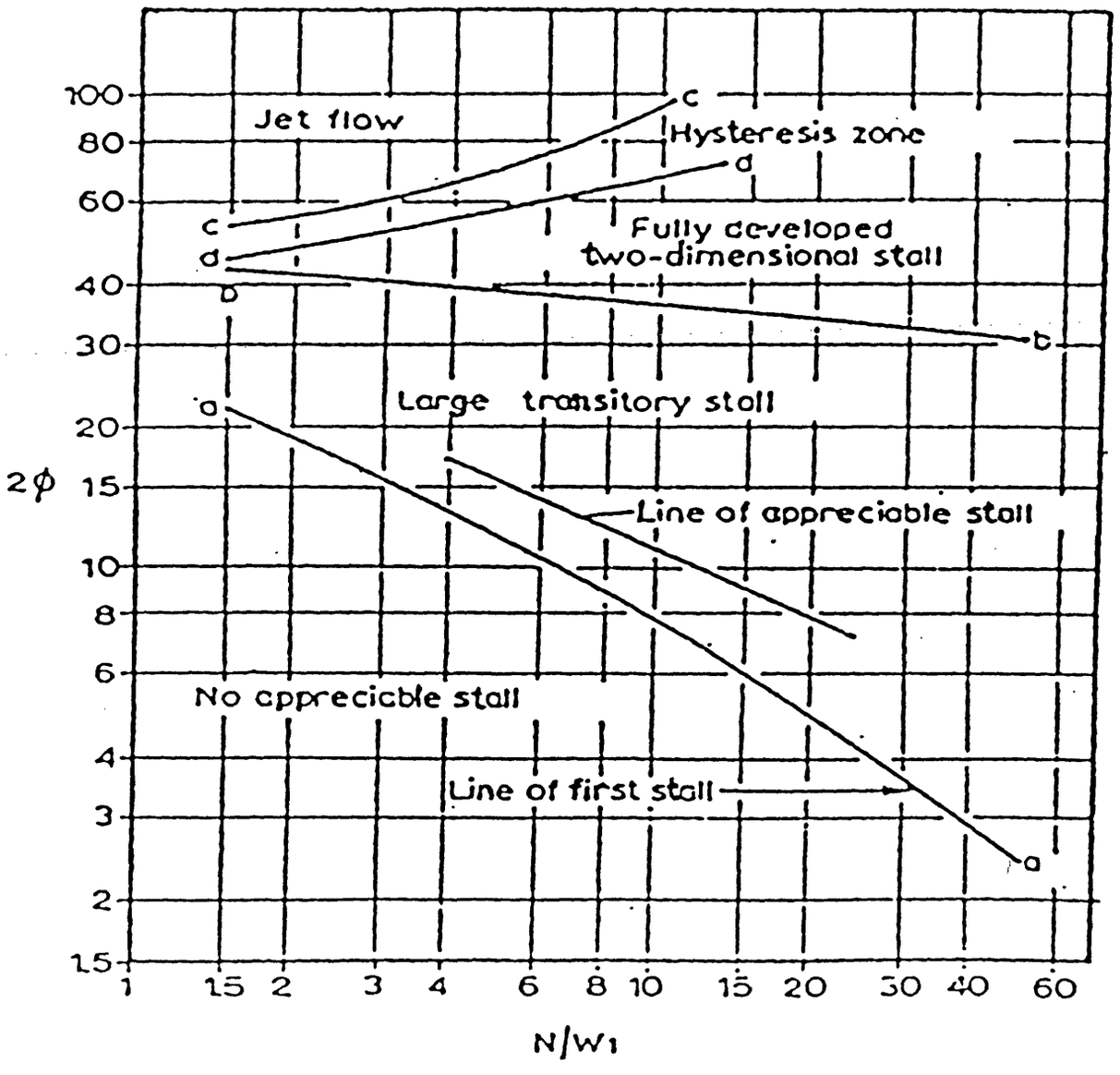

FIG 1.7 FLOW REGIMES IN CONICAL DIFFUSERS WITH INLET SWIRL; REF.[44]

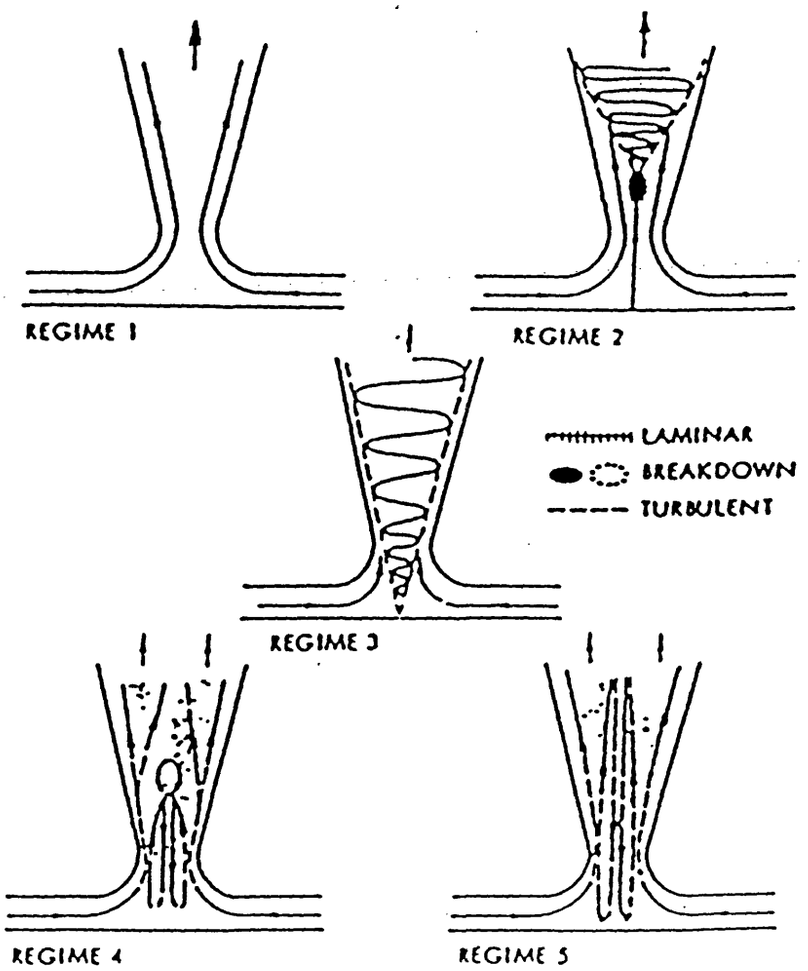

FIG 1.8 CONTOURS OF CONSTANT PRESSURE RECOVERY COEFFICIENT; REF.[49]

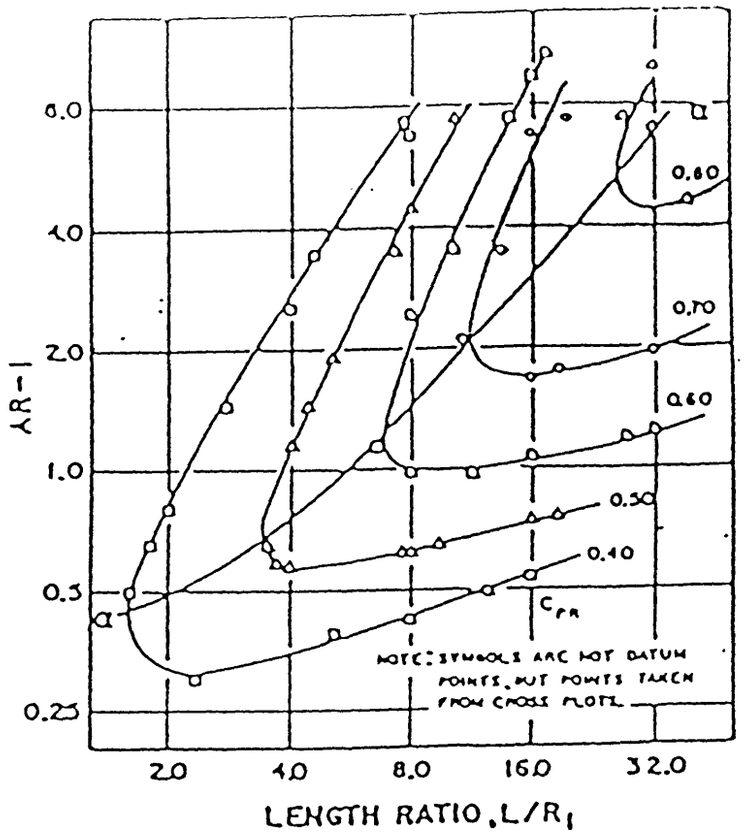

Without Swirl

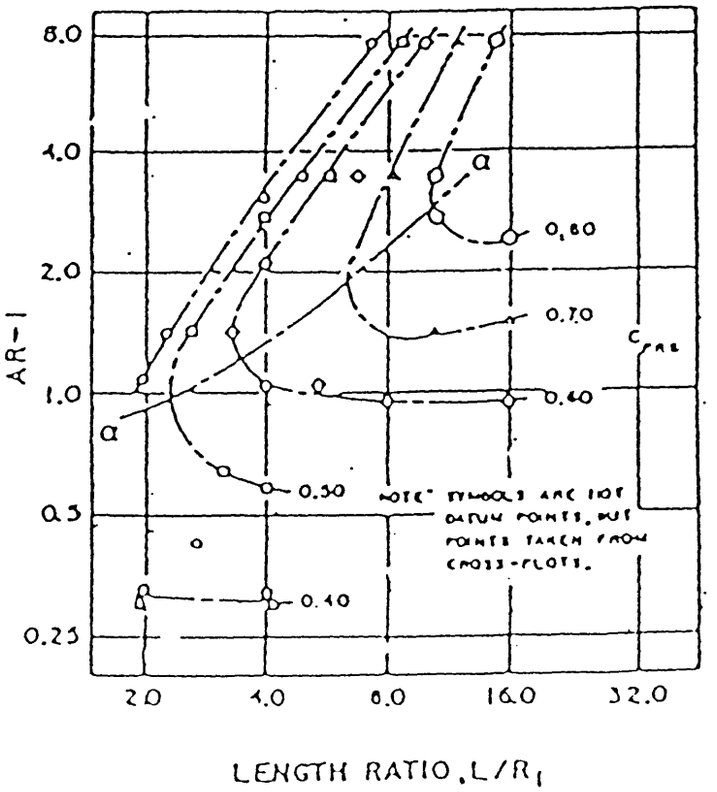

With Swirl

FIG 1.9 PRESSURE RECOVERY COEFFICIENT FOR CONICAL DIFFUSERS WITH INLET SWIRL; REF.[50]

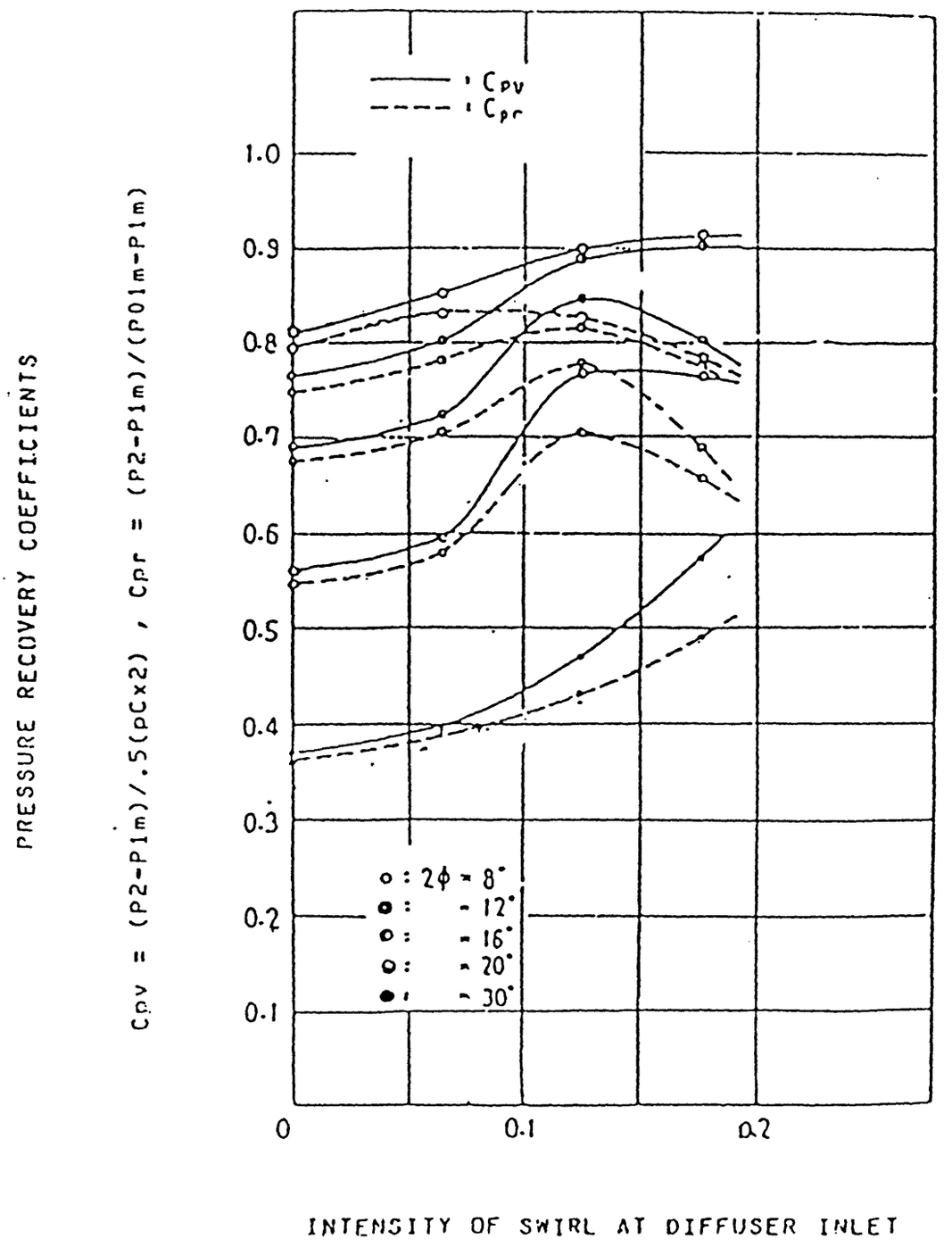

CHAPTER -11-

---

2. THEORETICAL STUDY

In order to support the experimental work it was desirable to develop theoretical procedures to predict (i) the flow through the volute and V.G. nozzles, and (ii) the nature of the flow at rotor exit which must be accepted by any exhaust diffuser. Existing streamline curvature techniques were not suitable for application to the volute nozzle flows and it was decided to develop procedures based upon the finite element method as this is most suitable for complex geometries.

Initially an analysis procedure was developed for the flow in the meridional plane of the rotor, however, it was decided to give priority to the development of theoretical procedures for the volute nozzle assembly; consequently the rotor analysis remains unfinished and it is necessary to develop a blade to blade analysis to support the existing meridional flow procedure for a full three dimensional analysis.

The fluid motion in the turbomachinery passages is represented by the Navier-Stockes equations in their general form. If the fluid is considered as unsteady, viscous, compressible, and with body forces, the complete form of the equation of the motion in cartesian

coordinates and in the X-direction takes the form :

$$\frac{\partial C_x}{\partial t} + C_x \frac{\partial C_x}{\partial x} + C_y \frac{\partial C_x}{\partial y} + C_z \frac{\partial C_x}{\partial z} =$$

$$= \rho F_x - \frac{\partial P}{\partial x} + \mu\left(\frac{\partial^2 C_x}{\partial x^2} + \frac{\partial^2 C_x}{\partial y^2} + \frac{\partial^2 C_x}{\partial z^2}\right) + \qquad 2.1$$

$$+ \mu \frac{\partial}{\partial x}\left(\frac{\partial C_x}{\partial x} + \frac{\partial C_x}{\partial y} + \frac{\partial C_x}{\partial z}\right) - \frac{2}{3}\mu \frac{\partial}{\partial x}(\nabla \cdot \bar{C})$$

together with the other equations in the Y and Z directions this can be written vectorially as

$$\frac{D\bar{C}}{Dt} = \bar{F} - \frac{1}{\rho}\nabla P + \nu \nabla^2 \bar{C} + \frac{\nu}{3}\nabla\nabla\cdot\bar{C} \qquad 2.2$$

These equations are of limited use because of the extreme difficulty of finding a solution. When numerical solutions are to be applied considerable simplifying assumptions have to be made before a solution is attempted.

CHAPTER -11-

2.1 Finite Element Analysis Of The Flow In The Rotor

2.1.1 Derivation Of The Equations

The general form of the Navier-Stockes and continuity equations in polar cylindrical coordinates are

$$\frac{\partial \bar{C}}{\partial t} + \Omega \times \bar{C} + (\bar{C}\cdot\nabla)\bar{C} = \bar{F} - \frac{1}{\rho}\nabla P + \nu\left(\nabla \bar{C} + \frac{1}{3}\nabla\nabla\cdot\bar{C}\right) \qquad 2.3$$

$$\nabla(\rho\bar{C}) = 0 \qquad 2.3$$

By using the vector identity

$$\nabla^2\bar{C} = \nabla\nabla\bar{C} - \nabla\times\nabla\times\bar{C} \qquad 2.4$$

equation 2.3 can be written in the form

$$\frac{\partial \bar{C}}{\partial t} + (\bar{C}\cdot\nabla)\bar{C} + \Omega\times\bar{C} = \bar{F} - \nabla\frac{P}{\rho} - \nu\left[\nabla\times\nabla\times\bar{C} + \frac{4}{3}\nabla(\nabla\cdot\bar{C})\right] \qquad 2.5$$

For steady, inviscid flow, and without body Forces this equation takes the form

$$\nabla\frac{P}{\rho} + (\bar{C}\cdot\nabla)\bar{C} + \Omega\times\bar{C} = 0 \qquad 2.6$$

and for a blade row rotating with angular velocity becomes

$$\nabla \frac{P}{\rho} + (\bar{W} \cdot \nabla)\bar{W} + 2\Omega \times \bar{W} + \Omega \times (\Omega \times \bar{W}) = 0 \qquad 2.7$$

The continuity equation is given by

$$\nabla(\rho W) = 0 \qquad 2.8$$

Equations 2.5 and 2.7 can be expanded for the three axis R,θ,X to give the simplified form of the Navier-Stockes equations

$$C_r \frac{\partial C_r}{\partial r} + \frac{C_\theta}{r} \frac{\partial C_r}{\partial \theta} + C_x \frac{\partial C_r}{\partial x} - \frac{C_\theta^2}{r} = -\frac{1}{\rho} \frac{\partial P}{\partial r}$$

$$C_r \frac{\partial C_\theta}{\partial r} + \frac{C_\theta}{r} \frac{\partial C_\theta}{\partial \theta} + C_x \frac{\partial C_\theta}{\partial x} - \frac{C_r C_\theta}{r} = -\frac{1}{\rho} \frac{\partial P}{\partial \theta} \qquad 2.9$$

$$C_r \frac{\partial C_x}{\partial r} + \frac{C_\theta}{r} \frac{\partial C_x}{\partial \theta} + C_x \frac{\partial C_x}{\partial x} = -\frac{1}{\rho} \frac{\partial P}{\partial x}$$

and for the rotor

$$W_r \frac{\partial W_r}{\partial r} + \frac{W_\theta}{r} \frac{\partial W_r}{\partial \theta} + W_x \frac{\partial W_r}{\partial x} -$$

$$-(\Omega r + W_\theta)^2 = -\frac{1}{\rho} \frac{\partial P}{\partial r}$$

$$h_0 = h + \frac{1}{2}c^2$$

$$h = h_{01} - \frac{1}{2}c^2 + u(u+W\theta) \longrightarrow$$

$$W_r \frac{\partial W_\theta}{\partial r} + \frac{W_\theta}{r} \frac{\partial W_\theta}{\partial \theta} + W_x \frac{\partial W_\theta}{\partial x} + \frac{W_r W_\theta}{r} + 2\Omega W_r = -\frac{1}{\rho} \frac{\partial P}{\partial \theta} \quad 2.10$$

$$W_r \frac{\partial W_x}{\partial r} + \frac{W_\theta}{r} \frac{\partial W_x}{\partial \theta} + W_x \frac{\partial W_x}{\partial x} = -\frac{1}{\rho} \frac{\partial P}{\partial x}$$

The pressure term in the above equations can be eliminated by the application of the first law of thermodynamics which is of the form

$$T ds = dh - \frac{1}{\rho} dP \quad 2.11$$

and for an isentropic process

$$dh = \frac{1}{\rho} dP \quad 2.12$$

The Euler turbomachinery equation is

$$\Delta W = U C_\theta - U_1 C_{\theta_1} = h_o - h_{o1} = \Omega r C_\theta - \Omega_1 r_1 C_{\theta_1} \quad 2.13$$

with $\Omega_1 r_1 C_{\theta_1} = \lambda$ as the prewhirl

$$h_o = h_{o1} + \Omega r C_\theta - \lambda \quad 2.14$$

$$h = h_{01}\left\{-\tfrac{1}{2}c^2 + u(u+w_\theta)\right\} \rightarrow$$

with
$$\left.\begin{aligned} w^2 &= w_\theta^2 + w_m^2 \\ c^2 &= c_\theta^2 + w_m^2 \\ c_\theta &= u + w_\theta \end{aligned}\right\} \quad \text{fig 2.1}$$

$$\therefore \left\{-\tfrac{1}{2}c^2 + u(u+w_\theta)\right\} = \tfrac{1}{2}(u^2 - w^2) \longrightarrow$$

$$dh_{01} = \left[h_1 + \tfrac{1}{2}c_1^2\right]_{\text{I}} - \left[h_1 + \tfrac{1}{2}c_1^2\right]_{\text{II}}$$

$h_{1\text{I}} = h_{1\text{II}}$ at entry ..

& $\tfrac{1}{2}\left[c_{1\text{I}}^2 - c_{1\text{II}}^2\right] = 0$ irrotational flow.

CHAPTER -11-

By substituting the velocity vector from the velocity triangle, fig. 2.1, equation 2.14 can be readily developed to

$$h = h_{o1} + \frac{1}{2}U^2 - \frac{1}{2}W^2 - \lambda \qquad 2.15$$

Then differentiating and assuming

$$dh_{o1} = 0$$
$$d\lambda = 0$$
$$dh = u\,du - w\,dw = \frac{1}{\rho}dP \qquad 2.16$$

Substituting into equation 2.12 yields

$$\frac{dP}{\rho} = u\,du - w\,dw \qquad 2.17$$

and with respect to r is

$$\frac{1}{\rho}\frac{\partial P}{\partial r} = u\frac{\partial u}{\partial r} - w\frac{\partial w}{\partial r} \qquad 2.18$$

Substituting into the first equation of 2.10 and noting that

$$u = \Omega r$$

$$u\frac{\partial u}{\partial r} = \Omega^2 r \qquad 2.19$$

$$\bar{w}\frac{\partial \bar{w}}{\partial r} = w_x\frac{\partial w_x}{\partial r} + w_r\frac{\partial w_r}{\partial r} + w_\theta\frac{\partial w_\theta}{\partial r}$$

yields

$$\Omega^2 r - W_x \frac{\partial W_x}{\partial r} + W_r \frac{\partial W_r}{\partial r} + W_\theta \frac{\partial W_\theta}{\partial r} + \\ + W_r \frac{\partial W_r}{\partial r} + \frac{W_\theta}{r} \frac{\partial W_r}{\partial \theta} + W_x \frac{\partial W_r}{\partial x} - \frac{(\Omega r + W_\theta)^2}{r} = 0 \qquad 2.20$$

With $\frac{\partial}{\partial \theta} = 0$ for axial symmetry, and rearranging yields

$$\frac{\partial W_x}{\partial r} - \frac{\partial W_r}{\partial x} + \frac{W_\theta}{W_x}\left(\frac{\partial W_\theta}{\partial r} + \frac{W_\theta}{r} + 2\Omega\right) = 0 \qquad 2.21$$

Introducing the stream function which satisfies the continuity equation as

$$W_x = k \frac{\partial \Psi}{\partial r}$$

$$W_r = -k \frac{\partial \Psi}{\partial x} \qquad 2.22$$

$$k = \frac{1}{\rho r b}$$

and rearranging yields

$$\frac{\partial}{\partial r}\left(k \frac{\partial \Psi}{\partial r}\right) + \frac{\partial}{\partial x}\left(k \frac{\partial \Psi}{\partial x}\right) =$$

$$= -\frac{W_\theta}{W_x}\left[\frac{1}{r}\frac{\partial}{\partial r}(r W_\theta) + 2\Omega\right] \qquad 2.23$$

CHAPTER -11-

By developing the last equation of 2.10 following the same procedure and using relations 2.22 yields

$$\frac{\partial}{\partial r}\left(k\frac{\partial \Psi}{\partial r}\right)+\frac{\partial}{\partial x}\left(k\frac{\partial \Psi}{\partial x}\right)=$$

$$=-\frac{W_\theta}{W_r}\left[\frac{1}{r}\frac{\partial}{\partial x}\left(rW_\theta\right)\right] \qquad 2.24$$

Equations 2.23 and 2.24 represent the final equations in the r,x directions which represent the flow in the meridional plane.

2.1.2 Derivation Of The Density Equation

The density is calculated from the gas law

$$\rho = \frac{P}{RT} \qquad 2.25$$

and it is therefore necessary to develop relationships for the pressure and temperature at any position in the rotor. The temperature is given through the relative stagnation enthalpy as

$$T = T_{oir} - \frac{\gamma-1}{2\gamma R}\left(U_1^2 - U^2 + W^2\right) \qquad 2.26$$

where

$$W^2 = W_x^2 + W_r^2 + W_\theta^2 \qquad 2.27$$

In terms of the stream function

$$W_x^2 = \frac{1}{\rho^2}\left(\frac{1}{rb}\frac{\partial \psi}{\partial r}\right)^2$$
$$W_r^2 = \frac{1}{\rho^2}\left(\frac{1}{rb}\frac{\partial \psi}{\partial x}\right)^2 \qquad 2.28$$

from the velocity triangles, figure 2.1,

$$W_\theta^2 = W_x^2 \tan^2\Phi = \left(\frac{\tan\Phi}{r}\right)^2 r^2 W_x^2 = C_d^2 r^2 W_x^2 \qquad 2.29$$

Then

$$W^2 = \frac{1}{\rho^2}\left[\left(\frac{1}{rb}\frac{\partial \psi}{\partial r}\right)^2\left(1 + C_d^2 r^2\right) + \left(\frac{1}{rb}\frac{\partial \psi}{\partial x}\right)^2\right] \qquad 2.30$$

Substituting into equation 2.26 yields

$$T = T_{oir} - \frac{\gamma - 1}{2\gamma R}\left(U_1^2 - U^2\right) -$$
$$- \frac{1}{\rho^2}\left\{\frac{\gamma - 1}{2\gamma R}\left[\left(1 + C_d^2 r^2\right)\left(\frac{1}{rb}\frac{\partial \psi}{\partial r}\right)^2 + \left(\frac{1}{rb}\frac{\partial \psi}{\partial x}\right)^2\right]\right\} \qquad 2.31$$

i.e.

$$T = A - \frac{B}{\rho^2} \qquad 2.32$$

where :

$$A = T_1 + \frac{\gamma-1}{2\gamma R}\left(U^2 - U_1^2\right) + \frac{\gamma-1}{2\gamma R} W^2$$

$$B = \frac{\gamma-1}{2\gamma R}\left[\left(1 + C_d^2 r^2\right)\left(\frac{1}{rb}\frac{\partial \psi}{\partial r}\right)^2 + \left(\frac{1}{rb}\frac{\partial \psi}{\partial x}\right)^2\right] \qquad 2.33$$

The pressure is calculated through the empirical loss coefficient ξ defined as the drop in relative stagnation pressure over the isentropic process, from fig. 2.2

$$\xi = \frac{P_s - P_{or}}{P_s} = 1 - \frac{P_{or}}{P_s} = 1 - \frac{P_{or}}{P_{oir}}\frac{P_{oir}}{P_s} \qquad 2.34$$

leading to

$$(1 - \xi)\left(\frac{T_{or}}{T_{oir}}\right)^{\frac{\gamma}{\gamma-1}} = \frac{P_{or}}{P_{oir}} \qquad 2.35$$

Then

$$P = P_{oir}(1 - \xi)\left(\frac{T}{T_{oir}}\right)^{\frac{\gamma}{\gamma-1}} = \left[\frac{(1 - \xi) P_{oir}}{T_{oir}^{\frac{\gamma}{\gamma-1}}}\right] \cdot T^{\frac{\gamma}{\gamma-1}} \qquad 2.36$$

and this leads to

$$\rho = \frac{K_d}{R}\left(A - \frac{B}{\rho^2}\right)^{\frac{1}{\gamma-1}} \qquad 2.37$$

which is solved iteratively for the value of ρ.

2.1.3 Formulation Of The Finite Element Equation

There are several methods for evaluating the finite element equation such as the variational principle, the weighted residual, the least squares method, etc...

The approach used here is the Galerkin weighted residual method. In this procedure an interpolation or shape function is assumed for the dependent variable (in this analysis the stream function). By substitution of this approximation into the original partial differential equation and boundary conditions, a resultant error, or residual is calculated. This residual is then made to vanish over the entire domain in an average sense. From this sequence of operations will result a system of linear equations to be solved for the stream function at each nodal point.

The meridional flow equations 2.23 and 2.24 are of the

CHAPTER -11-

Poisson form

$$\nabla^2 \Psi + F = 0 \qquad 2.38$$

The solution domain, figure 2.3, is divided into a number of non-overlapping elements, here four noded quadrilateral elements are used. At each node the unknown stream function Ψ is approximated by $\tilde{\Psi}$ and is assumed to be given by :

$$\Psi = \tilde{\Psi} = \sum_{i=1}^{4} N_i \Psi_i \qquad 2.39$$

Where :

Ψ - is the exact value

$\tilde{\Psi}$ - is the approximate value

Ni - is the assumed interpolation function

n - is the number of nodes

The interpolation function is only a function of the coordinates of the element nodes By substituting this approximate value into the main partial differential equation results in an error ϵ

$$\nabla^2 \tilde{\Psi} + F = \varepsilon \qquad 2.40$$

CHAPTER -11-

The weighted residual method defines the unknowns in such a way that the residual ϵ will be forced to be zero over the domain by forming a weighted average of it and specifying that this average vanish over the domain i.e.

$$\int \varepsilon \cdot W_t \, d\Gamma = 0 \qquad 2.41$$

This result in a system of equations for each element :

$$[K]^e[\Psi]^e = [f]^e \qquad 2.42$$

Where $[K]^e$ is the stiffness matrix for the element

A similar equation is obtained for the entire domain by assembling all the equations associated with each element.

In the Galerkin approach, the weight function wt is chosen to be equal to the interpolation function then equation 2.41 becomes

$$\int \varepsilon \, N_j \, d\Gamma = 0 \qquad 2.43$$

Which gives in many cases a symmetrical global matrix.

The details of the derivation of the Galerkin equation is given in appendix "A".

CHAPTER -11-

2.2 Finite Element Analysis Of Flow In The Volute Nozzle Assembly

2.2.1 Two Dimensional Flow About An Isolated Aerofoil

In order to develop the finite element analysis for flow in the volute nozzle assembly an analysis of flow around an isolated aerofoil was first considered, prior to application to a cascade of blades. The validity and accuracy of the procedure was checked by comparing results with those presented in reference [57]. The analysis considered a steady inviscid, incompressible, and two dimensional flow by applying the Galerkin method of weighted residual. The solution domain, figures 2.4a,b, is divided into a number of elements (quadrilateral with four nodes), and within each of these elements the solution is approximated by a polynomial function. The residual which results from this approximation is averaged by applying the weight function as the interpolation function itself and forced to be zero over the domain.

2.2.1.1 Choice Of The Field Variable

The velocity potential was chosen as the field variable. This is derived from the irrotationality defined as

$$\omega = \frac{\partial C_x}{\partial y} - \frac{\partial C_y}{\partial x} = 0 \qquad 2.44$$

which leads to the definition of the potential function as :

$$C_x = \frac{\partial \Phi}{\partial x}$$
$$C_y = \frac{\partial \Phi}{\partial y} \qquad 2.45$$

Introducing these into the continuity equation assuming incompressibility yields a Laplace equation

$$\nabla^2 \Phi = 0 \qquad 2.46$$

By applying the Galerkin method of weighted residual to this equation yields :

$$\int \nabla^2 \tilde{\Phi} \cdot N_j \, d\Gamma = 0 \qquad 2.47$$

where :

$$\tilde{\Phi} = \sum_{i=1}^{4} N_i \Phi_i$$

and $\tilde{\Phi}$ is the approximate value of the field variable

By substituting this in the main equation 2.46, and applying the divergence theorem yields :

$$\left[\iint \nabla N_i \nabla N_j \, d\Gamma \right] \cdot \Phi_i = \int \frac{\partial \Phi}{\partial n} \, ds \qquad 2.48$$

This gives the elementary stiffness matrix $[K]^e$:

$$[K_e]^e[\Phi_i]^e = [f]^e \qquad 2.49$$

Now by introducing the appropriate boundary conditions this equation can be solved for the potential function values at the nodes.

2.2.1.2 Boundary Conditions

From equation 2.48, the following equation was derived (the details are in appendix "A")

$$\left[\iint_n \left(\frac{\partial N_i}{\partial x}\frac{\partial N_j}{\partial x} + \frac{\partial N_i}{\partial y}\frac{\partial N_j}{\partial y}\right) dx\,dy\right]\Phi_i =$$

$$= \int_s \frac{\partial \Phi}{\partial n} N_j\, ds \qquad 2.50$$

where $$h_i = \int_s \frac{\partial \Phi}{\partial n} N_j\, ds \qquad 2.51$$

represent the linear integral of the derivative along a normal to the boundary.

If the flow is assumed to be uniform far upstream and downstream of the domain, the velocity at inlet will be purely axial. The exit velocity can then be determined from the conservation of mass condition. This implies

that the derivitives along the normal at inlet and exit boundaries are known and are equal to the velocities. This is a Neuman type boundary which is a result of using the velocity potential as the field variable. Along solid boundaries the normal component of the derivitive is zero, as there is no flow crossing these boundaries. This implies that a solid surface in potential flow requires no specification of the boundary condition, the solution will automatically take up the correct value.

2.2.1.3 The Solution Domain

In applying the finite elment method in problems which encounter circulation or lift the domain of integration is no longer a simply connected domain and constitutes a multiply connected one. This multiconnectivity renders the application of the divergence theorem incorrect. The multiply connected domain, figure 2.4a, can be transformed into a simply connected domain by introducing a cross-cut connecting the two boundaries; this will transfer the two regions into one domain bounded by 1-2-3-4-5-6'-6-6''-1. Since the points 2,4 and 1,5 are of infinitesimal width apart, the integrals along them are equal and of opposite sign, ie :

$$\int (1-2) = -\int (4-5) \qquad 2.52$$

and :

$$\int (1\text{-}2\text{-}3\text{-}4\text{-}5\text{-}6'\text{-}6\text{-}6'') = \int (1\text{-}2) + \int (2\text{-}3\text{-}4) + \int (4\text{-}5) + \int (5\text{-}6\text{-}1) = \int (2\text{-}3\text{-}4) + \int (5\text{-}6\text{-}1) = \int \Gamma_1 + \int \Gamma_2 \qquad 2.53$$

which represent the actual boundary Γ.

The circulation and lift in potential flow problems would only occur if a slit boundary such as that mentioned above crosses the flow field. The nodes on either side of this cross will have identical velocities but will differ in potential which is equal to the circulation. The circulation is to be applied either externally refs. [36,38], or to be determined within the solution as a function of the inlet and exit flow conditions depending upon the numerical solution applied .

The technique reported in ref. [57] is best suited to the finite element applications and is used here. The circulation is considered as an additional degree of freedom but is not connected to any node. This nodeless variable is associated with the elements that have one or more nodes on either side of the splitting boundary. The interpolating function for these elements has a special form and differs from the rest of the elements by including the circulation term.

CHAPTER -11-

The details of the derivation of the interpolating function for these elements and their solution is in appendix "C".

2.2.1.4 Solution Procedure

The element used was a quadrilateral isoparametric one with four nodes. The local coordinates were placed at the centroid of the element. The solution was carried out as follows :

Firstly, an automatic mesh construction was set up from the geometrical data which consisted of a set of coordinate points on both aerofoil surfaces, the suction and the pressure surface. At far upstream and downstream, and far upper and lower regions, the elements were large while at locations closer to the aerofoil the mesh was made fine. Secondly, the boundary conditions were specified, and the elementary matrices built up, then following the assembly procedure by elements the global matrix was constructed. To this global matrix the prescribed boundary conditions were introduced. The global matrix was then solved by a direct method using the diagonal pivoting strategy [62]. This procedure of solution has been pursued because the number of nodes were relatively small, and no special arrangements were made in

order not to operate with zero elements. In other cases, however, spacial methods ,see section 2.2.2.3, were adopted for solving the system of equations where only the non zero elements are operated upon.

2.2.2 Flow Investigation In Volute Nozzle Assembly

In reviewing the literature it can be seen that a large number of prediction methods have been developed for turbomachinery impellers. Starting from the early work of Wu [23] where the classical theory of analysing the flow in radial and mixed flow impellers was set, and ending with the recent developments using two and three dimensional finite element analysis [38,39,40]. Researchers have concentrated mainly on the moving parts of the turbomachine because it was considered to be the main area affecting turbomachine efficiency. It was not until recently that research into variable geometry techniques involving the stationary parts of the volutes and guide vanes showed the need for further study in this area [58].

Because of the three dimensional nature of the flow within the volute the flow properties at the inlet of the nozzle blades will be strongly affected by the volute

design. The blockage in the flow passage caused by the developing boundary layer on the walls will cause each vane to have different inlet conditions this will result in different blade loadings around the nozzle ring. A study in which the flow is described in the volute and stationary vanes will, therefore, contribute to better design and eventually lead to improved performance of the machine as a whole. Such developments have become increasingly important with the development and application of the variable geometry turbines.

In this section, a method which investigates the flow field in an volute nozzle assembly in two dimensional space is described. The flow is assumed to be inviscid, incompressible and without body forces. The finite element method is applied, with the basic equations being of the same structure to those used in the previous section equations 2.46 and 2.50.

2.2.2.1 The Choice Of The Dependant Field Variable

In applying the finite element method in flow problems, it is often convenient that the field dependent variables chosen be either the stream function or the velocity potential. In either case the governing equation is of the

Laplace or Poisson form. Each of these approaches is characterized by the boundary conditions. The stream function gives rise to Dirichlet conditions, ie the value of the variable is specified. The velocity potential, however, leads to Neuman type boundary conditions where the derivatives of the variable normal to the boundary is specified. These derivatives are zero along solid boundaries, whilst along the boundaries of inlet and exit they represent the velocities

In cascade problems, Norrie [59], applied the stream function and in an iterative way adjusted the location of the stagnation stream line. The value of the stream function. at the nodes were determined by superposition. The stream function was expressed as a sum of harmonic functions $\Psi 1$, $\Psi 2$, $\Psi 3$ such that

$$\Psi = \Psi_1 + a_2 \Psi_2 + a_3 \Psi_3 \qquad 2.54$$

and the problem subjected to the boundary conditions :

(1) Ψ is constant at surface

(2) $\Psi = F(x,y)$ at boundaries

(3) The Kutta condition applied at the trailing edge (where there is a stagnation point).

The constants a2, a3 were determined as :

$$\nabla^2 \Psi_1 = 0 \quad \begin{cases} \Psi_1 = 0 & \text{on } \Gamma_1 \\ \Psi_1 = -Cx\,y & \text{" } \Gamma_2 \end{cases} \qquad 2.55$$

$$\nabla^2 \Psi_2 = 0 \quad \begin{cases} \Psi_2 = 0 & \text{" } \Gamma_1 \\ \Psi_2 = 1 & \text{" } \Gamma_2 \end{cases} \qquad 2.56$$

$$\nabla^2 \Psi_3 = 0 \quad \begin{cases} \Psi_3 = 1 & \text{" } \Gamma_1 \\ \Psi_3 = 0 & \text{" } \Gamma_2 \end{cases} \qquad 2.57$$

By solving the Laplace equation for each set of boundary conditions the values Ψ1, Ψ2, Ψ3 were determined.

Now for each element surrounding the trailing edge the velocity component was determined for each case respectively. The Kutta condition was applied as : Cxt = Cyt = 0 ,see fig. 2.4b, which leads to the determination of the constants a2, a3.

The above procedure could be applied to a straight cascade, where the velocity at exit is to be found from the continuity condition. But it is not applicable to the case where the cascade is of a circular shape, as the case of the present problem, as at the far downstream station only the radial velocity can be found from continuity;

this is not sufficient for the stream function formulation where the boundary condition requires the tangential component of the velocity as well.

In the case of a nozzleless volute this may be found from a free vortex condition, while for nozzled volutes this is not valid due to the presence of the vanes, figure 2.5. The application of the potential function was therefore, considered more convenient for the nozzled volute case, as the derivative along the normal to the boundary leads to the radial component of velocity only.

2.2.2.2 Boundary Conditions

Refering to figure 2.5, the boundary conditions are of the form :

(1) On solid boundaries, the Neuman type condition is set to zero

(2) At the inlet station the derivatives along the normal is equal to the axial velocity and is constant as the flow conditions here are assumed to be uniform.

(3) At the exit station, the Neuman boundary condition is applicable which is equal to the radial component of velocity.

(4) Across the radial cuts it is considered that there is no flow crossing these boundaries, and then the Neuman

type condition is set to zero

2.2.2.3 Solution Procedure

The mesh generation and the coordinates of the nodal points is an important part in the solution. This has been done from the geometrical data which includes the volute area variation and the outer boundary which is taken as a logarithmic spiral variation. The geometric data consists of : the volute inlet diameter, the nozzle inlet diameter, the blade chord, the blade inlet angle and the nozzle subtended angle. The nozzle blade is symmetrical and is characterized at the leading edge by a circle of 3 mm diameter. The blade surfaces being straight lines extending from the trailing edge are tangent to this circle.

The far downstream station is taken as 4/3 of the nozzle ring length, as any further increase in distance did not affect the computed flow field. The solution domain was divided into three distinctive zones, namely : the volute , the nozzle ring and the far downstream zone. Each of these could be divided to any specified number of subregions according to the refinement of the mesh required and the whole mesh was automatically generated, figures 5.9a,b,c, show three different mesh sizes.

CHAPTER -11-

The fluid properties at the far upstream station include, the stagnation pressure and temperature and the mass flow rate. The radial component at the far downstream station was then determined from the continuity condition assuming incompressible flow.

The finite element equation was of the Galerkin type which has been derived earlier. There are two important aspects with respect to this problem, (i) The assembly of the global matrix, and (ii) the method of solving a large system of equations resulting from this method.

Generally, the most common technique in finite element methods is Iron's frontal procedure [60] for symmetric matrices and that of Hood's [61] for unsymmetric cases. These two techniques are based on the principle of assembly and elimination (Gauss elimination strategy) in the same time , using the core store to back up the completely assembled equation, and eventually, recalling these equations in reverse order for back substitution.

Here in this problem a rather different method of assembly and solving the global matrix is presented. This method assembles the elementary matrices by nodes and not by elements. Each node gives an equation which is a result of all the elements surrounding that particular node.

Accordingly all the nodes have been classified as a function of their position as : corner nodes with one or three elements; line nodes with two elements and central nodes with four elements, see appendix "C". Each group of nodes is stored in a one dimensional array with their corresponding elements. As with fine meshes a very large number of elements is involved, the assembly of the equations was made instantaneously and without creating new vectors. This strategy resulted in a considerable space saving. The method of deriving the equations and assembling by nodes is given in appendix "C". Because the global matrix resulted in a large and sparse matrix, only the non zero elements were retained, this led to further space saving. Eventually this procedure led to the creation of two matrices, one containing the non zero elements and the other containing only their column identifications.

As a comparison between this method and the direct methods, it can be shown that for the fine mesh the global matrix is of the order of 1200 x 1200 while by using the method presented here the global matrix is 1200 x 10 only and shows a large saving in computer space.

The method of solving the two resultant matrices is the direct elimination and back substitution procedure given

by ref. [63]. This method does not require the global matrix to be definite positive, and is equally applicable to symmetric as well as non symmetric matrices.

The principle of the solution is that of using the two partially packed arrays, one from the non zero elements, and the other from their column identifications in a Gauss elimination technique. The pivot is taken as the maximum element in the row that contains a minimum number of non zero elements, and by back substitution reaches the solution sought. The final results are then stored in the same array as that used for the input vector.

After solving the system of equations for Φ, the constant potential function contours are plotted and the pressure distribution on each blade surface found.

The pressure was derived by considering an isentropic process and by defining a pressure coefficient as

$$C_p = \frac{P_i - P_\infty}{P_{o\infty} - P_\infty} \qquad 2.58$$

For isentropic flow this becomes :

$$C_p = 1 - \left(\frac{C_i}{C_\infty}\right)^2 \qquad 2.59$$

which is a function of the calculated velocities at the centroid of each element; hence

$$P_i = (P_{ox} - P_x) \cdot C_p + P_x \qquad 2.60$$

FIG 2.1 VELOCITY TRIANGLES AND FLOW ANGLES FOR A ROTOR BLADE

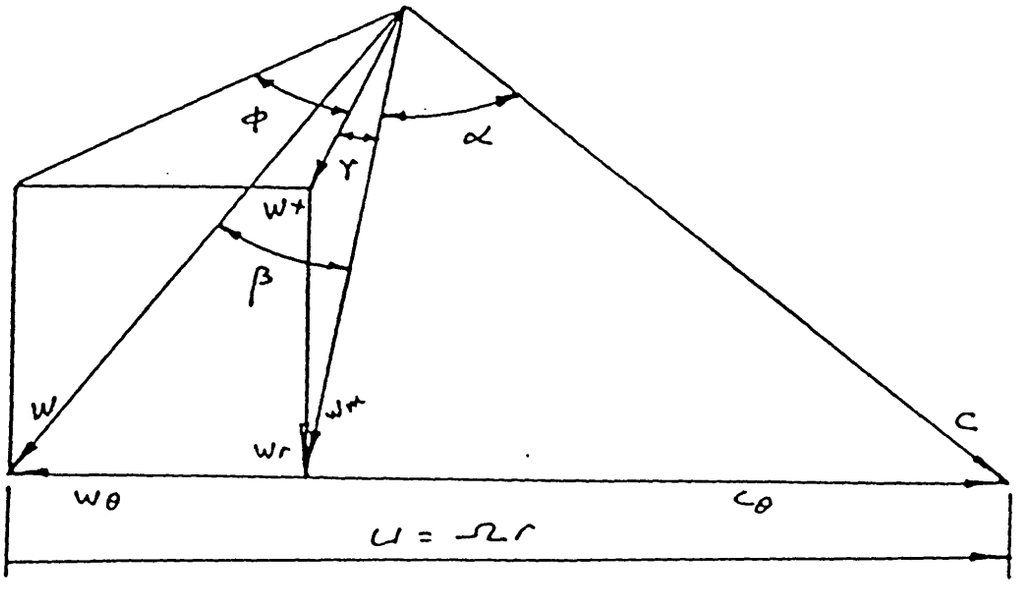

FIG 2.2 ENTHALPY ENTROPY DIAGRAM FOR A POINT IN THE ROTOR PASSAGE

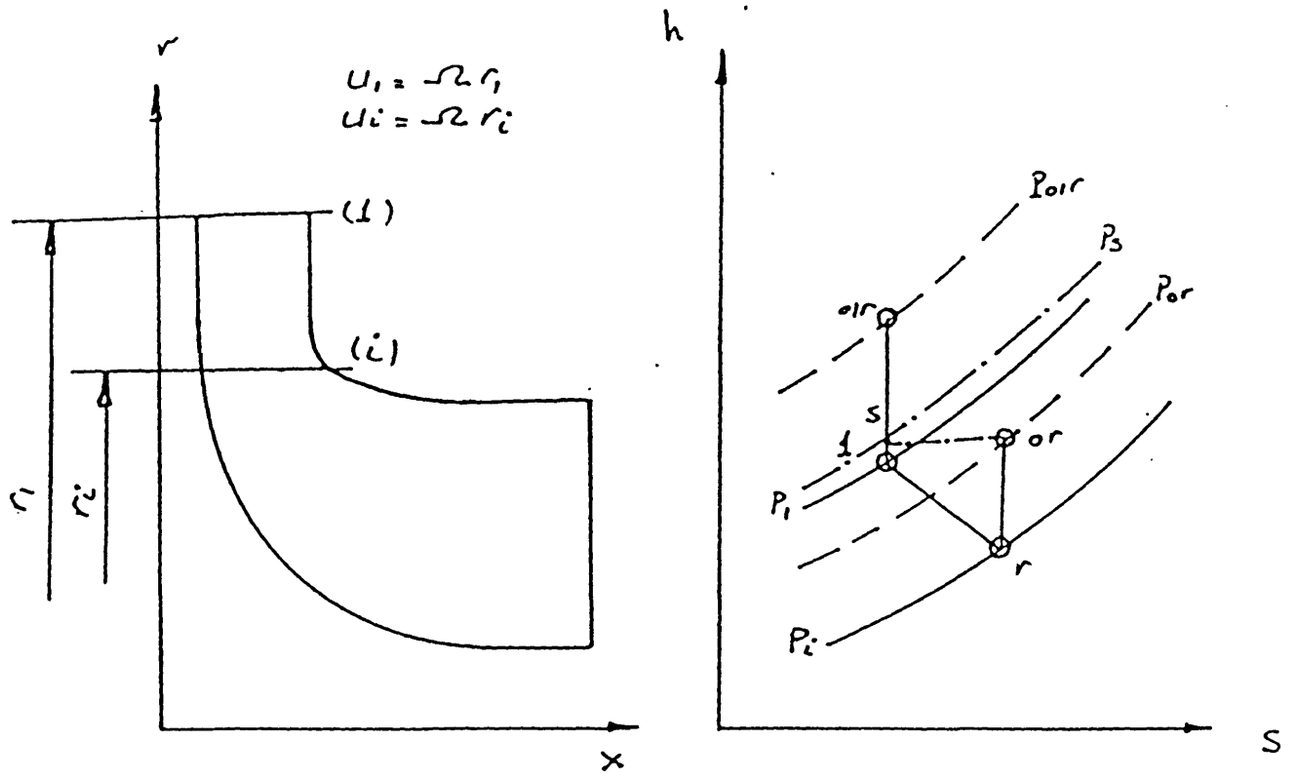

FIG 2.3 HUB SHROUD SOLUTION DOMAIN AND ITS BOUNDARIES FOR THE FINITE ELEMENT ANALYSIS

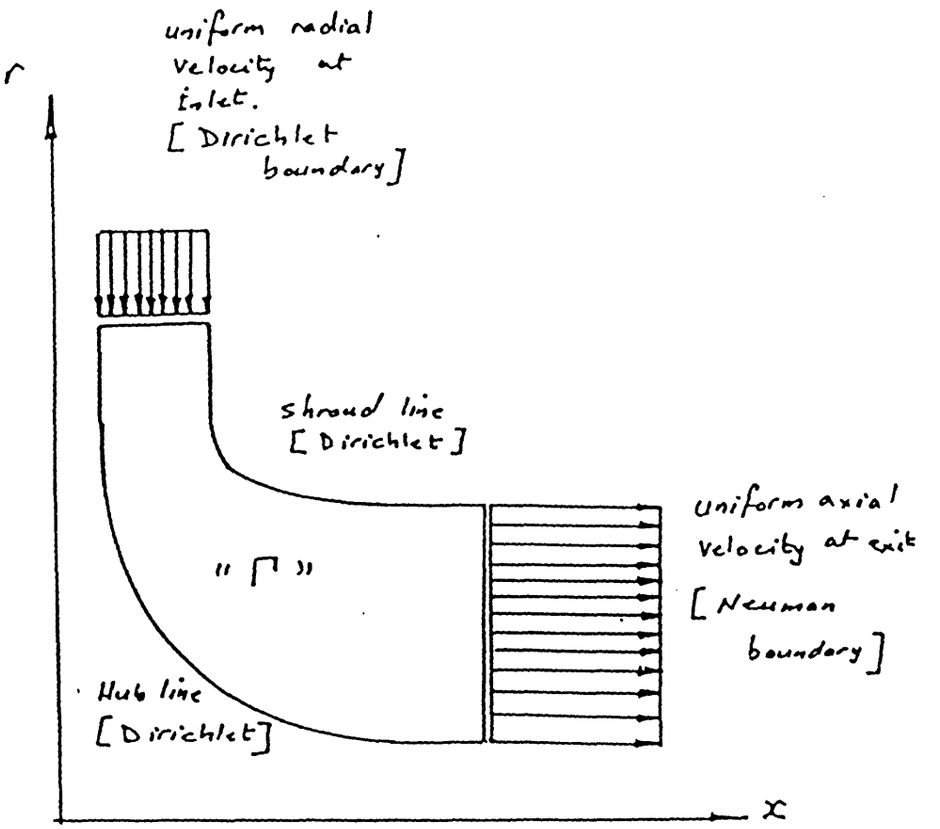

FIG 2.4a SOLUTION DOMAIN FOR THE ISOLATED AEROFOIL USING THE VELOCITY POTENTIAL FUNCTION

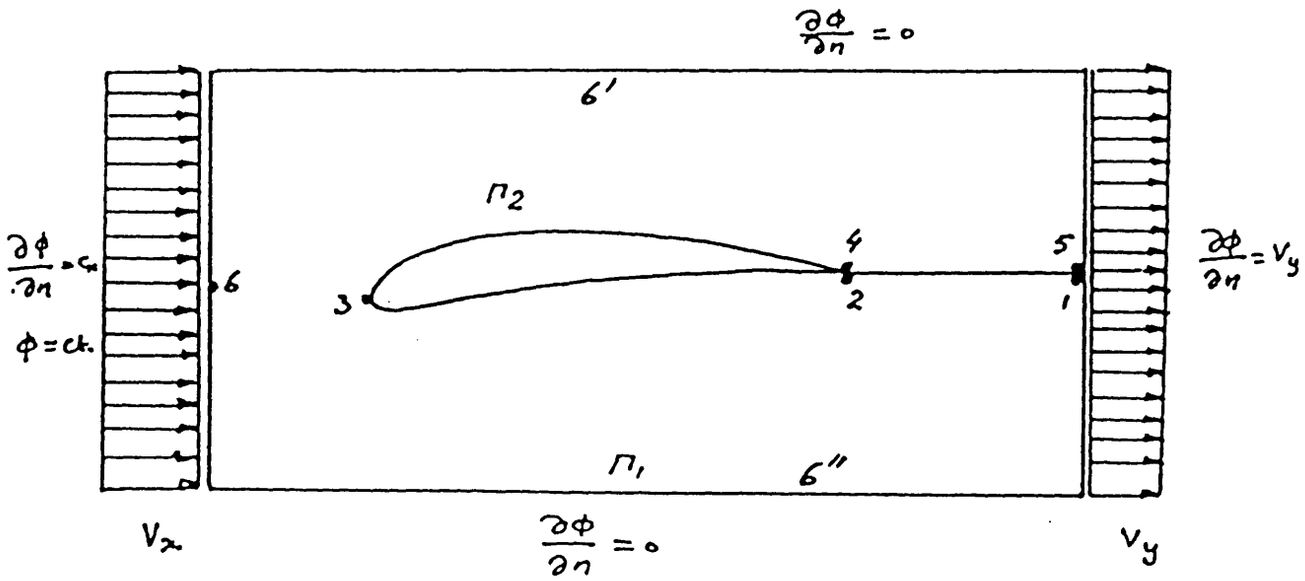

FIG 2.4b SOLUTION DOMAIN FOR THE ISOLATED AEROFOIL USING THE STREAM FUNCTION

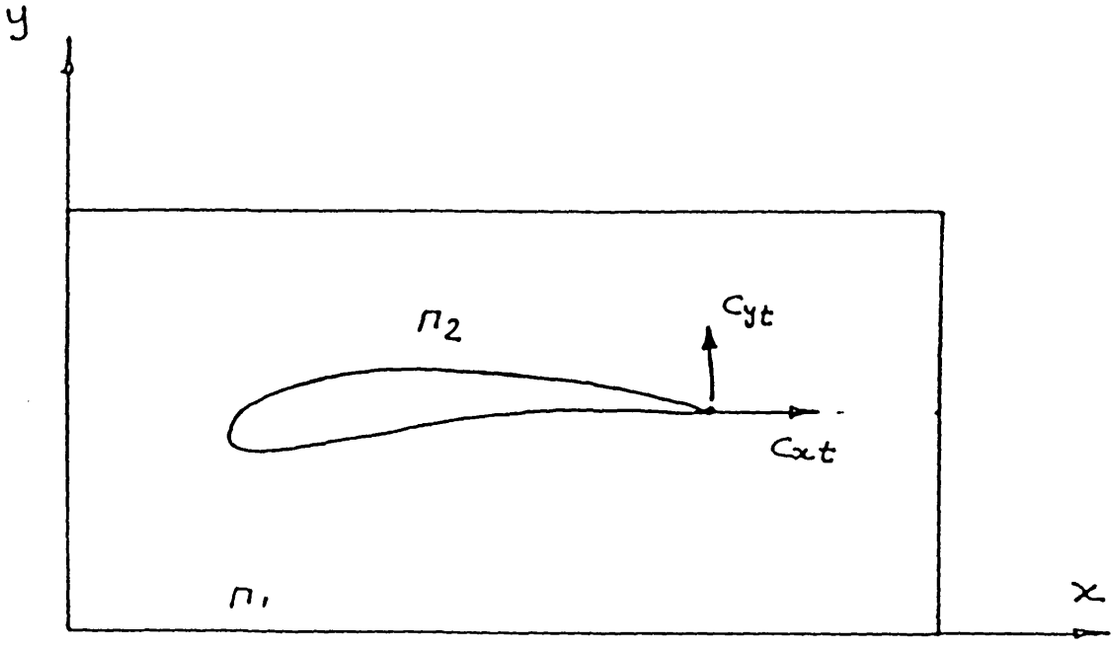

FIG 2.5 SOLUTION DOMAIN FOR THE VOLUTE NOZZLE ASSEMPLY ANALYSIS

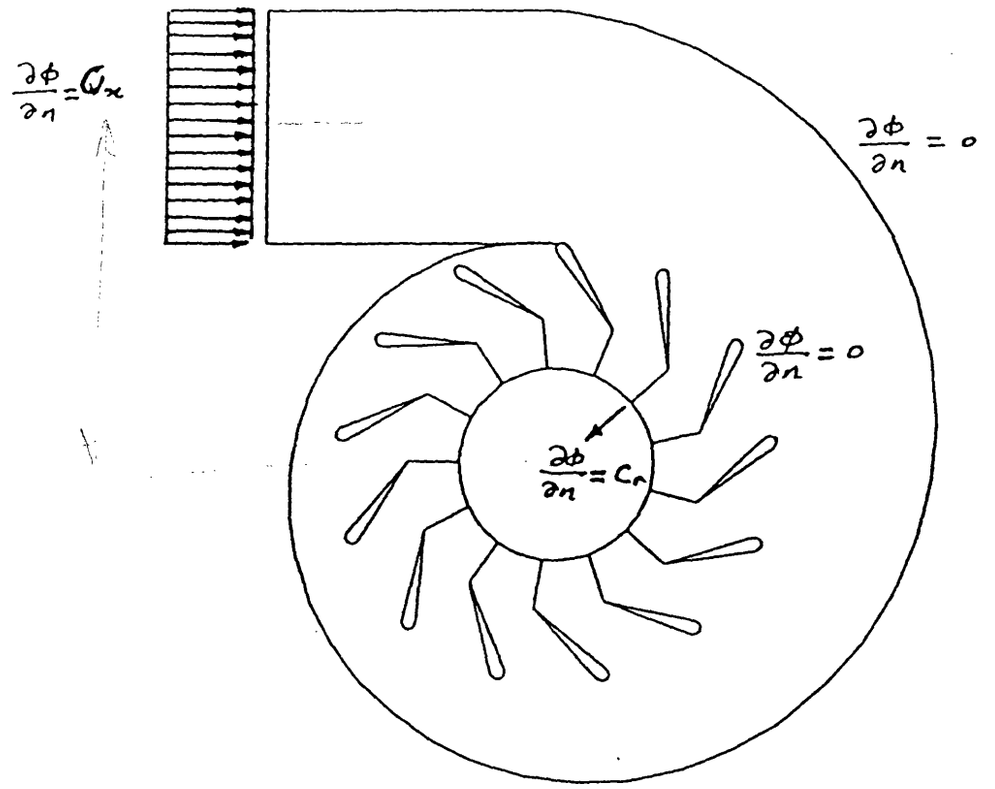

CHAPTER -111-

3. DESCRIPTION OF APPARATUS AND EXPERIMENTAL INVESTIGATIONS

3.1 TURBINE RIG

The test rig and associated instrumentation is shown in figure 3.1 and a schematic layout is given in fig. 3.2. The test rig consisted of a turbine, a dynamometer, inlet piping and, diffuser fitted at the turbine discharge. The turbine rotor and the dynamometer wheel were mounted on the same shaft. Initially the rig was fitted with a combustion chamber at the turbine inlet to provide the necessary power for high turbine loads and speeds. It was, however, not found possible to obtain exhaust flow traverse measurements when running with the combustion chamber operating. Exhaust dirt and unburnt fuel fouled the yaw probe and led to repeated stoppages to clean the probe. similar problems were encountered when the rig was operated with cold air, condensation and icing being the cause of probe blockage. In order to overcome these difficulties, the combustion chamber was replaced by an electric heater consisting of six elements of six kilowatts each.

The compressed air from a high pressure reciprocating compressor was passed through pressure control valves, an

orifice plate for mass flow measurement, and the electric heater described above, before entering the turbine. After passing through the turbine the air was exhausted to the atmosphere.

The dynamometer, fig. (3.3), was attached to the turbine casing, and consisted of two main parts, the outer (fixed) assembly and the inner (floating) assembly, the outer body completely surrounded the inner parts and in turn floated on hydrostatic air bearings separating it from the air bearing assembly. The brake oil chamber completely surrounded the absorption wheel. The brake oil supply pipes were made of flexible transparent plastic material to keep the degree of aeration under strict observation. The torque force on the floating inner part was measured by a torque balance arm, which carried two weights on either side and a load cell. The whole assembly was balanced statically by adjusting the weights on the balance arm.

The instrument measuring stations are shown in fig. 3.2. The mass flow was measured at station (1) with an orifice plate manufactured and assembled according to the BS1042. The static pressure at turbine inlet was measured by four static pressure tappings and the total temperature by a chrome/alamel type thermocouple. At turbine exit a

similar thermocouple was used for the total temperature measurements. A five hole probe was traversed radially at a number of cross sections in the exhaust diffuser. The thermodynamic quantities recorded were the total pressure, flow angle and the indicated static pressures. These were eventually used to calculate the true static pressure and flow velocity components in the diffuser. The rotational speed of the turbine was measured by an electronic counter and the torque force by a calibrated strain gauge load cell.

3.1.1 The Exhaust Diffuser

At off-design points the flow from the rotor has a degree of swirl which is dependent up on the geometry of the rotor and pressure ratio across the turbine. This swirl is not necessarily determintal to the performance of the conical diffuser which in turn should have a beneficial effect on the overall turbine performance. It has been shown by many researchers [49,50,51,52,53] that with low magnitudes of swirl, diffuser performance is actually improved and that separation in wide angle diffusers is suppressed. In order to investigate these effects three conical diffusers with the same area ratio of approximately 2.8 and different cone angles of 8,16 and 29 degrees were manufactured, figures 3.4a,b, show two of

these diffusers.

In turbocharger applications, space considerations are very often extremely important, short wide angle diffusers have therefore, been included in this study. Substantial separation would normally be expected in these diffusers, however, in this investigation it is anticipated that the large degree of swirl will help to prevent or delay separation, thereby leading to satisfactory performance.

3.1.2 Inlet Nozzles

In order to assess the turbine performance at a number of nozzle restrictions, a nozzled plug was used. This consisted of a circular plug on which the nozzle blades were cut with a width corresponding to the desired restriction. Figure 3.5 shows the dimension of these rings which were designed and manufactured by Ziarati [7]. Figure 3.6 shows the configuration of the three nozzled plugs chosen for this experiment, namely, the non-restricted ring which has a 10.5 mm blade width, the 20% restricted ring with a 9 mm width, and the 50% restricted ring with a 5 mm width. Each of these nozzle rings has 13 blades, one blade of each configuration has a special shape to block the flow entering the end area of the volute. Each of the nozzle rings mentioned were

tested for four rotor speeds of 30000, 40000, 50000 and 60000 revs/min and a number of pressure ratios in order, to cover the operating range of the turbine.

3.2 Experimental Procedure

The turbine performance was evaluated using three nozzle rings with three conical diffusers with different cone angles described in the previous section. A five hole commercially available probe was traversed radially at a number of cross sections in order to measure stagnation and static pressure and the flow direction. For the three diffusers tested the turbine speed was maintained constant while the pressure ratio across it was varied to give a number of different swirl intensities at rotor exit. All tests were carried out with the diffuser exit open to the atmosphere. In addition to measuring the radial pressure distribution with the five hole probe, the static pressure was calculated using a theoretical technique based upon the radial equilibrium and energy equations, as it was anticipated that the probe would not give accurate readings close to the duct wall. The static pressure distribution was calculated from the measured wall static pressure and the measured stagnation pressure and flow angle distribution. The full procedure is given in section 3.4.1.

CHAPTER -111-

3.3 Instrumentation

3.3.1 Static Pressure And Scanivalve

The geometry of the static pressure tappings plays a very important role in the accuracy of the pressure measurements. It was assumed that if the hole size approached zero the error in static pressure approached zero, but for practical measurements, the size and the dimension of these holes must be properly designed. In this experiment the static pressure holes were designed following the recommendations of ref. [54], and the static pressure tapping diameter was 1 mm.

The locations of the static pressure tappings around the volute, on a selected number of nozzle blades, and along the shroud are shown in figs. 3.7a,b,c. A scanivalve and a single pressure transducer was used for pressure measurements and controlled by a PDP8 computer system. Each time the computer readings were logged a coupled mercury manometer for one pressure tapping was also recorded to provide a calibration. Fig. 3.8 shows a typical calibration curve. Other pressures at turbine exit and for mass flow measurements were measured directly by mercury manometers. An absolute pressure transduser was connected to position No. 1 of the five hole probe as

the pressure there was high; whilst water manometers were used for the other positions

3.3.2 Five Hole Probe

The total and static pressures at traverse points were calculated through the following measured quantities :

P1 : The indicated total pressure

P2(=P3) : The Indicated static pressures

P4,P5 : The pitch angle indicated pressures

By setting P2=P3 the flow angle was recorded directly by the traverse gear protractor.

The static pressure is more sensitive and more subject to errors in measurements than the total pressure. The introduction of the probe into the passage can modify the static pressure due to the reduction in the cross sectional area. For cylindrical probes perpendicular to the flow, the drop in static pressure at the probe cross section and downstream of it has been found experimentally to be :

$$\frac{P_{s1} - P_{s2}}{P_t - P_{s1}} = 1.2 \frac{a}{A} \qquad 3.1$$

Where :

Ps1 :- Measured static pressure

Ps2 :- Modified static pressure

Pt :- Total pressure

a :- Projected probe area

A :- passage area

The static pressure was obtained using the calibration curves supplied with the probe in the following manner :

(1) The pressures P1,P2,P3,P4,P5 were recorded

(2) The coefficients A1,A2,A3,A4 were computed as

$$A_1 = \left(\frac{P_4 - P_5}{P_1 - P_2}\right)$$

$$A_2 = \left(\frac{P_t - P_s}{P_1 - P_2}\right)$$

$$A_3 = \left(\frac{P_1 - P_t}{P_t - P_s}\right) \qquad 3.2$$

$$A_4 = 1.2 \times \left(\frac{a}{A}\right)$$

The pitch angle was found from the probe calibration chart, fig. (3.9), as a function of the coefficient A1 The static and total pressures were then calculated by combining equations 3.1 and 3.2 to give :

$$Ps = Pt - B2 \qquad 3.3$$

$$Pt = p1 - B3$$

where

B1 = P1-P2

$$B2 = B1 \times A2$$
$$B3 = B2 \times A3 \qquad 3.4$$

The values of the static pressure were then adjusted as a function of the insertion depth in each cross section as follow :

$$Ps2 = Ps1 - A4 \times (Pt - Ps1) \qquad 3.5$$

The appropriate factor A4 being obtained from the manufacturers calibration.

3.4 Analysis Of The Experimental Data

3.4.1 Theoretical Method For Static Pressure Calculation

This analysis was developed as an alternative to the measured static pressure distribution, see section 3.3.2. It has been carried out in order to check the accuracy of the measurements taken by the probe in the regions close to the wall, as it was anticipated that at these locations the probe measurements would be affected by the proximity of the wall.

The calculated pressure was obtained from the total pressure and flow angle distribution and the measured static pressure at the wall. For a small layer Δr, between

the two traverse points 1 and 2, see figure 3.10, the radial equilibrium condition was applied as :

$$\frac{1}{\rho}\frac{dP}{dr} = \frac{C_\theta^2}{r}$$

$$\frac{dP}{dr} = \frac{\rho C^2 \sin^2\alpha}{r} \qquad 3.6$$

The flow was considered to be incompressible within the layer Δr , and the quantities ρ , α , and c were then considered constants, hence :

$$\int_{P_1}^{P_2} dP = (\rho C^2 \sin^2\alpha)\int_{r_1}^{r_2}\frac{dr}{r} \qquad 3.7$$

Integrating between P1,P2 and between radii r1,r2 leads to :

$$P_2 - P_1 = (\rho C^2 \sin^2\alpha)\, \ln\frac{r_2}{r_1}$$

$$\frac{P_2 - P_1}{\ln\frac{r_2}{r_1}} = \rho C^2 \sin^2\alpha = \beta \qquad 3.8$$

Now at position (2), the energy equation is given by :

$$P_{o2} = P_2 + \frac{1}{2}\rho C_2^2$$

$$2\left(P_{o2} - P_2\right)\cdot \sin^2\alpha = \rho C_2^2 \sin^2\alpha = \beta \qquad 3.9$$

Combining equations 3.8 and 3.9, yields :

$$P_2 = \frac{\gamma P_{o2} + P_1}{1 + \gamma} \qquad 3.10$$

where

$$\gamma = 2\sin^2\alpha \cdot \mu \frac{r_2}{r_1} \qquad 3.11$$

Initially position (1) is considered to be at the duct wall and the measured wall static pressure gives (P1). With the measured flow angle and stagnation pressure P02, the static pressure P2 at the new radius r2 can be found. The computation is then repeated in steps across the duct passage with the computed pressure becoming the required initial pressure P1 for the next step.

The velocity at each position was then calculated from the energy equation and the gas property relationship as

$$C_2 = \sqrt{\frac{2\,P_{o2} - P_2}{\rho_2}} \qquad 3.12$$

3.4.2 Averaging Techniques And Swirl

From the non-uniform pressure and velocity distributions at the diffuser inlet and discharge it was necessary to calculate average values in order to quantify the operating conditions and diffuser performance. Generally the averaged values do not satisfy the laws of continuity, energy, and momentum simultaneously in any particular application. Therefore the averaging method used should be consistent in its domain of application. In this section it is shown that for the energy equation to be satisfied all pressures must be mass averaged and the velocity momentum averaged. In order to define these averaged quantities a brief description of the method is presented first.

Any thermodynamic quantity (q) can be averaged by using the following relationship :

$$Q = \frac{\int q\,dX}{\int dX} \qquad 3.13$$

Where :

Q is the averaged value

X is a parameter that defines the kind of averaging used, it could be an area, mass flow or momentum, and the

averaged value then is called an area, mass, or momentum averaged value.

Area averaged velocity, in relation 3.13, is given by :

$$C_A = \frac{\int c\,dA}{\int dA} \qquad 3.14$$

For a circular cross section, dA = 2 x π x r x dr

then

$$C_A = \frac{\int_o^R C(2\pi r\,dr)}{\int_o^R 2\pi r\,dr} =$$

$$= \int_o^R C\left(2\frac{r}{R^2}\right)dr \qquad 3.15$$

This area averaged velocity satisfies the continuity condition i.e. m = ρ x A x C . But does not satisfy the momentum or kinetic energy condition.

An average velocity which satisfies the momentum condition is given by :

$$C_m \cdot m = \int c\,dm$$

$$C_m = \frac{1}{m}\int c\,dm \qquad 3.16$$

This is a mass averaged velocity and leads to :

$$C_m = \frac{\int_o^R C^2 \left(2 \frac{r}{R^2}\right) dr}{C_A} \qquad 3.17$$

The momentum coefficient β is usually defined as :

$$\beta = \frac{C_m \dot{m}}{C_A \dot{m}} = \frac{\int_o^R C^2 \left(2 \frac{r}{R^2}\right) dr}{\left[\int_o^R C \left(2 \frac{r}{R^2}\right) dr\right]^2} \qquad 3.18$$

Similarly an average velocity can be defined to satisfy the kinetic energy condition, then :

$$C_E^2 = \frac{1}{C_A} \int C^3 \left(2 \frac{r}{R^2}\right) dr \qquad 3.19$$

The kinetic energy coefficient is then defined as :

$$\alpha = \frac{\frac{1}{2} m C_E^2}{\frac{1}{2} m C_A^2} = \frac{\int C^3 \left(2 \frac{r}{R^2}\right) dr}{\int C \left(2 \frac{r}{R^2}\right) dr} \qquad 3.20$$

For a distorted flow,

$$\alpha > \beta > 1$$

Similar averaging techniques can be applied to the pressure. However, it is only the mass averaged pressure which is meaningful, the mass averaged static and total pressures are given by :

$$P_m = \frac{\int p\,dm}{\int dm} = \int P \left(\frac{C_x}{C_A}\right)\left(2\frac{r}{R^2}\right) dr \qquad 3.21$$

$$P_{om} = \frac{\int p_o\,dm}{\int dm} = \int p_o \left(\frac{C_x}{C_A}\right)\left(2\frac{r}{R^2}\right) dr \qquad 3.22$$

Substituting for $P_o = P + \frac{1}{2}\rho C^2$ and subtracting yields :

$$P_{om} - P_m = \int_0^R \frac{1}{2}\rho C^2 \left(\frac{C}{C_A}\right)\left(2\frac{r}{R^2}\right) dr$$

$$P_{om} - P_m = \frac{1}{C_A}\int_0^R \frac{1}{2}\rho C^3 \left(2\frac{r}{R^2}\right) dr \qquad 3.23$$

$$P_{om} - P_m = \frac{1}{2}\rho C_E^2$$

Consequently the difference of the mass averaged stagnation and static pressures satisfies the kinetic energy condition for incompressible flow. From this it is clear that : Area-averaged velocity satisfies continuity

condition, Mass-averaged velocity satisfies momentum condition, and Momentum-averaged velocity satisfies the kinetic energy condition. Hence, from now onwards, the axial velocity must be area averaged, the absolute velocity momentum averaged, and the static and total pressures mass averaged.

The pressure recovery coefficient in the diffuser Cp and the stagnation pressure loss coefficient w, can be written using these averaged values as :

$$C_p = \frac{P_{2m} - P_{1m}}{\frac{1}{2}\rho C_E^2} = \frac{P_{2m} - P_{1m}}{P_{01m} - P_{1m}} \qquad 3.24$$

and

$$\omega = \frac{P_{01m} - P_{02m}}{P_{01m} - P_{1m}} \qquad 3.25$$

A second pressure recovery coefficient based on the measured wall pressure at inlet and exit of the diffuser has also been calculated as :

$$C_{pw} = \frac{P_{2w} - P_{1w}}{P_{01m} - P_{1m}} \qquad 3.26$$

The derivation of the pressure recovery coefficients

are derived in appendix "E".

In order to quantify the degree of swirl in the diffuser a swirl intensity parameter was defined as the ratio of angular momentum flux to the axial momentum flux. The ratio of angular momentum M_θ and the axial momentum yields the swirl intensity as :

$$Sw = \frac{\frac{1}{R}\int_{r_h}^{r_s}(C_\theta r)(2\pi r\,dr)\rho C_x}{\int_{r_h}^{r_s}(C_x)(2\pi r\,dr)\rho C_x}$$

$$Sw = \frac{\frac{1}{R}\int_{r_h}^{r_s} C_\theta C_x r^2\,dr}{\int_{r_h}^{r_s} C_x^2\, r\,dr} \qquad 3.27$$

3.4.3 Calculation Of Rotor Inlet Conditions From The Discharge Measurements

From the measured rotor exit swirl, mass flow rate and torque, the mean velocity triangles at rotor inlet and exit were constructed. This then gives a picture of the mean flow at rotor inlet and a means of assessing the performance of the variable geometry nozzles. The mean velocity triangle at rotor exit was calculated from the experimental results. The velocity is a function of radial position, ie C = f(r), and the mean axial velocity derived by area averaging between the hub and the shroud. The angular momentum at discharge was obtained by integrating

the tangential component of velocity between hub and shroud across the discharge passage ;

$$M_\theta = \int_{r_h}^{r_s} r C_{\theta 3}\, dm = \int_{r_h}^{r_s} r C_3 \sin\alpha_3 \rho C_3 \cos\alpha_3 (2\pi r\, dr)$$

$$= 2\pi\rho \int_{r_h}^{r_s} C_3^2 r^2 \sin\alpha_3 \cos\alpha_3\, dr \qquad 3.28$$

The mean tangential component of velocity $\bar{C}_{\theta 3}$ is then given by :

$$m\, r_m\, \bar{C}_{\theta 3} = M_\theta \qquad 3.29$$

Where the mean radius rm was considered to be

$$r_m = \frac{r_h + r_s}{2} \qquad 3.30$$

The mean flow angle at discharge was then found from 3.28 and 3.29 as :

$$\overline{\tan\alpha} = \frac{1}{r_m (r_s^2 - r_h^2) C_A^2} \int_{r_h}^{r_s} r^2 C_3^2 \sin\alpha_3 \cos\alpha_3\, dr \qquad 3.31$$

The discharge velocity triangle can then be constructed at the mean radius rm.

To construct the velocity triangle at rotor inlet the

measured rotor torque was equated to the rate of change of angular momentum, ie :

$$\tau = \dot{m}\left(r_2 C_{\theta 2} - r_m C_{\theta 3}\right) \qquad 3.32$$

from which the tangential component $\bar{C}_{\theta 2}$ was readily found.

The radial component of velocity at rotor inlet was derived from the measured mass flow rate as

$$\bar{C}_{r_2} = \frac{\dot{m}}{\rho_2 A_2} \qquad 3.33$$

where the density ρ_2 was found from the measured values of pressure and temperature. The inlet velocity triangle was then readily completed, figure 3.11, the flow angles being given by :

$$\overline{\tan \alpha_2} = \frac{\bar{C}_{\theta 2}}{\bar{C}_{r_2}} \qquad 3.34$$

$$\overline{\tan \beta_2} = \frac{(\bar{C}_{\theta 2} - U_2)}{\bar{C}_{r_2}} \qquad 3.35$$

3.4.4 Calculation Of Radial Distribution Of Losses At Rotor Exit

The radial distribution of losses through the rotor were derived from the total to total efficiency evaluated at each traverse point as a function of radius

$$\eta_{tt} = \frac{1 - \frac{T_{03}}{T_{01}}}{1 - \frac{1}{\left(\frac{P_{01}}{P_{03}}\right)^{\frac{\gamma-1}{\gamma}}}} \qquad 3.36$$

The loss coefficient was then derived from

$$\xi = 1 - \eta_{t\text{-}t} \qquad 3.37$$

3.4.5 Calculation Of Nozzle Efficiency

The nozzle efficiency was defined as

$$\eta_N = \frac{T_{oo} - T_1}{T_{oo} - T_{1S}} = \frac{1 - \frac{T_1}{T_{oo}}}{1 - \frac{1}{\left(\frac{P_{oo}}{P_1}\right)^{\frac{\gamma-1}{\gamma}}}} \qquad 3.38$$

Where : P1 is the measured pressure at nozzle exit, T00 is the measured stagnation temperature at nozzle exit, P00 is the measured stagnation pressure at volute inlet.

In order to obtain the static temperature at nozzle exit it was necessary to find the absolute discharge velocity. The continuity condition gives :

$$\dot{m} = \rho_1 A C_1 \cos\alpha_N \qquad 3.39$$

Which was combined with

$$T_{oo} = T_1 + \frac{\gamma-1}{2\gamma R} C_1^2 \qquad 3.40$$

to give

$$\frac{mR}{A\cos\alpha_N}\left(T_{o1} - \frac{\gamma-1}{2\gamma R} C_1^2\right) = P_1 C_1 \qquad 3.41$$

This is a quadratic equation and can be readily solved for the velocity C1. The static temperature T1 then readily follows from eq. 3.40.

3.4.6 Calculation Of The Turbine Characteristics From The Experimental Data

In order to derive the standard non dimensional performance parameters for the radial inflow turbine the main requirement is to calculate the stagnation pressure at inlet from the measured static pressure, stagnation temperature and mass flow rate. From the continuity condition :

$$C = \frac{\dot{m}}{\rho A} = \frac{\dot{m} R T}{A P} \qquad 3.42$$

Hence :

$$T_o = T + \frac{\gamma - 1}{2\gamma R} \left(\frac{\dot{m} R T}{A P} \right)^2 \qquad 3.43$$

This is a quadratic equation from which the temperature, T1 can be readily found. The stagnation pressure then follows from :

$$P_o = P * \left(\frac{T_o}{T} \right)^{\frac{\gamma}{\gamma - 1}} \qquad 3.44$$

The efficiency and the non-dimensional performance parameters can then be readily found as :

$$\eta_{t\text{-}s} = \frac{\left(\frac{\gamma - 1}{\gamma R T_{ox}} * \frac{\tau}{\dot{m}}\right)}{1 - P_r^{-\frac{\gamma-1}{\gamma}}}$$

$$NDM = \frac{\dot{m}\sqrt{\frac{RT_{ox}}{\gamma}}}{A P_{ox}} \qquad 3.45$$

$$NDS = \frac{N D}{\sqrt{R T_{ox}}}$$

$$NDT = \frac{\tau}{A P_{ox}}$$

In the present investigation only one turbine was tested with air as the working fluid. Therefore, the gas constant R , the ratio of specific heats γ, and the rotor tip area are constants and the pseudo-non-dimensional groups derived as

$$NDM = \frac{\dot{m}\sqrt{T_{ox}}}{P_{ox}}$$

$$NDS = \frac{N}{\sqrt{T_{ox}}} \qquad 3.46$$

$$NDT = \frac{\tau}{P_{ox}}$$

The rotational speed N is taken in place of the non-dimensional speed as the inlet temperature was approximately constant during the tests.

CHAPTER -111-

Two types of characteristics were used in plotting the performance maps, namely :

(1) The non dimensional mass flow, the non dimensional torque, and the efficiency were plotted as a function of pressure ratio across the turbine for a number of fixed speeds. (2) The efficiency was plotted as a function of speed ratio U/Co for constant rotational speeds. The spouting velocity used in the speed ratio term is defined as the velocity that would be achieved in isentropic expansion through the pressure ratio across the turbine from the inlet stagnation temperature TOx i.e.

$$T_{ox} = T_y + \frac{\gamma - 1}{2\gamma R} C_o^2$$

$$C_o = \sqrt{2C_p x \left[1 - \frac{1}{\left(\frac{P_{ox}}{P_y}\right)^{\frac{\gamma-1}{\gamma}}} \right]} \qquad 3.47$$

And hence the speed ratio is given by

$$\frac{U_T}{C_o} = \frac{\frac{\pi N D}{\sqrt{T_{ox}}}}{\sqrt{2C_p x \left[1 - \frac{1}{\left(\frac{P_{ox}}{P_y}\right)^{\frac{\gamma-1}{\gamma}}} \right]}} \qquad 3.48$$

FIG 3.1 THE TURBINE RIG AND ASSOCIATED INSTRUMENTATION

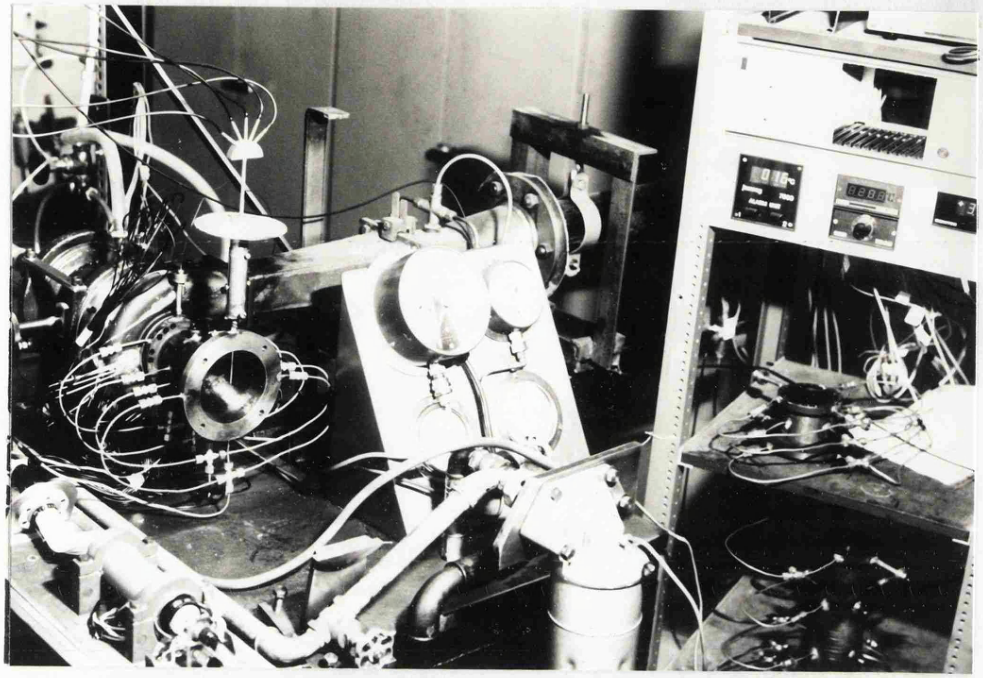

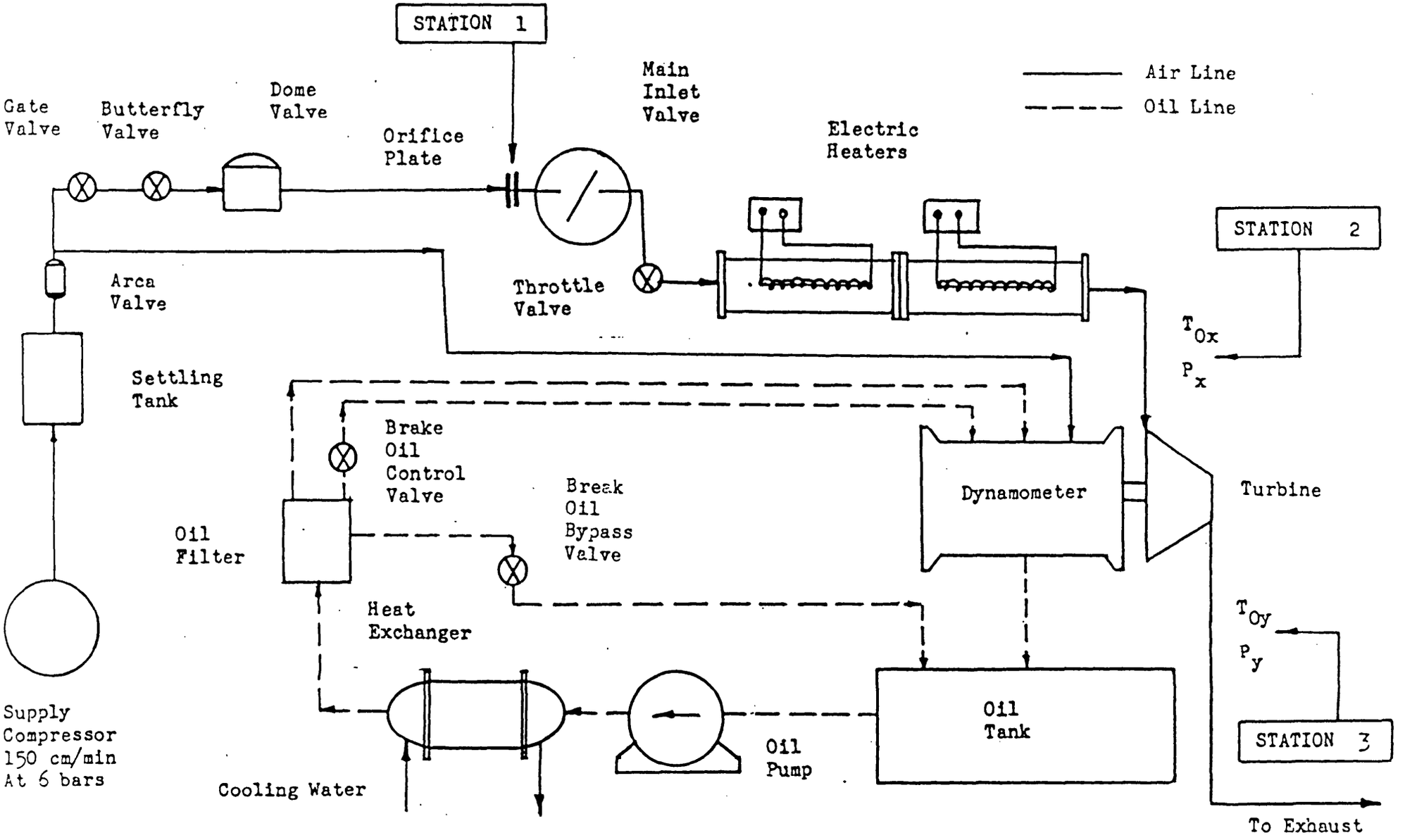

FIG 3.2 SCHEMATIC LAYOUT OF THE TURBINE RIG

FIG 3.3 CROSS SECTION OF THE DYNAMOMETER

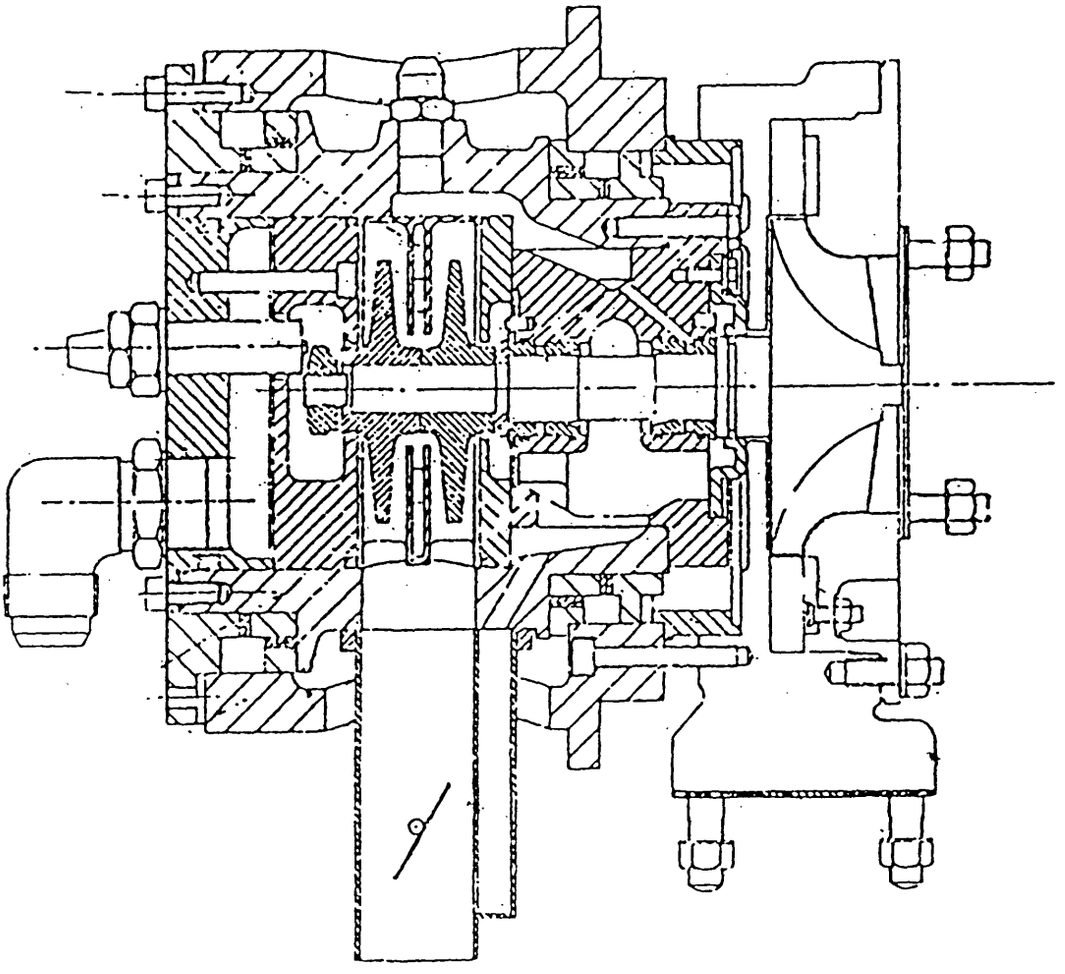

FIG 3.4a THE SHORT DIFFUSER (DOUBLE CONE ANGLE=29 DEG.)

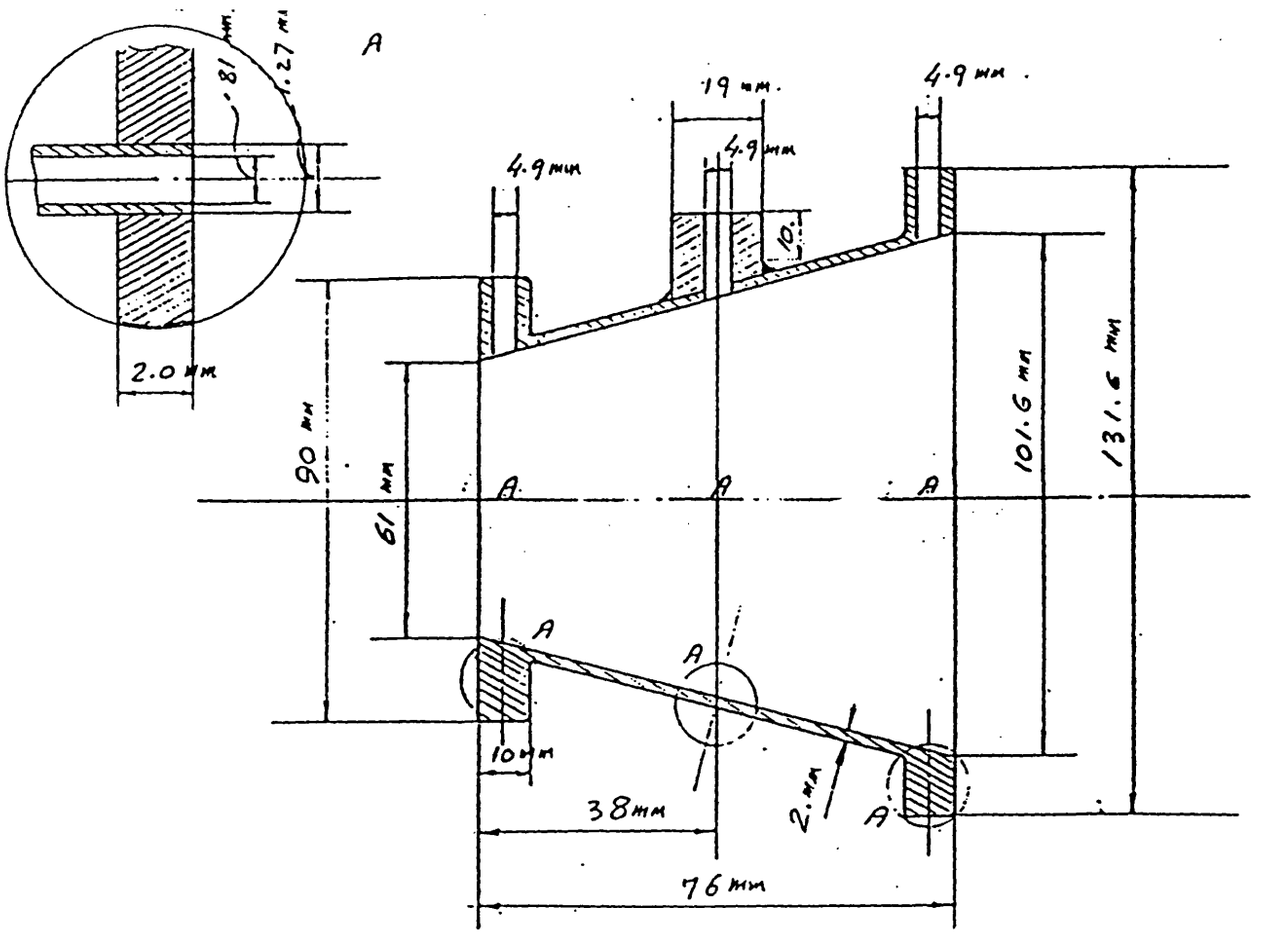

FIG 3.4b THE MEDIUM DIFFUSER (DOUBLE CONE ANGLE=16 DEG.)

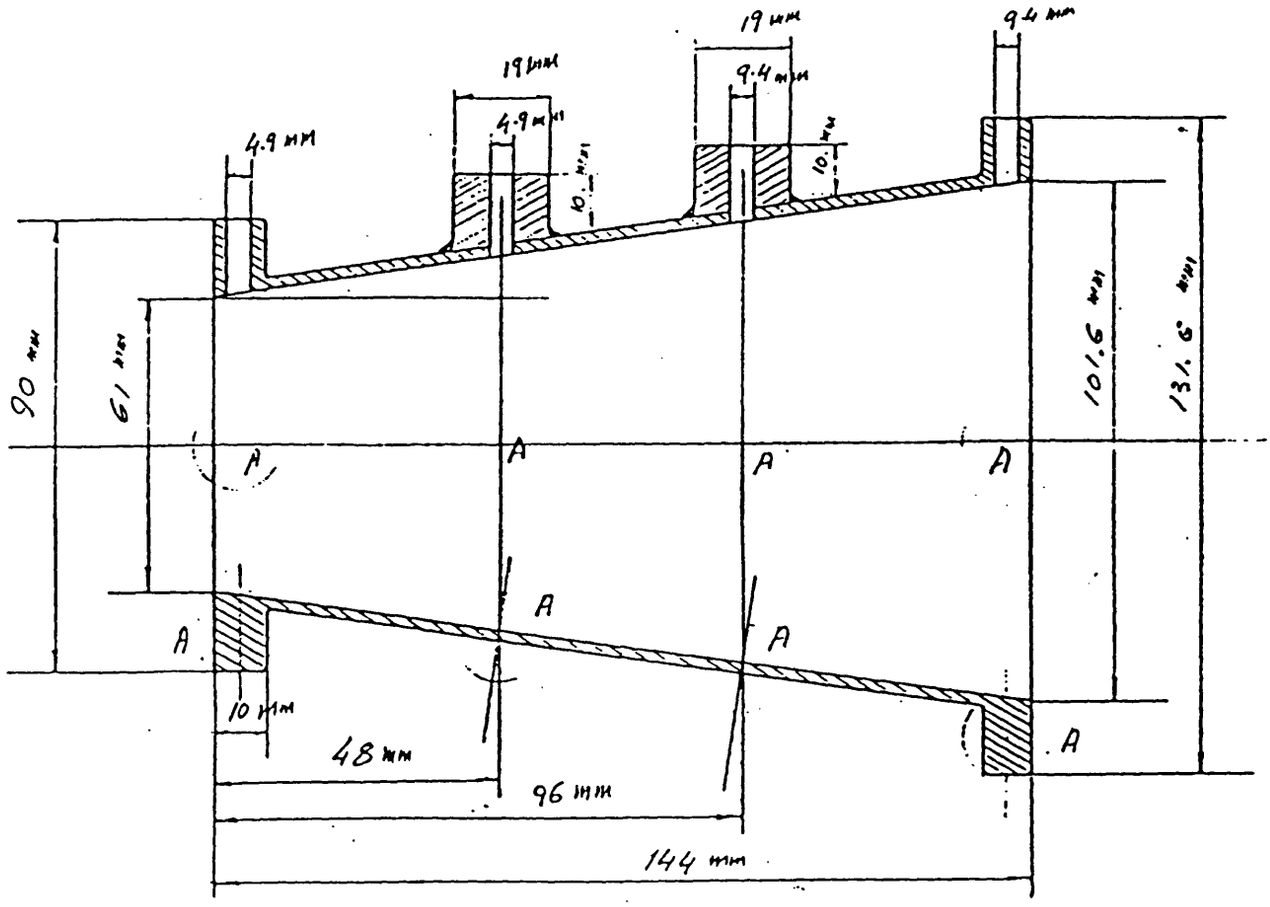

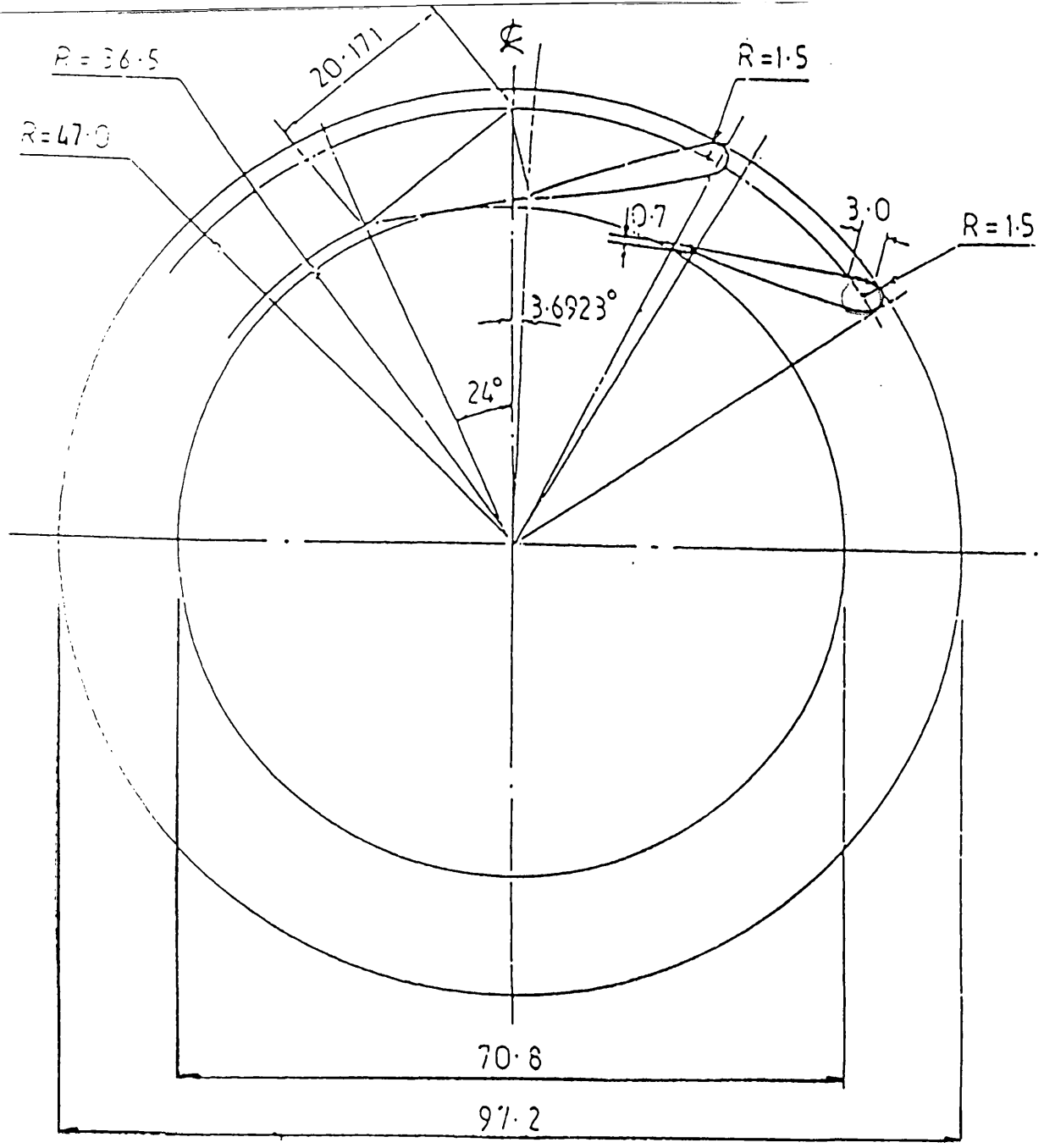

	A	B
a	10.5	3.0
b	8.5	5.0
c	4.5	9.0

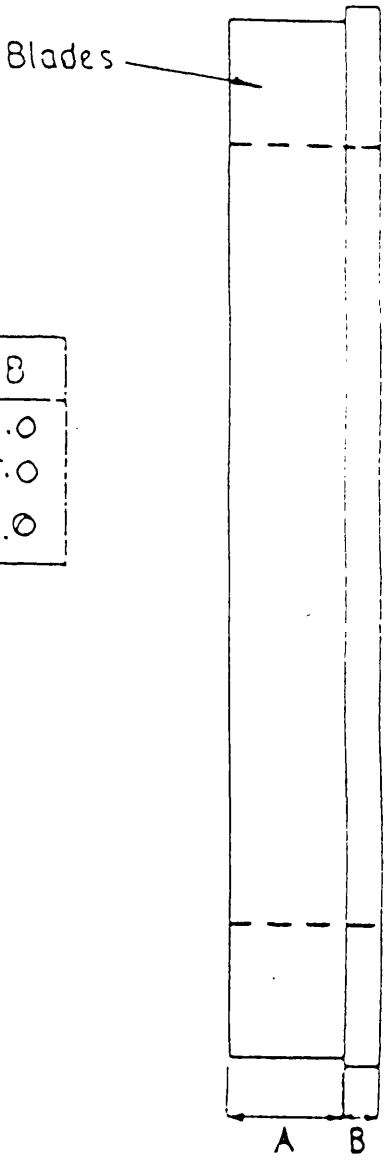

FIG 3.5 NOZZLED RING FOR THE NOZZLED PLUG SIMULATION

FIG 3.6 NOZZLE RINGS FOR THE INWARD FLOW RADIAL TURBINE

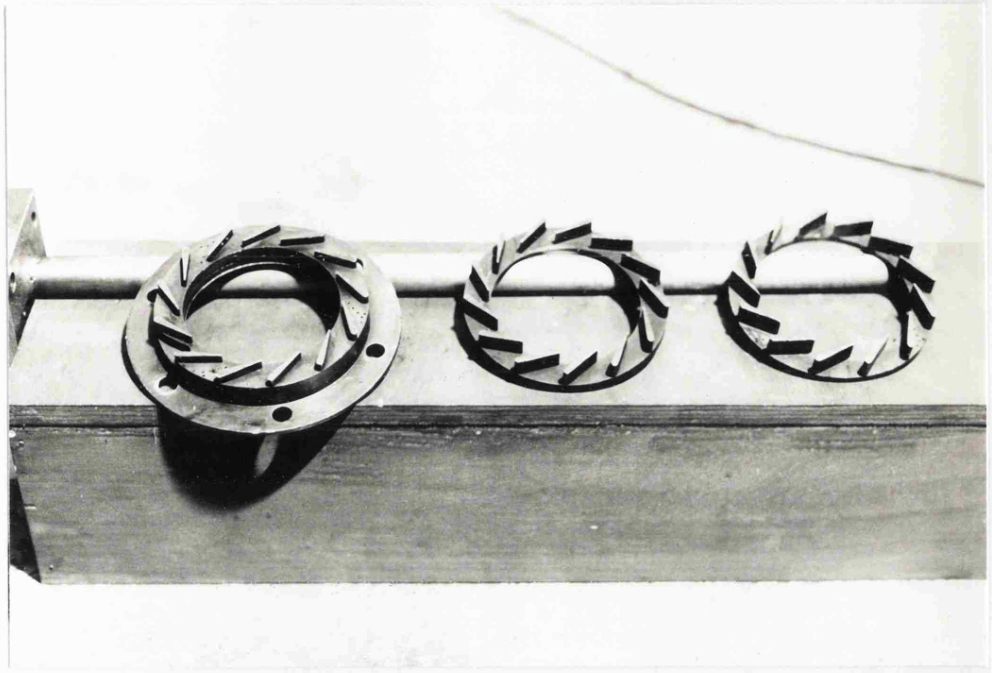

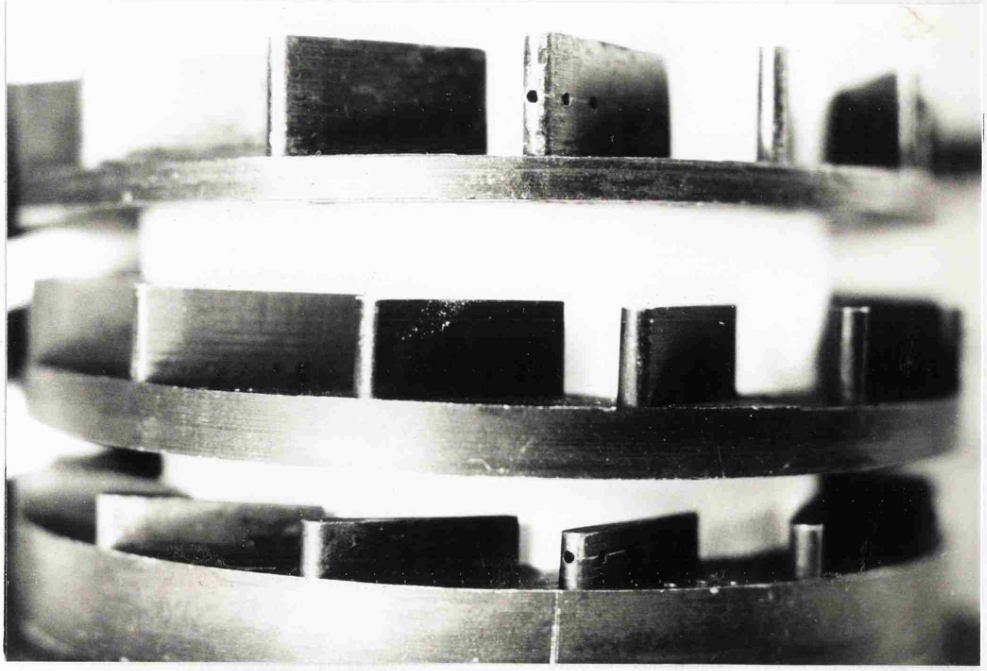

FIG 3.7a LOCATIONS OF THE STATIC PRESSURE TAPPINGS ON THE NOZZLE PLUG END PLATE

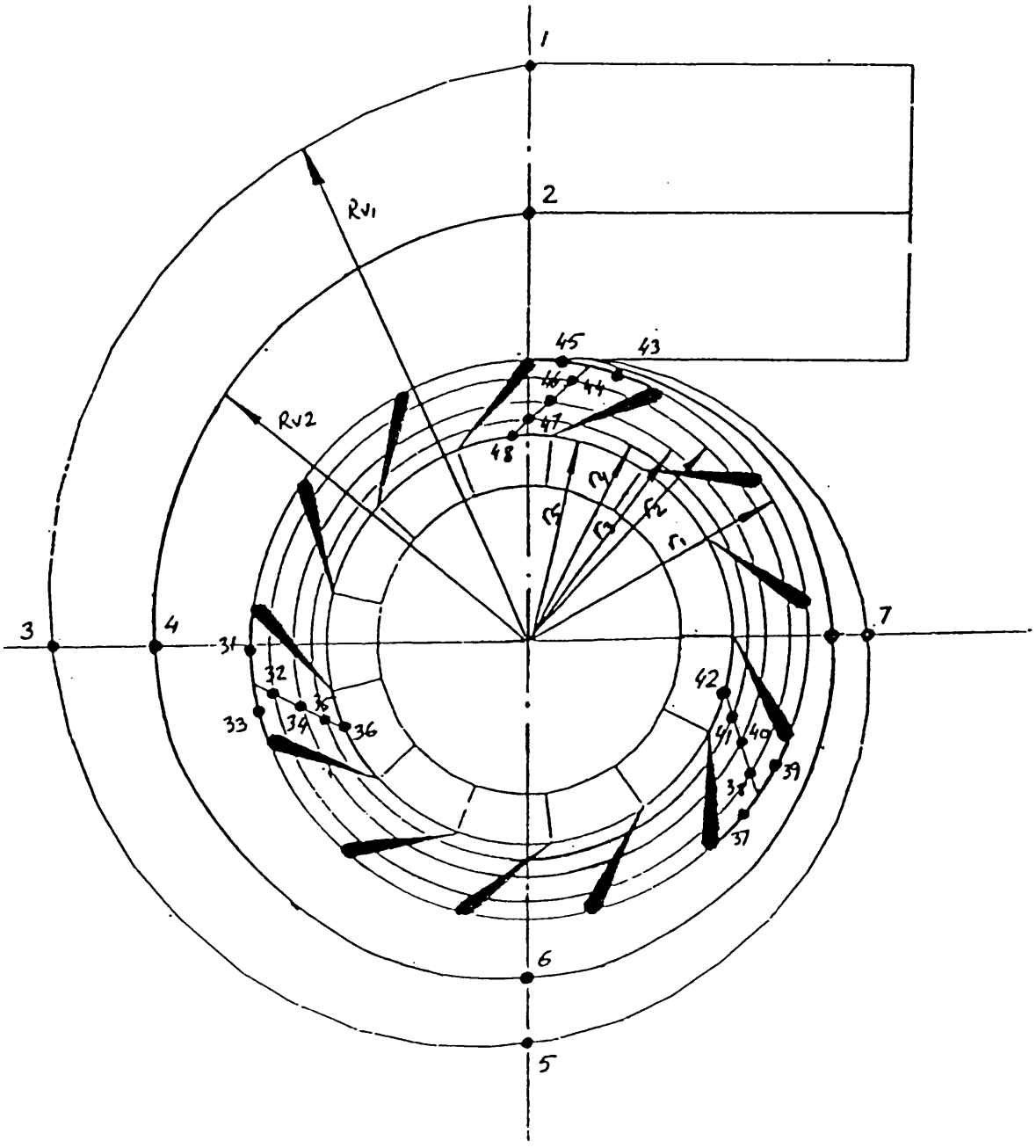

FIG 3.7b LOCATIONS OF THE STATIC PRESSURE TAPPINGS ON THE NOZZLE BLADE SURFACES

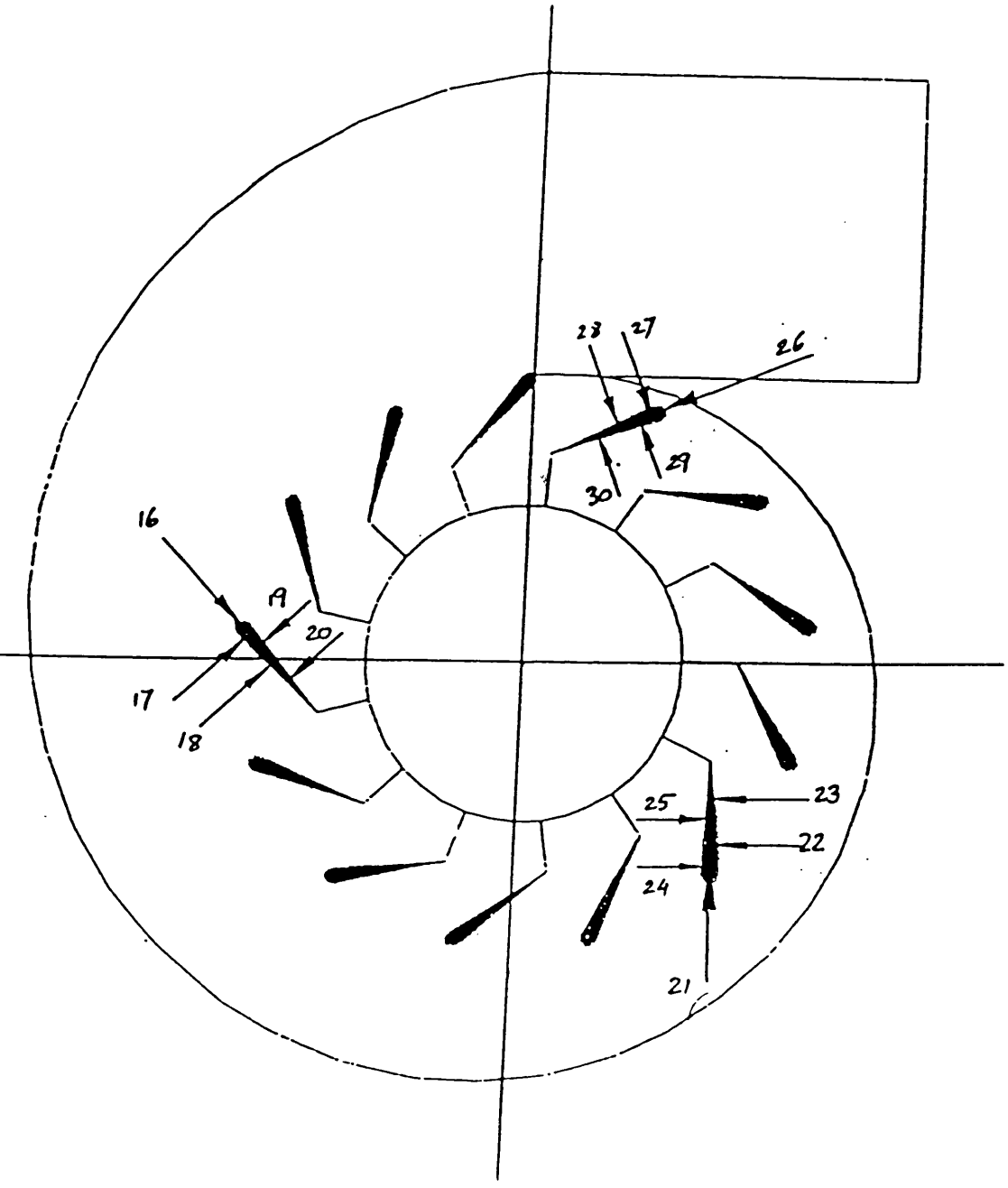

FIG 3.7c LOCATIONS OF THE STATIC PRESSURE TAPPINGS ALONG THE SHROUD

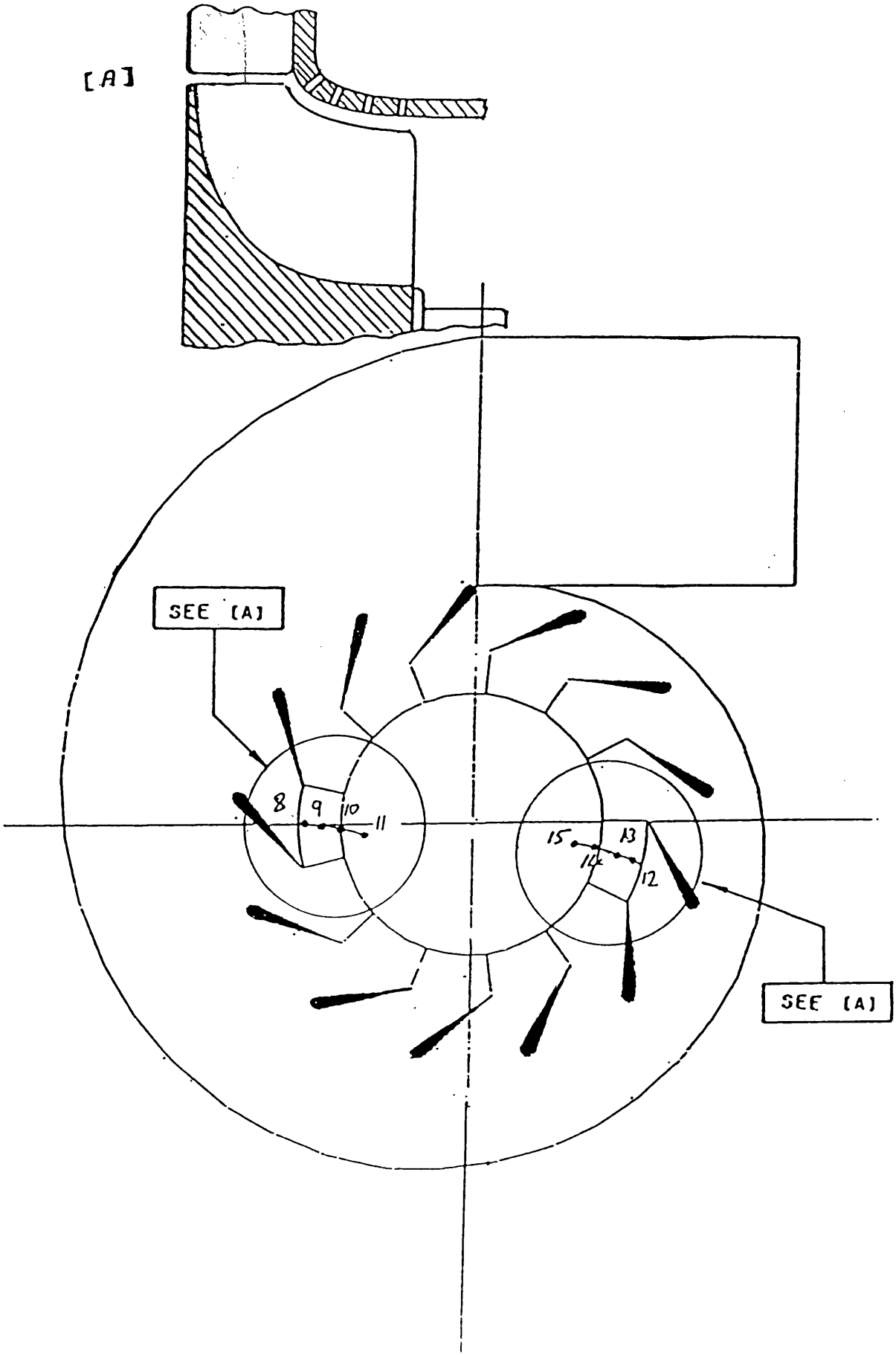

FIG 3.8 PRESSURE CALIBRATION CURVES

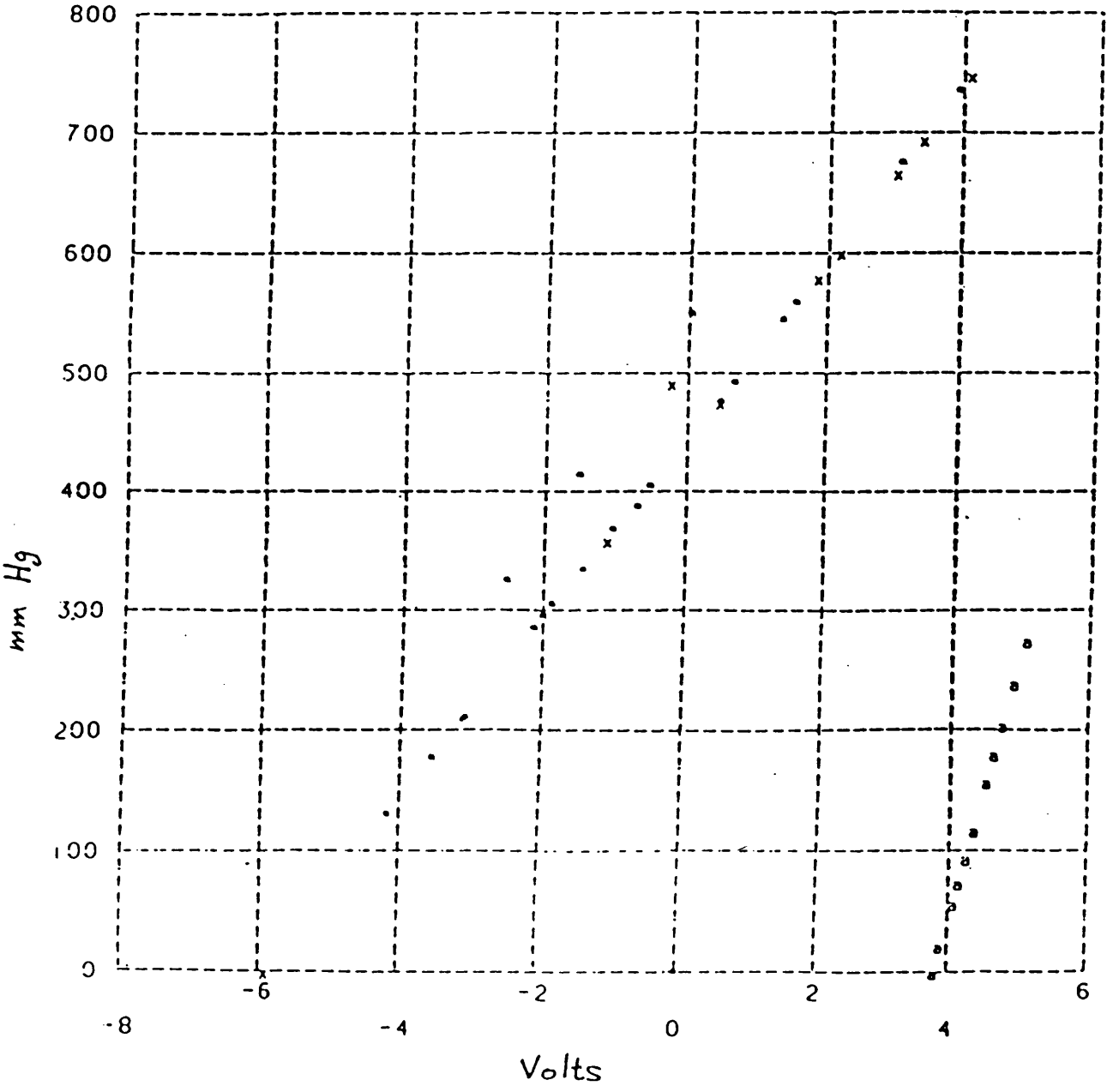

(*) FIRST CALIBRATION DATA
(x) SECOND CALIBRATION DATA
(a) ABSOLUTE PRESSURE TRANSDUSER DATA

FIG 3.9 CALIBRATION DATA FOR THE FIVE HOLE PROBE

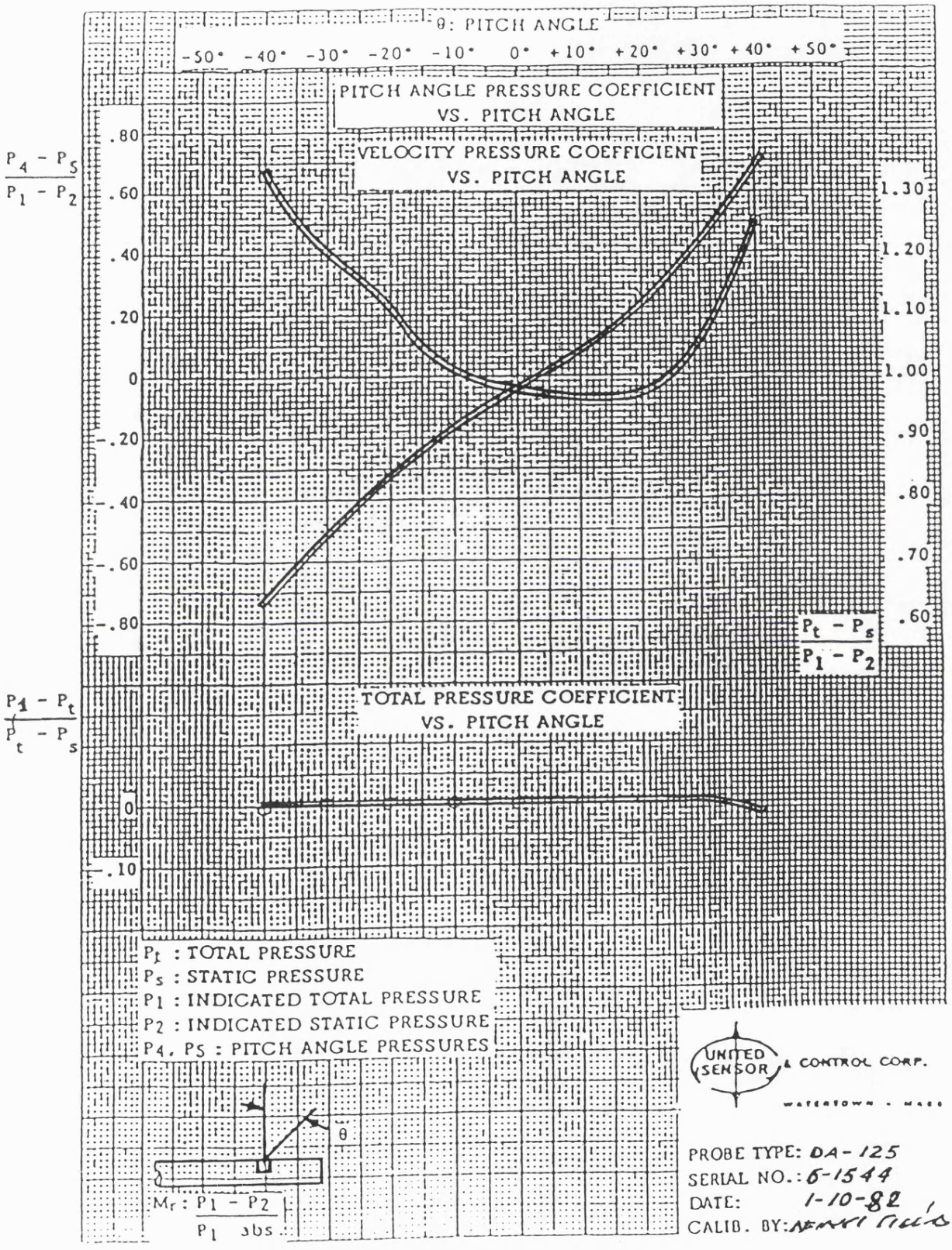

FIG 3.10 THEORETICAL CALCULATION OF RADIAL STATIC PRESSURE

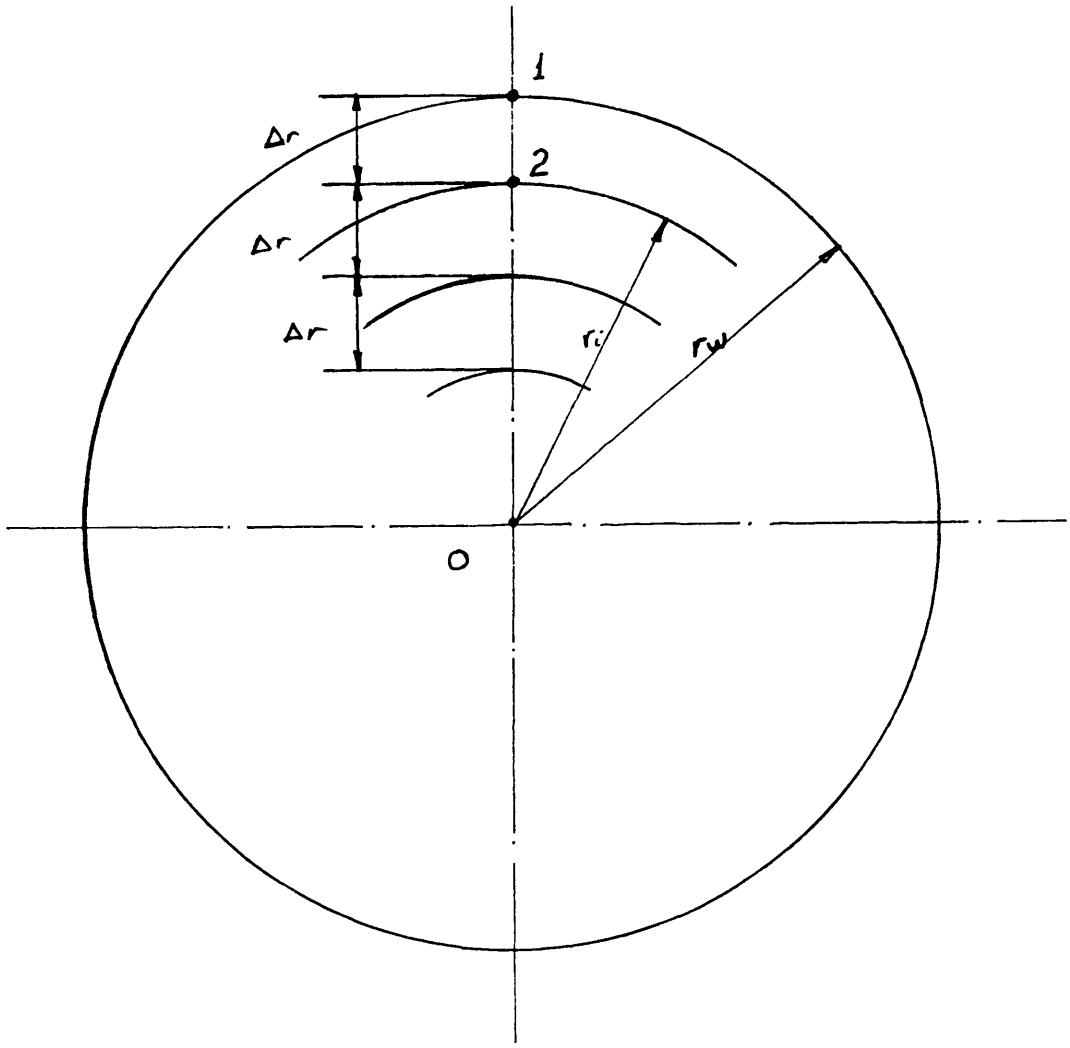

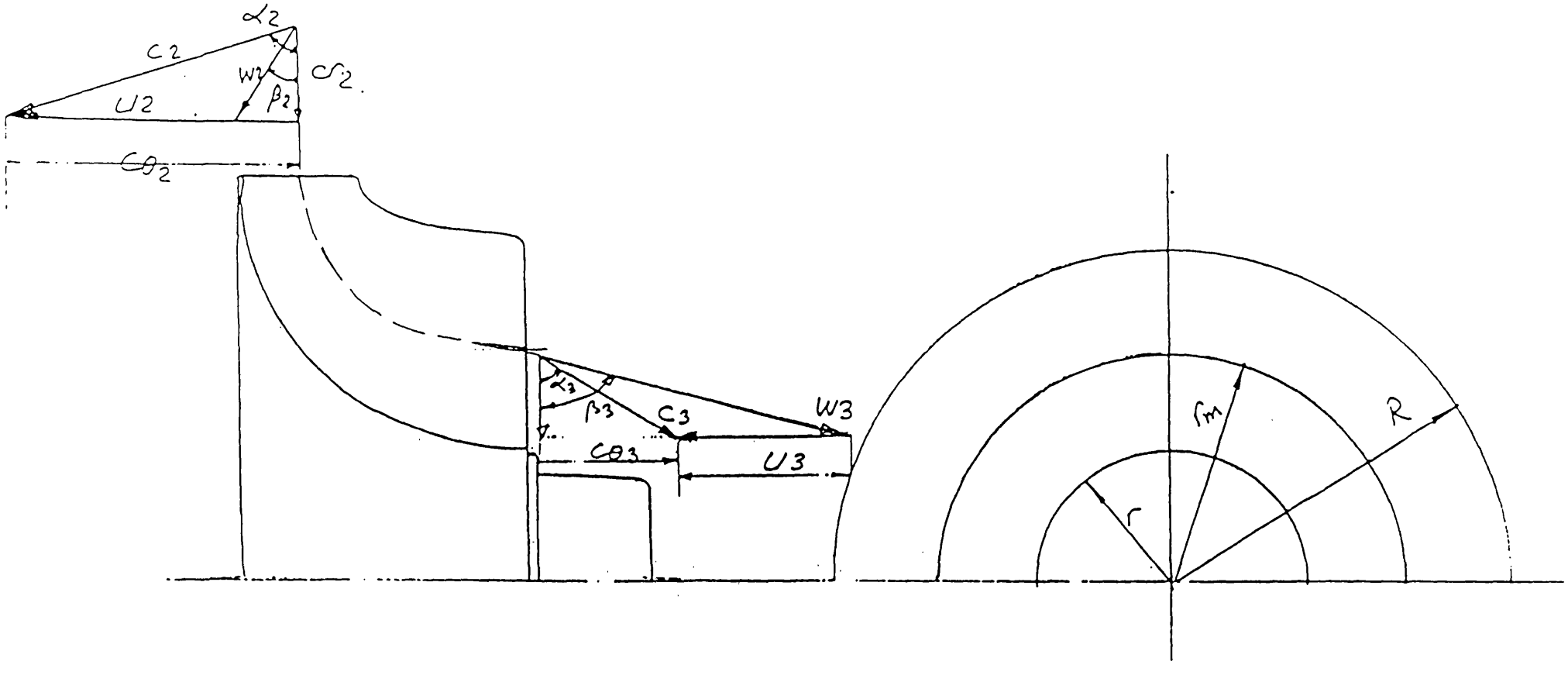

FIG 3.11 MEAN VELOCITY TRIANGLES AT ROTOR INLET AND EXIT

CHAPTER -1V-
---

4. PRESENTATION AND DISCUSSION OF EXPERIMENTAL RESULTS

The effect of alternative inlet nozzles and exhaust diffusers on the performance of inward flow radial turbines has been studied. The results of the diffuser study are presented first. Initially the effect on overall performance is presented followed by the detailed component study. The performance maps are presented in terms of non-dimensional values of mass flow rate and torque, and total to static efficiency as derived in section 3.4.6, as a function of pressure ratio across the turbine over the operating range of the turbine up to a maximum speed of 60000 revs/min.

4.1 Study Of Exhaust Diffuser

The overall turbine performance has been measured with three exhaust diffusers and three inlet nozzle rings as described in the previous chapter. Figures 4.1a,b,c,d show the effect of these diffusers on the turbine performance with the non restricted nozzle ring. The range of pressure ratios considered was approximately 1.1 to 2.3, and the results without a diffuser were similar to those associated with the 29 deg. diffuser. With this operating range the non dimensional mass flow

characteristic is only slightly affected by introducing the diffuser. It can be seen from figure 4.1a that there is no significant change in mass flow rate between the 29 deg. and 8 deg. diffusers ; while the 16 diffuser gave a slight increase of mass flow. This is relatively high at high speeds and pressure ratios.

The non dimensional torque is again slightly modified by the diffusers, figure 4.1b shows that the 16 deg. diffuser is associated with slight increase in torque. At low speeds and pressure ratios no significant change is detactable with the other diffusers.

The efficiency, figure 4.1c, is increased by the introduction of the diffuser. The 16 deg. diffuser gave the highest increase among the three diffusers.

Figure 4.1d presents the total to static efficiency as a function of rotor tip speed to spouting velocity ratio. The speed ratio of 0.66 is associated with the optimum efficiency for all diffusers tested. Again the 16 deg. diffuser is consistently located in the high efficiency region.

Whilst the changes in performance due to the introduction of the diffuser are not substantial, the general trends indicate improved performance with the 16

deg. diffuser over the operating range tested. It is probable that the swirl at diffuser inlet has assisted in stabilizing the flow in this diffuser but was not sufficient to stabilize the wide angle (29 deg.) diffuser.

4.1.1 Detailed Diffuser Performance

Traverses at a number of diffuser cross sections were made for a range of turbine pressure ratios and rotational speeds. Over this range of operation a variety of flow conditions were created at the diffuser inlet. These traverses were made primarily to enable the nozzle discharge-rotor inlet conditions to be computed. The application to the diffuser study was considered to be secondary; however, traverse measurements were carried out along the diffuser length with a five-hole probe at three stations for the 29 deg. diffuser, and four stations for the 16 deg. and 8 deg. diffusers.

The static and total pressures were then obtained following the probe calibration curves as described in section 3.4.2. In order to estimate the wall effect upon the probe static pressures a theoretical method of estimating the static pressure based upon radial equilibrium conditions was applied, section 3.5.1. It was observed that at points close to the core region the pressure and flow angle readings were not steady. Figure

4.2 shows that the measured static pressures and those calculated are close to each other near the wall and that they diverge at radii in the core region. The calculated static pressures depend largely upon the measured flow angle, and since these were poor in the core region the calculated pressures cannot be considered as satisfactory. The calculated static pressures show that no correction due to the wall effect is necessary and the experimental values have, therefore, been used for data reduction.

4.1.1.1 Accuracy Of Measurements

In order to check the accuracy of the traverses at different cross sections, the orifice mass flow rate was compared with that calculated using the measured values of velocity. It can be seen, figure 4.3a that they rarely agree precisely, and the difference between them was often high. This was believed to be caused by the inaccuracy of the measurements in the core due to the wake produced by the rotor hub. Figure 4.3a shows the error in mass flow relative to the orifice flow. The values of mass flow were, therefore, recalculated by evaluating the integral for the mass flow rate over a limited cross sectional area, excluding the wake zone close to the hub. The wake zone radius was chosen according to the pressure profile at the cross sections where the effect of the wake is

noticeable. The recalculated mass flows are shown as percentage errors with reference to the orifice flow in figure 4.3b. Better agreement is now shown at all stations.

4.1.1.2 Diffuser Flow Conditions

A large number of measurements were taken with different turbine pressure ratios and at a number of cross sections for each diffuser. The rotational speed of the turbine was maintained constant at 50000 revs/min.

Due to the similarities in the results for the three diffusers at different operating conditions, one set of these results is presented, namely the 29 deg. diffuser results for a number of pressure ratios. Some of the 16 deg. diffuser results have been included where a noticeable difference in the flow behaviour was observed. All the results are presented in terms of (i) Radial distribution of pressures; (ii) Radial distribution of velocities and flow angles; and(iii) Axial distribution of averaged pressures and velocities. For the axial distributions the variation of averaged static and total pressures were normalized relative to the dynamic head measured at diffuser inlet. The averaged velocities were normalized relative to the momentum-averaged absolute

velocity at diffuser inlet. By this procedure the static pressures are equivalent to the pressure recovery coefficient while the total pressure is represented by the pressure loss coefficient. All variables such as velocities and flow angles were considered zero at the wall. The flow angle was considered positive if the tangential velocity had the same direction as the rotor blades. The traverse measurements for the 29 deg. diffuser were taken for pressure ratios across the turbine between 1.35 - 1.77, figure 4.4 shows this range of pressure ratios and the corresponding swirl intensities at diffuser inlet. Figures 4.5a to 4.5g represent the effect of the swirl on pressures and velocities at the inlet traverse station. Figure 4.5a shows that the static pressure has low values at strong negative swirls and increased as the swirl went from negative to positive. The stagnation pressure, however, has the highest values associated with the high negative swirl. For each swirl intensity the stagnation pressure has a peak value ; which, for the high negative swirl, is situated at the centre of the annular passage and moves towards the wall when the swirl becomes positive. From this maximum value the stagnation pressure decreasing towards the centre. The rate of the reduction is relatively low with positive swirl while it is more pronounced at high negative swirls.

This indicates that a wake is developing at rotor exit at this high negative swirl, while it is less pronounced when the swirl is weak and positive. The effect of swirl on the tangential velocity is shown in figures 4.5b to 4.5d. It is clear that the magnitude of the velocity increases from the wall to a maximum value then decreases towards the centre. This variation is common for all cases where the swirl is weak or strongly negative, and generally has the shape of a Rankine vortex having an outer part as a free vortex distribution and an inner core of forced vortex flow. The radius of the forced vortex core is a function of the swirl intensity. It is clear from the above figures that when the swirl is strongly positive the forced vortex distribution is predominant over the entire cross section, this is seen in fig. 4.5b for the case of +0.31 swirl. At the low positive swirl of.04 it appears that the flow is unstable, it changes its direction at some distance from the wall from positive, to negative, similar behaviour can be seen with the 20% restricted nozzle ring (see figures 4.5c to 4.5d). Whether this is due to a stall region or an error in the measurements cannot be clearly seen and needs to be confirmed by additional flow visualization techniques.

The variation of axial and absolute velocities are

shown in figures 4.5e and 4.5f. Here as would be expected from the rotor discharge, the velocities have low values when the swirl is positive, and increase as the swirl becomes nagative. At the core the defect in axial velocity, i.e. the ratio of maximum to minimum velocity, is large when the swirl has high negative values. This shows that a central wake is developing when the turbine is highly loaded.

The flow angles, figure 4.5g show a similar distribution to the tangential velocity profile. The transition from a negative swirl in the central region to positive at the wall is again shown. Whether this is real or a measurement error cannot be ascertained without further tests. The positive swirl shown near the wall is dependent upon a single measurement which is attempting to distinguish between a small positive or negative swirl, the likelihood of a measurement error must be considered to be quite probable.

The development of these diffuser inlet conditions as the flow passes along the diffuser are illustrated in figures 4.6a to 4.6f for the maximum negative swirl condition. The static pressure fig. 4.6a has a maximum value at the wall then decreases gradually towards the centre. This radial variation is less pronounced at the

downstream stations where the pressure is nearly constant and approaching the atmospheric pressure at exit. The stagnation pressure, however, increases to a peak value at some radius, then decreases towards the core region. These peak values of pressure decrease with downstream distance and move towards the wall. This indicates that the wake flow behind the rotor hub is extending downstream and mixing with the outer flow.

Figures 4.6b to 4.6f show the radial variation of velocities and flow angles at three diffuser cross sections. It has been shown previously, see figure 4.5b, that at negative swirls the tangential velocity has a Rankine type vortex distribution and that the radius of the forced vortex decreases as the swirl becomes positive. This is however, affected by the position along the diffuser too. Figures 4.6b and 4.6c show the tangential velocity variation for two diffusers. It is clear that the free vortex distribution is preserved along the diffuser at different cross sections at this particular swirl intensity, The axial velocity, see figure 4.6d, has lower values at the downstream stations and the peak velocity has a larger radius, this supports the theory of the wake diverging as it passes down the diffuser and that the core is picking up momentum from the outer region. A similar

downstream distance. This decay is mainly dependent upon the diffuser geometry, the wall surface roughness and upon the frictional forces as it passes downstream. The rate of swirl decay is higher with the long, 16 deg., diffuser than with the 29 deg. diffuser

The variation of pressure recovery coefficient with inlet swirl intensity is shown in figures (4.8a,b,c) for each diffuser. Two types of pressure recovery coefficients are presented. One is based on the wall static pressure at diffuser inlet and exit, and the other is derived from mass averaged static pressures at the inlet and exit cross sections. The pressure recovery coefficient based upon the averaged static pressures was computed at the 50000 revs/min turbine speed only. These figures show that for each case there is an optimum swirl for maximum pressure recovery. This swirl is always negative and approximately 10%. It has been shown in previous sections that the negative swirl was associated with high pressure ratios across the turbine. It is concluded that the flow at rotor exit is more stable with the turbine operating near its design point, but with negative swirl, i.e. high pressure ratio than it is at low pressure ratios which yield a similar magnitude but positive swirl. It can be seen from the above figures that the optimum swirl is not affected

by turbine speed, while higher speeds resulted in a better pressure recovery in the diffusers.

A significant difference can be seen between the wall pressure recovery coefficient and that of the mass-averaged based pressure coefficient. This is due to the fact that the radial variation of the static pressure has decreasing values from the wall towards the centre which results in lower averaged values within the diffuser cross sections.

CHAPTER -1V-

4.2 Study Of Inlet Nozzles

Figures 4.9a,b,c,d present the effect of nozzle restriction on the overall turbine performance. Fig. 4.9a shows the variation of the non dimensional mass flow with the inlet total to exit static pressure ratio for the case of the turbine exhausting to the atmosphere. These characteristics of mass flow rate are shown with nozzle restrictions of 20% and 50% relative to the non restricted nozzle ring. It can be seen that with the non restricted nozzle the variation is a function of rotational speed and pressure ratio, and there is a slight reduction in mass flow rate at 20% restriction, While at 50% restriction this reduction is more significant. In this figure it is shown that at a constant speed of 30000 revs/min and pressure ratio of 1.5 the 20% restricted nozzle gives a 10% reduction in mass flow rate, while at 50% restriction the reduction is of the order of 50%, and this is maintained at high speeds and pressure ratios. It can be seen that with the 50% restriction nozzle, the non dimensional mass flow rate characteristics at different rotational speeds are close to each other and nearly form a single flattened curve. This indicates that a near chock flow occurs at this range of pressure ratios.

The non dimensional torque is presented in fig. 4.9b for the same nozzle restrictions. Generally at 20% restriction the torque variation is small, as was the case for the mass flow, however, a substantial decrease in torque was observed with the 50% restriction nozzle. From this figure it can be seen that at a given speed and pressure ratio the torque was reduced by 40%, while at high speeds and pressure ratios the reduction was approximately 52%. In all cases the torque variation is approximately linear over the operating range considered.

The total to static efficiency characteristics are the most sensitive to the nozzle restrictions. Fig. 4.9c shows that in the case of 50% restriction there is a decrease in efficiency varying between 8-10% over the operating range. However, an increase in efficiency between 5-8% was observed at 20% restriction

The variation of efficiency with speed ratio is shown in fig. 4.9d. It can be seen that with 20% restriction the highest efficiency of 82% lies near the optimum value of the speed ratio i.e. U/Co=0.68. The speed ratio has a lower value, approximately 0.64 for the non restricted nozzle ring. For the maximum restriction the highest efficiency of 75% corresponds to a speed ratio of 0.59. From this figure it can be concluded that the efficiency

is substantially dependent upon the tip speed ratio. It is shown in ref. [55], that the optimum value of tip speed ratio for the ideal radial turbine with complete recovery of exhaust energy is approximately 0.707. For the case of this experiment this indicates that the overall losses in the turbine are relatively high at high restrictions, and these, together with energy dissipated at exit, contribute to the reduction in efficiency and the optimum speed ratio.

A one dimensional performance prediction program was used to compute the turbine performance for the three nozzle rings tested and the results compared to those obtained experimentally in figures 4.10a,b,c to 4.13a,b,c. The results are shown in figures 4.10a,b,c for the mass flow characteristics, figures 4.11a,b,c for the non dimensional torque, figures 4.12a,b,c for the total to static efficiency, and figures 4.13a,b,c for variation of efficiency with the tip speed ratio. The predicted results show that the non dimensional mass flow values are slightly lower than those obtained experimentally, particularly at high rotational speeds. Similar differences can be seen for the torque characteristics, whilst the efficiency, fig. 4.12c, obtained experimentally is lower than that predicted. In figures 4.13a,b,c a

comparison between the speed ratio variation with efficiency curves obtained experimentally and that predicted for all the three restrictions is presented. It is clearly shown that the predicted speed ratio value of approximately.68 coincided with that of the 20% restriction for the optimum efficiency. The overall comparison between the predicted and experimental results can however, be considered satisfactory.

4.2.1 Detailed Volute Nozzle Assembly Investigation

Experimental static pressure measurements at different locations around the volute, along the shroud, and on a selected number of blades were made using a pressure transducer and a scanivalve. A total of 48 pressure tappings were scanned for two nozzle rings at different flow conditions. Tests were performed for the two nozzles, the non restricted and the fully restricted, i.e. 50% restriction. Figures 3.7a,b,c show the positions of the static pressure tappings

Figures 4.14a,b show the results of the pressure distribution around the volute, for the two nozzle rings, at different radii and at a rotational speed of 50000 revs/min. It is clear that the pressure variation with

azimuth angle is small, generally not in excess of 10%, whilst the pressure decreases with radius as shown in figure 4.15. The rate of pressure reduction through the nozzle is larger with the 50% restricted nozzle ; this is as expected due to the greater acceleration of the air through the narrower nozzle. From this it is evident that the flow in the volute is very sensitive to the introduction of the nozzle restriction and has a three dimensional nature affecting the nozzle inlet area. From figure 4.14b it is noticeable that there is a sharp fall of pressure at the angular position of 360 deg. at radius r5. This is believed to be caused by the end nozzle blade which is specially designed to prevent the flow recirculating.

Figure 4.16 shows the variation of the pressure along the rotor shroud surface for 50000 revs/min and at two angular positions, namely 90 deg. and 270 deg. (see fig. 3.7c for the location of the pressure tappings). The pressure distribution has approximately the same trend for the range of pressure ratios tested. The results at the two angular positions were very similar but the restricted nozzle showed higher values at the shroud exit at position 270 deg.

Figures 4.17a,b represent the pressure distribution on the nozzle blades for the two nozzle rings tested at 50000 revs/min. It can be seen that the blades are not uniformly loaded. They are subject to higher loads at the downstream positions. The blade loadings are more uniform with the fully restricted nozzle ring fig. 4.17b. It is noticeable from fig. 4.17a that at the angular position of 225 deg. the pressure surface of the blade has a lower pressure than the suction surface in the leading edge region, and this is maintained at a number of rotational speeds, while at the 90 deg. position the pressure on the blade surfaces are approximately equal. This is mainly due to the blade loading at different operating conditions, and hence to the non uniformity of the incidence at blade inlet at different angular positions. This is a direct result of flow mismatching at the blade inlet.

The nozzle row efficiency was calculated following the procedure described in section 3.4.5. The results are shown in fig. 4.18 for the two nozzles investigated. It can be seen that the nozzle efficiency has low values with the fully restricted nozzle at high turbine rotational speeds. This results from the sudden enlargement loss produced by the design of this type of nozzle restriction

CHAPTER -IV-

From the above investigations it can be concluded that the nozzle blades are not subjected to a uniform flow at the entire operating range and that the blade loadings vary with angular positions, the operating point, and the volute design itself. By thorough flow examinations the volute could be designed to give as uniform flow as possible to all blades. This will contribute to minimize the overall pressure losses.

An important feature is that the nozzle blades should be carefully designed for the variable geometry purposes. If the nozzle throat area could be reduced without causing a sudden area change then losses will be reduced. This could be achieved by controlling the area through increased blade thickness. This can be achieved by a variable geometry design that introduces thicker profiled blades over the initial design in order to increase the restriction.

More detailed tests are needed for better understanding of the flow behaviour, possibly using laser anemometry in the narrow flow passages, this should lead to better design and improved performance.

4.2.2 Calculated Nozzle Discharge Conditions From Rotor Discharge Measurements

The space limitations in the interspace between the nozzle exit and the rotor inlet made it difficult to make any detailed measurements in this area. In order to evaluate the internal flow conditions a method was developed for calculating the inlet flow parameters from the rotor exit traverse data.This method was described in section 3.4.3 where the swirl intensity at rotor exit was derived from which the flow angles at rotor inlet were calculated.

Figures 4.19a,b,c show the calculated swirl intensity at rotor exit plotted together with the efficiency curves versus pressure ratio with different nozzles and for the 16 deg. exhaust diffuser. These figures show that the swirl magnitude increases with increasing pressure ratio for a given rotational speed. The non restricted and the 20% restricted nozzles gave mainly negative swirl while the 50% restricted nozzle ring resulted in mainly positive swirl. From these figures it is clear that the swirl is only slightly affected by introducing the diffuser within the range of operation considered. It is noticeable that with the non-restricted nozzle and that of 20%

restriction, high efficiencies coincide with low swirl at low rotational speeds, while at high speeds the maximum efficiency coincides with negative swirl. With the 50% restriction high positive swirl is predominant and the efficiencies are generally low which indicates high incidence angles at rotor inlet. It can be concluded that by analysing the flow conditions and swirl at rotor discharge the internal flow conditions at rotor inlet can be predicted. The mean velocity triangles at rotor inlet and exit were constructed following the procedure in section 3.4.3. These results give a general picture of the mean flow behaviour at these positions. Figures 4.20-4.22 show the rotor incidence angle and the absolute rotor exit flow angle for the three nozzle rings and different diffusers. In these figures the mean angle of incidence at rotor inlet was assessed when the operating conditions gave zero swirl at rotor discharge. Figures 4.20a,b,c represent the variation of incidence angle for the three nozzle restrictions with the 29 deg. diffuser. Figures 4.21a,b,c with the 16 deg. diffuser, and figures 4.22a,b,c for the 8 deg. diffuser. It can be seen that the best match between zero incidence at rotor inlet and zero swirl at rotor discharge occurs when the 20% restriction nozzle is used. The incidence angles for zero discharge swirl are negative when the full nozzle is used and highly

positive when the nozzle is 50% restricted. Figures 4.23a,b,c summarize these variations of angle of incidence when the exit flow is axial. It can be clearly seen that the 20% restricted nozzle gave the best incidence for all three diffusers used, and that the 50% restricted nozzle was associated with high positive incidence.

This observation is in agreement with the high overall turbine efficiencies associated with the 20% restricted nozzle ring as shown earlier see fig. 4.9c.

4.2.3 Calculated Rotor Loss Coefficient

The loss coefficient was computed see section 3.4.4 at each traverse point as a function of the radial position in the passage. The results are plotted in figures 4.24a,b,c at various rotational speeds and for different nozzles associated with the 16 deg. cone angle diffuser. These results show that the minimum losses occur near the hub region and that they increase towards the outer wall. This variation is common in all cases tested and is a function of the pressure ratio for any rotational speed. From the variation of the losses in the passage between the shroud and the hub, it can be seen that there is a non uniform work distribution from the hub to the outer wall for all nozzles tested. The minimum work occurring along

the outer wall, this is due to the blade unloading resulting from tip leakages From these figures it can be seen that the minimum loss covers a wide range of pressure ratio at low speed, while they have a narrow range at high speeds. High losses are associated with the 50% restriction nozzle. Generally the total loss is a result of a number of factors, they include : the turbine design the geometry of the volute, and the design and the type of the nozzle restriction, and the operating conditions.

At 50% restriction, it is believed that the major part of the loss is due to the sudden enlargement and the large rotor incidence angle observed in the previous section.

FIG 4.1a NON DIMENSIONAL MASS FLOW CHARACTERISTICS

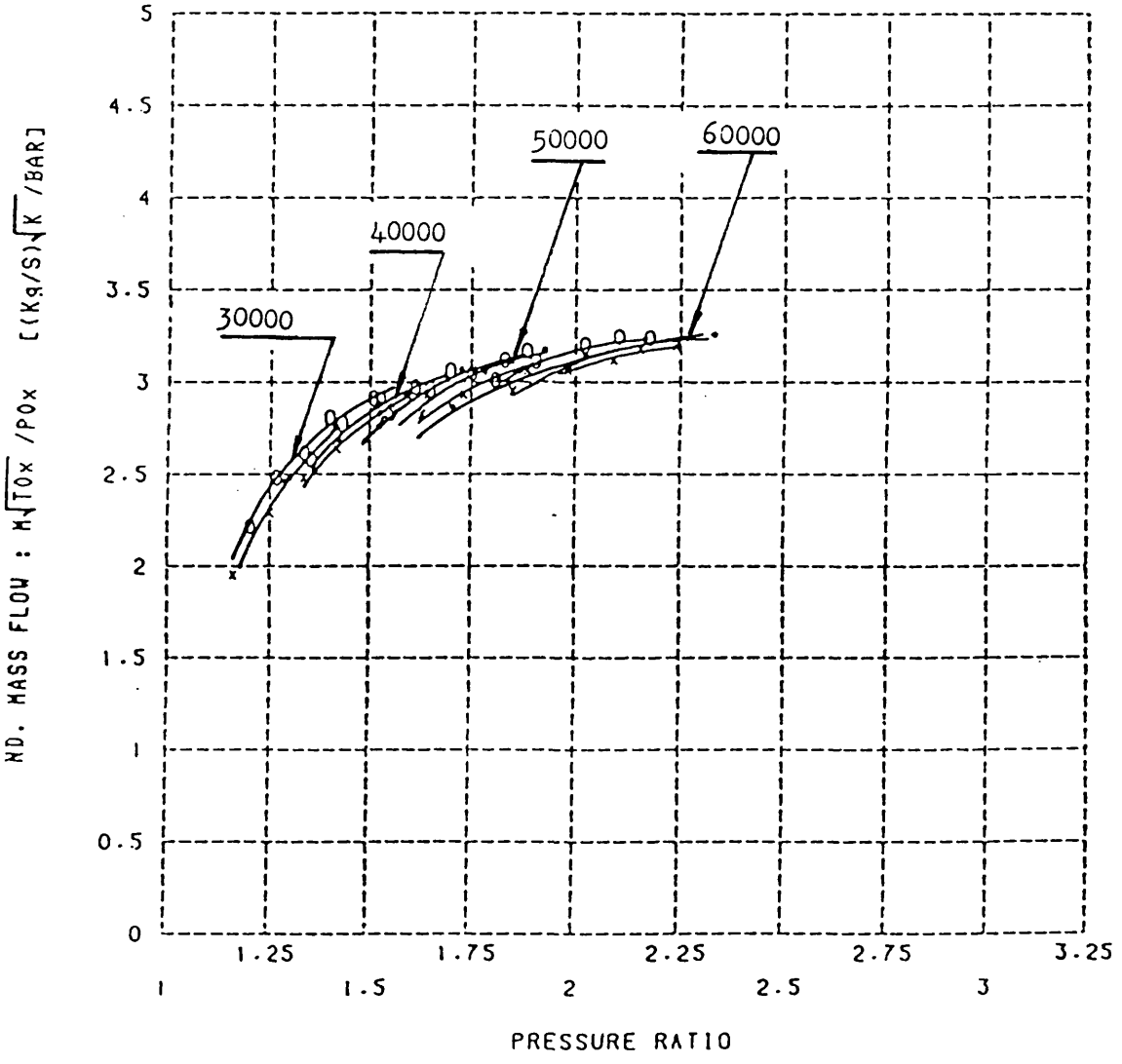

x : DIFFUSER CONE ANGLE = 29°

o : DIFFUSER CONE ANGLE = 16°

* : DIFFUSER CONE ANGLE = 8°

NOZZLE RESTRICTION = 0%

FIG 4.1b NON DIMENSIONAL TORQUE CHARACTERISTICS

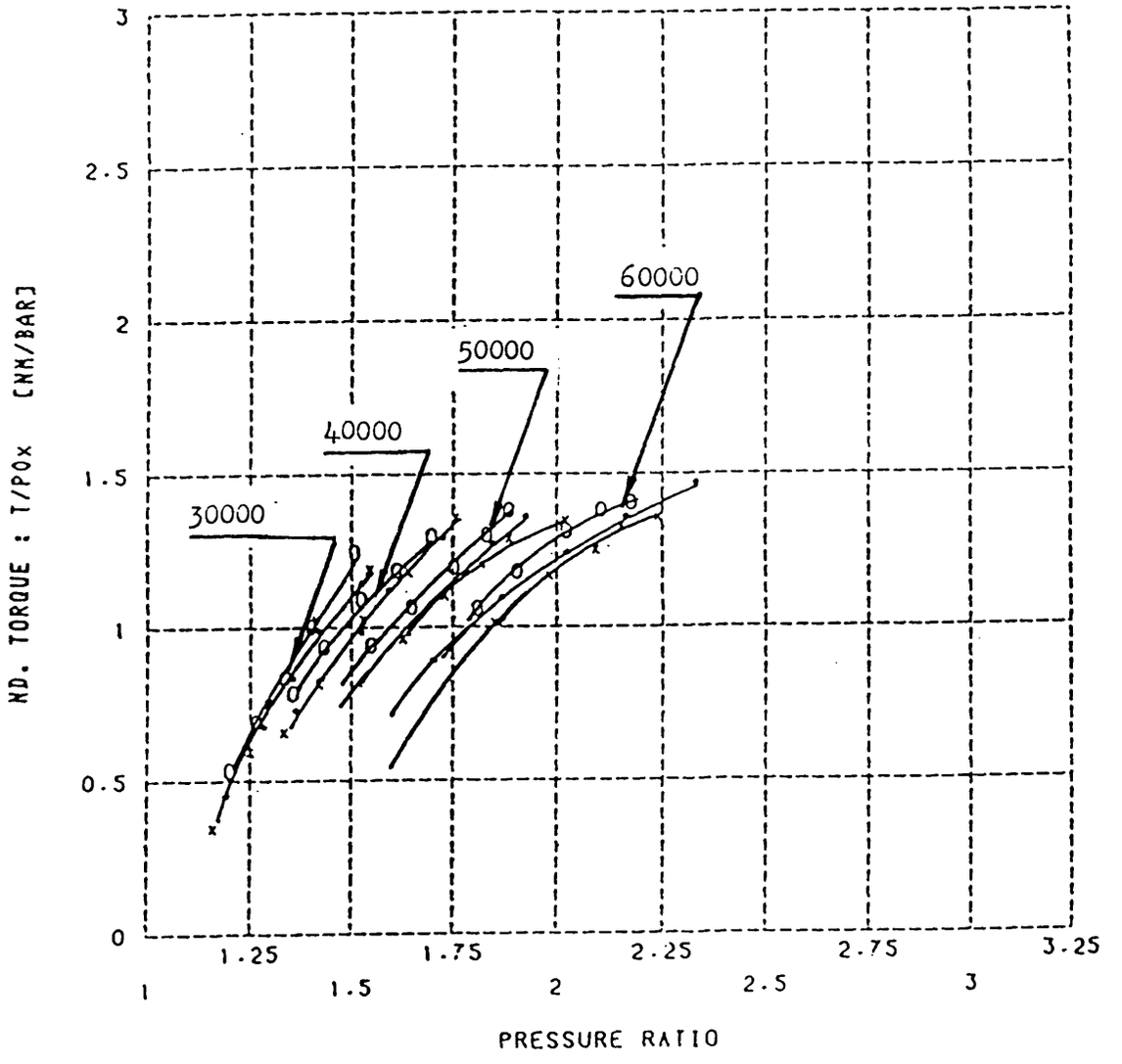

x : DIFFUSER CONE ANGLE = 29°

o : DIFFUSER CONE ANGLE = 16°

* : DIFFUSER CONE ANGLE = 8°

NOZZLE RESTRICTION = 0%

FIG 4.1c TOTAL TO STATIC EFFICIENCY VS PRESSURE RATIO

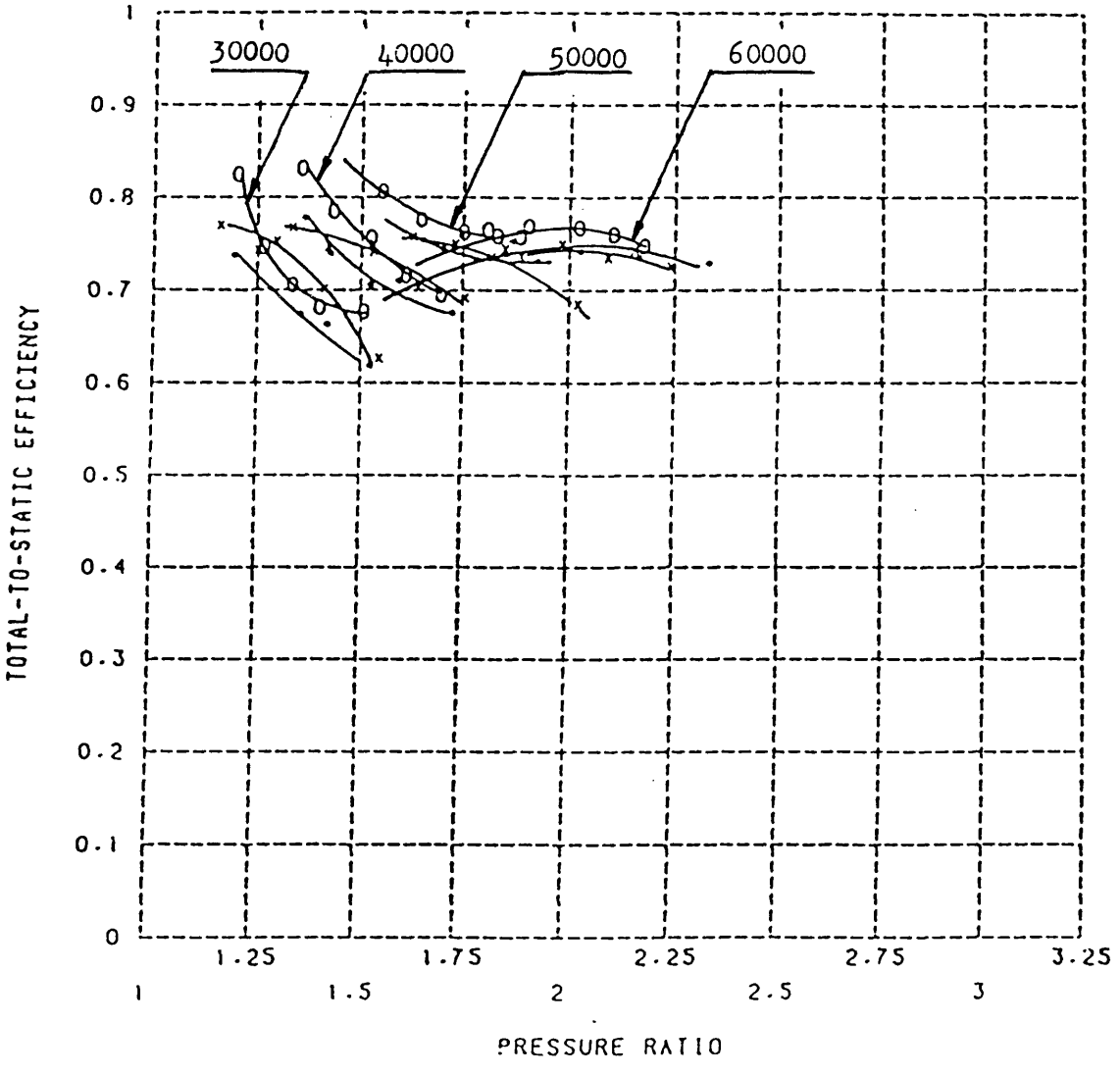

x : DIFFUSER CONE ANGLE = 29°

o : DIFFUSER CONE ANGLE = 16°

* : DIFFUSER CONE ANGLE = 8°

NOZZLE RESTRICTION = 0%

FIG 4.1d TOTAL TO STATIC EFFICIENCY VS SPEED RATIO

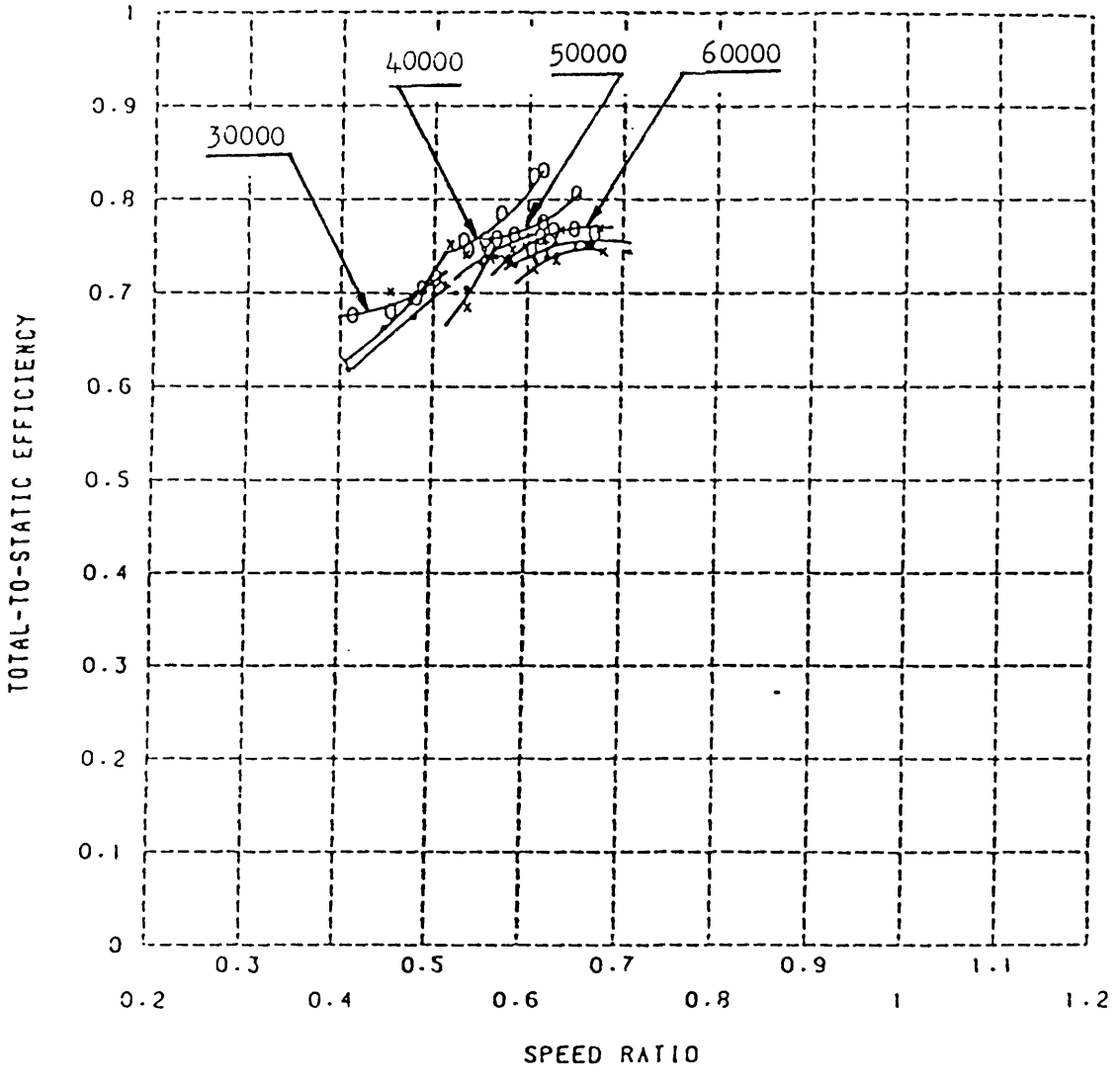

x : DIFFUSER CONE ANGLE = 29°

o : DIFFUSER CONE ANGLE = 16°

* : DIFFUSER CONE ANGLE = 8°

NOZZLE RESTRICTION = 0%

FIG 4.2 A COMPARISON BETWEEN MEASURED AND CALCULATED STATIC PRESSURE AT DIFFUSER CROSS SECTIONS

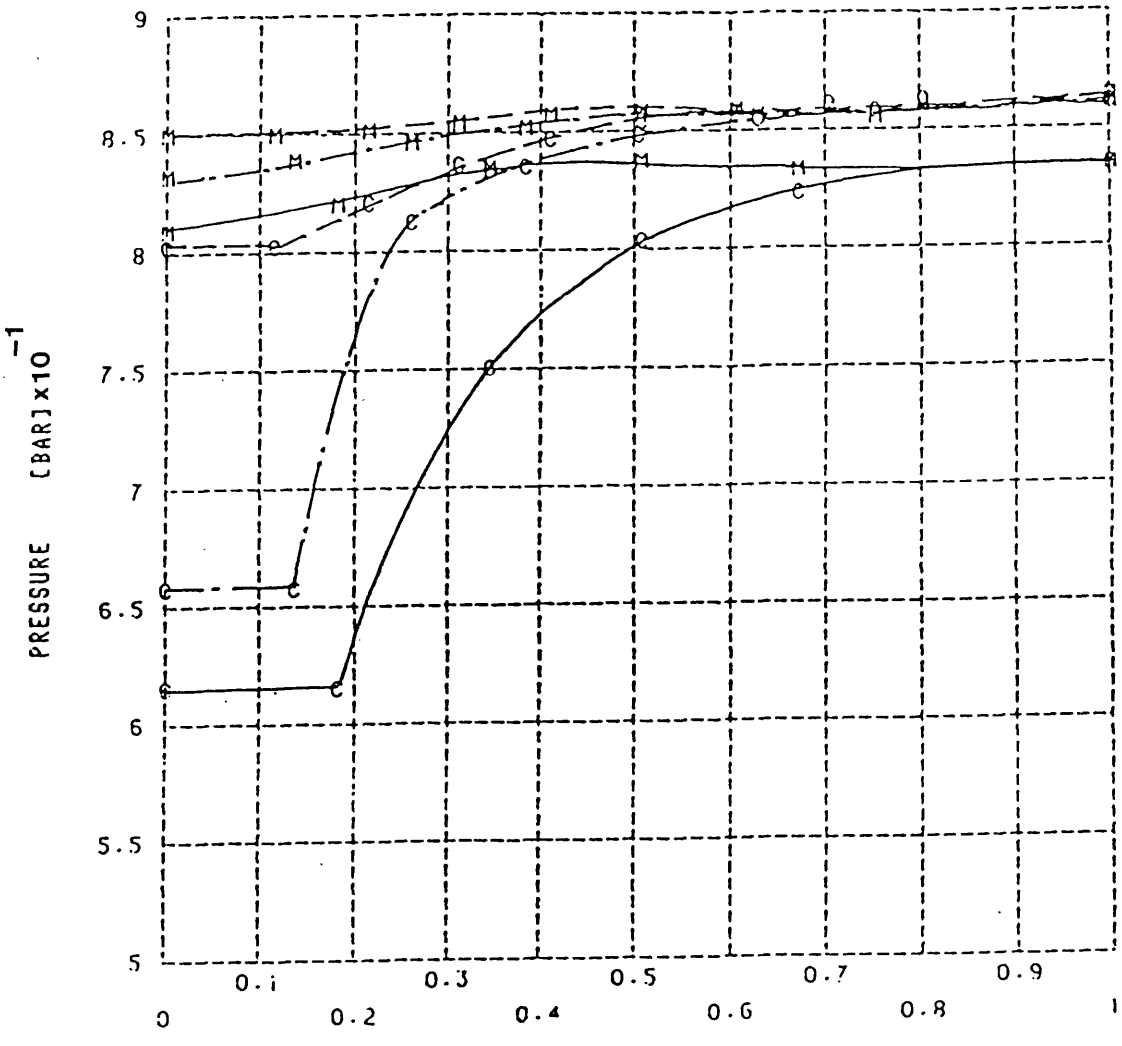

——————— INLET (WALL RADIUS = .0305 M)

—·—·—·— INTERMEDIATE (WALL RADIUS = .0405 M)

— — — — EXIT (WALL RADIUS = .0508 M)

M : MEASURED PRESURE

C : CALCULATED PRESSURE

SWIRL INTENSITY = -.44

FIG 4.3a PERCENTAGE ERROR IN MASS FLOW RATE AT DIFFUSER CROSS SECTIONS WITH THE CENTRAL WAKE

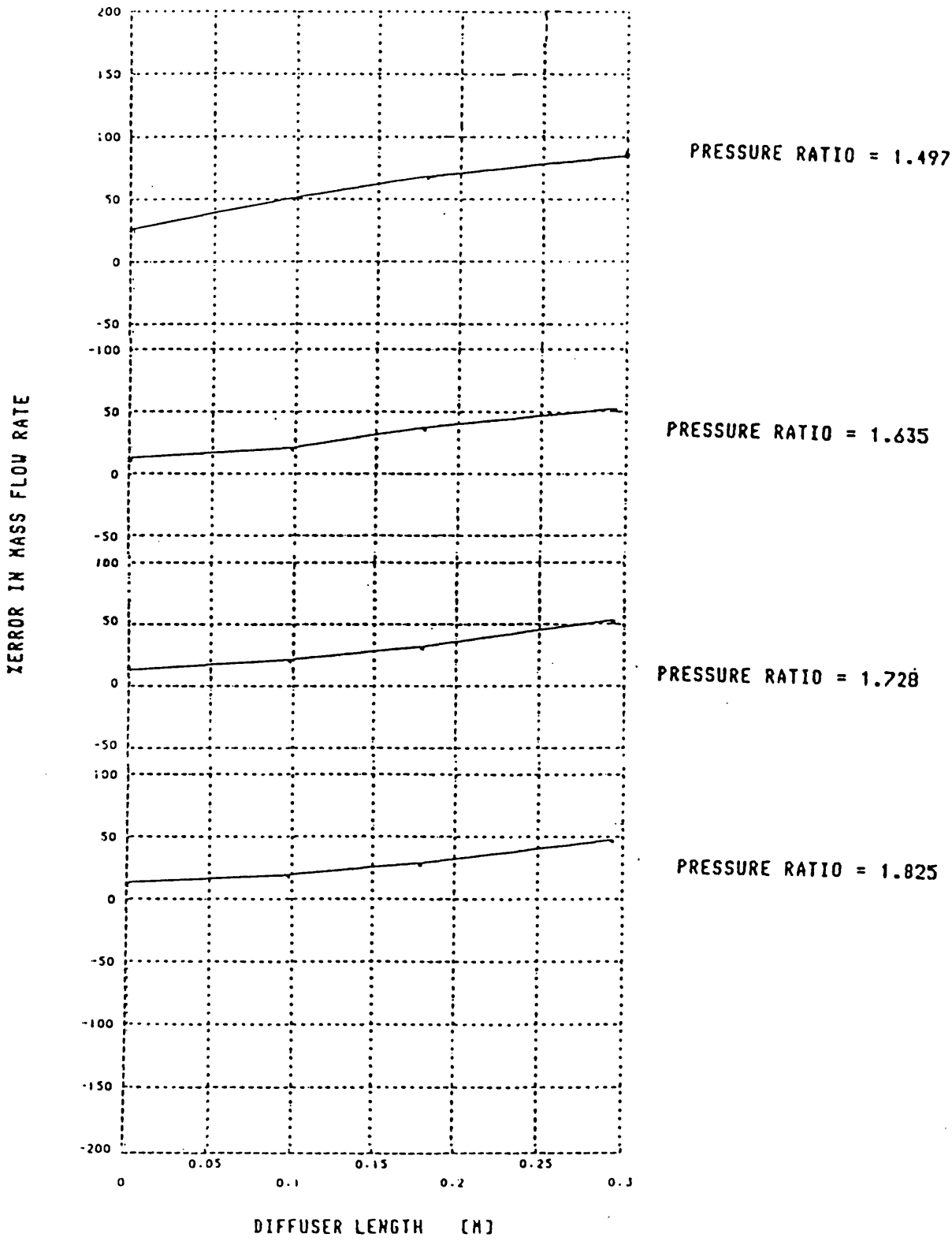

DIFFUSER CONE ANGLE = 8

NOZZLE RESTRICTION = 0%

FIG 4.3b PERCENTAGE ERROR IN MASS FLOW RATE AT DIFFUSER CROSS SECTIONS WITHOUT THE CENTRAL WAKE

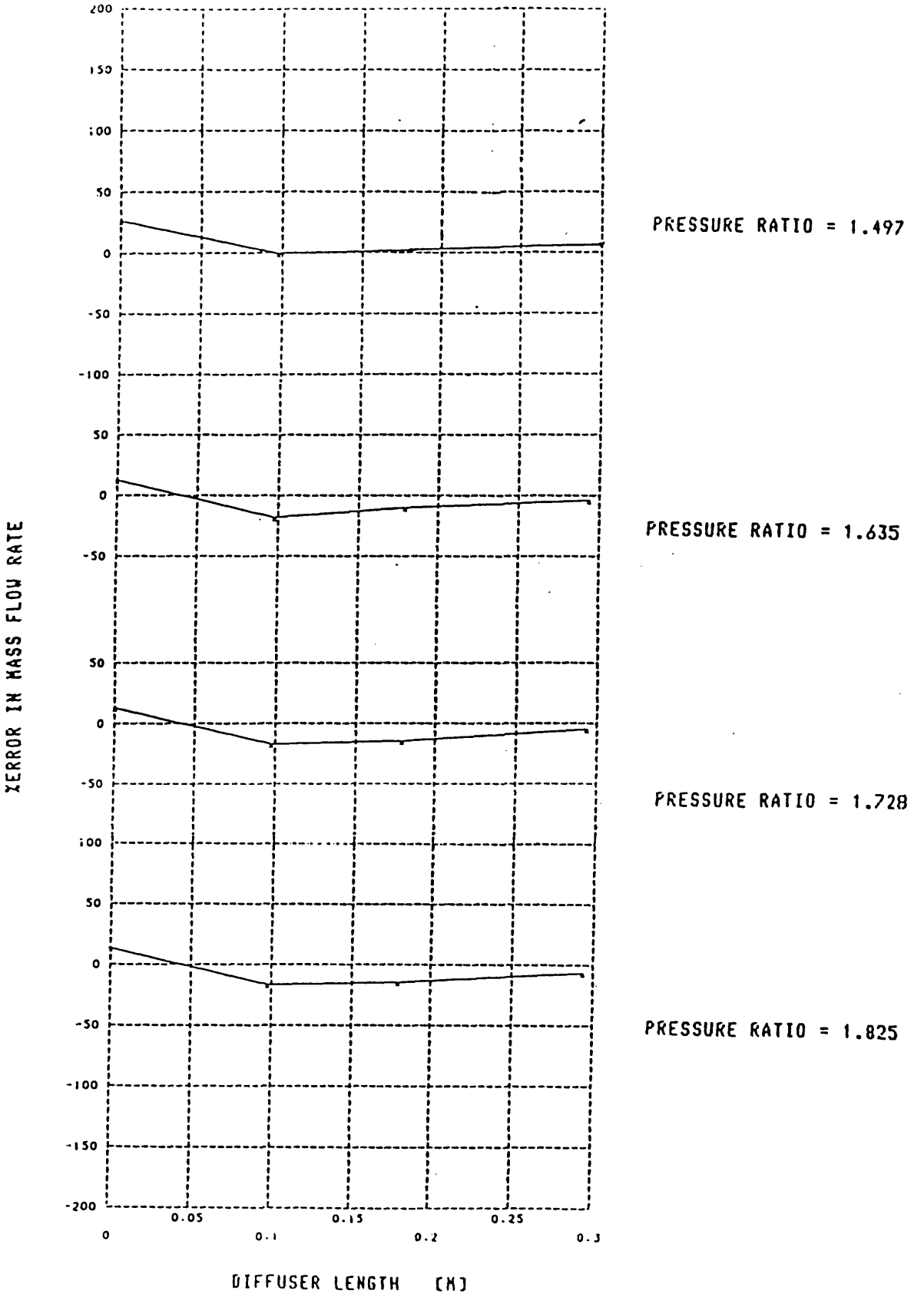

DIFFUSER CONE ANGLE = 8°

NOZZLE RESTRICTION = 0%

FIG 4.4 SWIRL VARIATION WITH PRESSURE RATIO

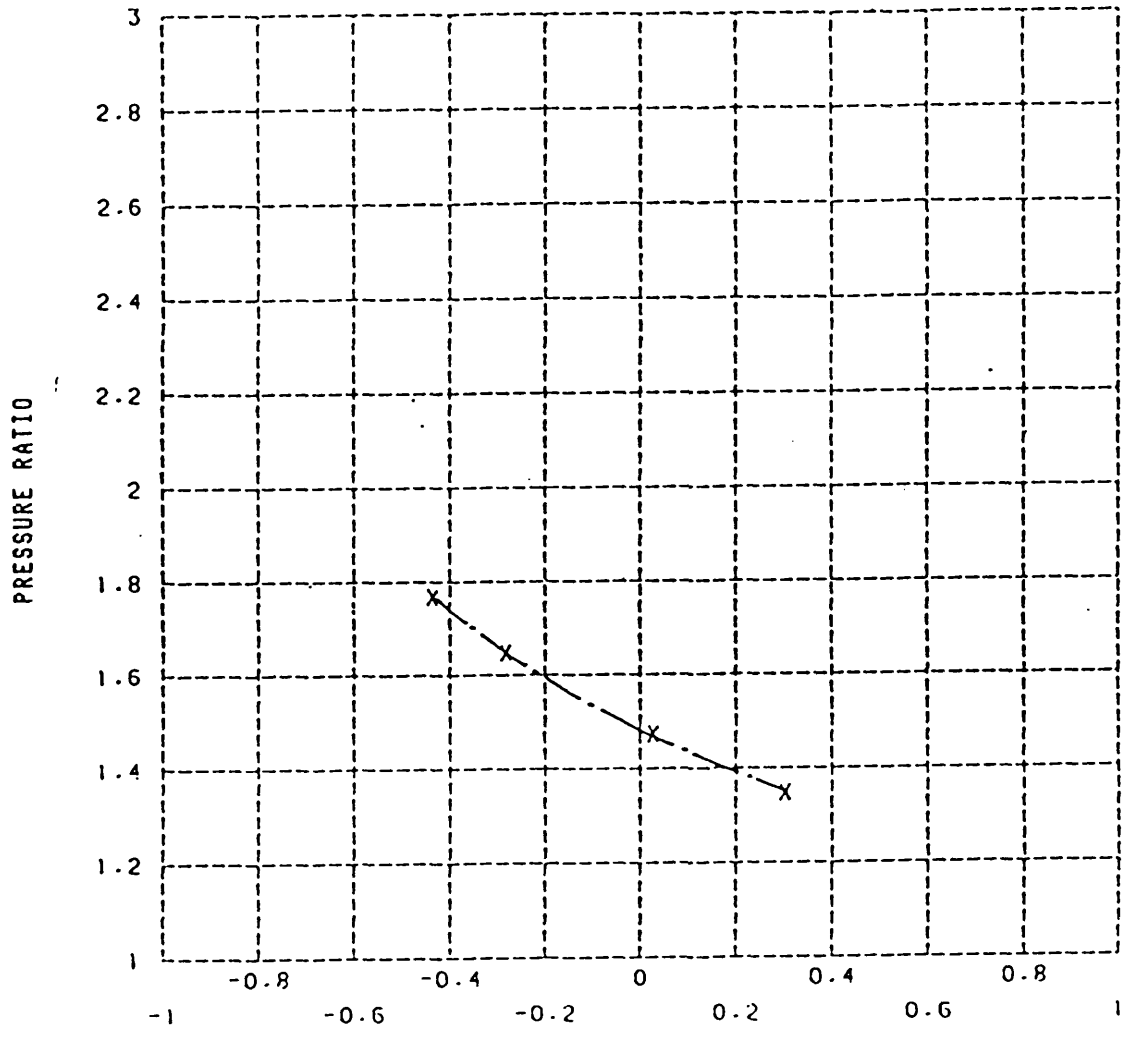

SPEED = 50000 [REVS/MIN]

DIFFUSER CONE ANGLE = 29°

NOZZLE RESTRICTION = 0%

FIG 4.5a STATIC AND STAGNATION PRESSURE VARIATION WITH INLET SWIRL (DIFFUSER ANGLE=29 DEG.)

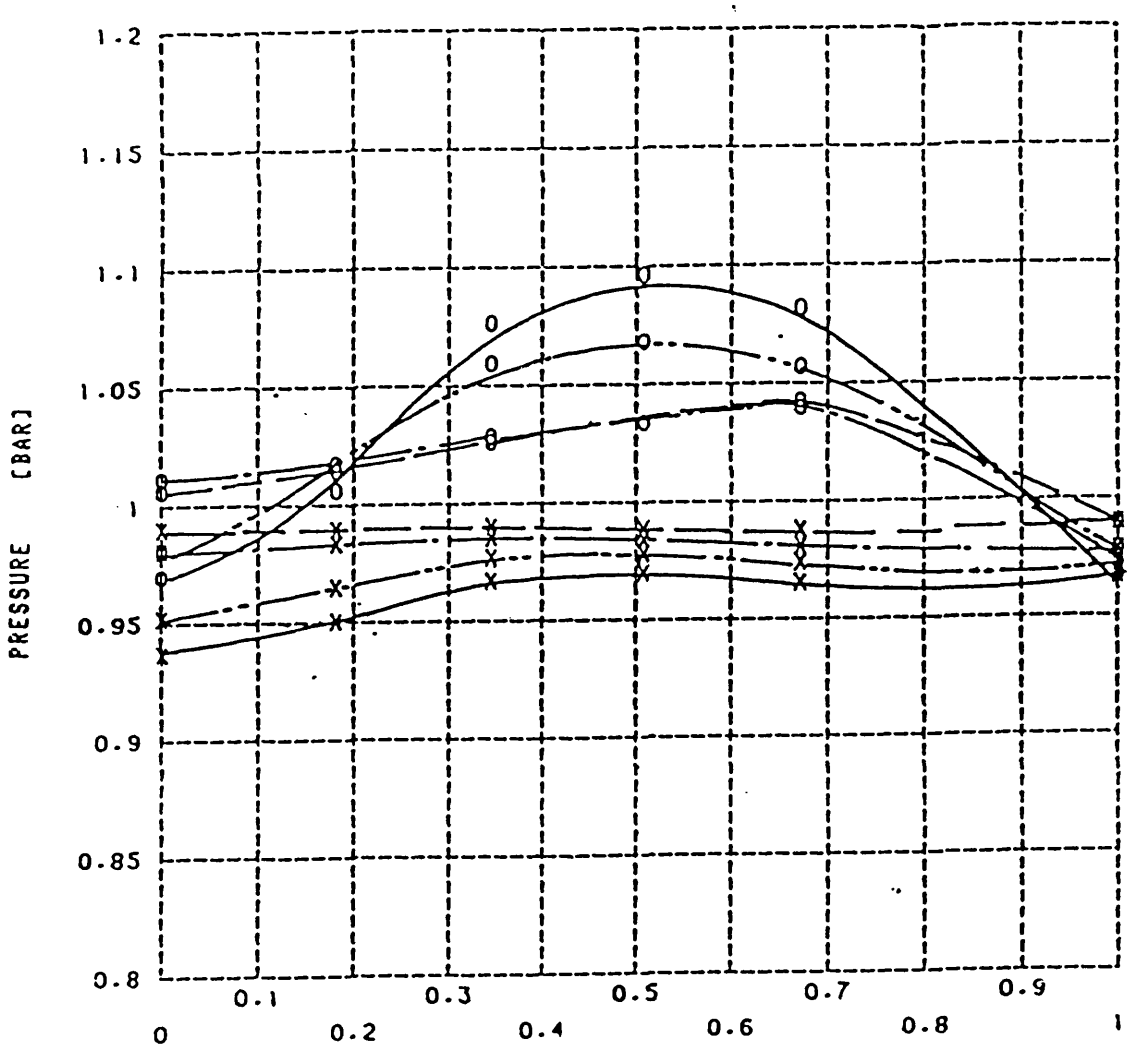

SWIRL INTENSITY

———— -.44

—·—·—·— -.28

—·—·—·— .04

— — — — .31

o : STAGNATION PRESSURE

x : STATIC PRESSURE

DIFFUSER CONE ANGLE = 29°

NOZZLE RESTRICTION = 0%

WALL RADIUS = .0305 [M]

FIG 4.5b TANGENTIAL VELOCITY VARIATION WITH INLET SWIRL (DIFFUSER ANGLE-29 DEG.)

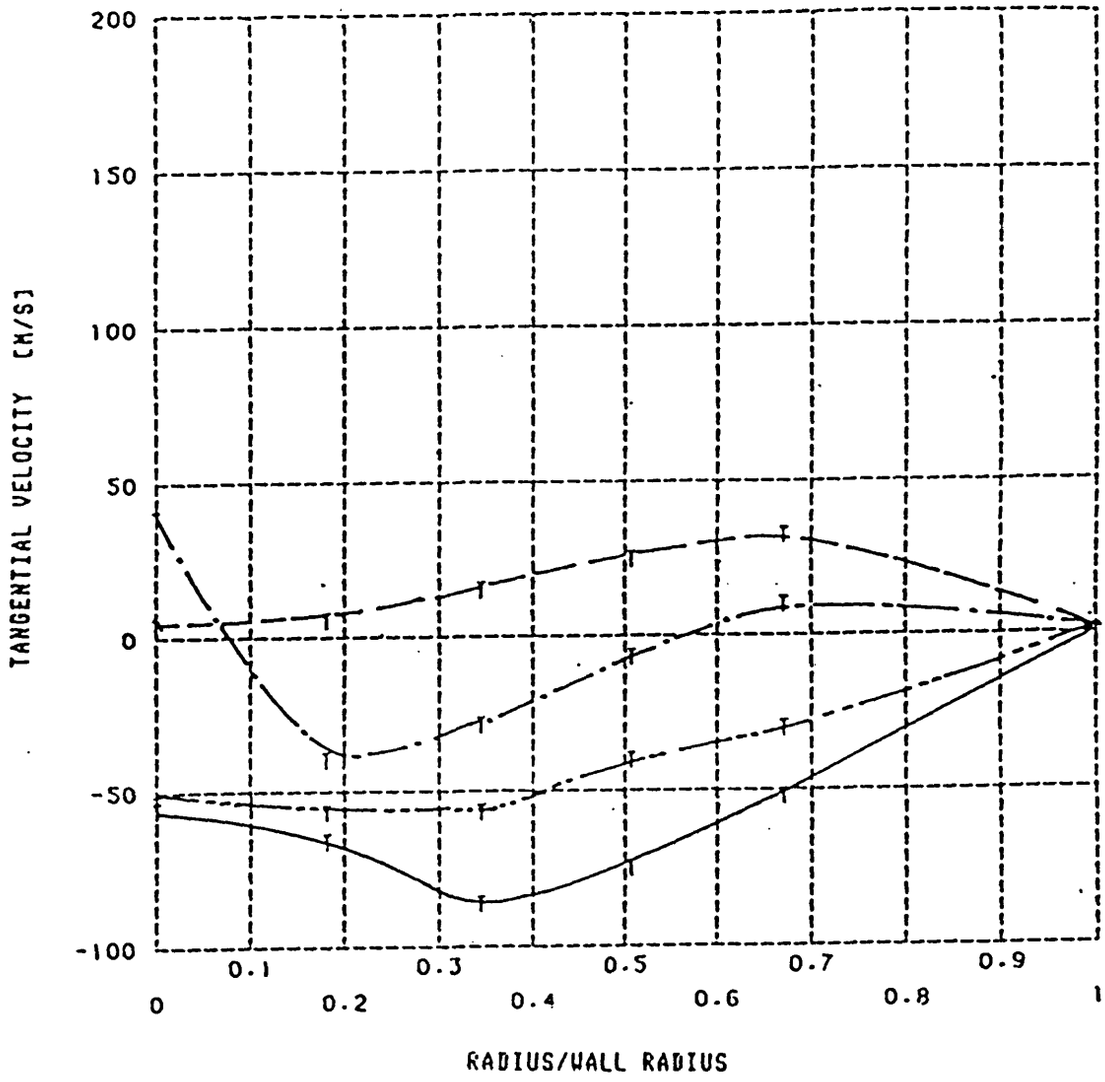

SWIRL INTENSITY

——————— -.44

—·——··——·—·— -.28

——·——·——·—— .04

— — — — — — .31

DIFFUSER CONE ANGLE = 29°

NOZZLE RESTRICTION = 0%

WALL RADIUS = .0305 (M)

FIG 4.5c TANGENTIAL VELOCITY VARIATION WITH INLET SWIRL
(DIFFUSER ANGLE=16 DEG.)

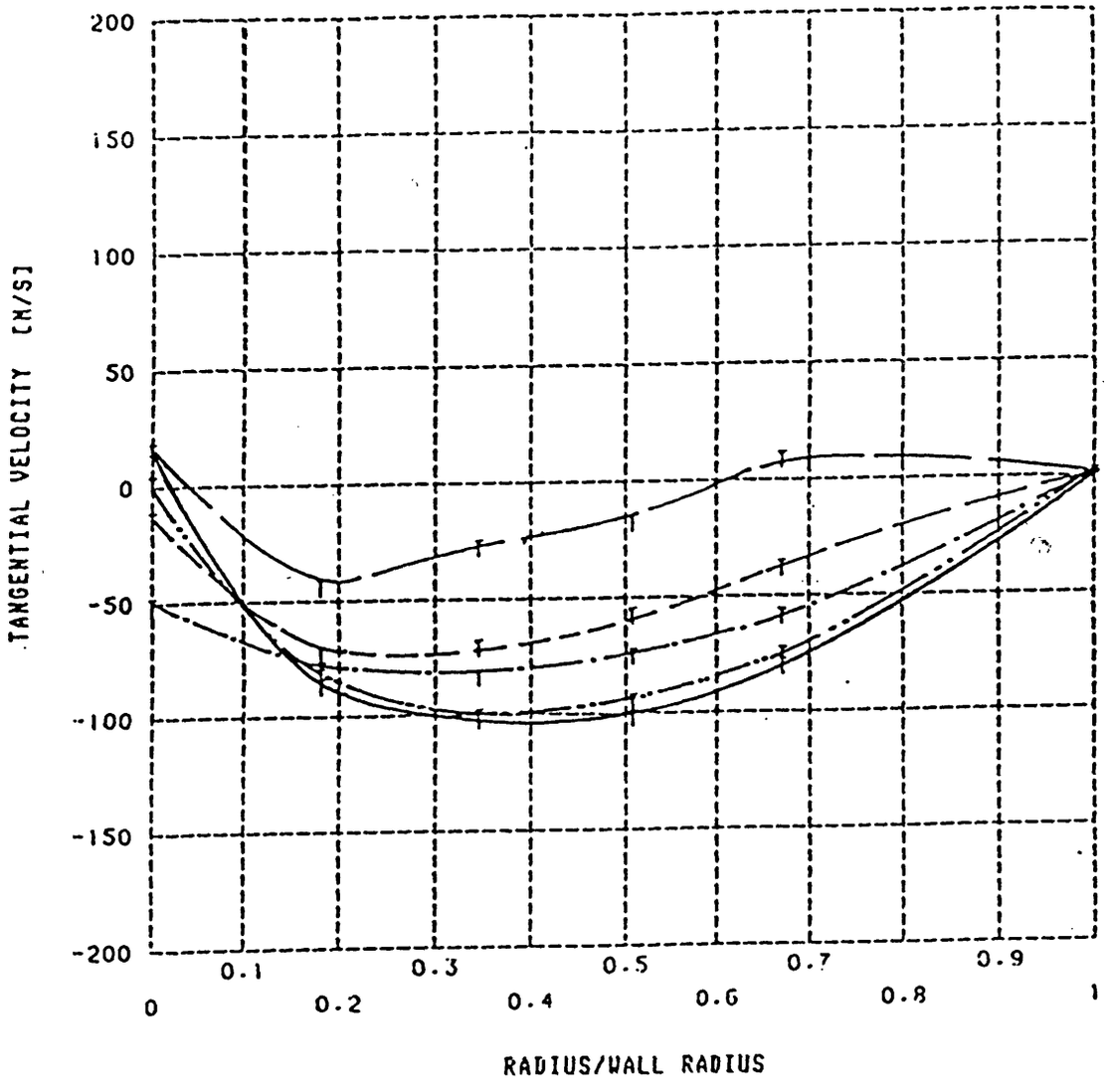

SWIRL INTENSITY

————————	-.70
—·——·——·——	-.63
——·—·——·—·——	-.59
— — — — — —	-.66
——— ———	-.44

DIFFUSER CONE ANGLE = 16°

NOZZLE RESTRICTION = 20%

WALL RADIUS = .0305 [M]

FIG 4.5d TANGENTIAL VELOCITY VARIATION WITH INLET SWIRL
(DIFFUSER ANGLE= 8 DEG.)

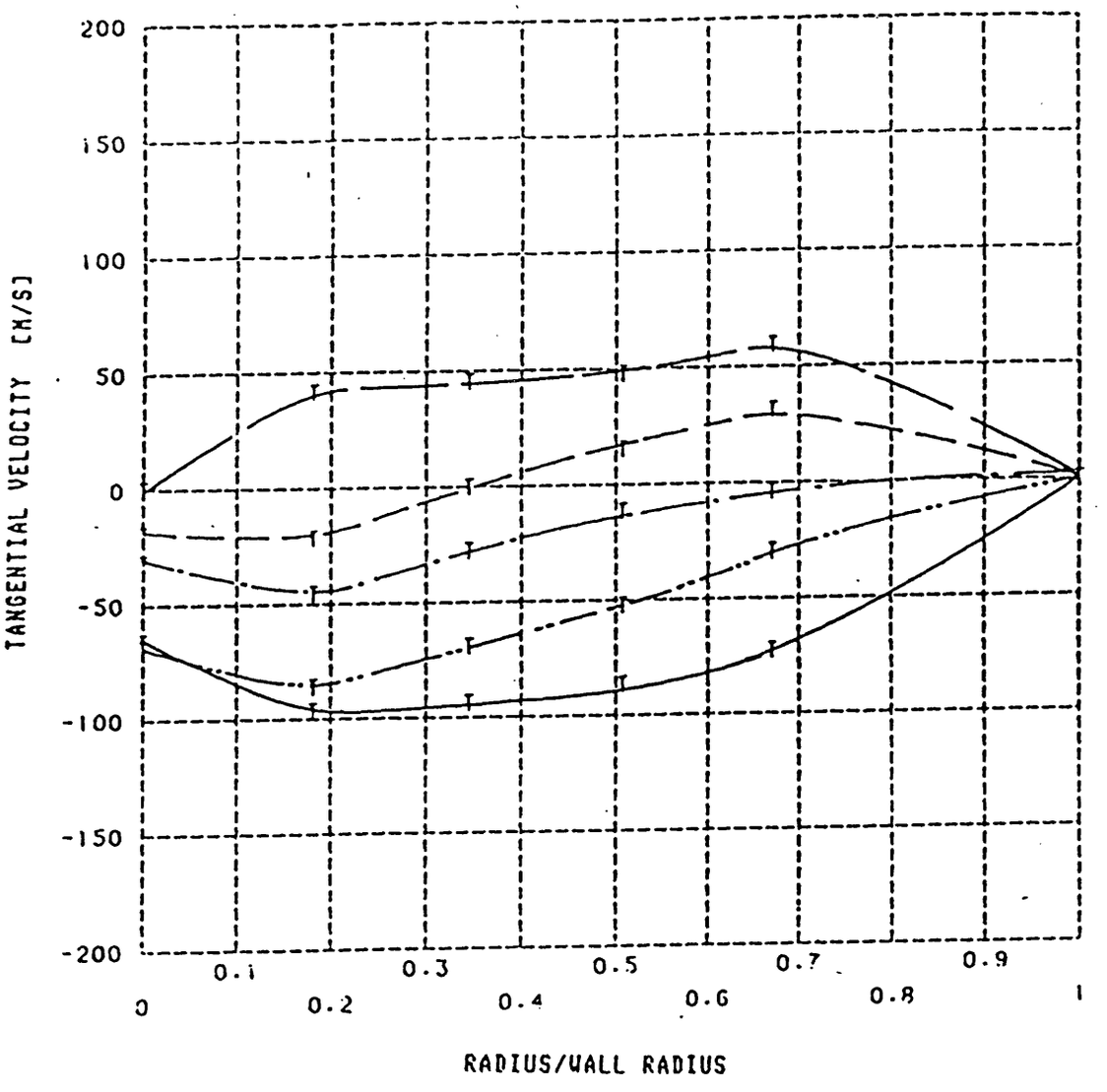

SWIRL INTENSITY

——————— -.84

—·—··—·—··— -.65

—·—·—·—·— -.57

— — — — — — -.17

——— ——— -.13

DIFFUSER CONE ANGLE = 8°

NOZZLE RESTRICTION = 20%

WALL RADIUS = .0305 [M]

FIG 4.5e AXIAL VELOCITY VARIATION WITH INLET SWIRL
(DIFFUSER ANGLE=29 DEG.)

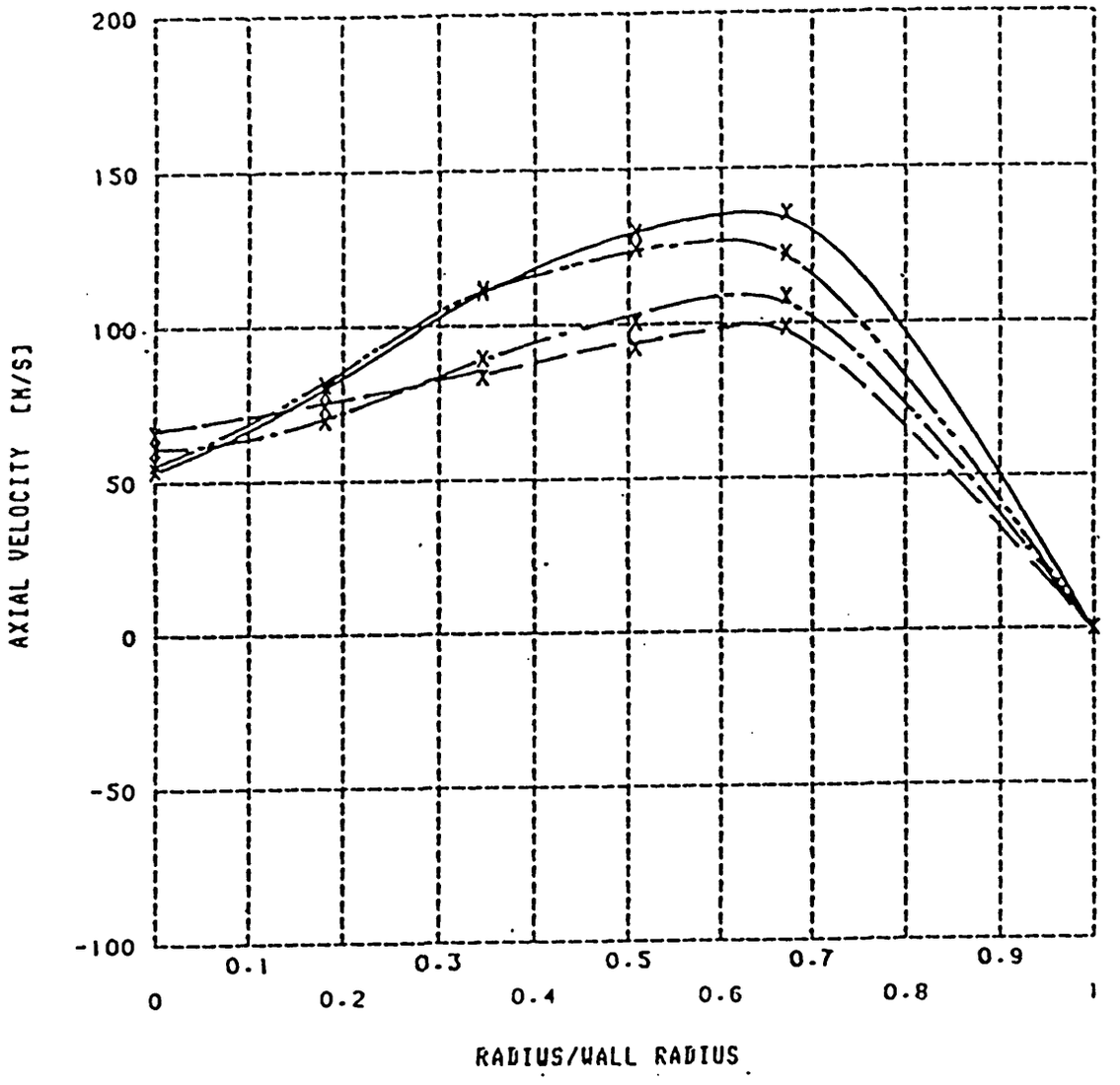

SWIRL INTENSITY

———————— -.44

———.———.———.——— -.28

———.———.———.——— .04

— — — — — — .31

DIFFUSER CONE ANGLE = 29°

NOZZLE RESTRICTION = 0%

WALL RADIUS = .0305 [M]

FIG 4.5f ABSOLUTE VELOCITY VARIATION WITH INLET SWIRL (DIFFUSER ANGLE=29 DEG.)

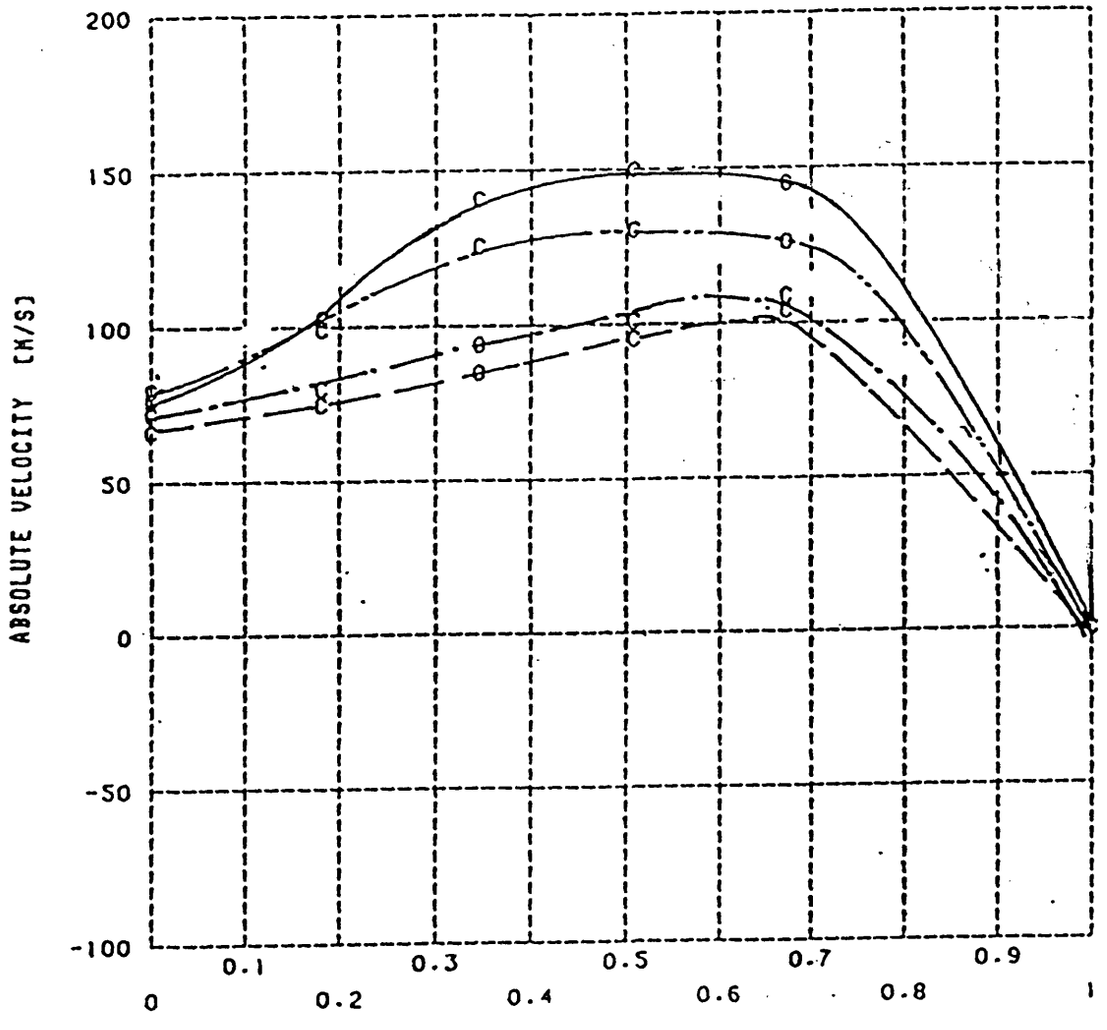

SWIRL INTENSITY

———————— -.44

———.———.——— -.28

———.—.—.——— .04

———— ———— .31

DIFFUSER CONE ANGLE = 29°

NOZZLE RESTRICTION = 0%

WALL RADIUS = .0305 (M)

FIG 4.5g FLOW ANGLE VARIATION WITH INLET SWIRL
(DIFFUSER ANGLE=29 DEG.)

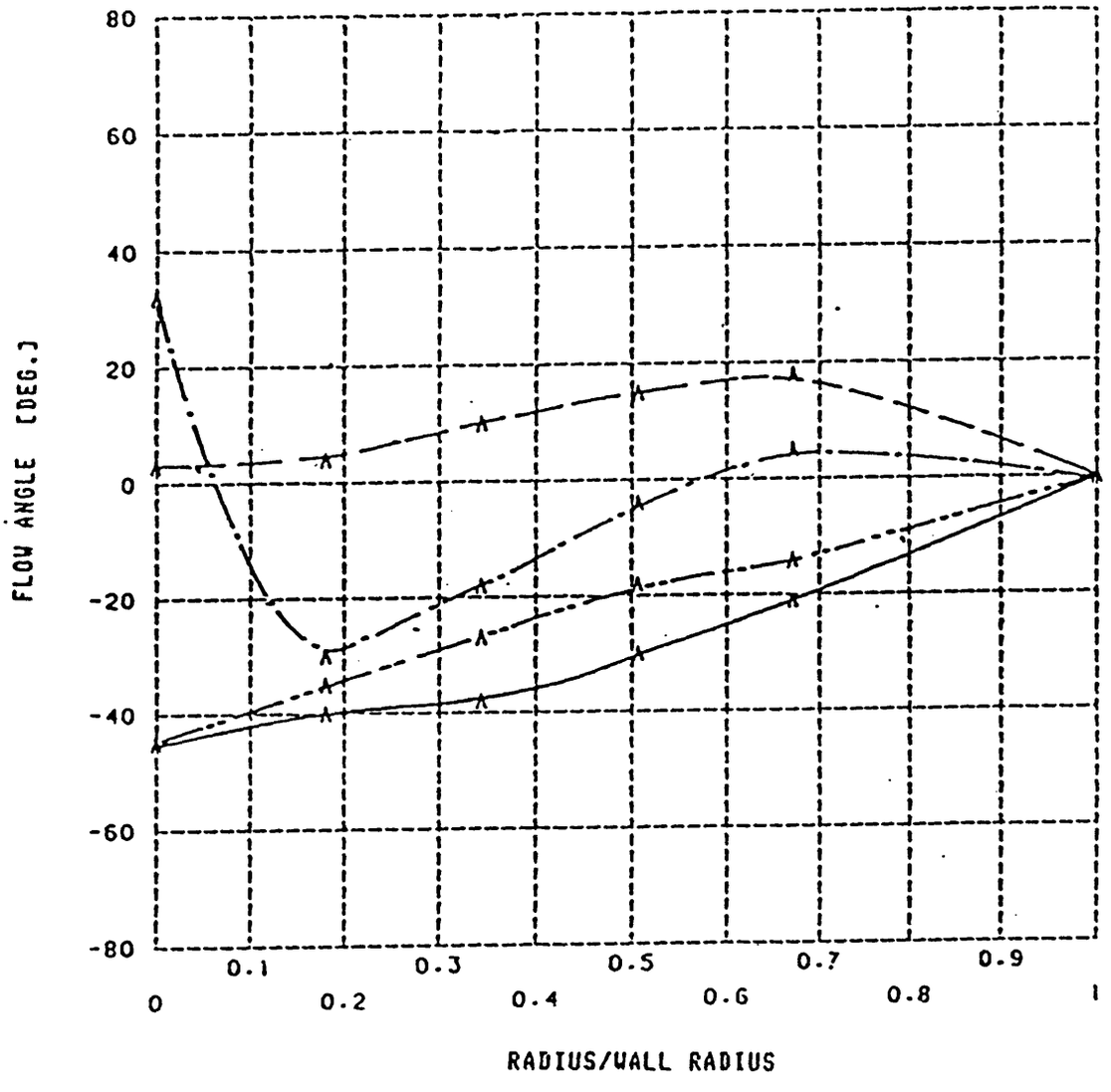

SWIRL INTENSITY

——————— -.44

——·——·—— -.28

——·—·—·— .04

— — — — — .31

DIFFUSER CONE ANGLE = 29°

NOZZLE RESTRICTION = 0%

WALL RADIUS = .0305 [M]

FIG 4.6a STATIC AND STAGNATION PRESSURE VARIATION AT DIFFUSER CROSS SECTIONS (DIFFUSER ANGLE-29 DEG.)

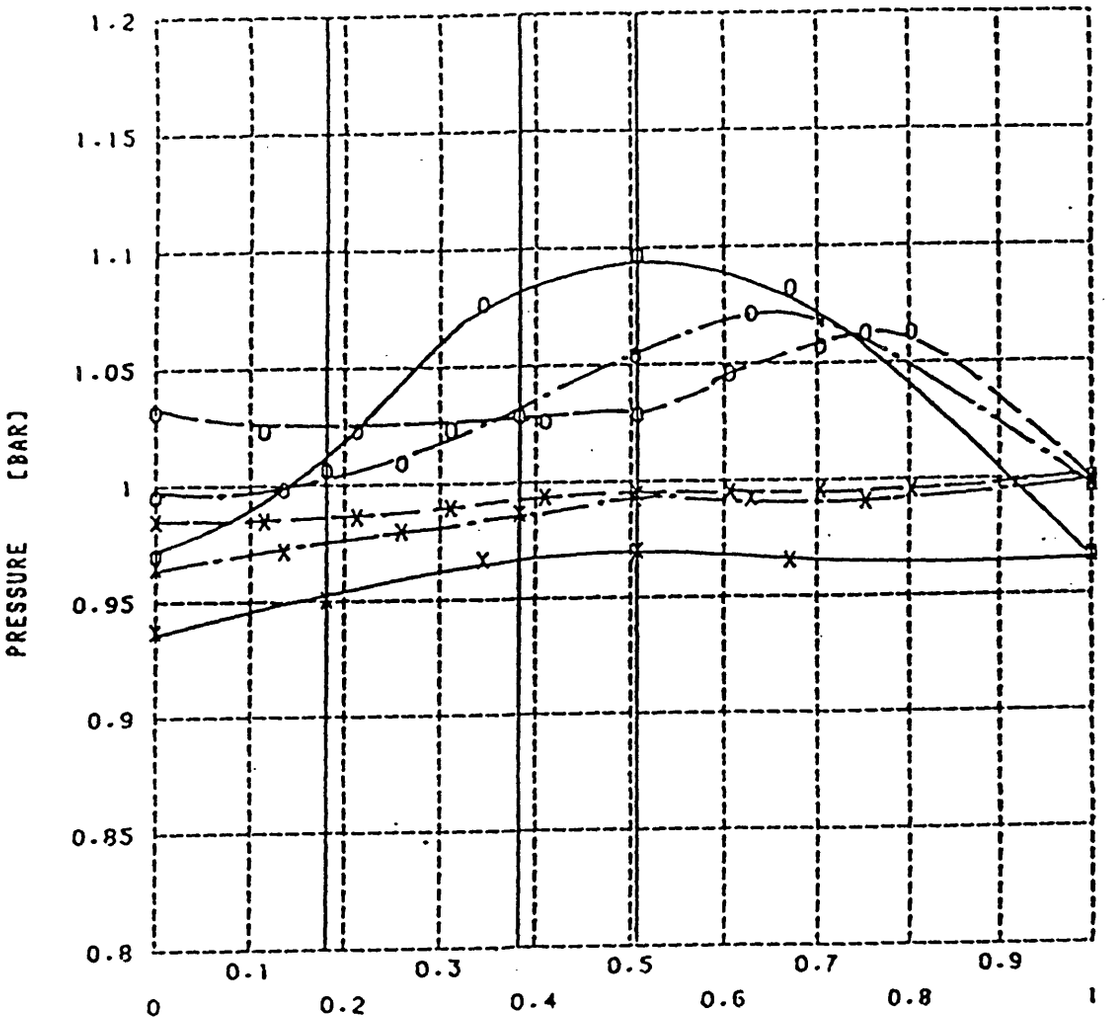

STATION

———————— INLET : WALL RADIUS = .0305 [M]

———·—·—·—·—— INTERMEDIATE : WALL RADIUS = .0405 [M]

———— —— —— —— EXIT : WALL RADIUS = .0508 [M]

DIFFUSER CONE ANGLE = 29°

NOZZLE RESTRICTION = 0%

(o) : STAGNATION PRESSURE

(x) : STATIC PRESSURE

FIG 4.6b TANGENTIAL VELOCITY VARIATION AT DIFFUSER CROSS SECTIONS (DIFFUSER ANGLE=20 DEG.)

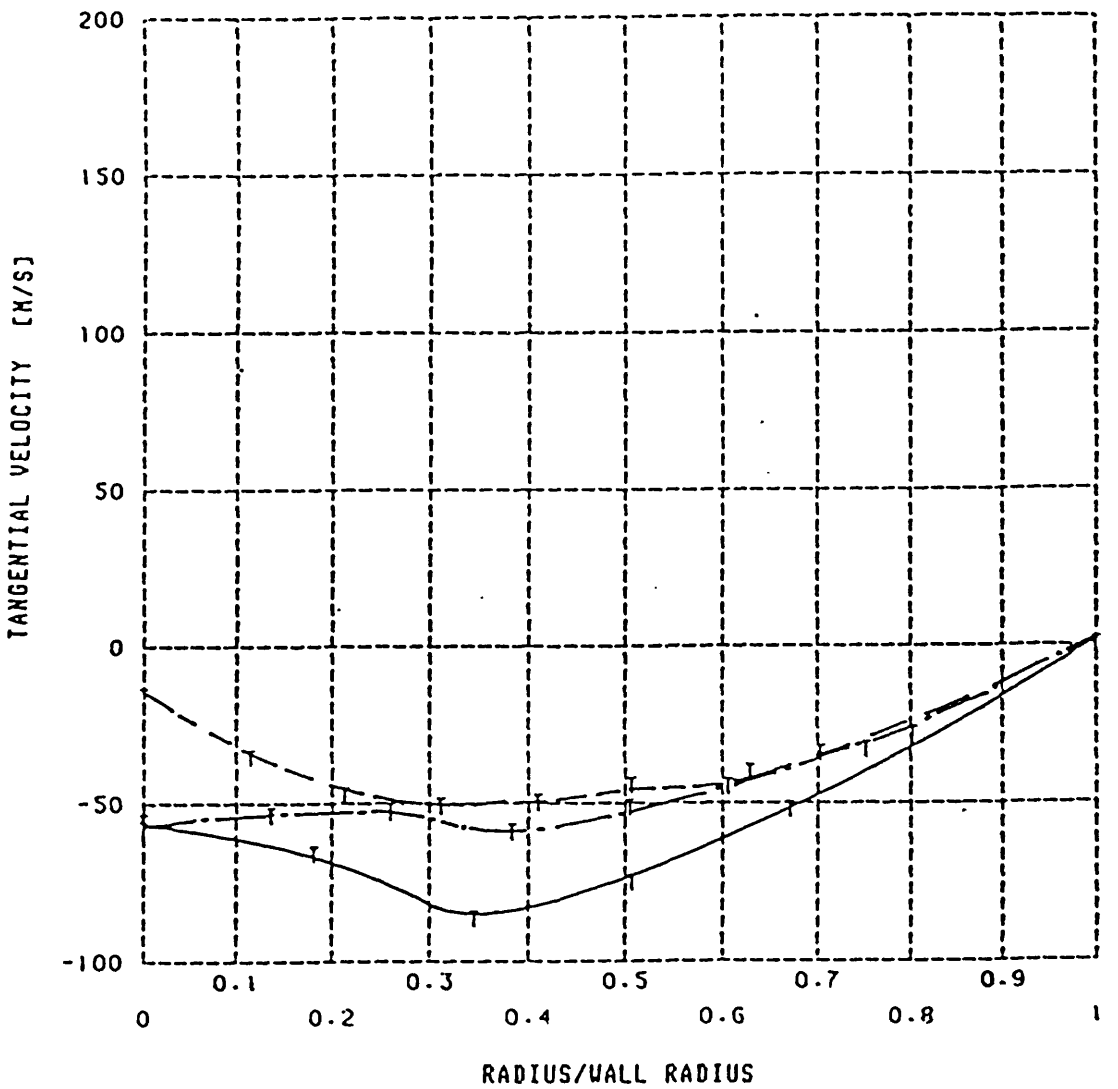

STATION

——————— INLET : WALL RADIUS = .0305 [M]

———·——·——·——— INTERMEDIATE : WALL RADIUS = .0405 [M]

— — — — — — EXIT : WALL RADIUS = .0508 [M]

DIFFUSER CONE ANGLE = 29°

NOZZLE RESTRICTION = 0%

SWIRL INTENSITY AT DIFFUSER INLET = -.44

FIG 4.6c TANGENTIAL VELOCITY VARIATION AT DIFFUSER CROSS SECTIONS (DIFFUSER ANGLE-16 DEG.)

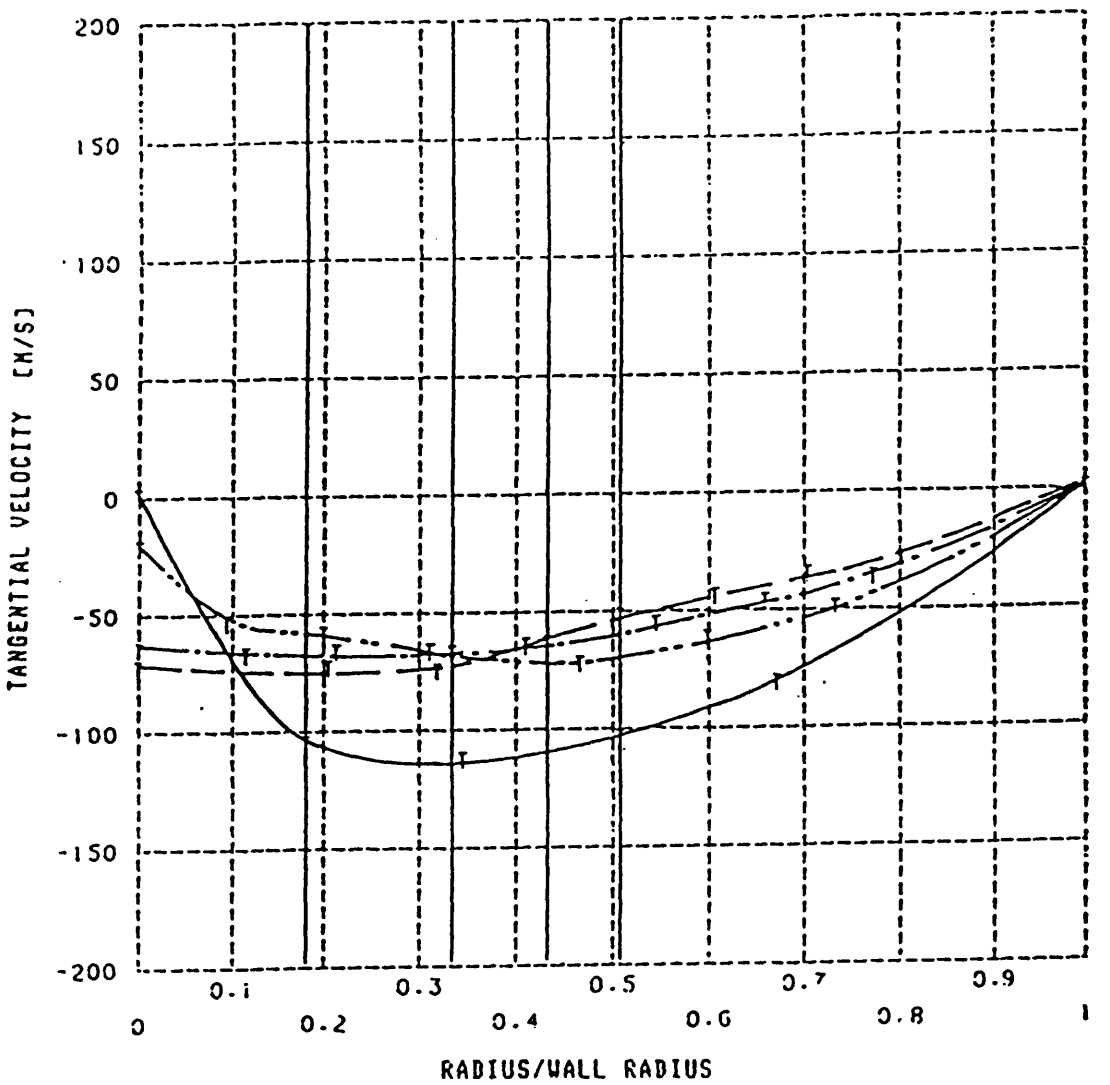

STATION

1 INLET WALL RADIUS = [M]

2 INTERMEDIATE WALL RADIUS = [M]

3 INTERMEDIATE WALL RADIUS = [M]

4 EXIT WALL RADIUS = [M]

DIFFUSER CONE ANGLE = 16°

NOZZLE RESTRICTION = 0%

SWIRL INTENSITY AT DIFFUSER INLET = -.58

FIG 4.6d AXIAL VELOCITY VARIATION AT DIFFUSER CROSS SECTIONS (DIFFUSER ANGLE=29 DEG.)

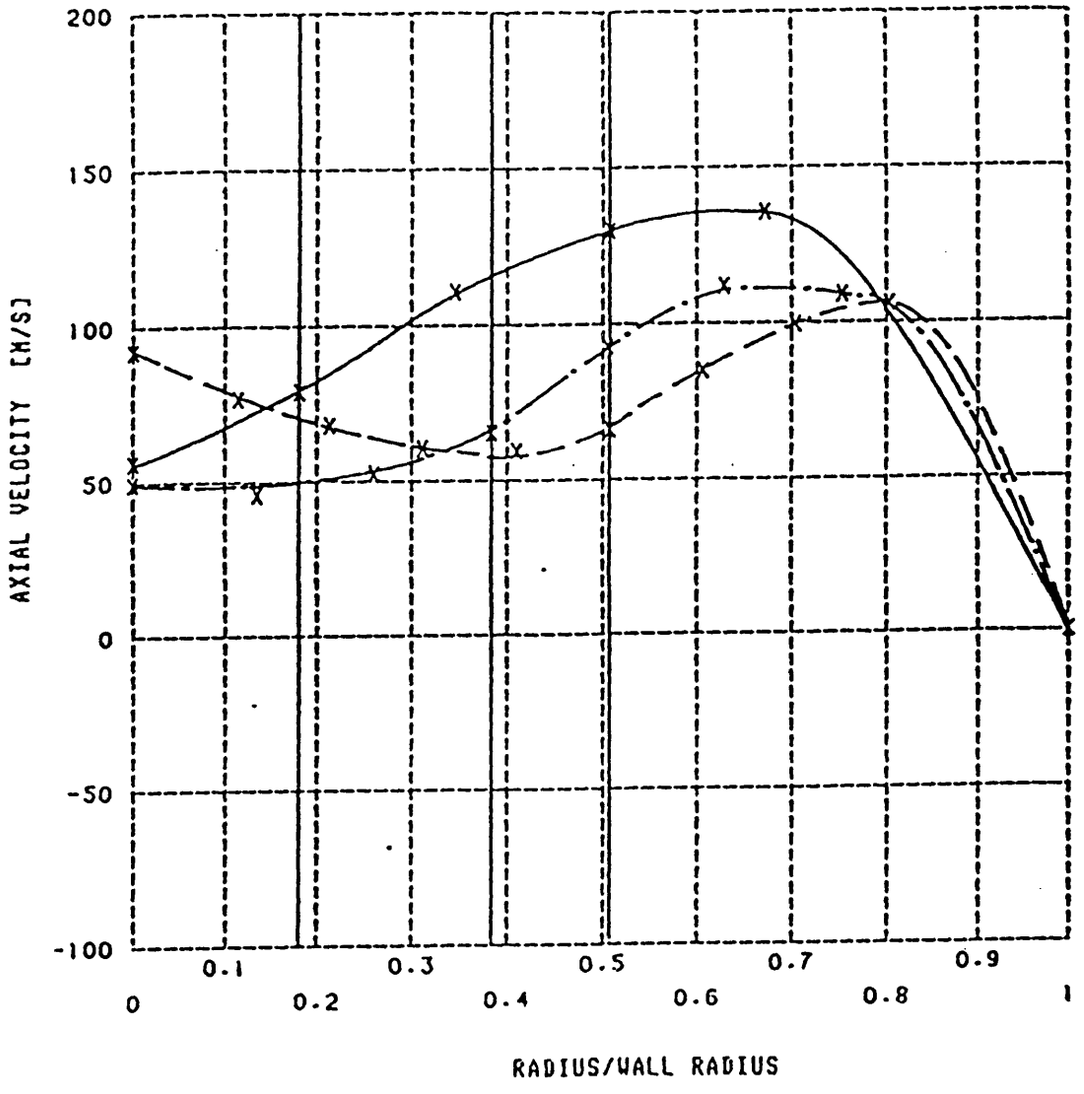

STATION

————	INLET	WALL RADIUS = .0305	[M]
——·——·——	INTERMEDIATE	WALL RADIUS = .0405	[M]
— — — — —	EXIT	WALL RADIUS = .0508	[M]

DIFFUSER CONE ANGLE = 29°

NOZZLE RESTRICTION = 0%

SWIRL INTENSITY AT DIFFUSER INLET = -.44

FIG 4.6e ABSOLUTE VELOCITY VARIATION AT DIFFUSER CROSS SECTIONS (DIFFUSER ANGLE=29 DEG.)

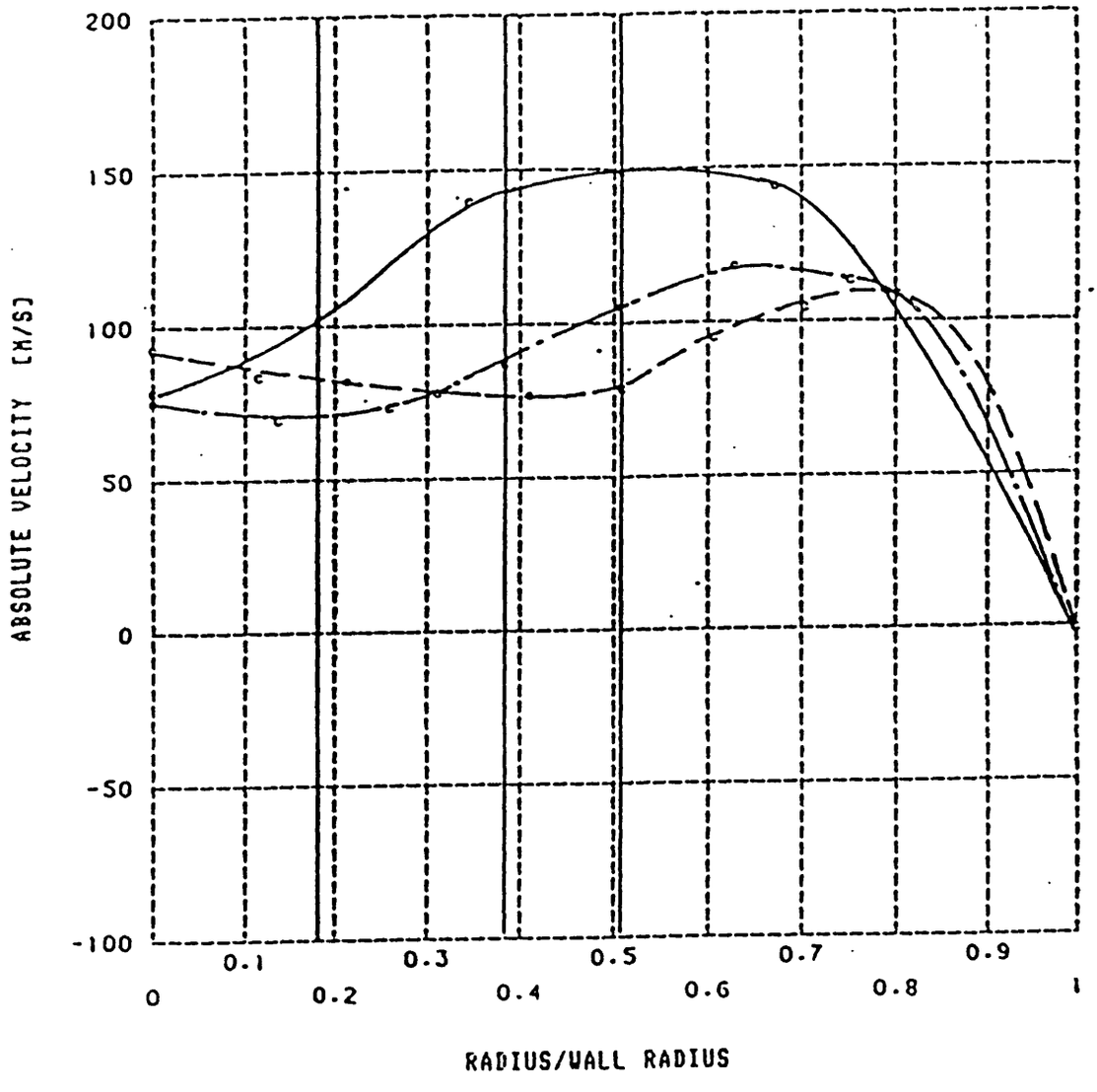

STATION

————	INLET	WALL RADIUS = .0305	[M]
——·——·——	INTERMEDIATE	WALL RADIUS = .0405	[M]
— — — — —	EXIT	WALL RADIUS = .0508	[M]

DIFFUSER CONE ANGLE = 29°

NOZZLE RESTRICTION = 0%

SWIRL INTENSITY AT DIFFUSER INLET = -.44

FIG 4.6f FLOW ANGLE VARIATION AT DIFFUSER CROSS SECTIONS (DIFFUSER ANGLE=29 DEG.)

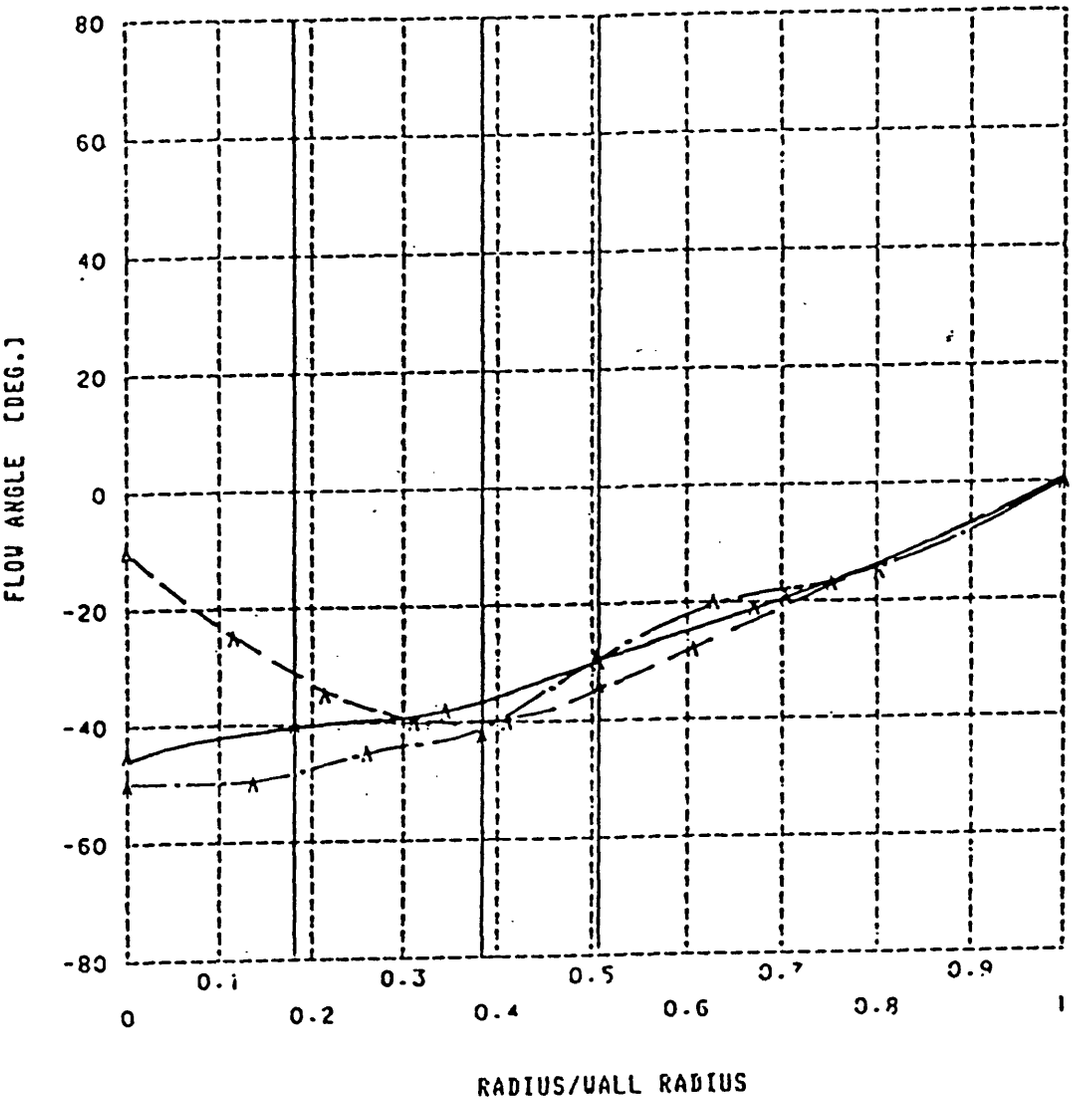

STATION

————————	INLET	WALL RADIUS = .0305	(M)
——·——·——·——	INTERMEDIATE	WALL RADIUS = .0405	(M)
— — — — — —	EXIT	WALL RADIUS = .0508	(M)

FIG 4.7a PRESSURE COEFFICIENTS AT DIFFERENT SWIRL INTENSITIES (DIFFUSER ANGLE=29 DEG.)

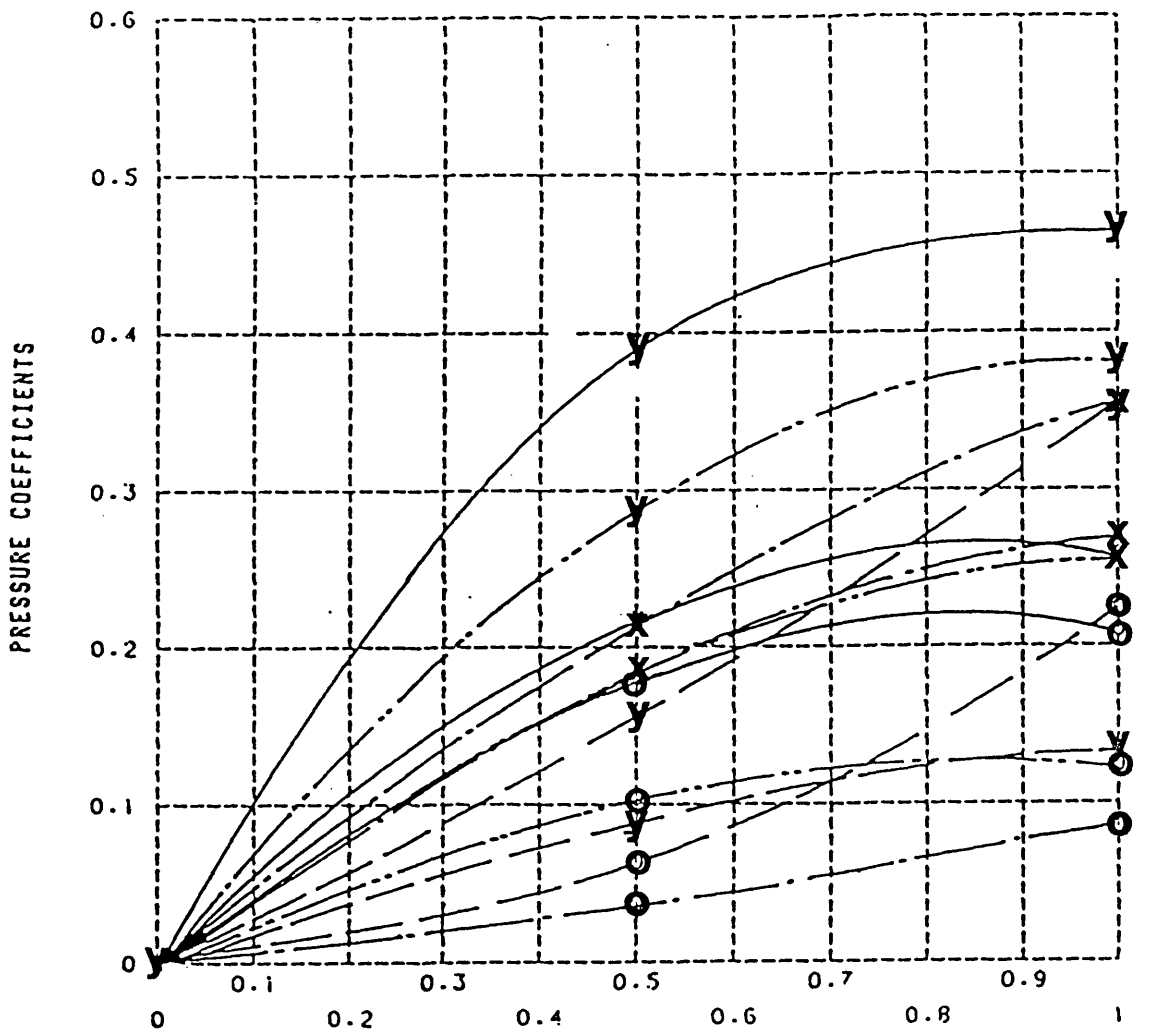

SWIRL INTENSITY

——————— -.44

——·——·——·—— -.28

——·——·——·—— .04

— — — — .31

Y : IDEAL PRESSURE RECOVERY COEFFICIENT

X : PRESSURE RECOVERY COEFFICIENT

O : STAGNATION PRESSURE LOSS COEFFICIENT

DIFFUSER CONE ANGLE = 29° DIFFUSER LENGTH = .076 (M)

NOZZLE RESTRICTION = 0%

FIG 4.7b SWIRL INTENSITY VARIATION ALONG THE DIFFUSER (DIFFUSER ANGLE=29 DEG.)

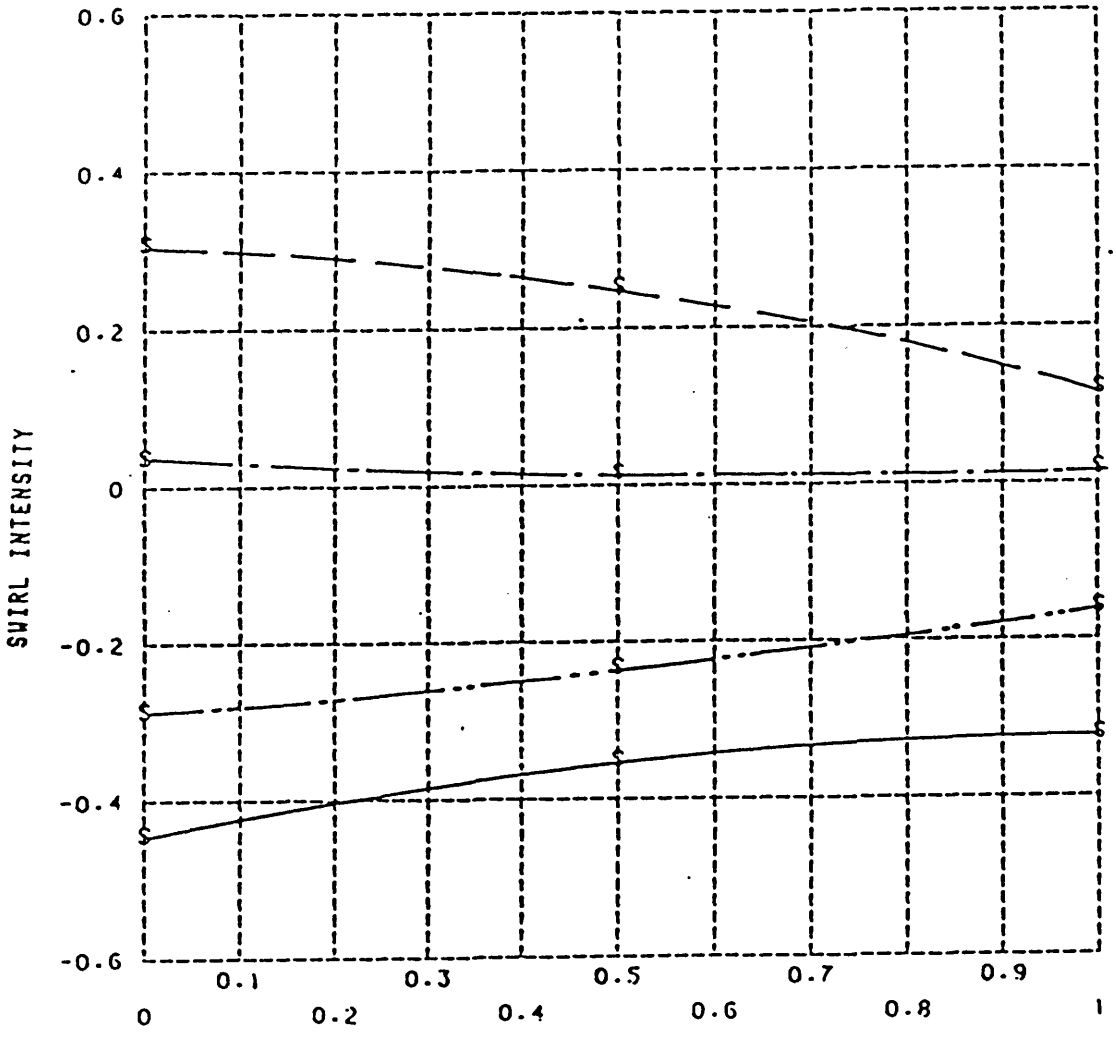

SWIRL INTENSITY PRESSURE RATIO

-.44 ———— 1.766

-.28 —.—.—.— 1.646

.04 —.—.—.— 1.470

.31 — — — — 1.346

DIFFUSER CONE ANGLE = 29°

NOZZLE RESTRICTION = 0%

DIFFUSER LENGTH = .076 [M]

FIG 4.7c SWIRL INTENSITY VARIATION ALONG THE DIFFUSER (DIFFUSER ANGLE=16 DEG.)

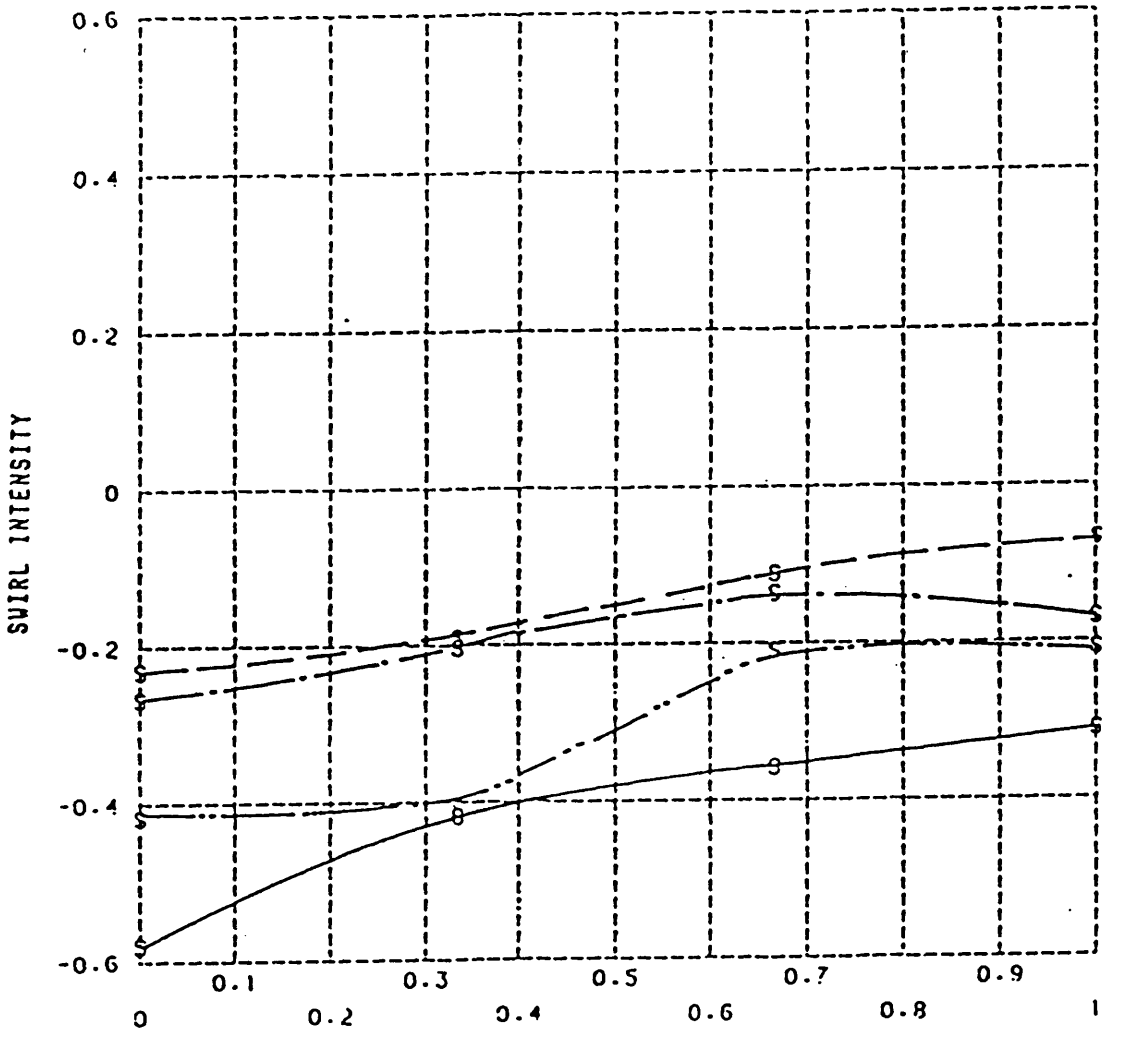

SWIRL INTENSITY	PRESSURE RATIO
-.58	1.859
-.42	1.741
-.27	1.680
-.23	1.620

DIFFUSER CONE ANGLE = 16°

NOZZLE RESTRICTION = 0%

DIFFUSER LENGTH = [M]

FIG 4.8a PRESSURE RECOVERY COEFFICIENT VS SWIRL
(DIFFUSER ANGLE-29 DEG.)

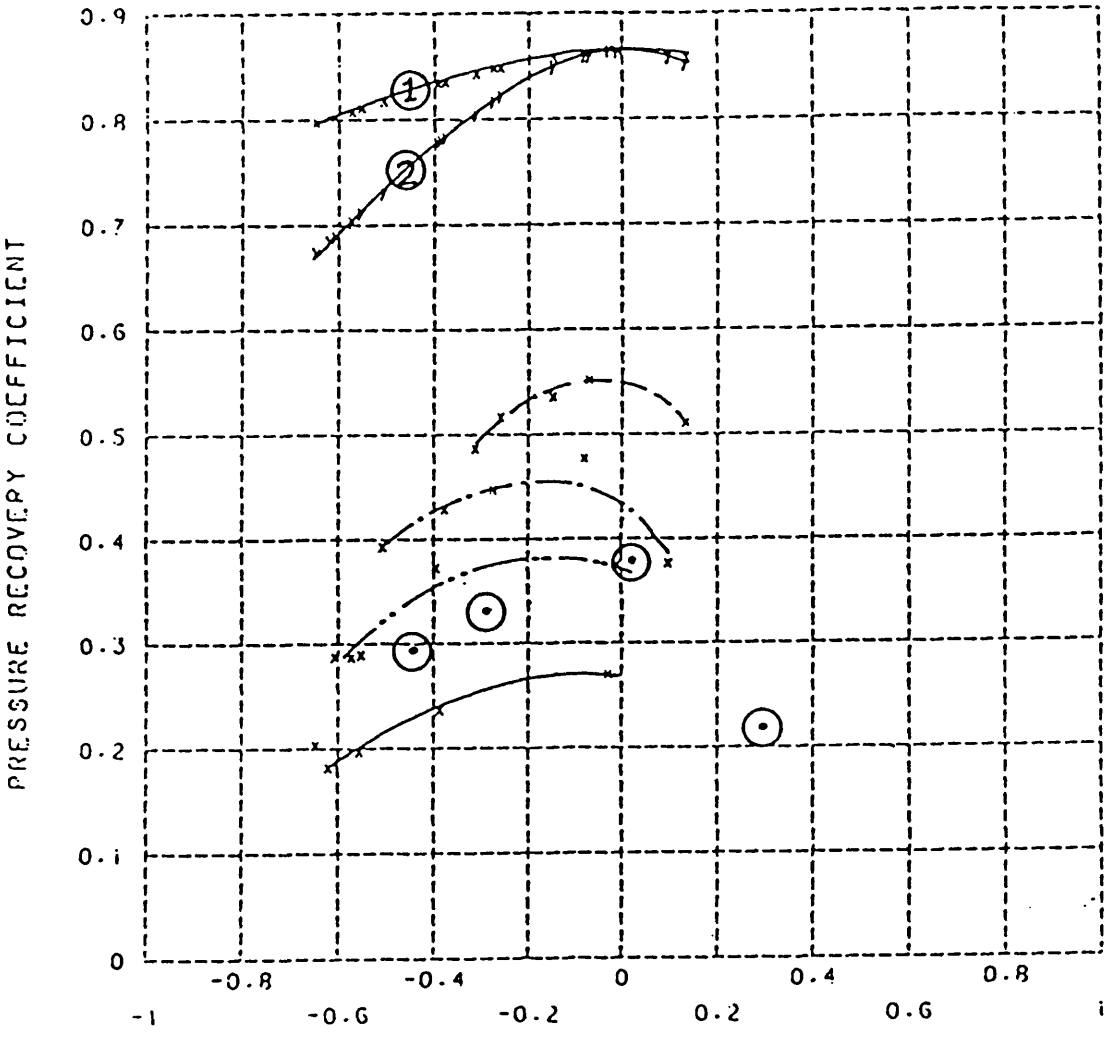

SPEED

——————— 30000 [REVS/MIN]

——·——·—— 40000 [REVS/MIN]

——·——·—· 50000 [REVS/MIN]

— — — — — 60000 [REVS/MIN]

DIFFUSER CONE ANGLE = 29°

NOZZLE RESTRICTION = 20%

× Cp = [Pu(exit)-Pu(inlet)]/[P0(inlet)-P(inlet)]

◉ Cp = [P(exit)-P(inlet)]/[P0(inlet)-P(inlet)] (At 50000 revs/min)

① $Cpi = [1-(1/Ar)] \times [1+(1/Ar) \times \cos^2\alpha_1]$

② $Cpi = [1-(1/Ar)] \times \cos^2\alpha_1 + [4/3(1-r1/r2)-1/2(1-r1/r2)] \times \cos^2\alpha_1$

FIG 4.8b PRESSURE RECOVERY COEFFICIENT VS SWIRL
(DIFFUSER ANGLE=16 DEG.)

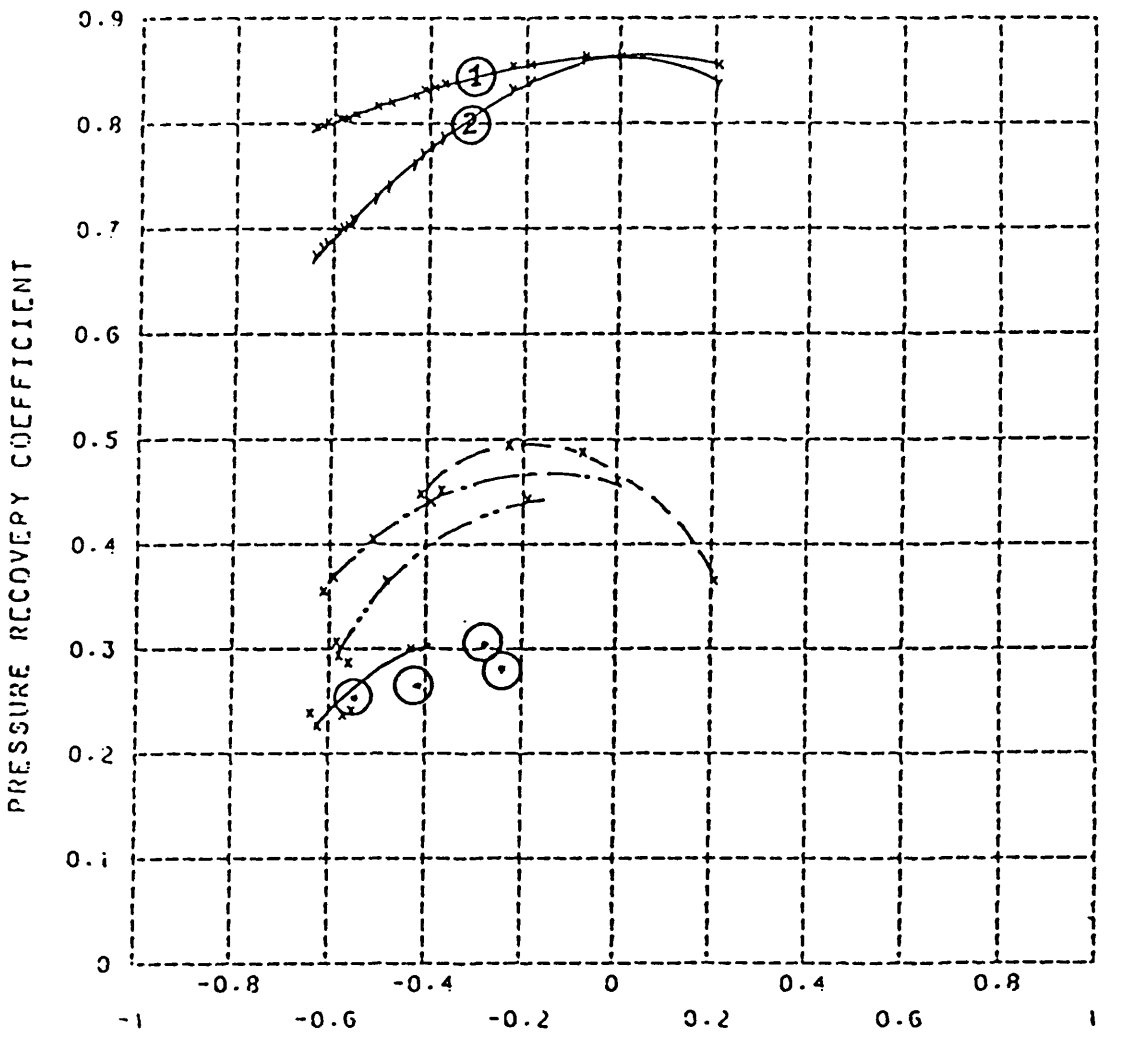

SPEED

——————— 30000 [REVS/MIN]

——·——·—— 40000 [REVS/MIN]

——·——·——·—— 50000 [REVS/MIN]

— — — — — — 60000 [REVS/MIN]

DIFFUSER CONE ANGLE = 16°

NOZZLE RESTRICTION = 20%

× C_p = [Pw(exit)-Pw(inlet)]/[P0(inlet)-P(inlet)]

● C_p = [P(exit)-P(inlet)]/[P0(inlet)-P(inlet)] (At 50000 revs/min)

(1) $C_{pi} = [1-(1/Ar)] \times [1+(1/Ar)\times\cos^2\alpha_1]$

(2) $C_{pi} = [1-(1/Ar)] \times \cos^2\alpha_1 + [4/3(1-r1/r2)-1/2(1-r1/r2)] \times \sin^2\alpha_1$

FIG 4.8c PRESURE RECOVERY COEFFICIENT VS SWIRL
(DIFFUSER ANGLE-8 DEG.)

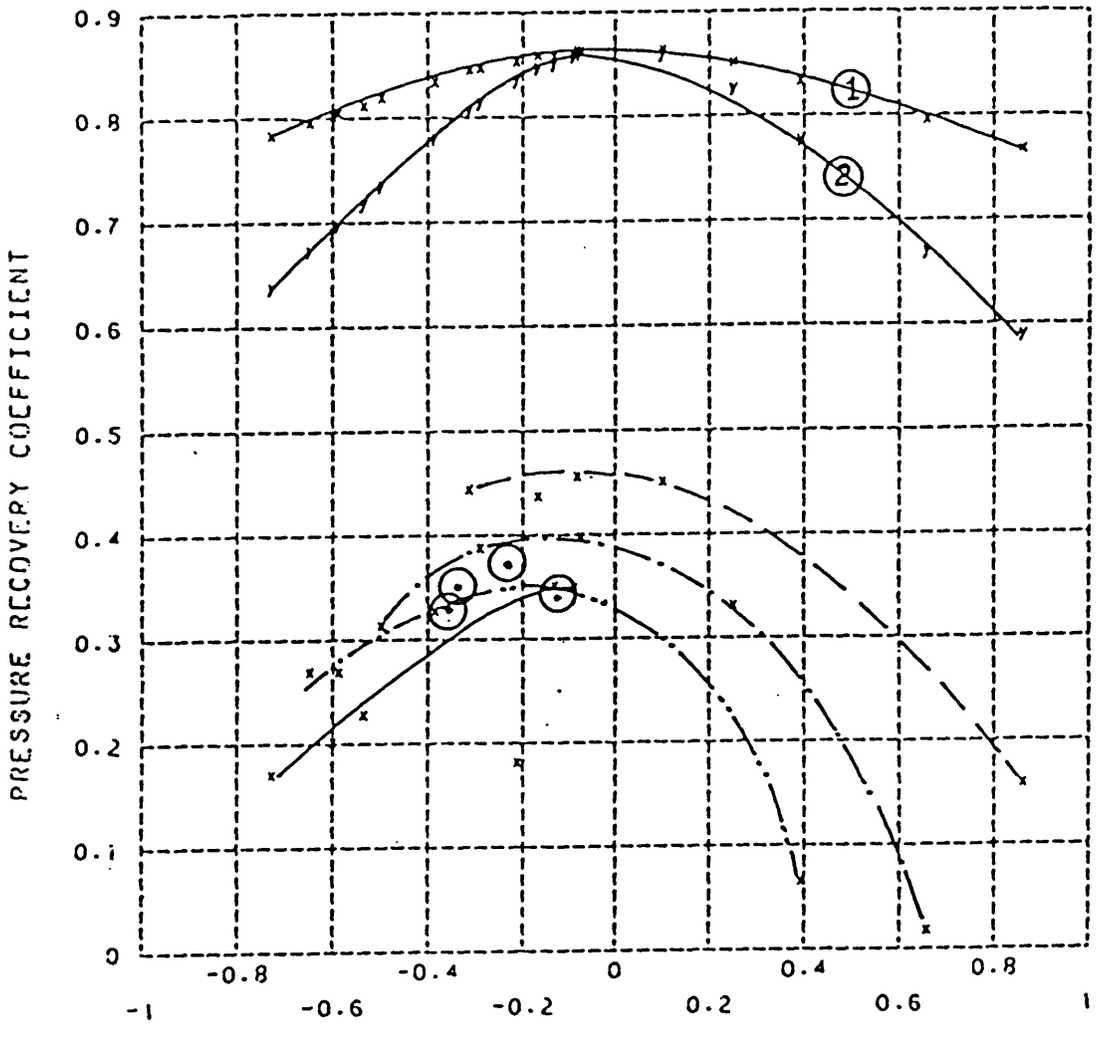

SPEED

——————— 30000 [REVS/MIN]

—·—·—·—·— 40000 [REVS/MIN]

—·——·—·— 50000 [REVS/MIN]

— — — — — 60000 [REVS/MIN]

DIFFUSER CONE ANGLE = 8°

NOZZLE RESTRICTION = 20%

× Cp = [Pu(exit)-Pu(inlet)]/[P0(inlet)-P(inlet)]

◉ Cp = [P(exit)-P(inlet)]/[P0(inlet)-P(inlet)] (At 50000 revs/min)

① $Cpi = [1-(1/Ar)] \times [1+(1/Ar)\times\cos^2\alpha_1]$

② $Cpi = [1-(1/Ar)] \times \cos^2\alpha_1 + [4/3(1-r1/r2)-1/2(1-r1/r2)] \times \sin^2\alpha_1$

FIG 4.9a NON DIMENSIONAL MASS FLOW RATE CHARACTERISTICS

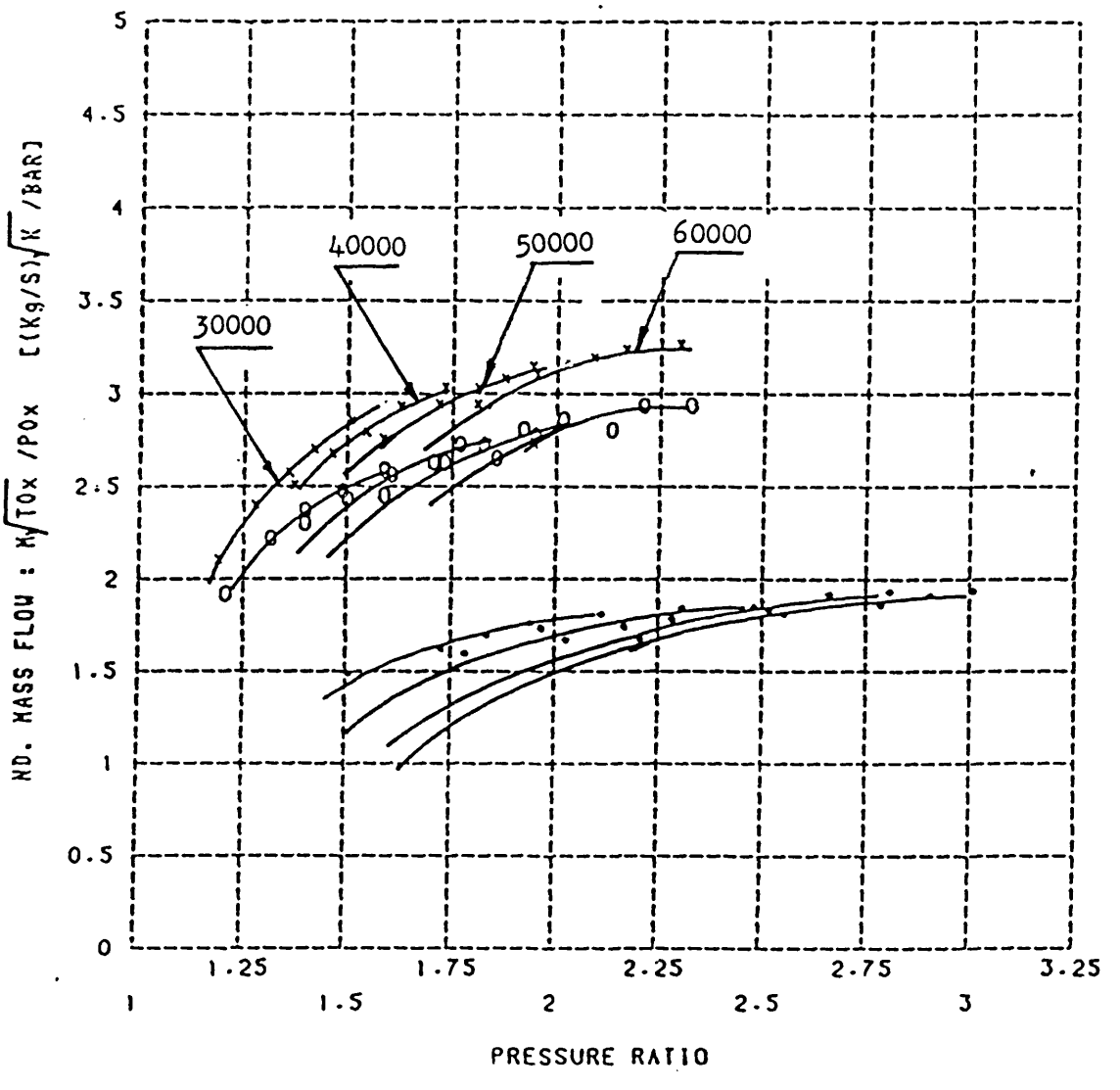

x : RESTRICTION = 0%

o : RESTRICTION = 20%

* : RESTRICTION = 50%

WITHOUT EXIT DIFFUSER

FIG 4.9b NON DIMENSIONAL TORQUE CHARACTERISTICS

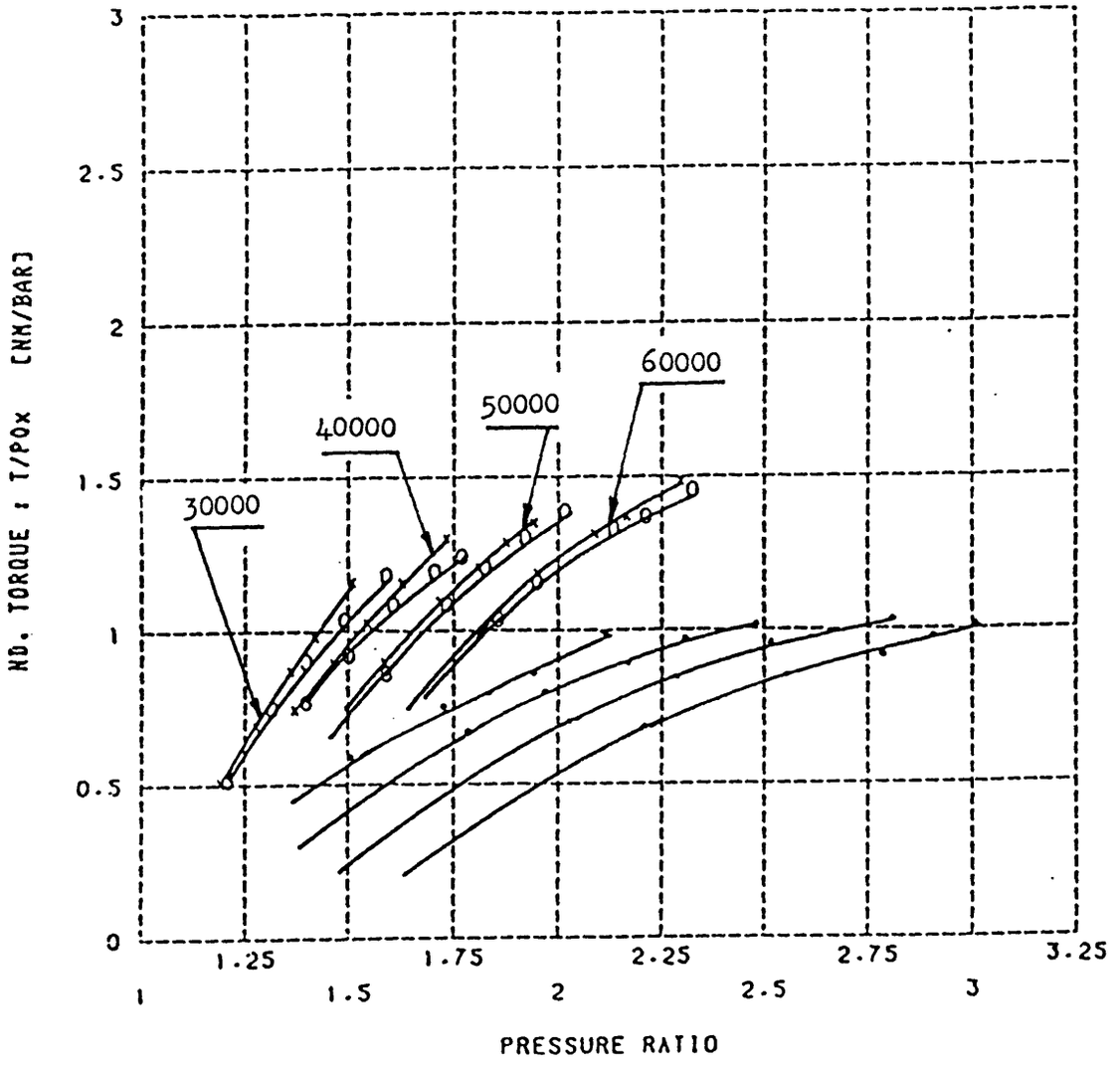

x : RESTRICTION = 0%

o : RESTRICTION = 20%

* : RESTRICTION = 50%

WITHOUT EXIT DIFFUSER

FIG 4.9c TOTAL TO STATIC EFFICIENCY VS PRESSURE RATIO

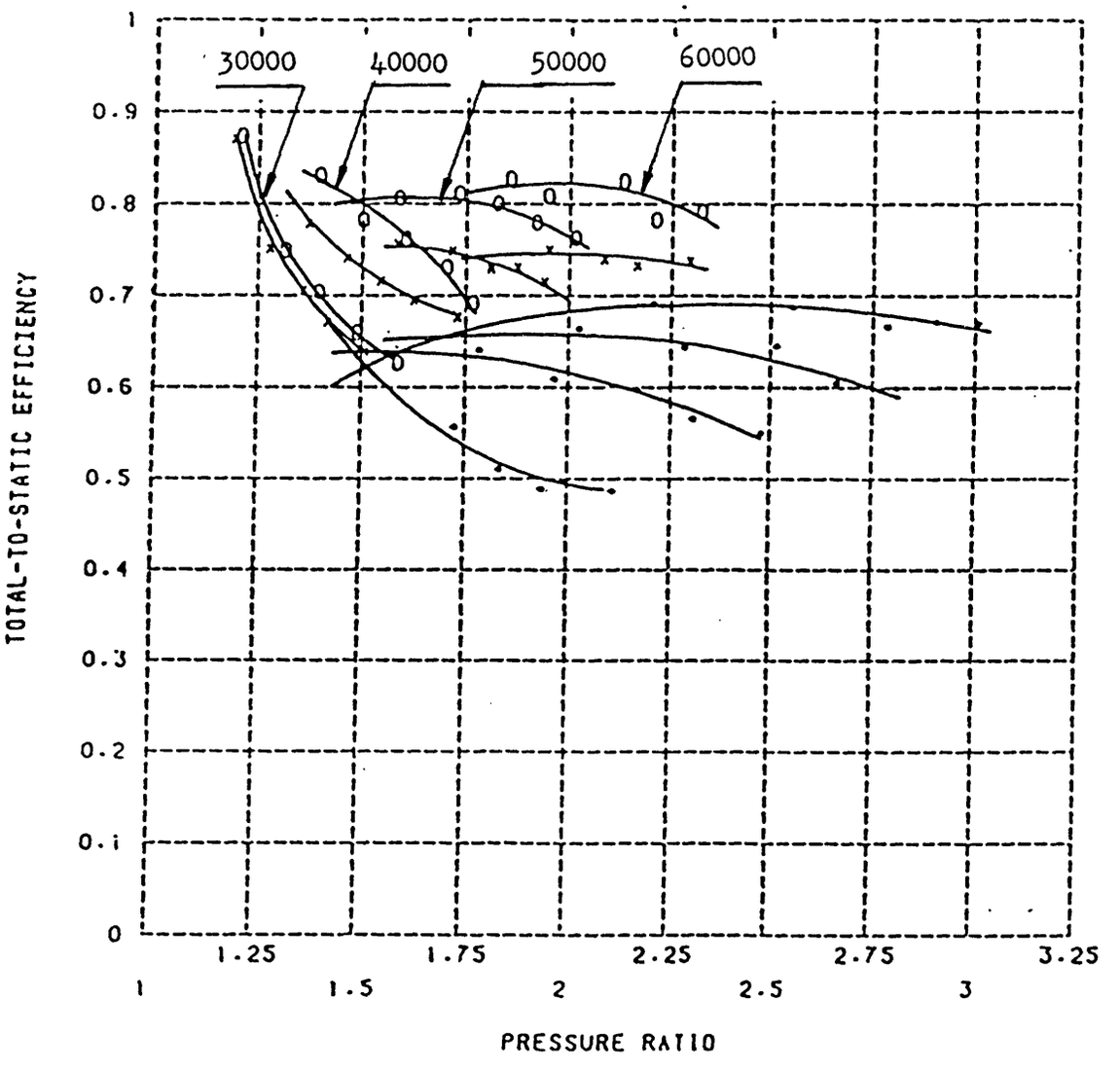

x : RESTRICTION = 0%

o : RESTRICTION = 20%

* : RESTRICTION = 50%

WITHOUT EXIT DIFFUSER

FIG 4.9d TOTAL TO STATIC EFFICIENCY VS SPEED RATIO

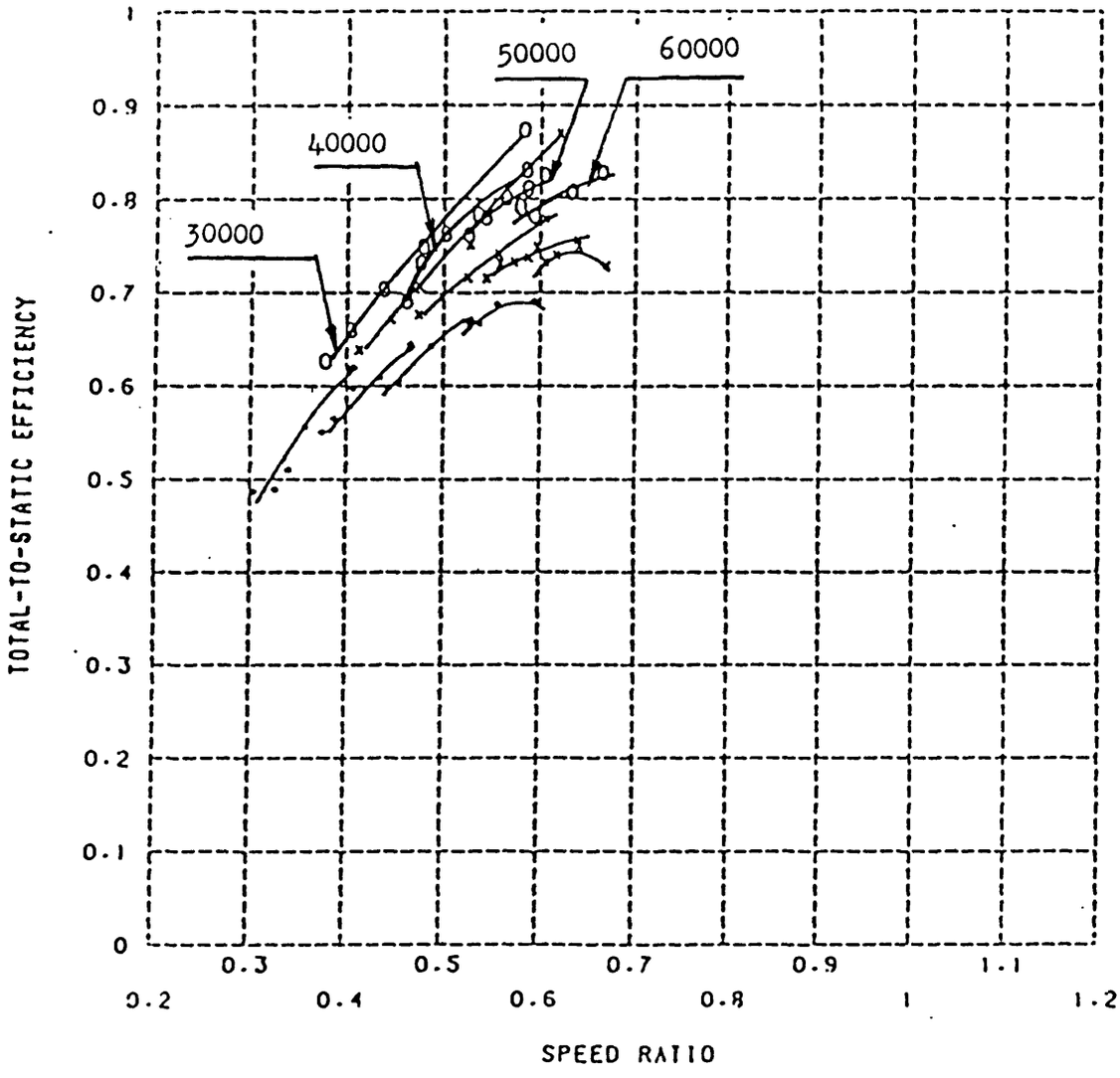

x : RESTRICTION = 0%

o : RESTRICTION = 20%

* : RESTRICTION = 50%

WITHOUT EXIT DIFFUSER

FIG 4.10a THEORETICAL AND EXPERIMENTAL MASS FLOW CHARACTERISTICS (NON RESTRICTED NOZZLE RING)

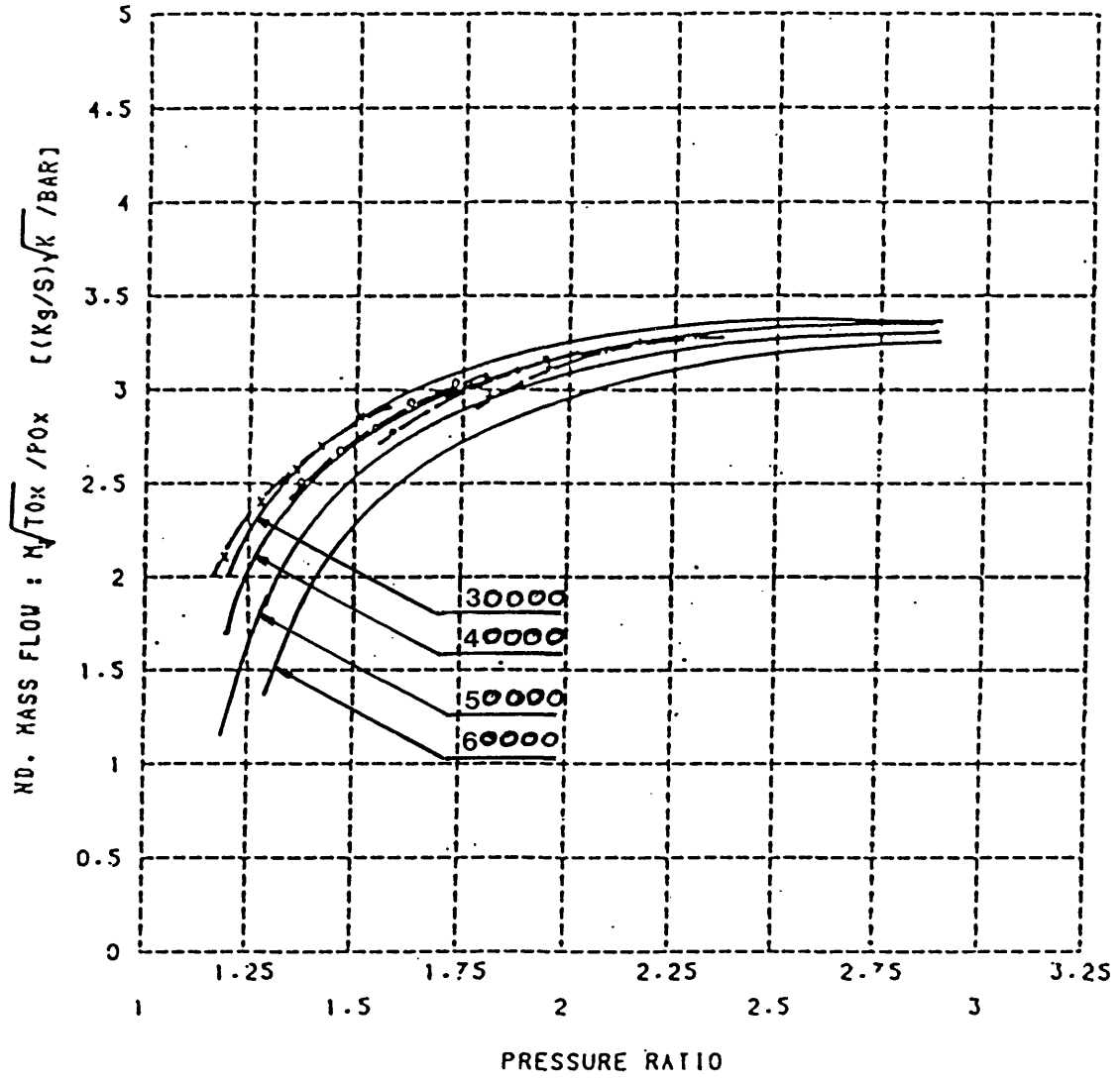

——————— ONE-DIMENSIONAL PREDICTION

— — — — — — EXPERIMENTAL

× : 30000 [REVS/MIN]

o : 40000 [REVS/MIN]

* : 50000 [REVS/MIN]

+ : 60000 [REVS/MIN]

NOZZLE RESTRICTION = 0%

WITHOUT EXIT DIFFUSER

FIG 4.10b THEORETICAL AND EXPERIMENTAL MASS FLOW CHARACTERISTICS (NOZZLE RESTRICTION=20%)

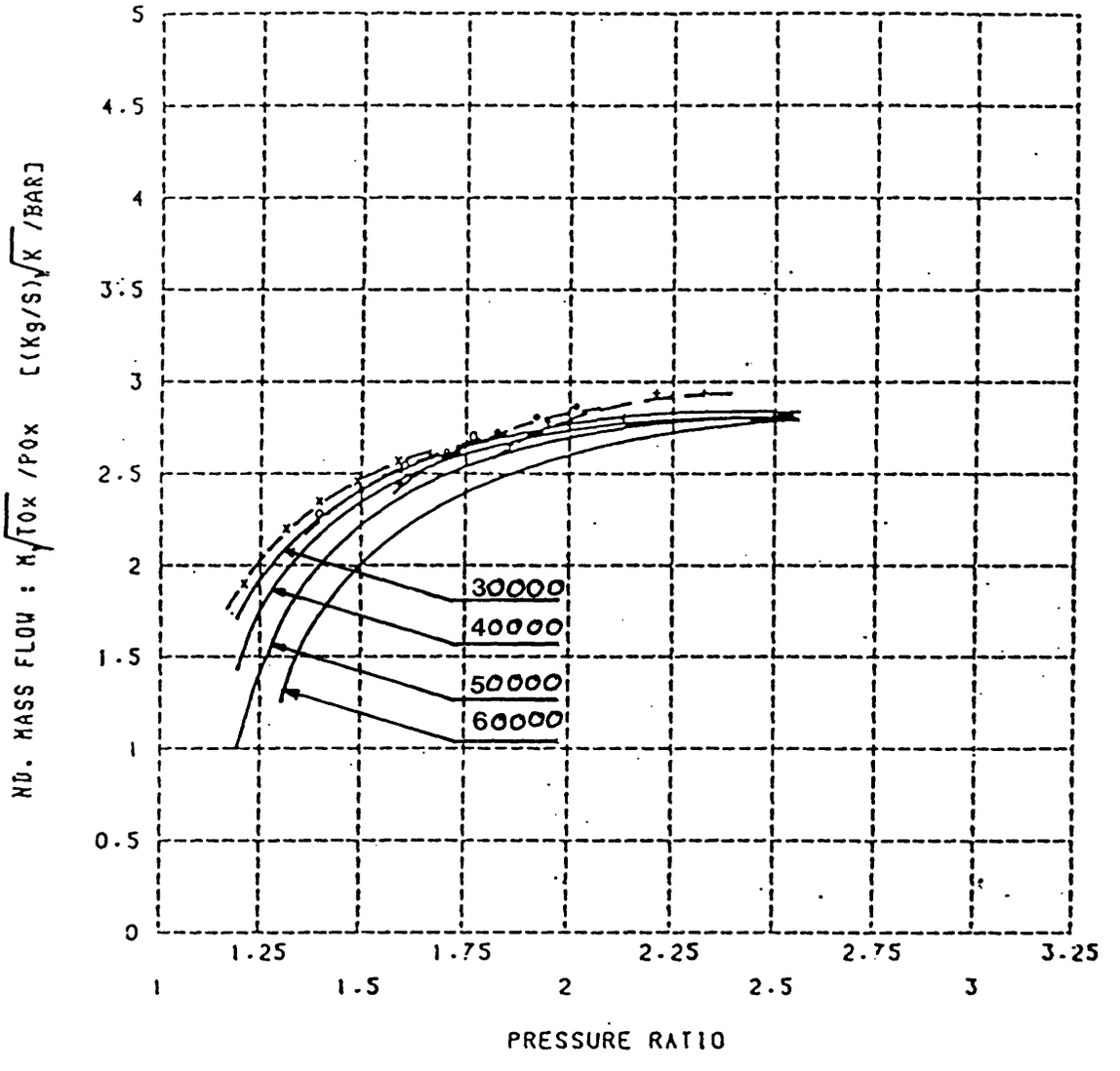

——————— ONE-DIMENSIONAL PREDICTION

— — — — — — EXPERIMENTAL

x : 30000 [REVS/MIN]

o : 40000 [REVS/MIN]

* : 50000 [REVS/MIN]

+ : 60000 [REVS/MIN]

NOZZLE RESTRICTION = 20%

WITHOUT EXIT DIFFUSER

FIG 4.10c THEORETICAL AND EXPERIMENTAL MASS FLOW CHARACTERISTICS (NOZZLE RESTRICTION=50%)

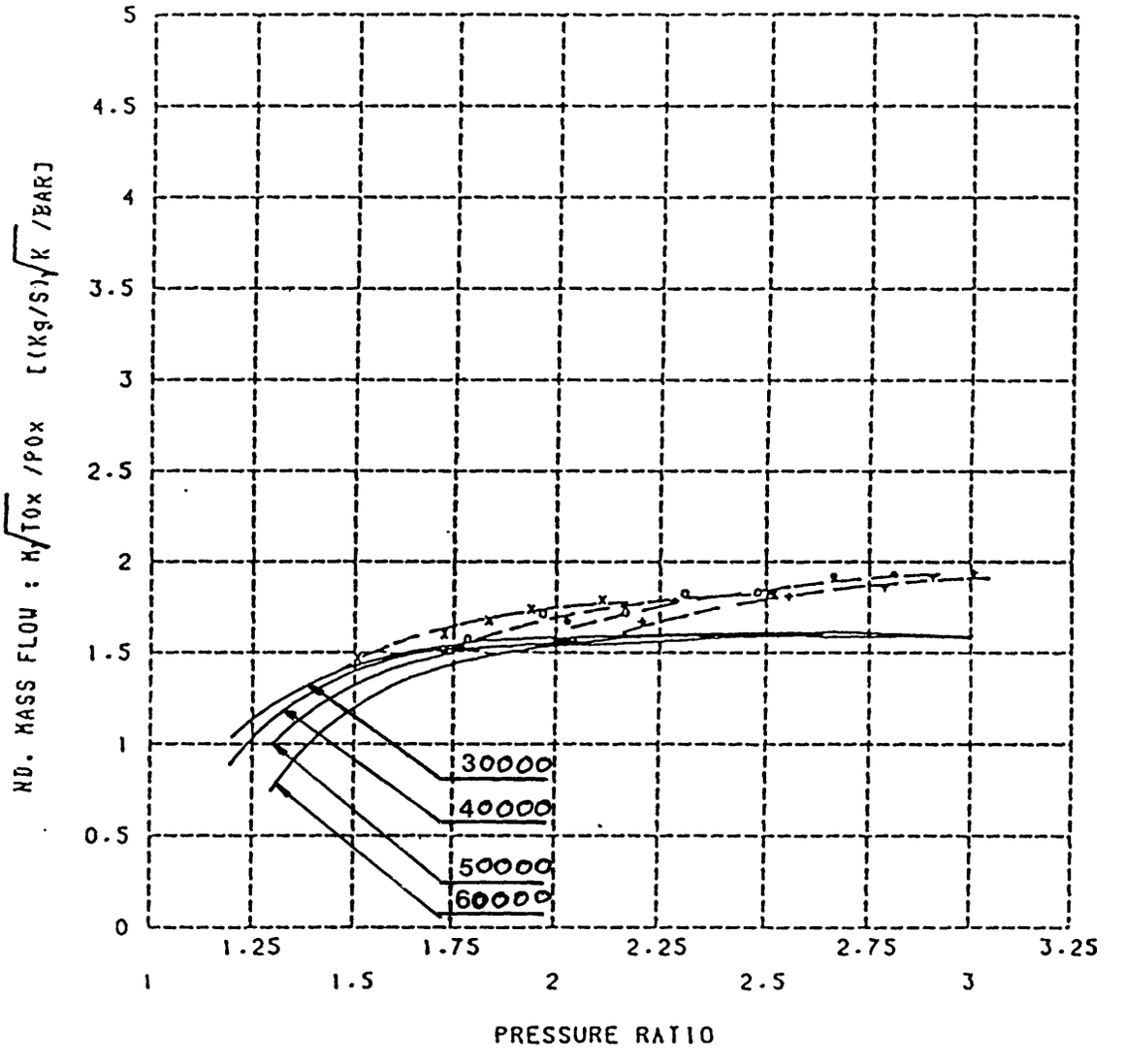

——————— ONE-DIMENSIONAL PREDICTION

— — — — — EXPERIMENTAL

× : 30000 [REVS/MIN]

o : 40000 [REVS/MIN]

* : 50000 [REVS/MIN]

+ : 60000 [REVS/MIN]

NOZZLE RESTRICTION = 50%

WITHOUT EXIT DIFFUSER

FIG 4.11a THEORETICAL AND EXPERIMENTAL TORQUE CHARACTERISTICS (NON RESTRICTED NOZZLE RING)

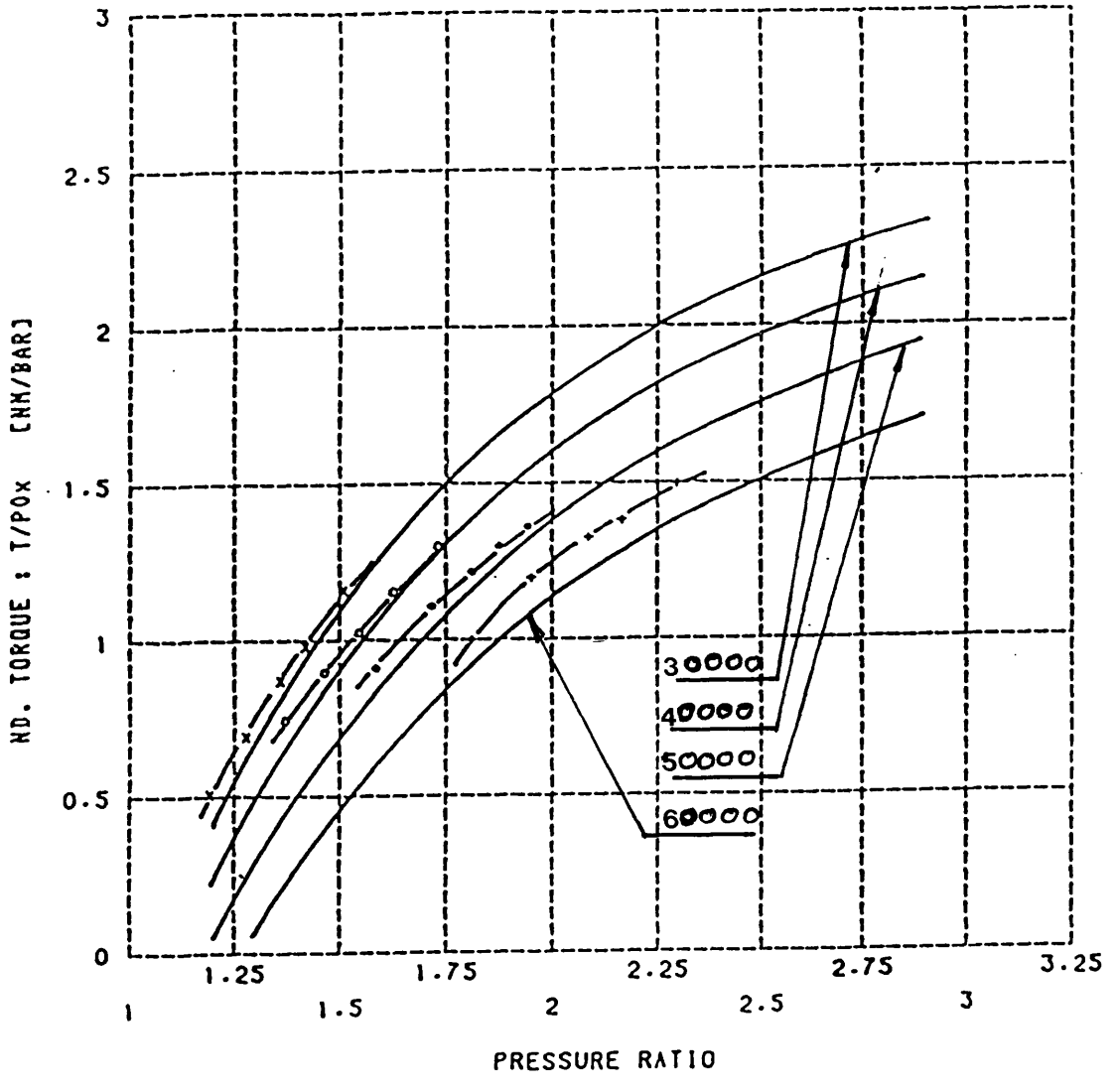

——————— ONE-DIMENSIONAL PREDICTION

——————— EXPERIMENTAL

x : 30000 [REVS/MIN]

o : 40000 [REVS/MIN]

* : 50000 [REVS/MIN]

+ : 60000 [REVS/MIN]

NOZZLE RESTRICTION = 0%

WITHOUT EXIT DIFFUSER

FIG 4.11b THEORETICAL AND EXPERIMENTAL TORQUE CHARACTERISTICS (NOZZLE RESTRICTION-20%)

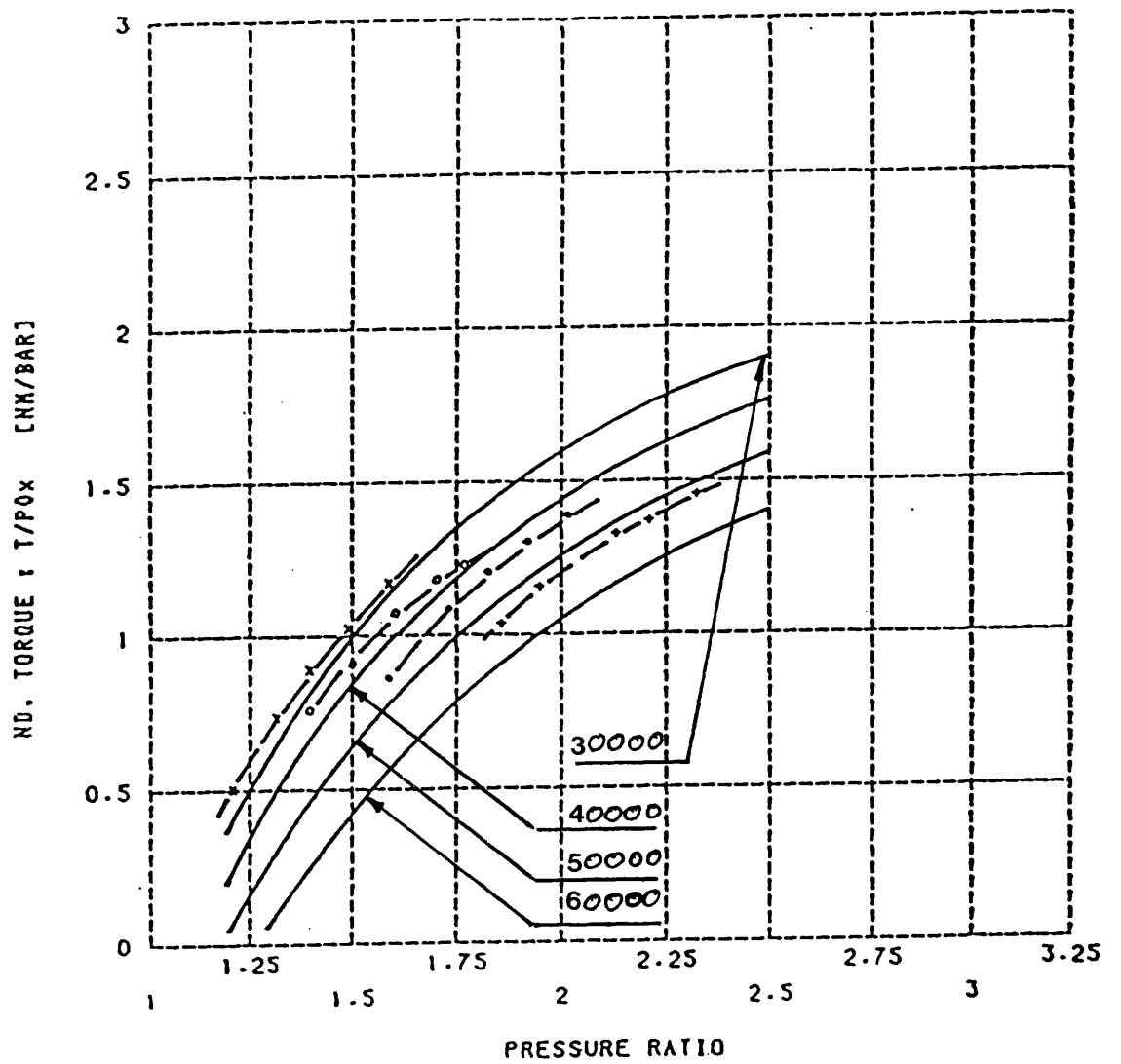

——————— ONE-DIMENSIONAL PREDICTION

— — — — — — EXPERIMENTAL

x : 30000 [REVS/MIN]

o : 40000 [REVS/MIN]

* : 50000 [REVS/MIN]

+ : 60000 [REVS/MIN]

NOZZLE RESTRICTION = 20%

WITHOUT EXIT DIFFUSER

FIG 4.11c THEORETICAL AND EXPERIMENTAL TORQUE CHARACTERISTICS (NOZZLE RESTRICTION-50%)

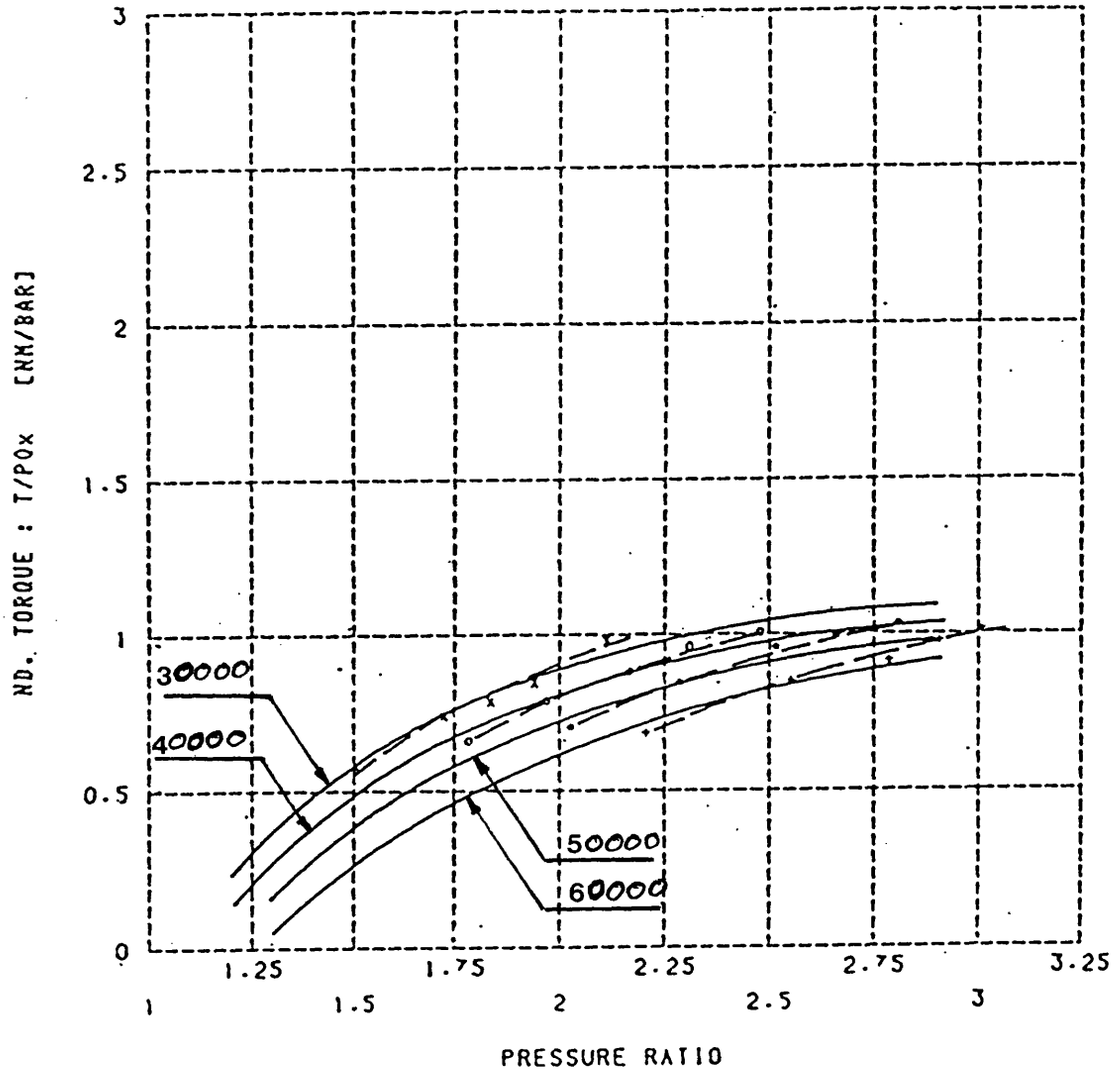

——————— ONE-DIMENSIONAL PREDICTION

— — — — — — EXPERIMENTAL

x : 30000 [REVS/MIN]

o : 40000 [REVS/MIN]

* : 50000 [REVS/MIN]

+ : 60000 [REVS/MIN]

NOZZLE RESTRICTION = 50%

WITHOUT EXIT DIFFUSER

FIG 4.12a THEORETICAL AND EXPERIMENTAL EFFICIENCIES VS PRESSURE RATIO (NON RESTRICTED NOZZLE RING)

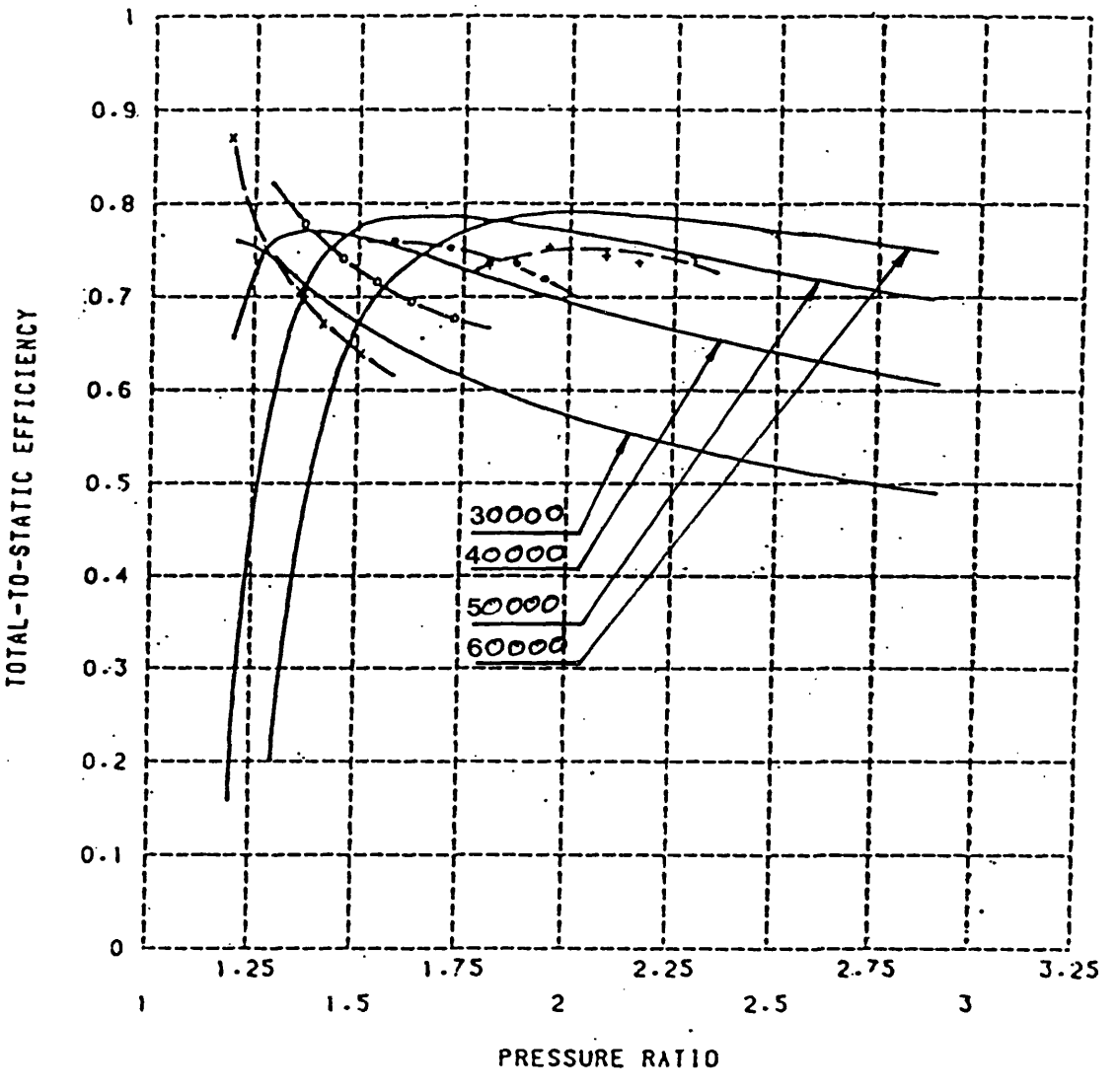

——————— ONE-DIMENSIONAL PREDICTION

— — — — — — EXPERIMENTAL

NOZZLE RESTRICTION = 0%

WITHOUT EXIT DIFFUSER

x : 30000 [REVS/MIN]

o : 40000 [REVS/MIN]

* : 50000 [REVS/MIN]

+ : 60000 [REVS/MIN]

FIG 4.12b THEORETICAL AND EXPERIMENTAL EFFICIENCIES VS PRESSURE RATIO (NOZZLE RESTRICTION-20%)

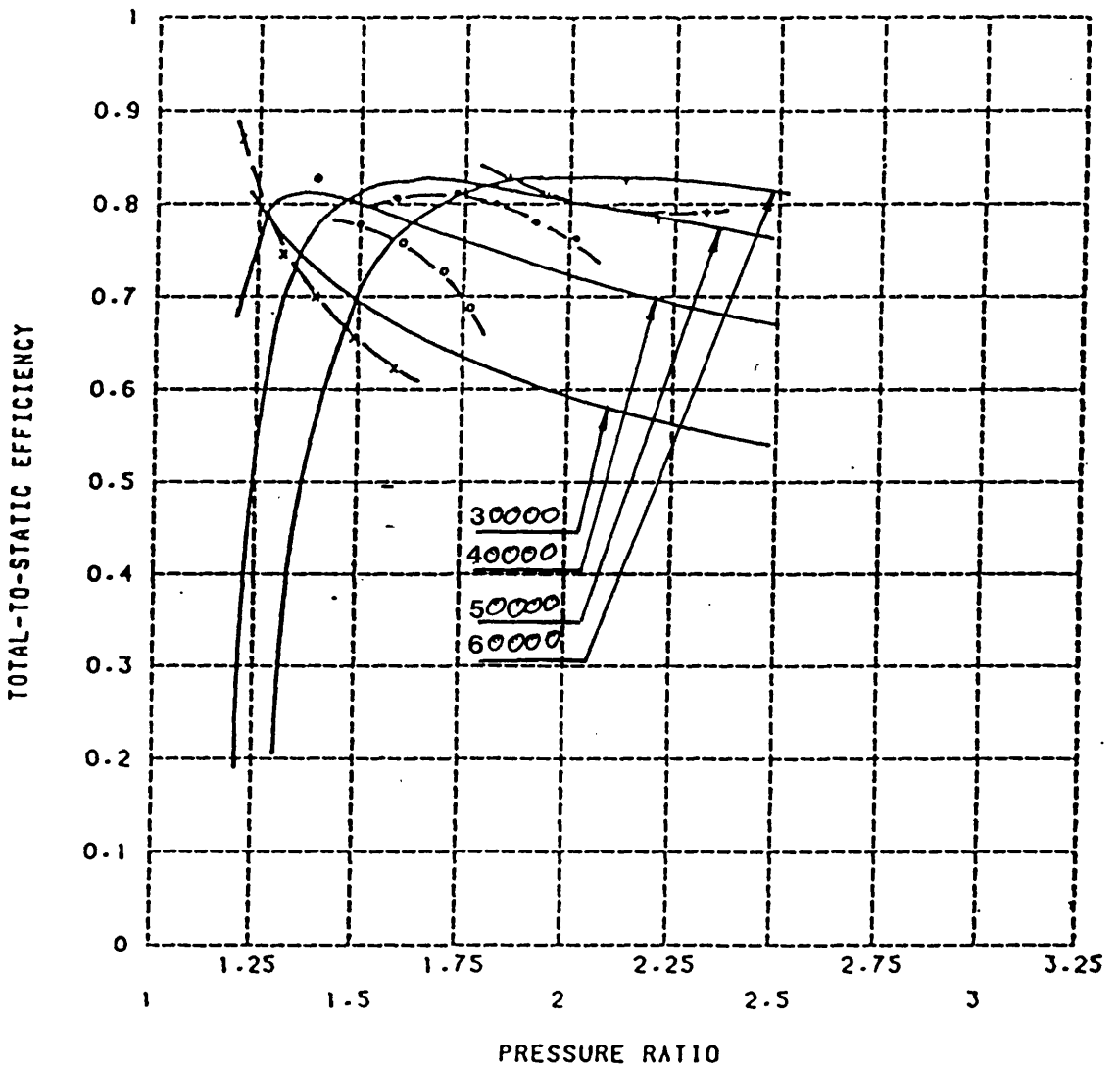

——————— ONE-DIMENSIONAL PREDICTION

— — — — — — — — EXPERIMENTAL

x : 30000 [REVS/MIN]

o : 40000 [REVS/MIN]

* : 50000 [REVS/MIN]

+ : 60000 [REVS/MIN]

NOZZLE RESTRICTION = 20%

WITHOUT EXIT DIFFUSER

FIG 4.12c THEORETICAL AND EXPERIMENTAL EFFICIENCIES VS PRESSURE RATIO (NOZZLE RESTRICTION=50%)

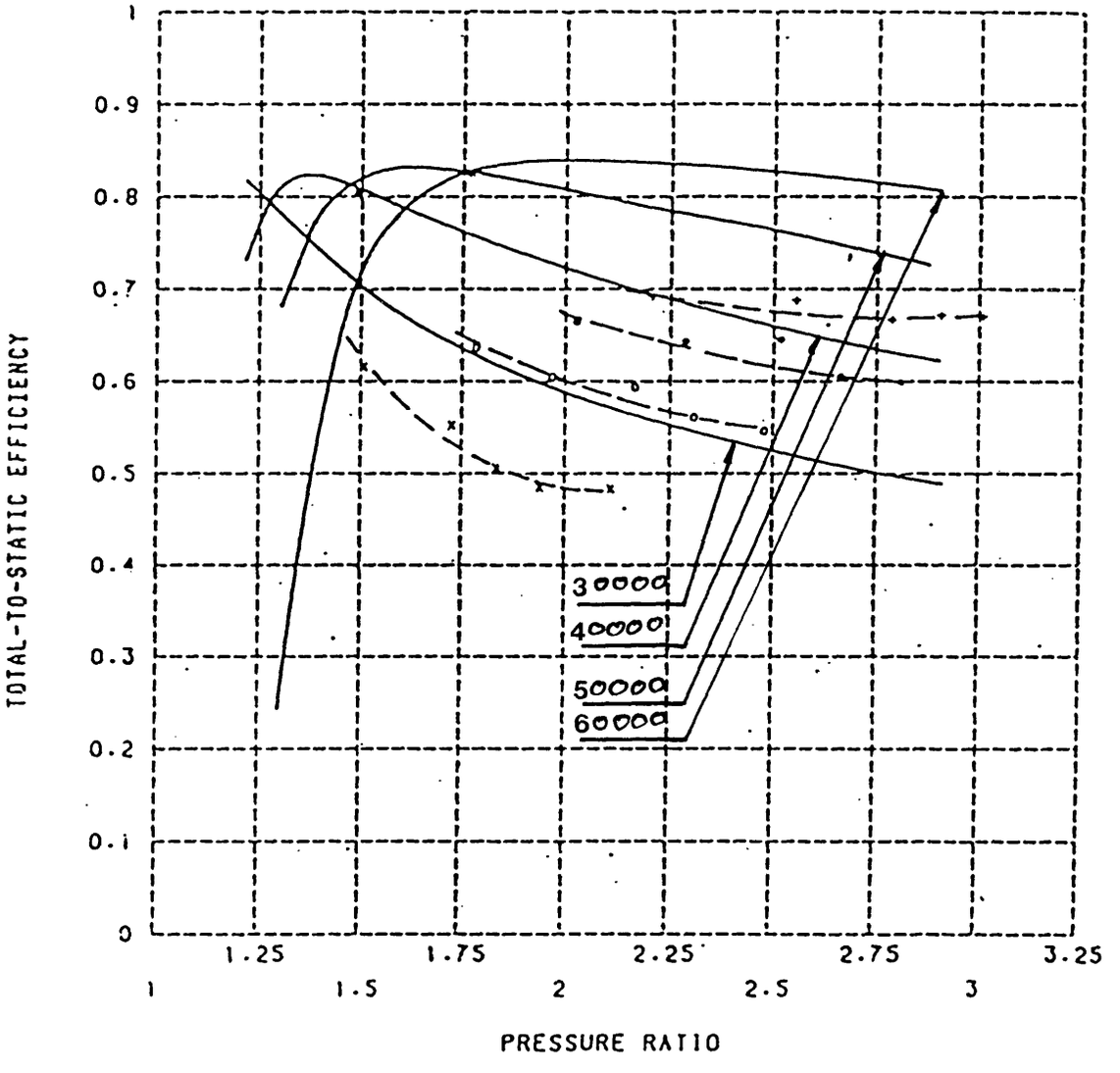

——————— ONE-DIMENSIONAL PREDICTION

— — ——— — — — EXPERIMENTAL

x : 30000 [REVS/MIN]

o : 40000 [REVS/MIN]

* : 50000 [REVS/MIN]

+ : 60000 [REVS/MIN]

NOZZLE RESTRICTION = 50%

WITHOUT EXIT DIFFUSER

FIG 4.13a THEORETICAL AND EXPERIMENTAL EFFICIENCIES VS SPEED RATIO (NON RESTRICTED NOZZLE RING)

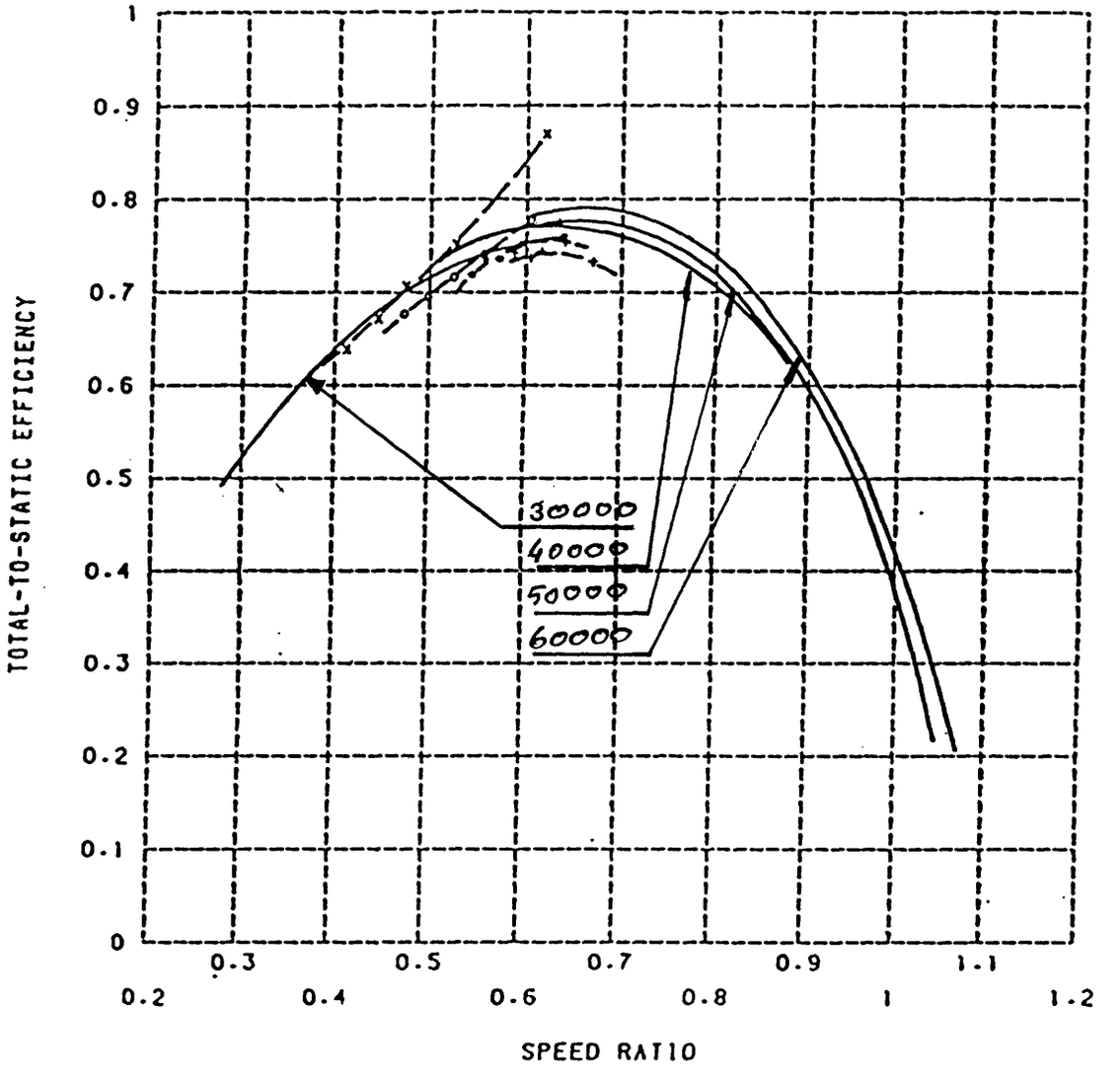

——————— ONE-DIMENSIONAL PREDICTION

— — — — — — EXPERIMENTAL

x : 30000 [REVS/MIN]

o : 40000 [REVS/MIN]

* : 50000 [REVS/MIN]

+ : 60000 [REVS/MIN]

NOZZLE RESTRICTION = 0%

WITHOUT EXIT DIFFUSER

FIG 4.13b THEORETICAL AND EXPERIMENTAL EFFICIENCIES VS SPEED RATIO (NOZZLE RESTRICTION=20%)

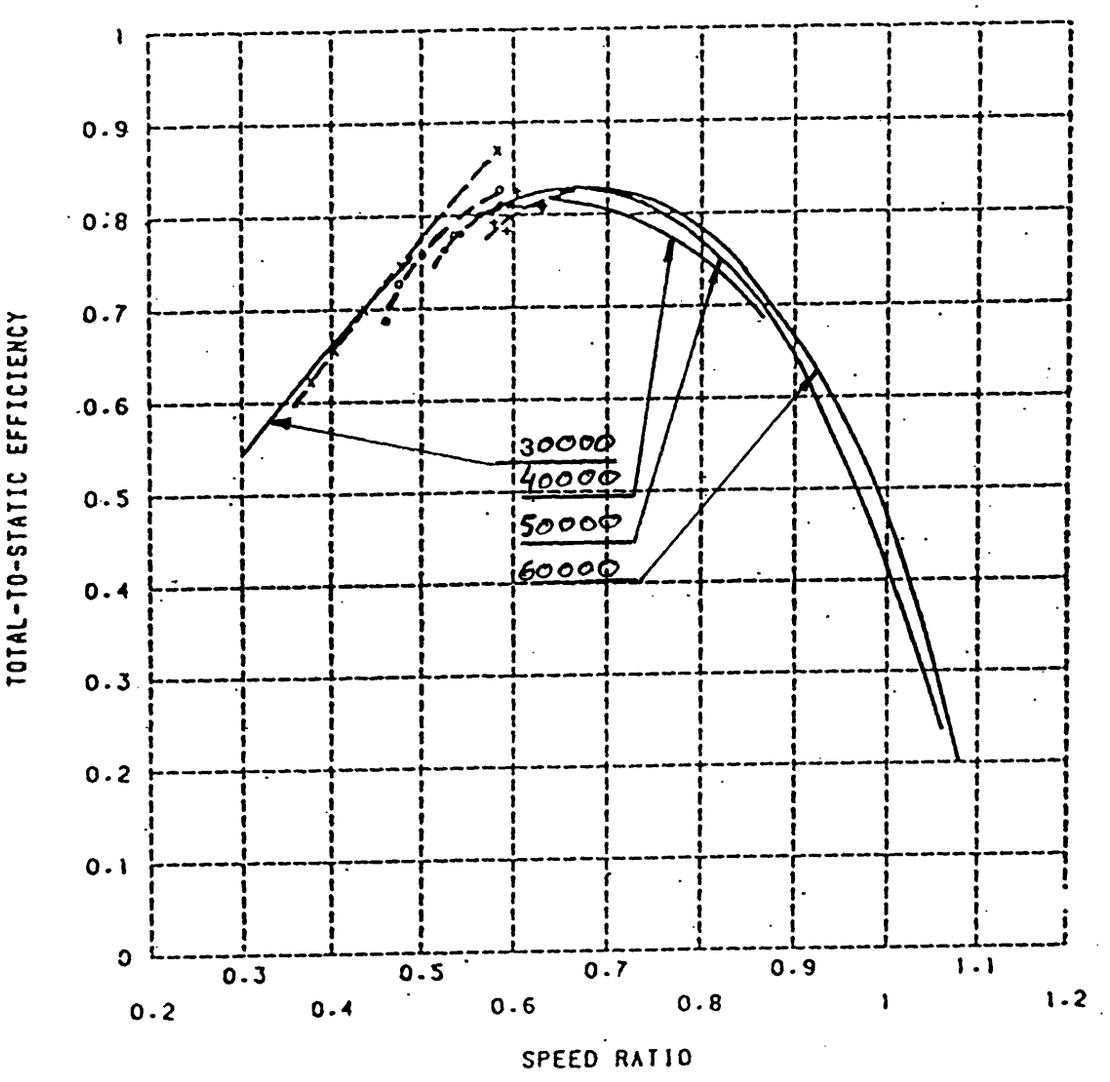

——————— ONE-DIMENSIONAL PREDICTION

— — — — — — EXPERIMENTAL

x : 30000 [REVS/MIN]

o : 40000 [REVS/MIN]

* : 50000 [REVS/MIN]

+ : 60000 [REVS/MIN]

NOZZLE RESTRICTION = 20%

WITHOUT EXIT DIFFUSER

FIG 4.13c THEORETICAL AND EXPERIMENTAL EFFICIENCIES VS SPEED RATIO (NOZZLE RESTRICTION=50%)

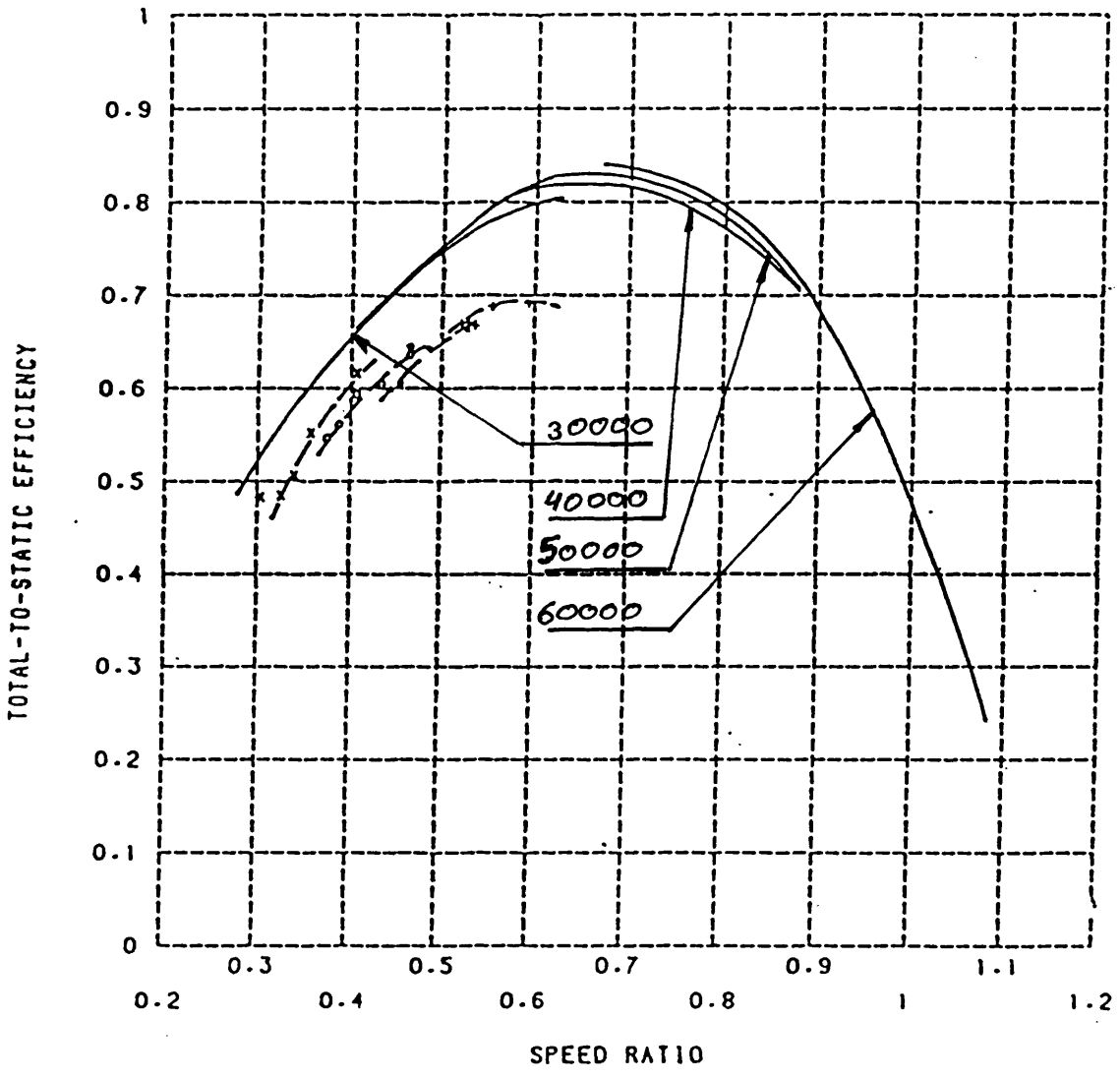

——————— ONE-DIMENSIONAL PREDICTION

— — — — — — — EXPERIMENTAL

x : 30000 [REVS/MIN]

o : 40000 [REVS/MIN]

* : 50000 [REVS/MIN]

+ : 60000 [REVS/MIN]

NOZZLE RESTRICTION = 50%

WITHOUT EXIT DIFFUSER

FIG 4.14a PRESSURE DISTRIBUTION ROUND THE VOLUTE
(NOZZLE RESTRICTION-0%)

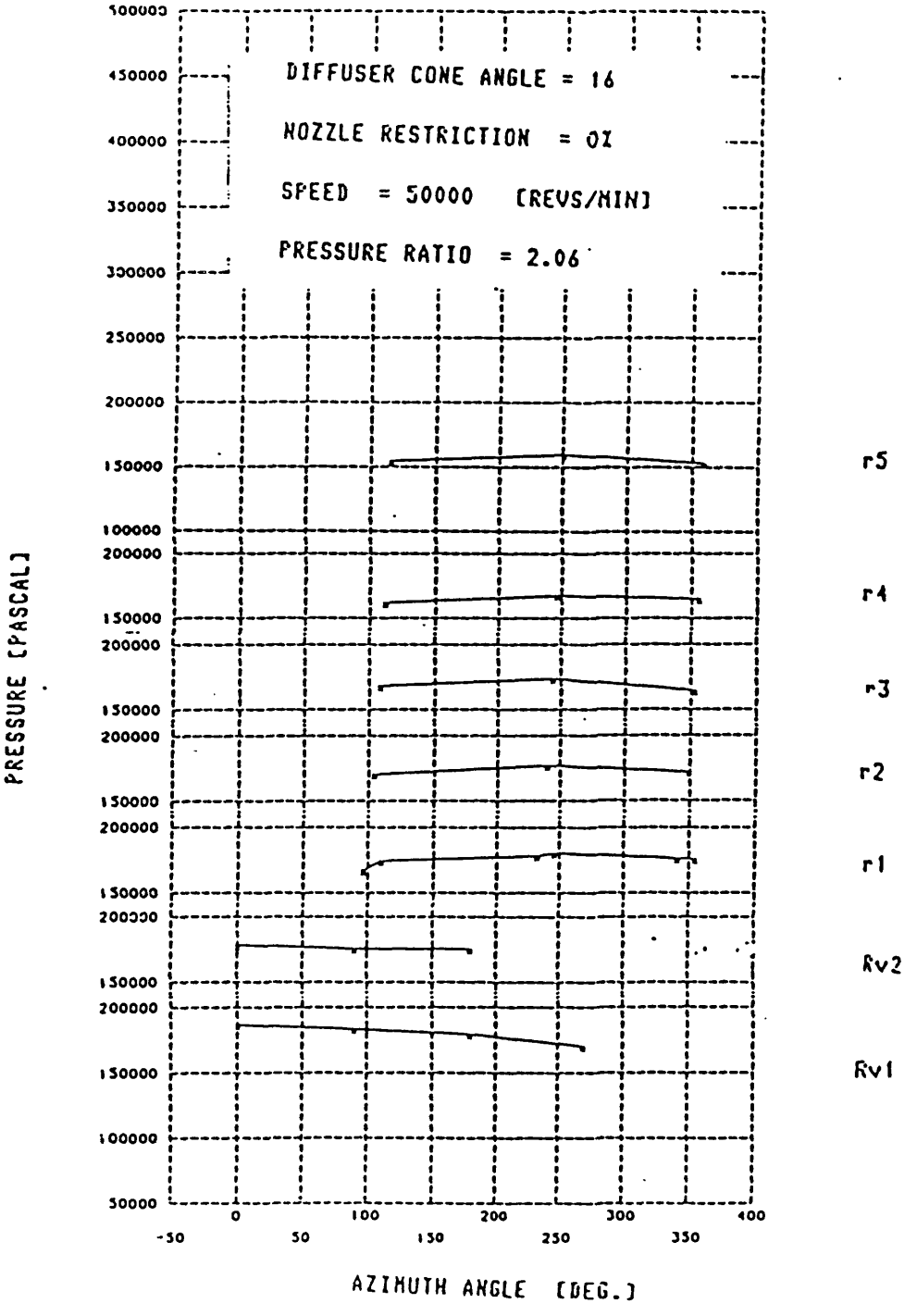

FIG 4.14b PRESSURE DISTRIBURTION ROUND THE VOLUTE
(NOZZLE RESTRICTION-50%)

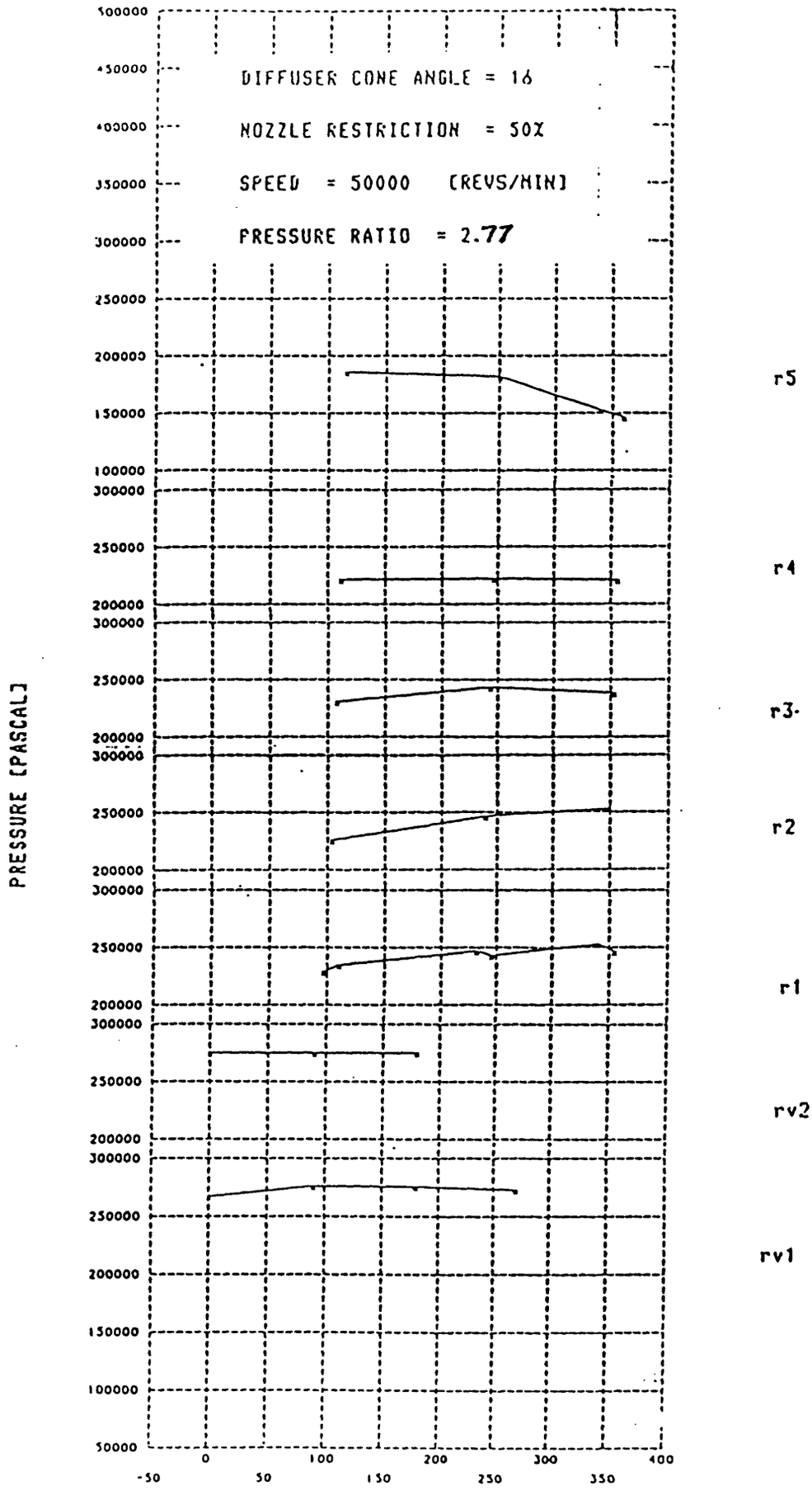

FIG 4.15 RADIAL PRESSURE DISTRIBUTION (AZIMUTH ANGLE-90)

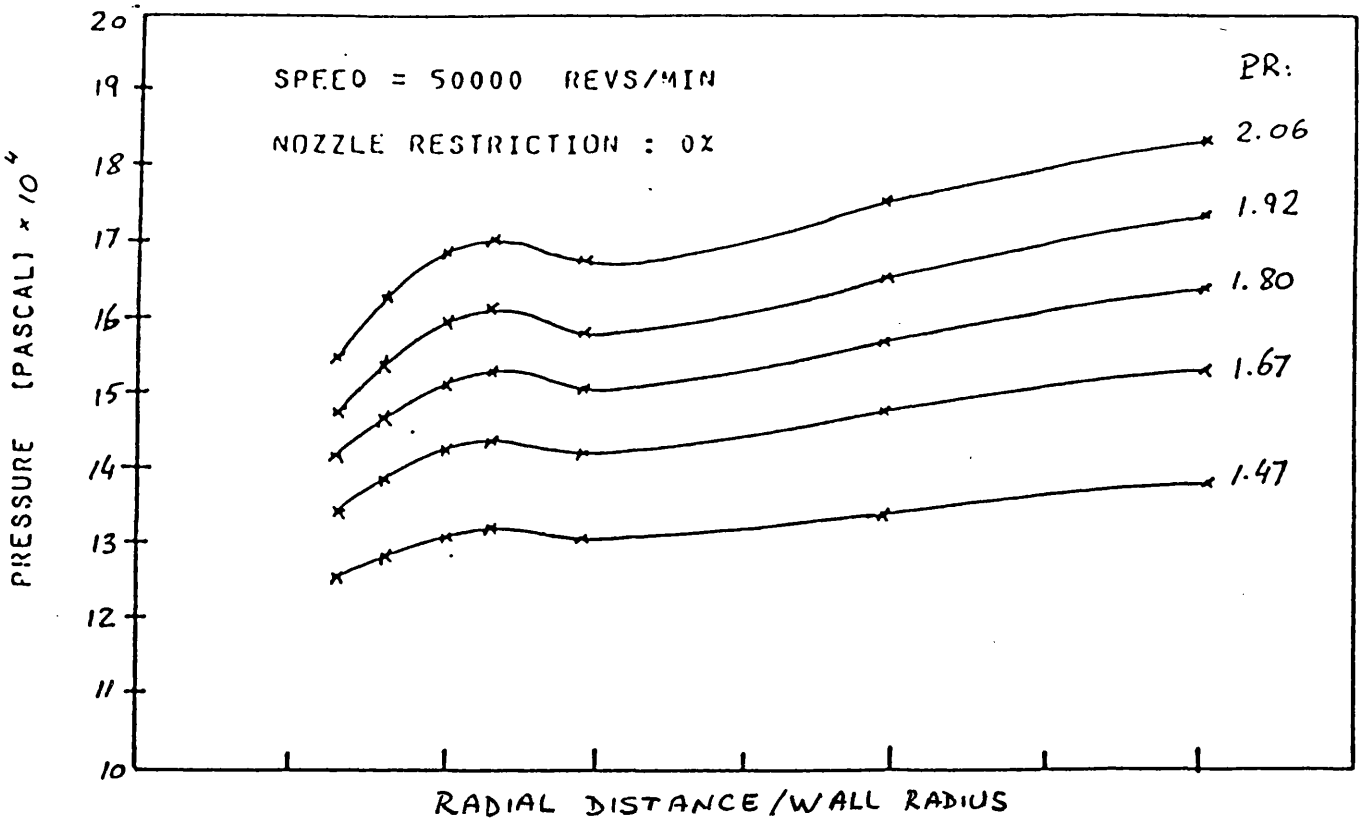

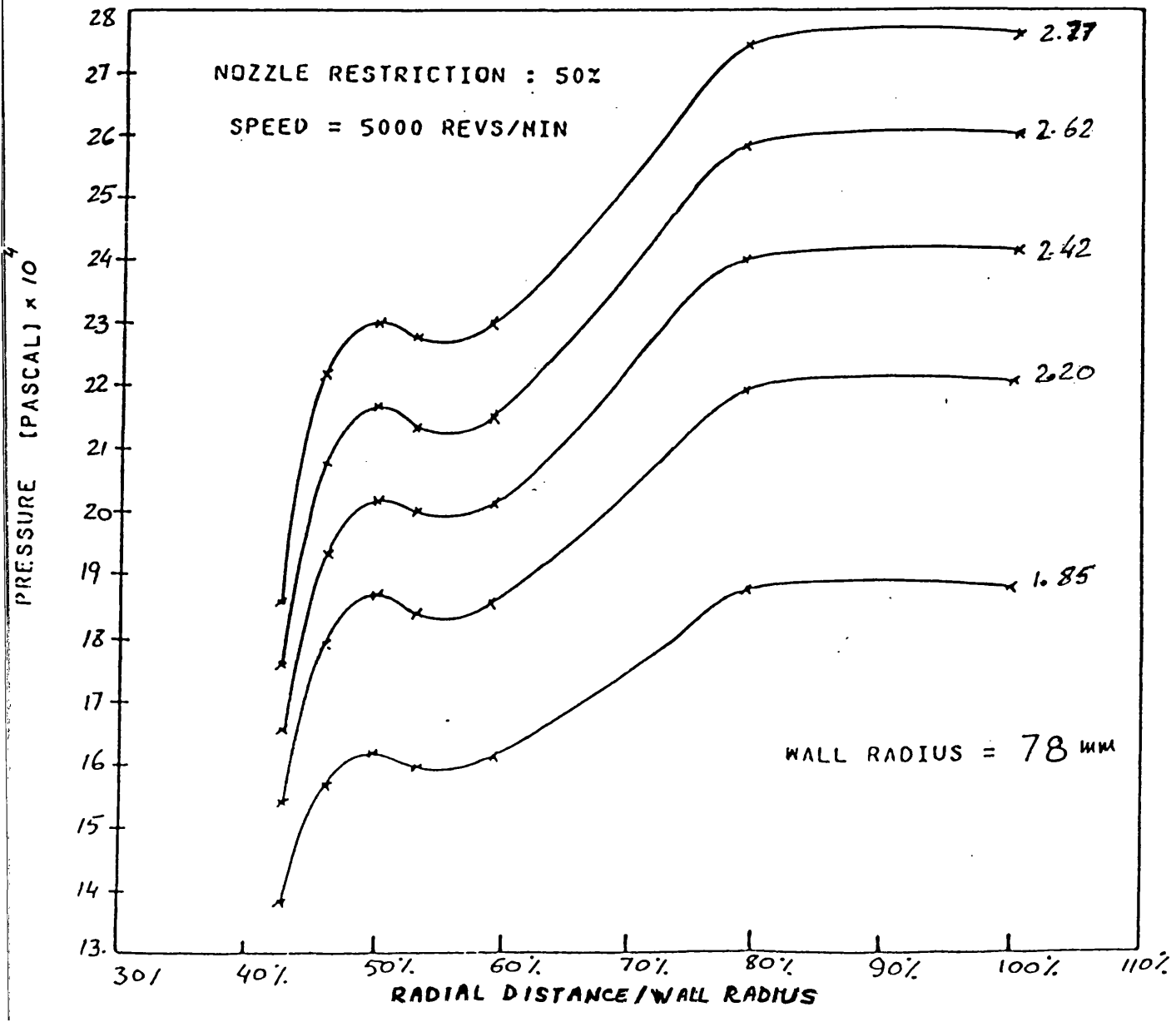

FOG 4.16 PRESSURE DISTRIBUTION ALONG THE SHROUD

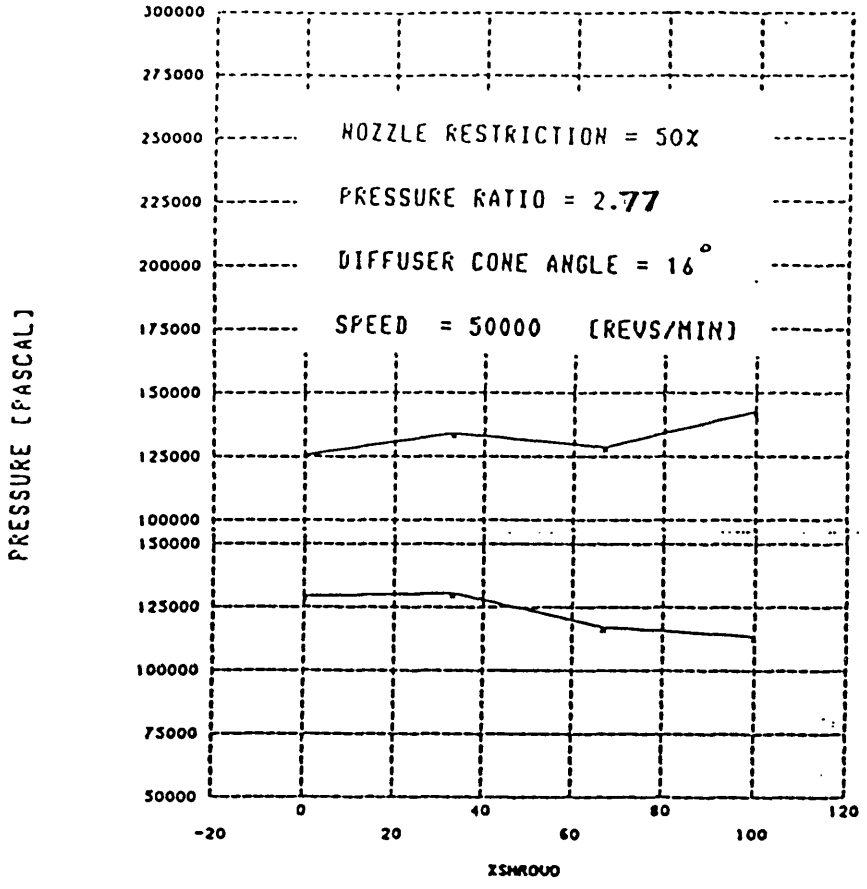

θ = 270°

θ = 90°

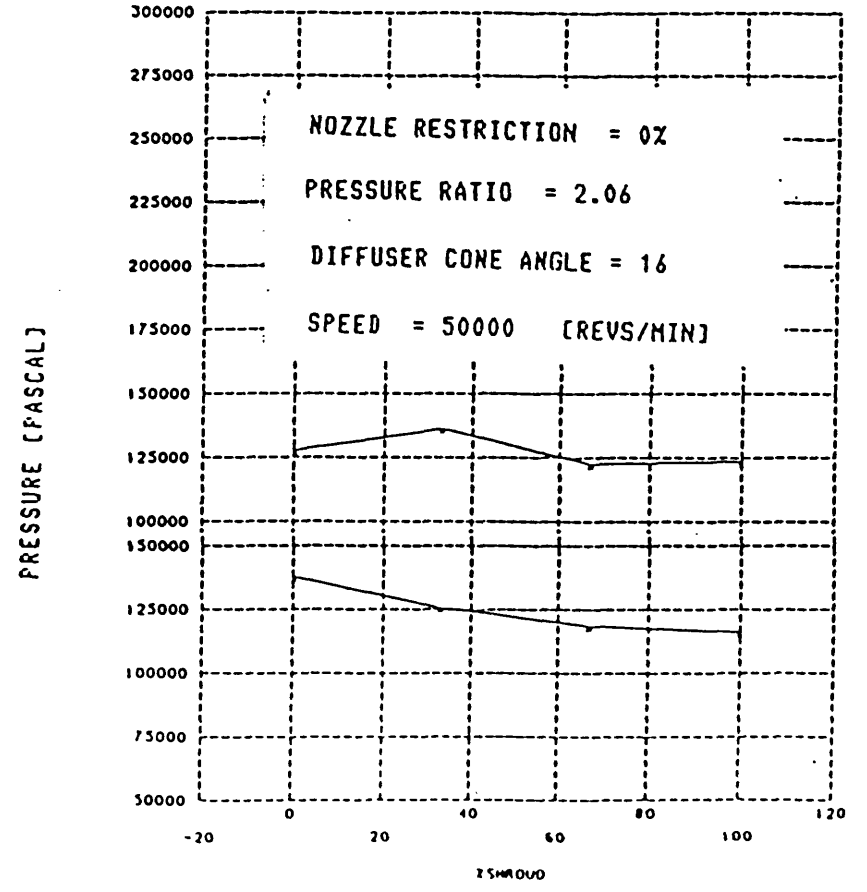

θ = 270°

θ = 90°

FIG 4.17a PRESSURE DISTRIBUTION ON THE BLADE SURFACES
(NOZZLE RESTRICTION-0%)

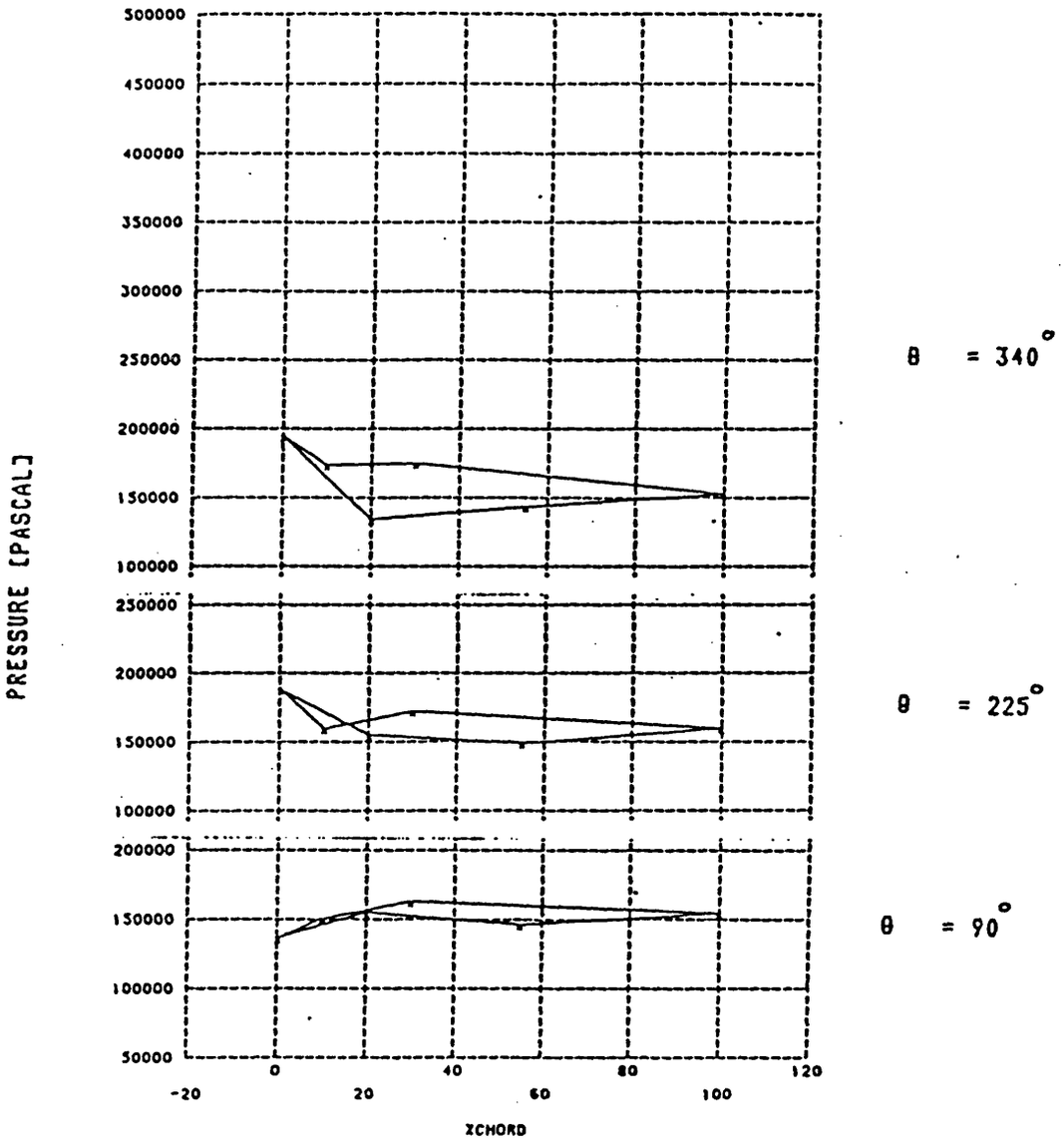

DIFFUSER ANGLE : 16°

NOZZLE RESTRICTION : 0%

SPEED = 5000 REVS/MIN

PRESSURE RATIO = 2.06

FIG 4.17b PRESSURE DISTRIBUTION ON THE BLADE SURFACES (NOZZLE RESTRICTION-50%)

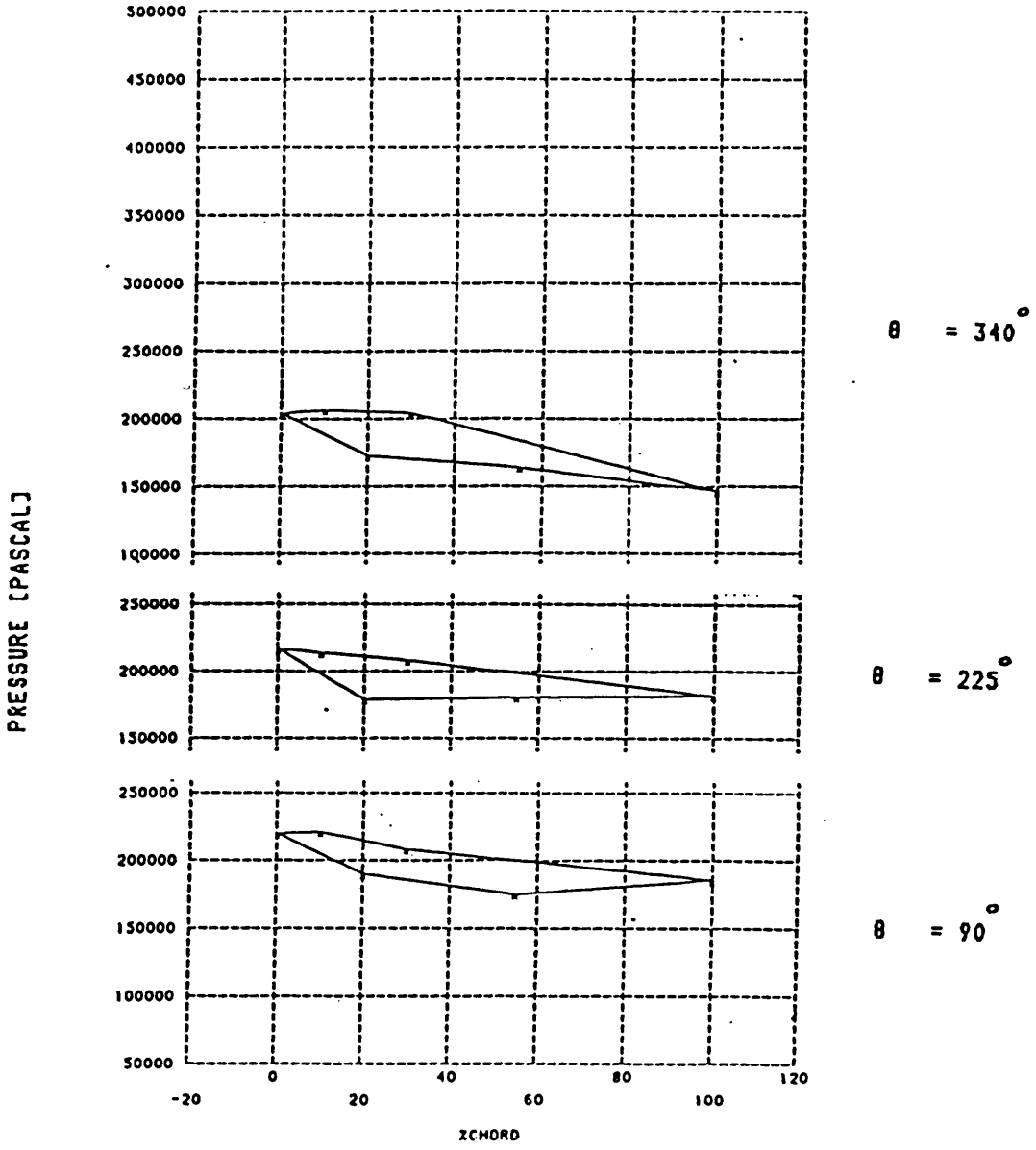

DIFFUSER CONE ANGLE = 16°

NOZZLE RESTRICTION = 50%

SPEED = 50000 [REVS/MIN]

PRESSURE RATIO = 2.77

FIG 4.18 NOZZLE EFFICIENCY

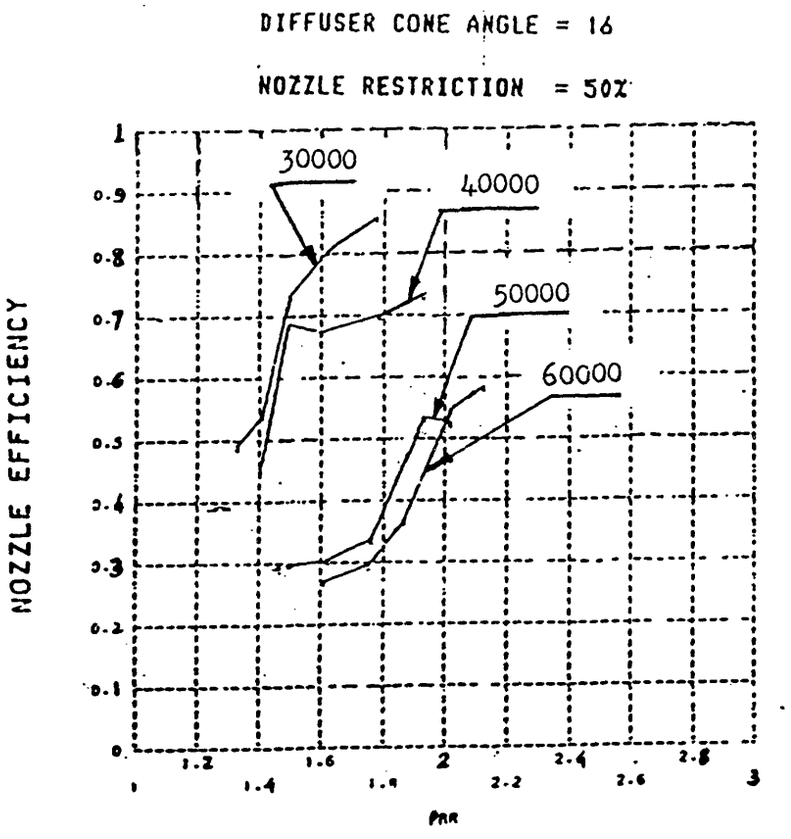

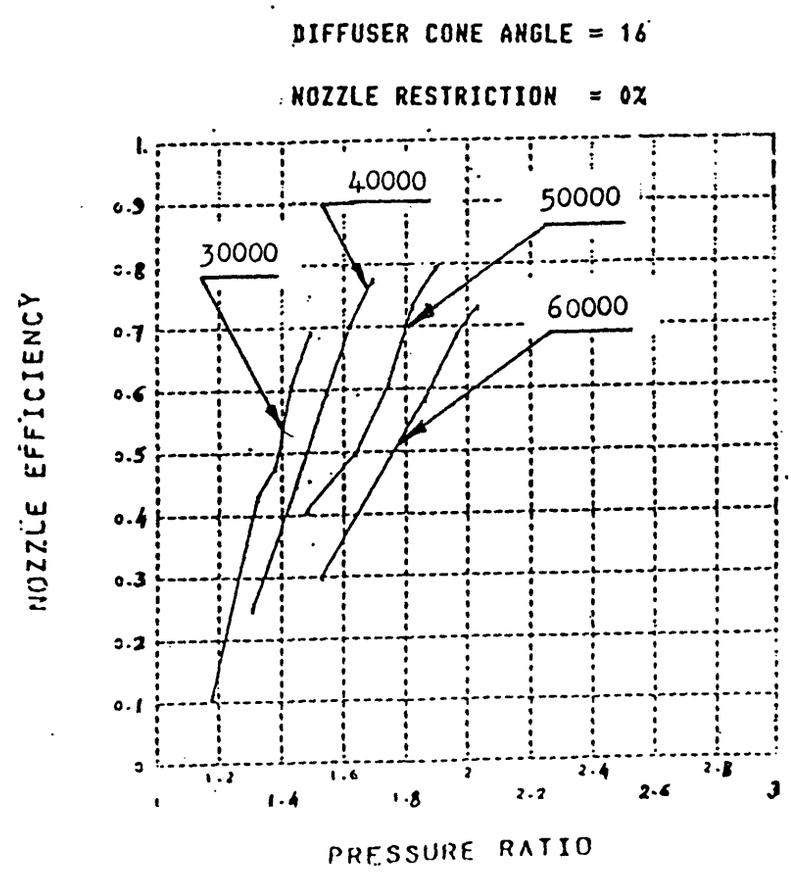

FIG 4.19a VARIATION OF SWIRL WITH PRESSURE RATIO

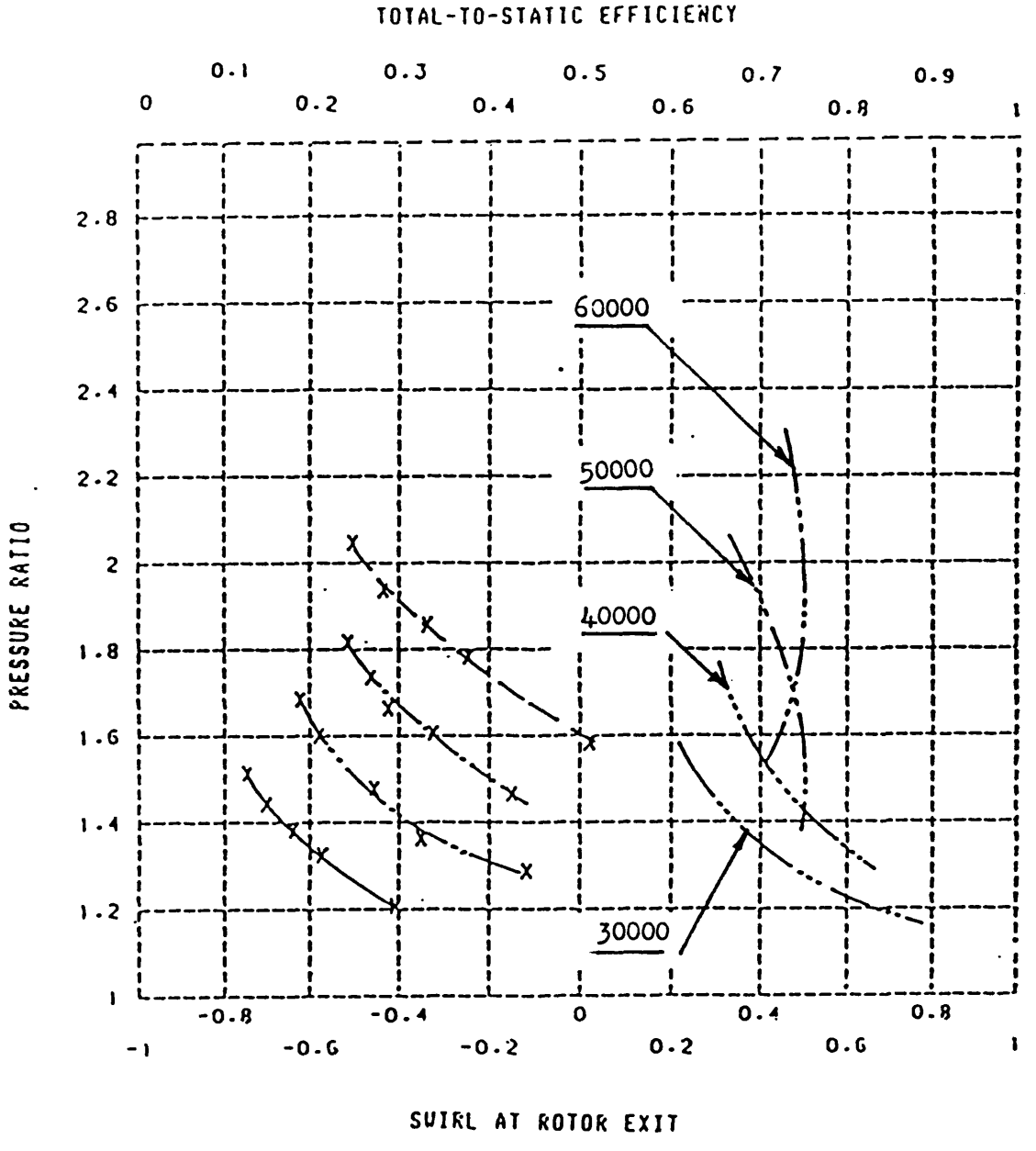

SPEED

30000 (REVS/MIN)

40000 (REVS/MIN)

50000 (REVS/MIN)

60000 (REVS/MIN)

EFFICIENCY CURVES

DIFFUSER CONE ANGLE = 16°

NOZZLE RESTRICTION = 0%

FIG 4.19b VARIATION OF SWIRL WITH PRESSURE RATIO

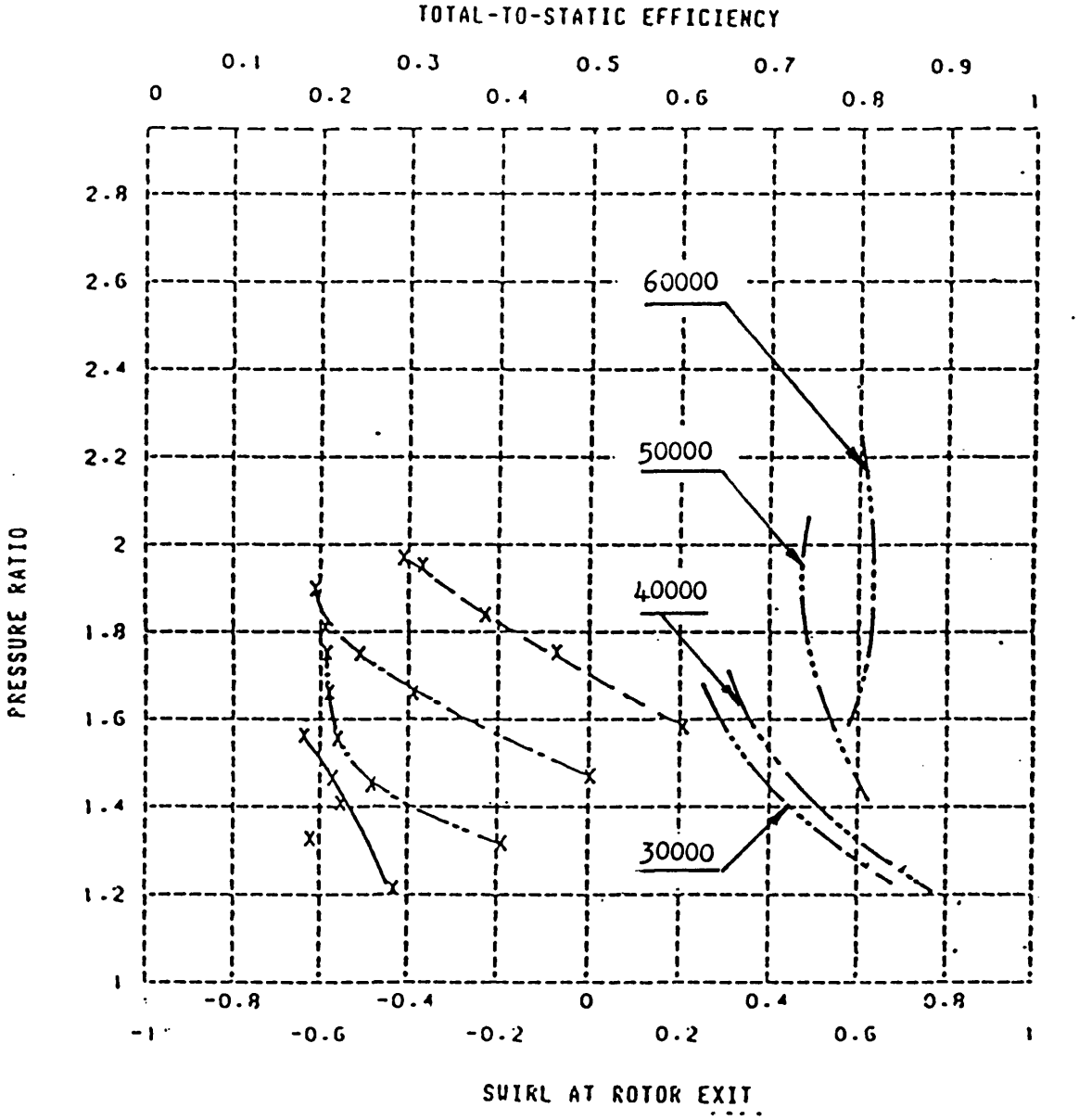

SPEED

30000 (REVS/MIN)

40000 (REVS/MIN)

50000 (REVS/MIN)

60000 (REVS/MIN)

EFFICIENCY CURVES

DIFFUSER CONE ANGLE = 16°

NOZZLE RESTRICTION = 20%

FIG 4.19c VARIATION OF SWIRL WITH PRESSURE RATIO

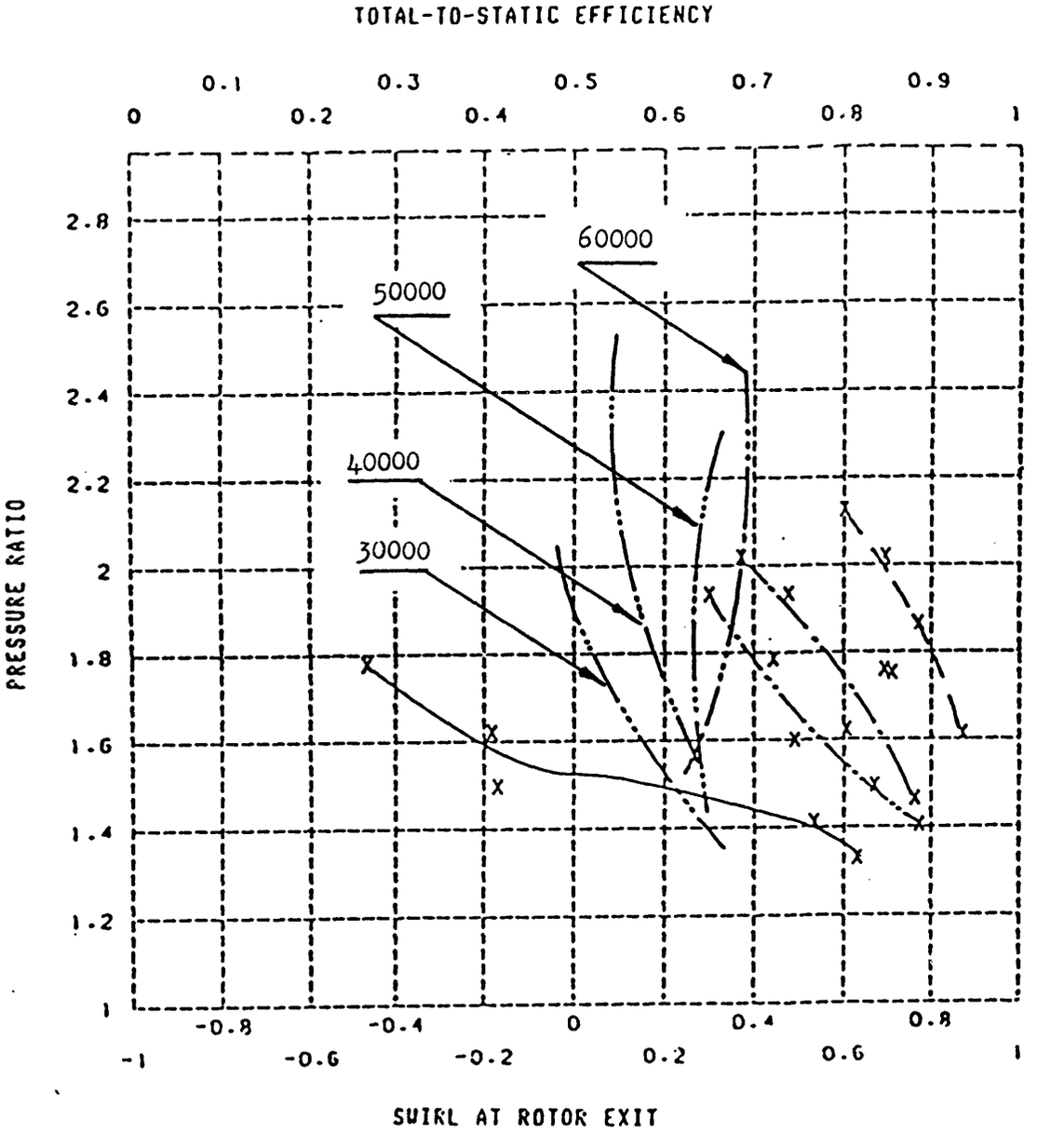

SPEED

——————— 30000 [REVS/MIN]

—·———·———· 40000 [REVS/MIN]

—·——·—·——· 50000 [REVS/MIN]

— — — — — — 60000 [REVS/MIN]

——·——·—··—— EFFICIENCY CURVES

DIFFUSER CONE ANGLE = 16°

NOZZLE RESTRICTION = 50%

FIG 4.20a ROTOR INCIDENCE AND FLOW EXIT ANGLES VS MASS FLOW

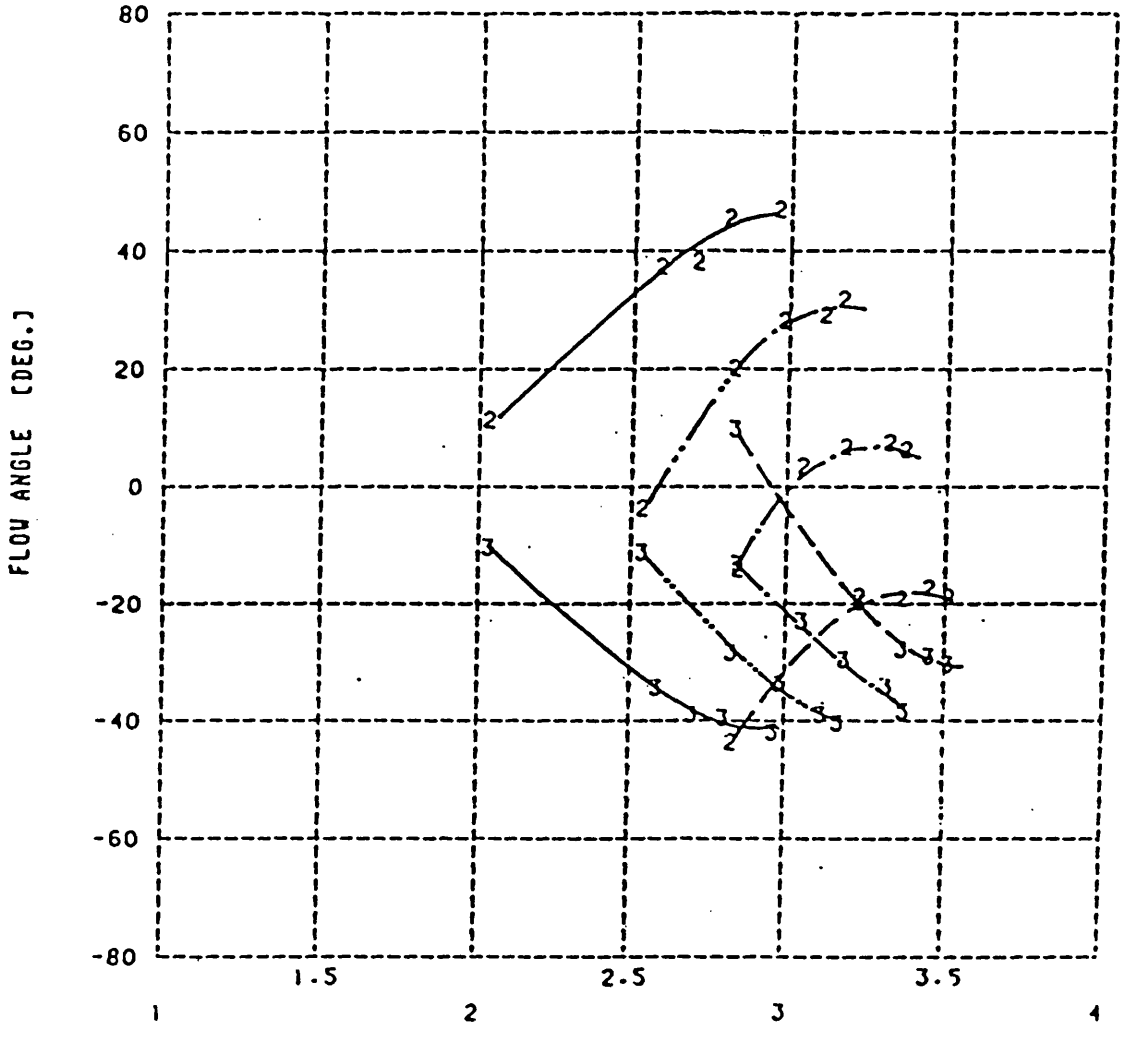

SPEED

——————— 30000 [REVS/MIN]

——·——·—— 40000 [REVS/MIN]

— — — — — — — 60000 [REVS/MIN]

DIFFUSER CONE ANGLE = 29°

NOZZLE RESTRICTION = 0%

2 : INCIDENCE ANGLE

3 : ABSOLUTE FLOW ANGLE AT ROTOR EXIT

FIG 4.20b ROTOR INCIDENCE AND FLOW EXIT ANGLES VS MASS FLOW

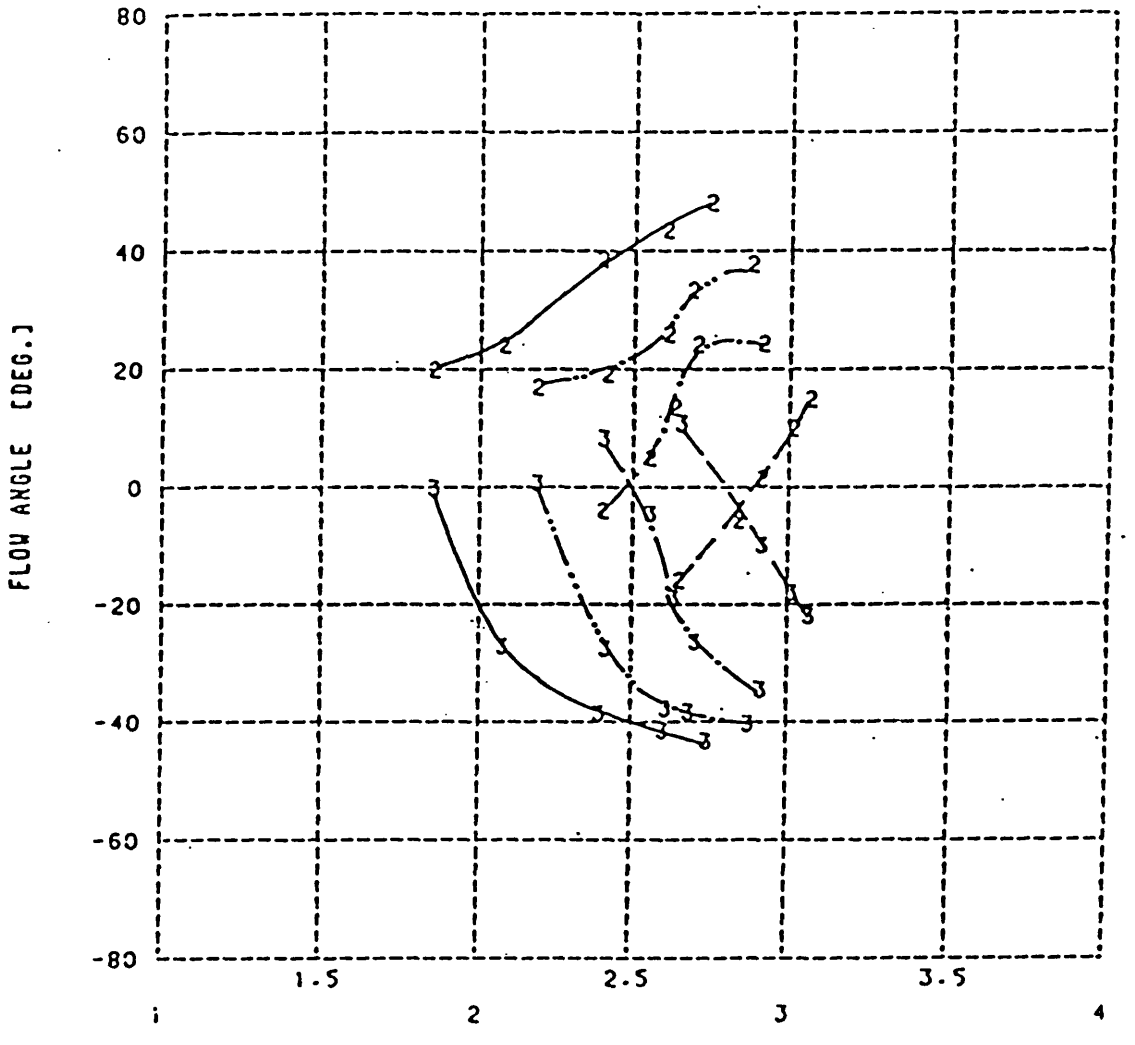

SPEED

30000 (REVS/MIN)

40000 (REVS/MIN)

50000 (REVS/MIN)

60000 (REVS/MIN)

DIFFUSER CONE ANGLE = 29°

NOZZLE RESTRICTION = 20%

2 : INCIDENCE ANGLE

3 : ABSOLUTE FLOW ANGLE AT ROTOR EXIT

FIG 4.20c ROTOR INCIDENCE AND FLOW EXIT ANGLES VS MASS FLOW

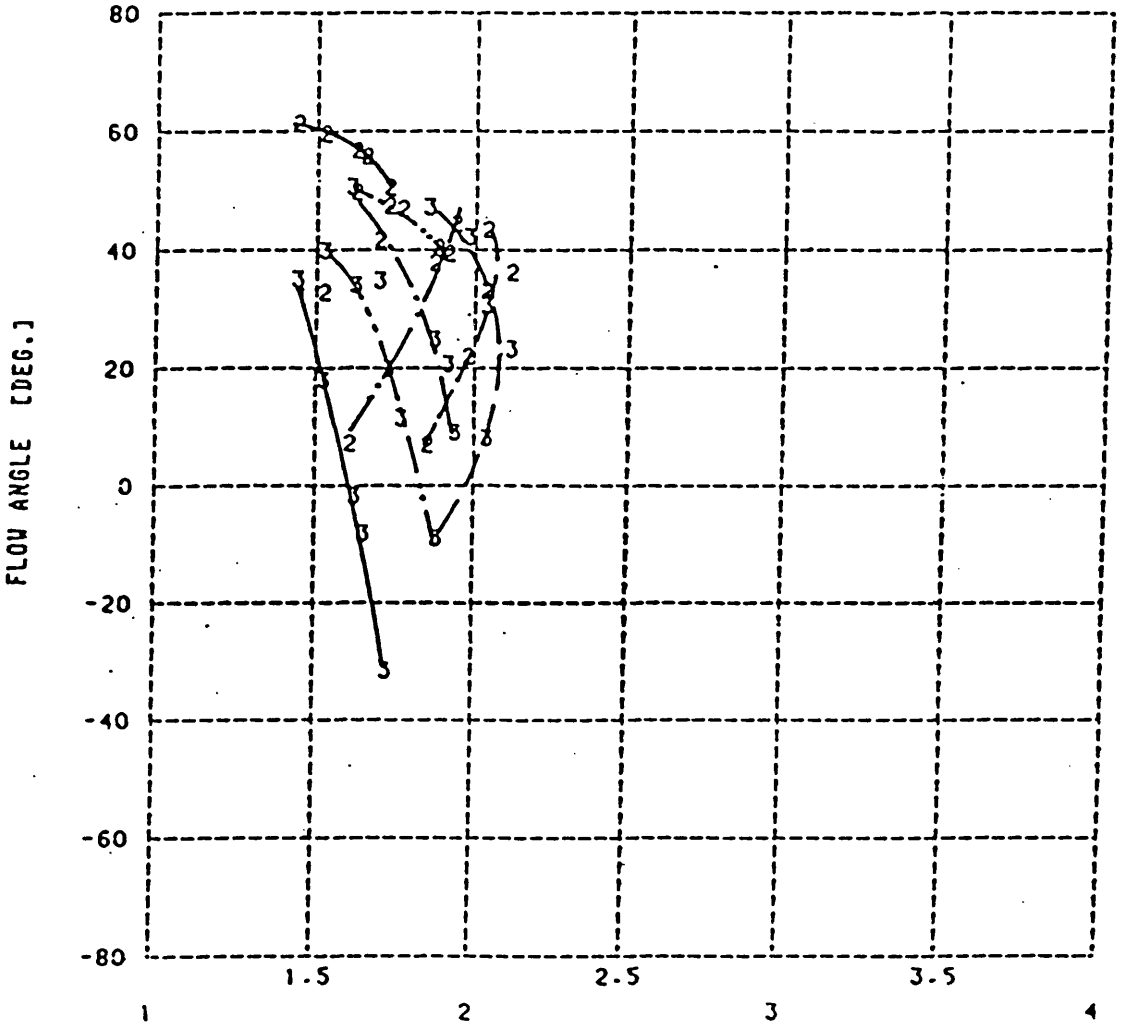

SPEED

——————— 30000 [REVS/MIN]

—·——·——·—— 40000 [REVS/MIN]

——·——·——·— 50000 [REVS/MIN]

— — — — — — 60000 [REVS/MIN]

DIFFUSER CONE ANGLE = 29°

NOZZLE RESTRICTION = 50%

2 : INCIDENCE ANGLE

3 : ABSOLUTE FLOW ANGLE AT ROTOR EXIT

FIG 4.21a ROTOR INCIDENCE AND FLOW EXIT ANGLES VS MASS FLOW

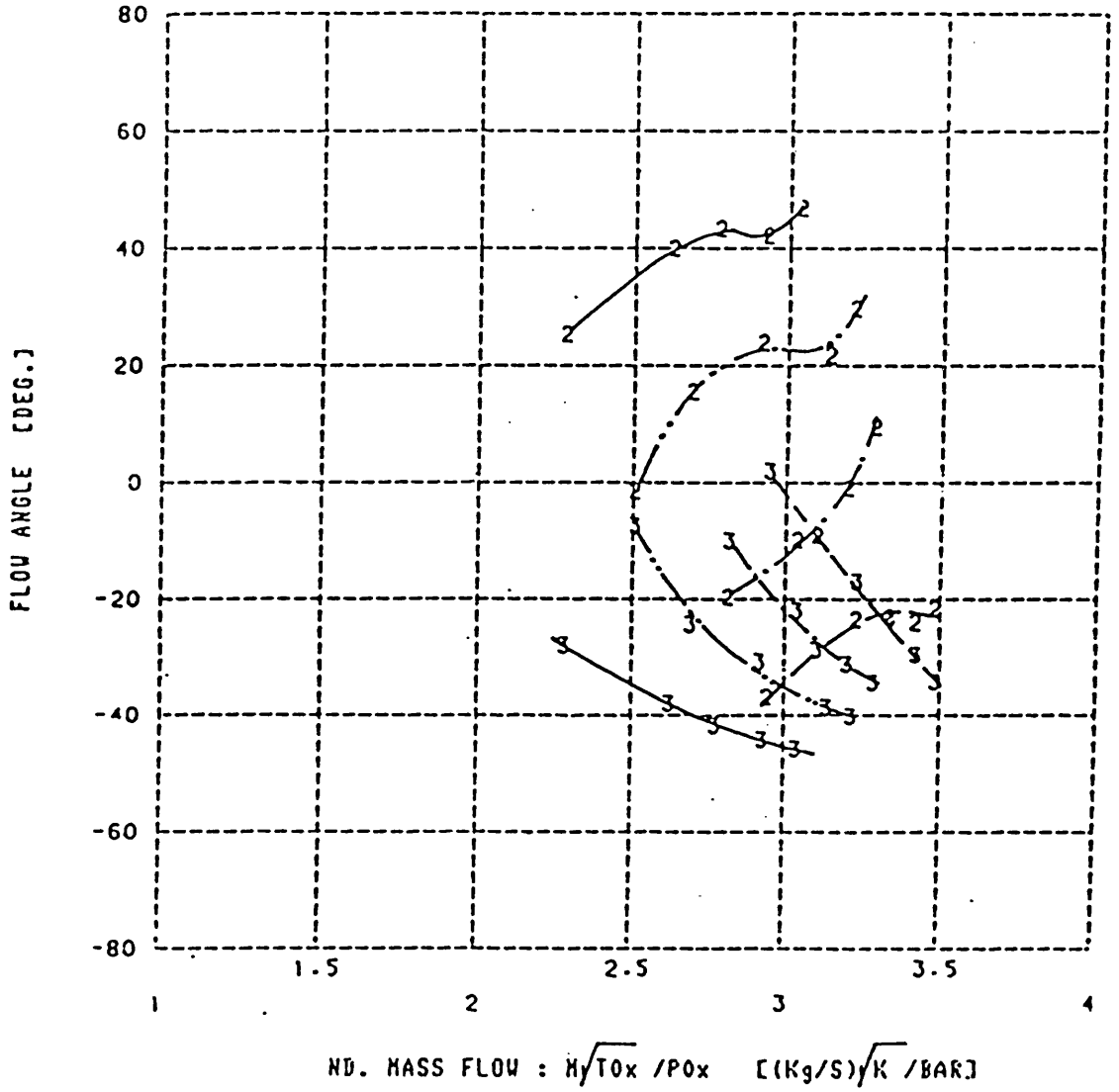

SPEED

30000 [REVS/MIN]

40000 [REVS/MIN]

50000 [REVS/MIN]

60000 [REVS/MIN]

DIFFUSER CONE ANGLE = 16°

NOZZLE RESTRICTION = 0%

2 : INCIDENCE ANGLE

3 : ABSOLUTE FLOW ANGLE AT ROTOR EXIT

FIG 4.21b ROTOR INCIDENCE AND EXIT FLOW ANGLES VS MASS FLOW

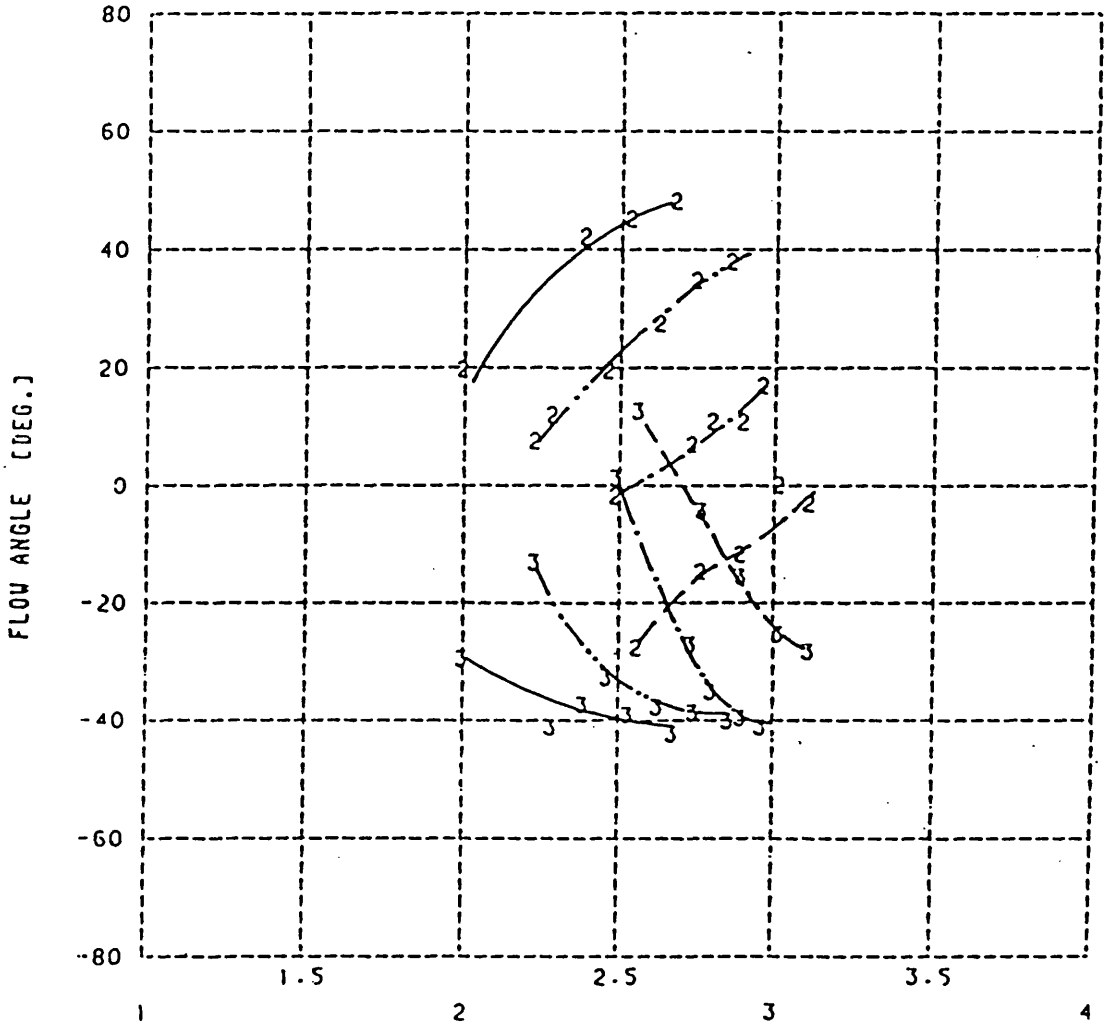

SPEED

——————— 30000 [REVS/MIN]

—·——·——·— 40000 [REVS/MIN]

——·——·——·— 50000 [REVS/MIN]

— — — — — — 60000 [REVS/MIN]

DIFFUSER CONE ANGLE = 16°

NOZZLE RESTRICTION = 20%

2 : INCIDENCE ANGLE

3 : ABSOLUTE FLOW ANGLE AT ROTOR EXIT

FIG 4.21c ROTOR INCIDENCE AND EXIT FLOW ANGLES VS MASS FLOW

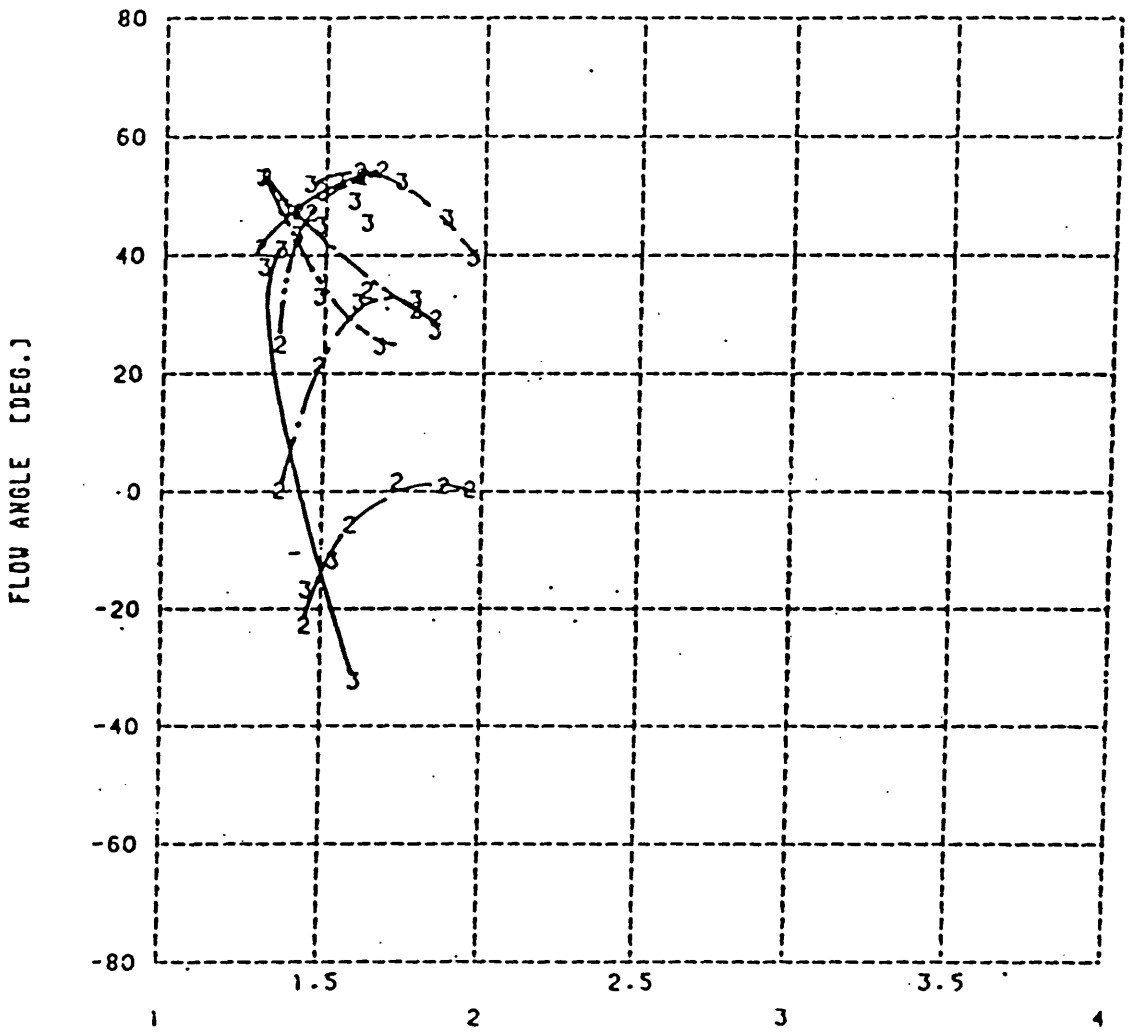

SPEED

——————— 30000 [REVS/MIN]

—·——··—·—·— 40000 [REVS/MIN]

—·——·——·— 50000 [REVS/MIN]

— — — — — — — 60000 [REVS/MIN]

DIFFUSER CONE ANGLE = 16°

NOZZLE RESTRICTION = 50%

2 : INCIDENCE ANGLE

3 : ABSOLUTE FLOW ANGLE AT ROTOR EXIT

FIG 4.22a ROTOR INCIDENCE AND EXIT FLOW ANGLES VS MASS FLOW

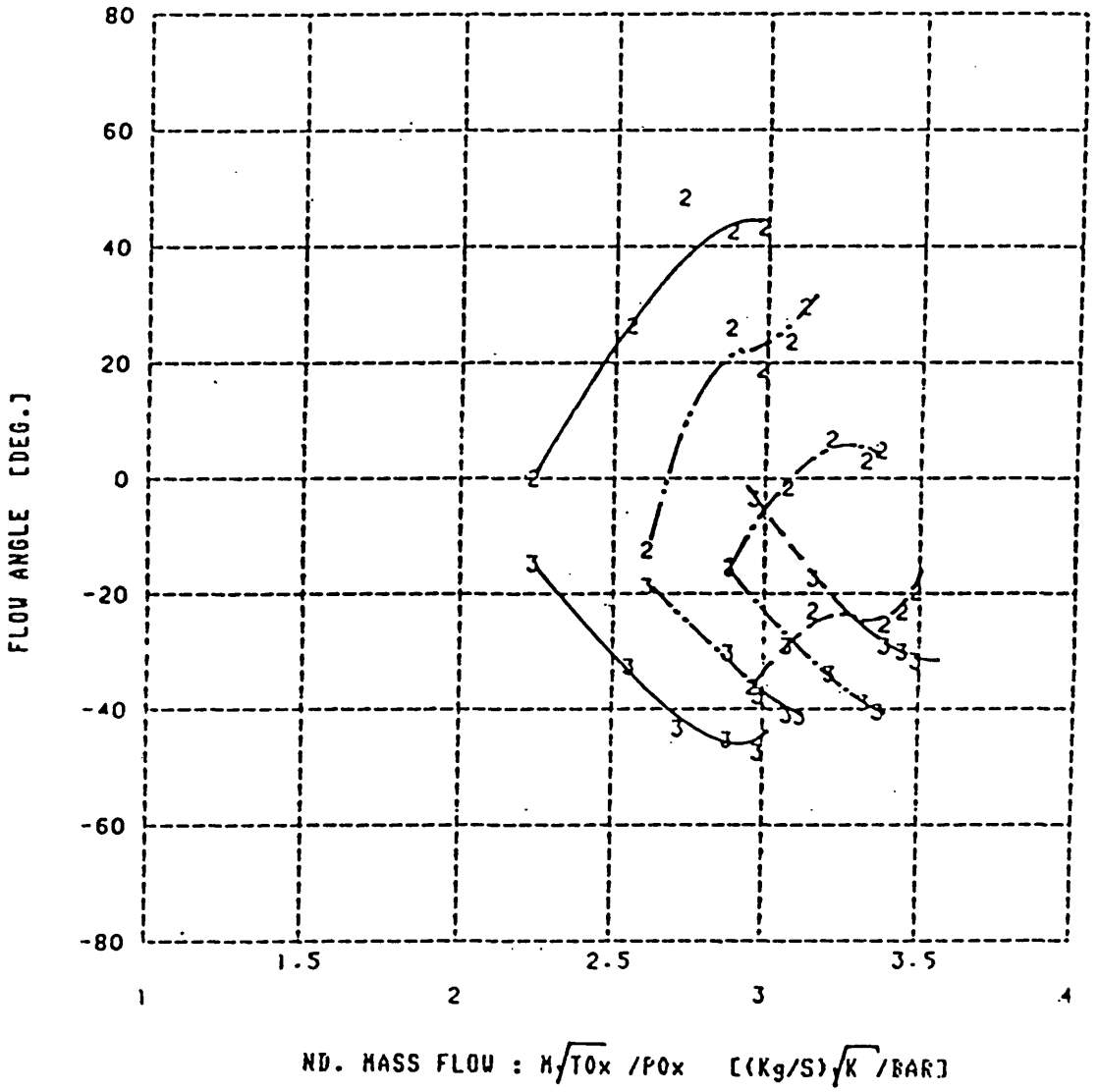

SPEED

30000 [REVS/MIN]

40000 [REVS/MIN]

50000 [REVS/MIN]

60000 [REVS/MIN]

DIFFUSER CONE ANGLE = 8°

NOZZLE RESTRICTION = 0%

2 : INCIDENCE ANGLE

3 : ABSOLUTE FLOW ANGLE AT ROTOR EXIT

FIG 4.22b ROTOR INCIDENCE AND EXIT FLOW ANGLES VS MASS FLOW

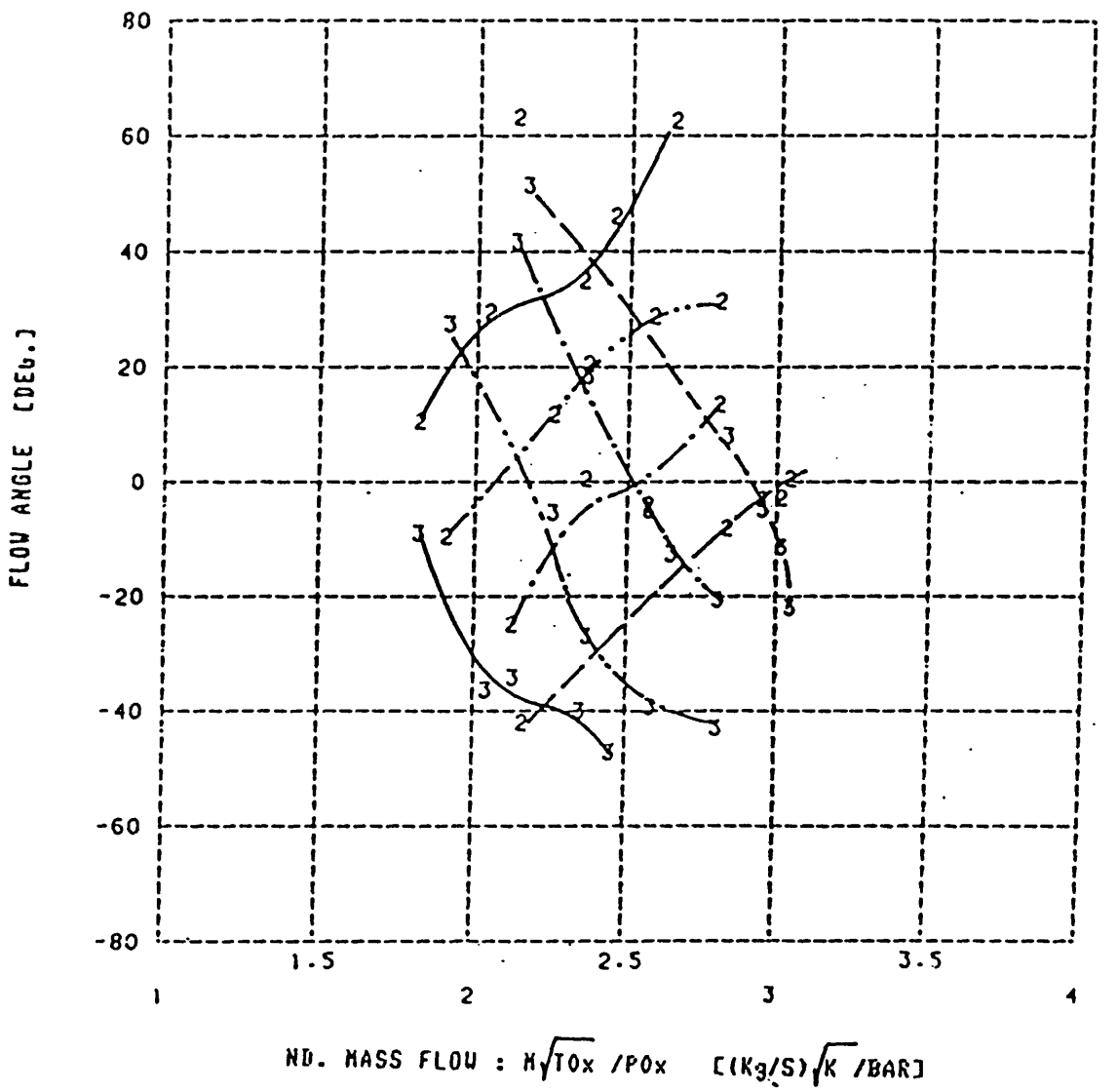

SPEED

——————— 30000 (REVS/MIN)

——·——··——·· 40000 (REVS/MIN)

——·——·——·—— 50000 (REVS/MIN)

— — — — — — 60000 (REVS/MIN)

DIFFUSER CONE ANGLE = 8°

NOZZLE RESTRICTION = 20%

2 : INCIDENCE ANGLE

3 : ABSOLUTE FLOW ANGLE AT ROTOR EXIT

FIG 4.22c ROTOR INCIDENCE AND EXIT FLOW ANGLES VS MASS FLOW

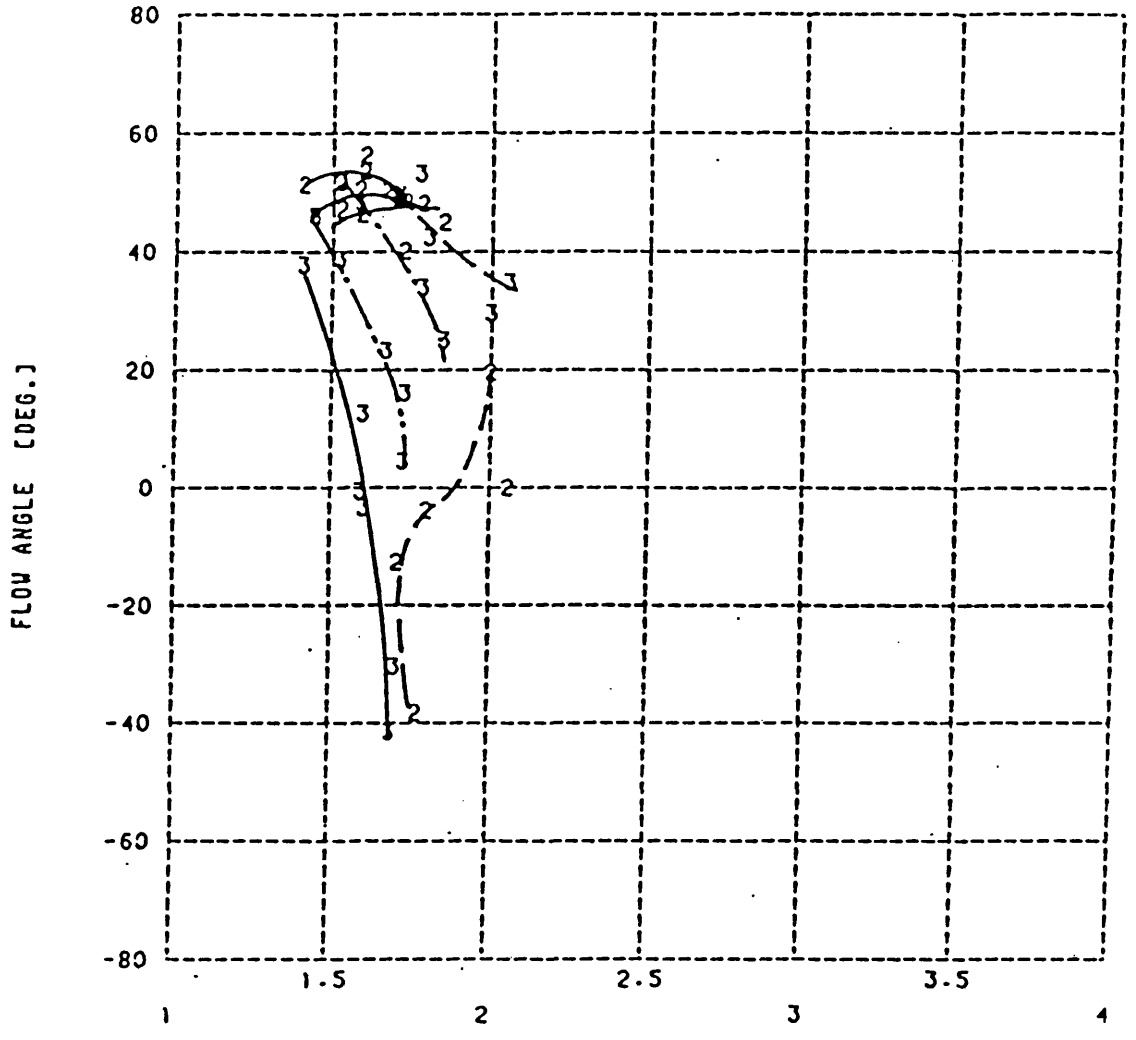

SPEED

——————— 30000 [REVS/MIN]

——··——··—·· 40000 [REVS/MIN]

——·——·——·— 50000 [REVS/MIN]

— — — — — — 60000 [REVS/MIN]

DIFFUSER CONE ANGLE = 8°

NOZZLE RESTRICTION = 50%

2 : INCIDENCE ANGLE

3 : ABSOLUTE FLOW ANGLE AT ROTOR EXIT

FIG 4.23a INCIDENCE ANGLE VARIATION AT AXIAL EXIT FLOW

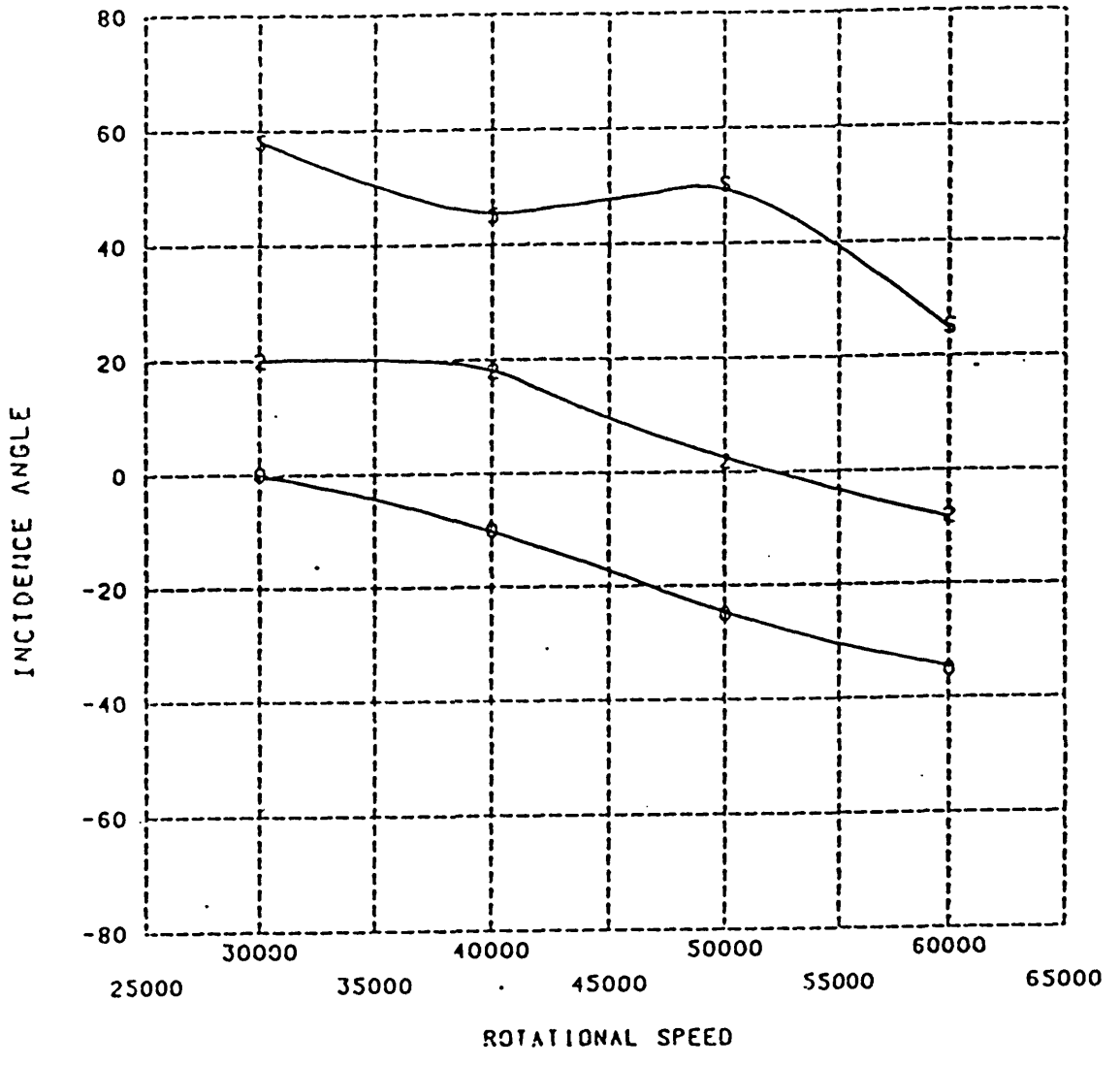

DIFFUSER CONE ANGLE = 29°

0 : NOZZLE RESTRICTION = 0%

2 : NOZZLE RESTRICTION = 20%

5 : NOZZLE RESTRICTION = 50%

FIG 4.23b INCIDENCE ANGLE VARIATION AT AXIAL EXIT FLOW

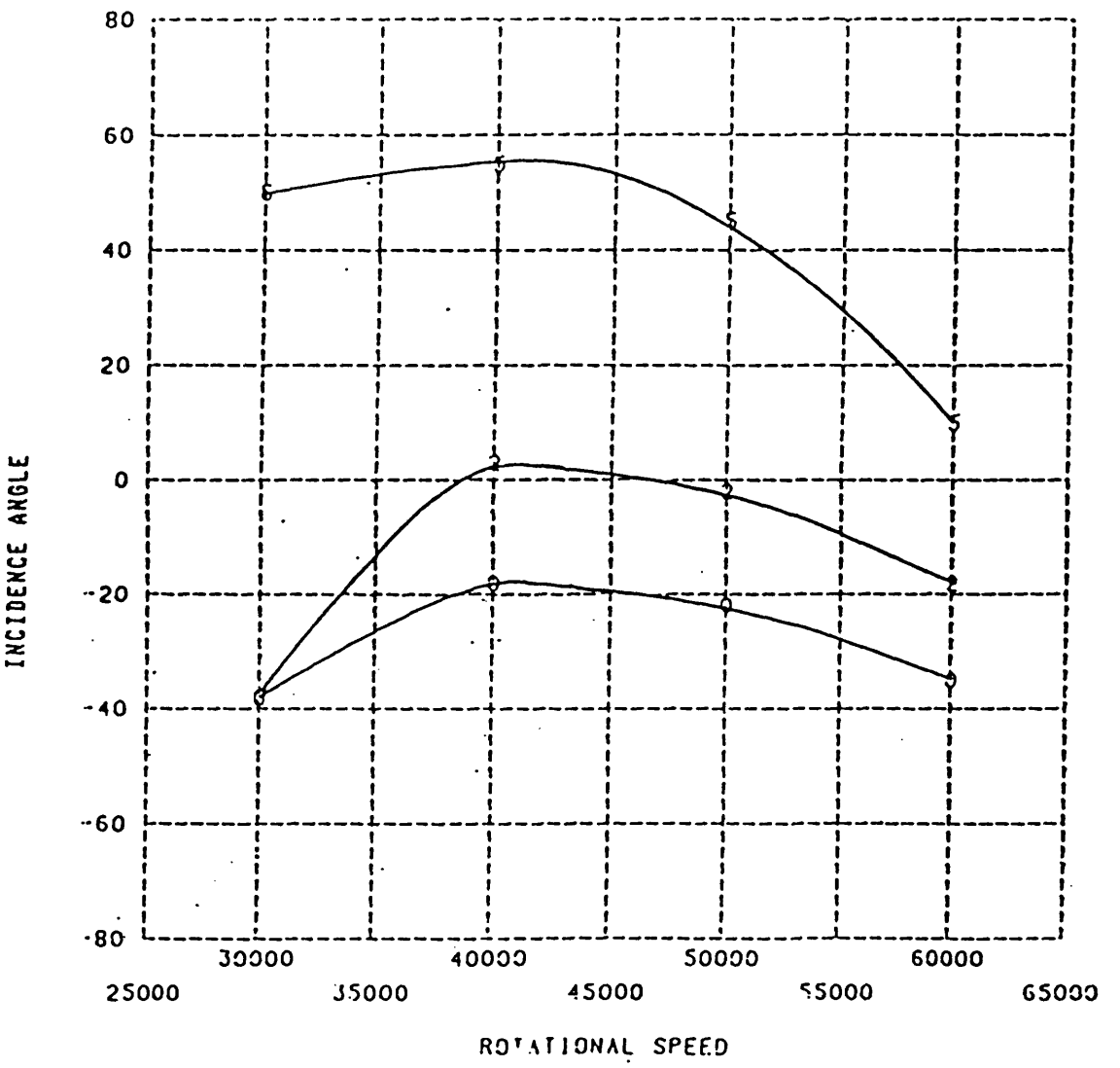

DIFFUSER CONE ANGLE = 16°

0 : NOZZLE RESTRICTION = 0%

2 : NOZZLE RESTRICTION = 20%

5 : NOZZLE RESTRICTION = 50%

FIG 4.23c INCIDENCE ANGLE VARIATION AT AXIAL EXIT FLOW

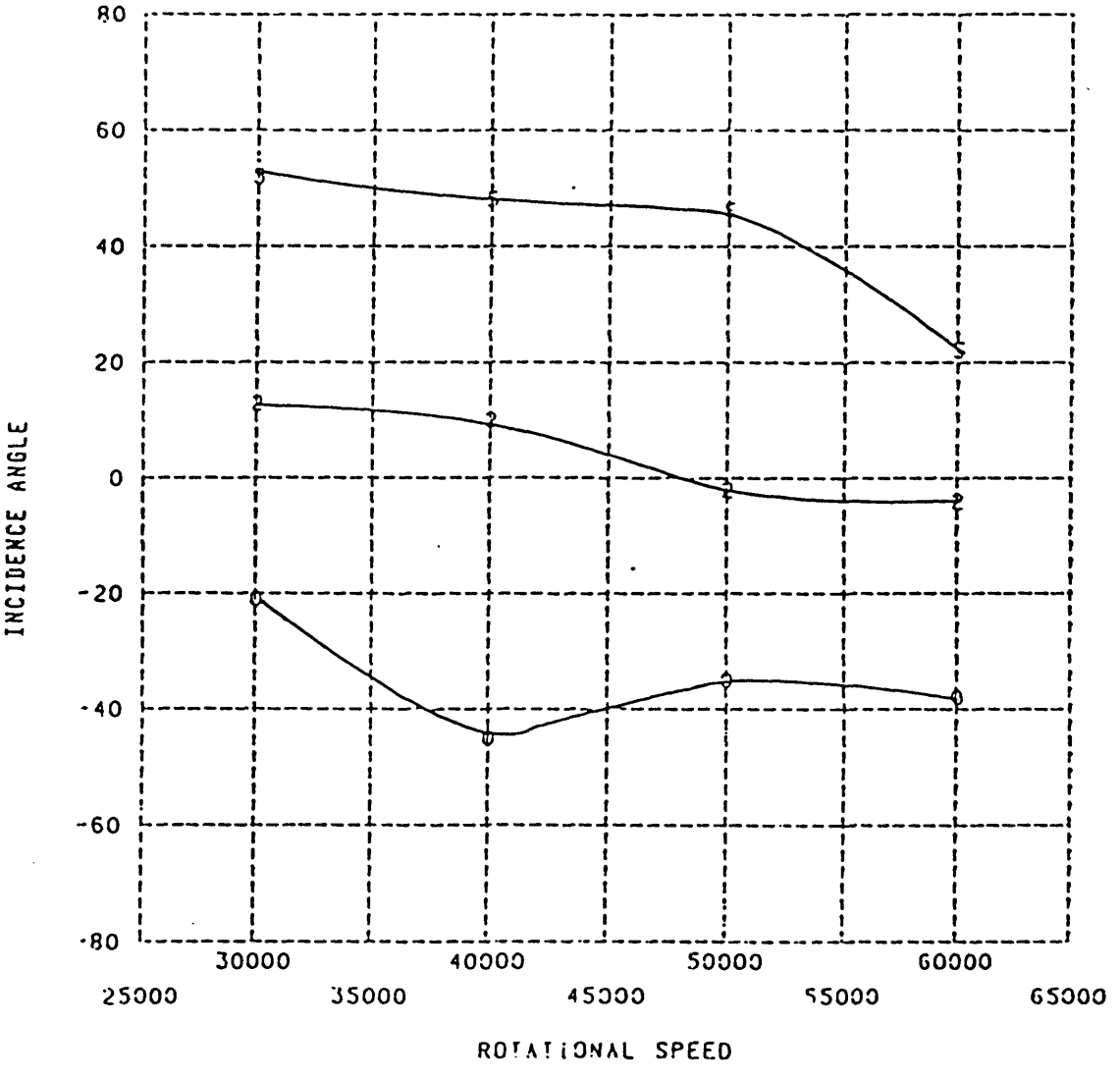

DIFFUSER CONE ANGLE = 8°

0 : NOZZLE RESTRICTION = 0%

2 : NOZZLE RESTRICTION = 20%

5 : NOZZLE RESTRICTION = 50%

FIG 4.24a ROTOR LOSS COEFFICIENT DISTRIBUTION

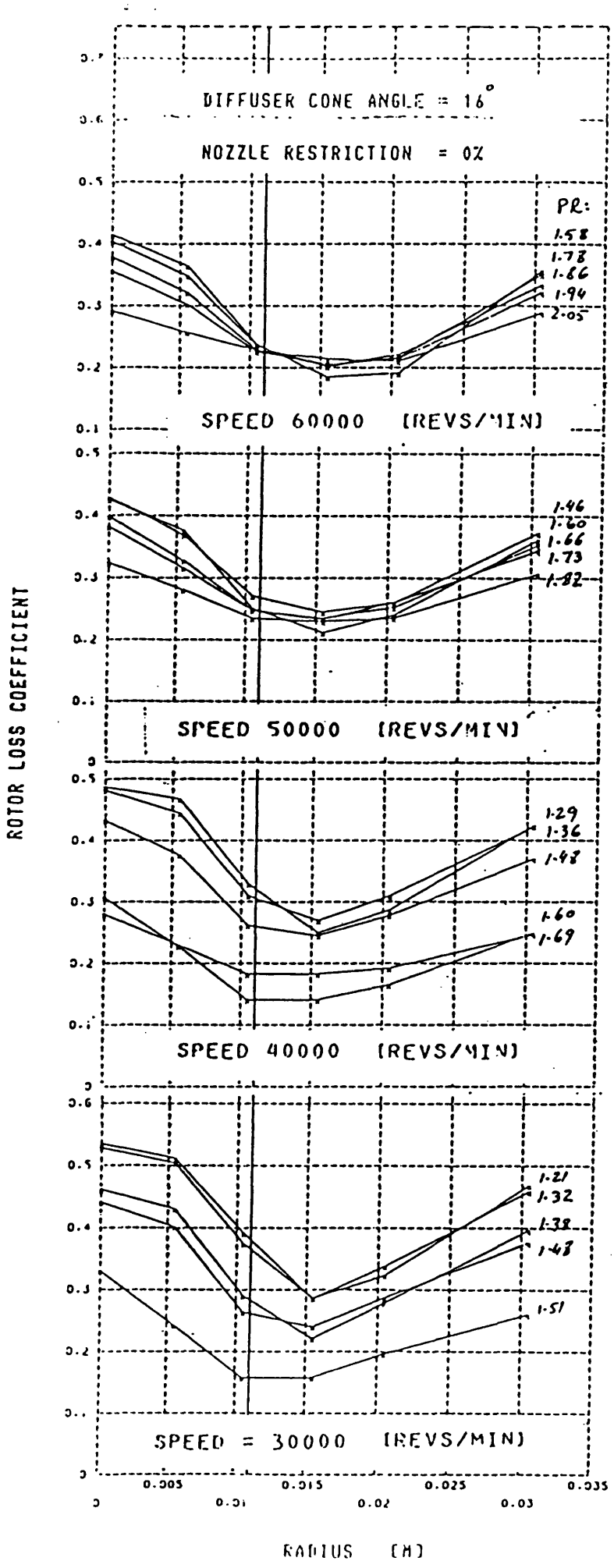

FIG 4.24b ROTOR LOSS COEFFICIENT DISTRIBUTION

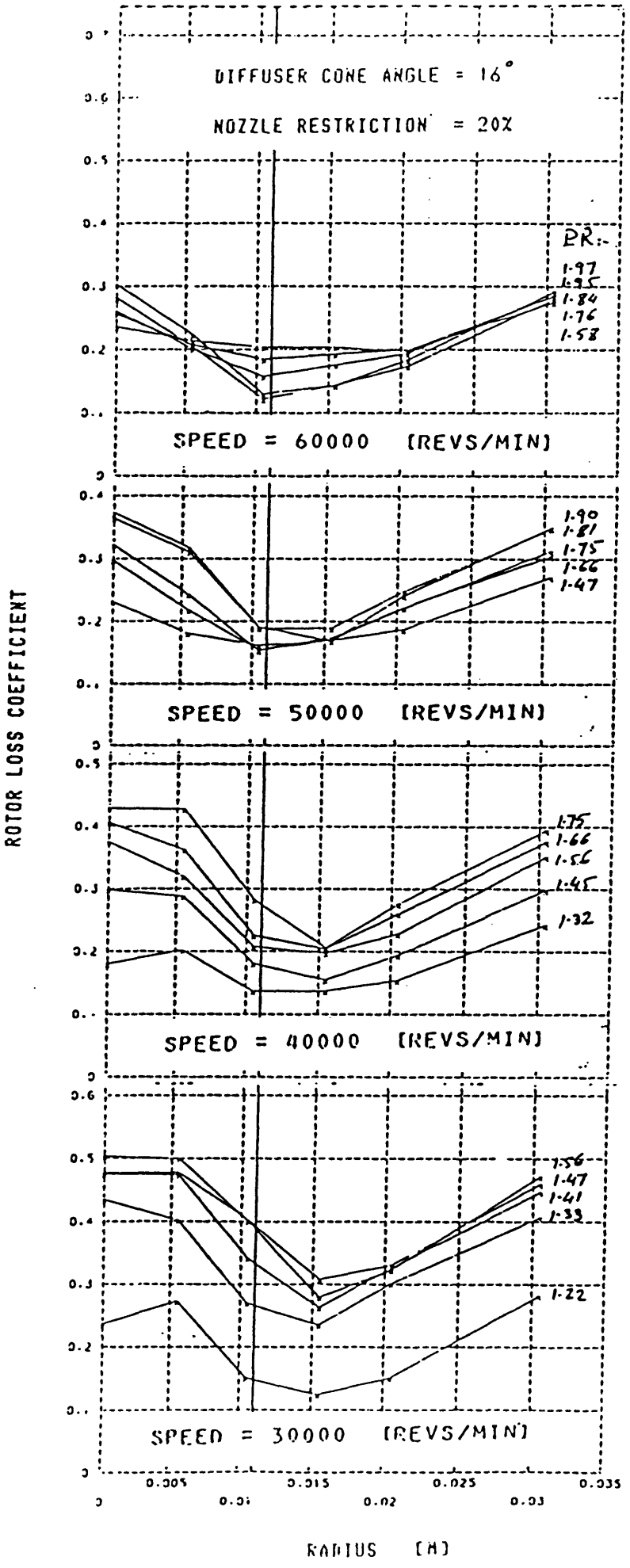

FIG 4.24c ROTOR LOSS COEFFICIENT DISTRIBUTION

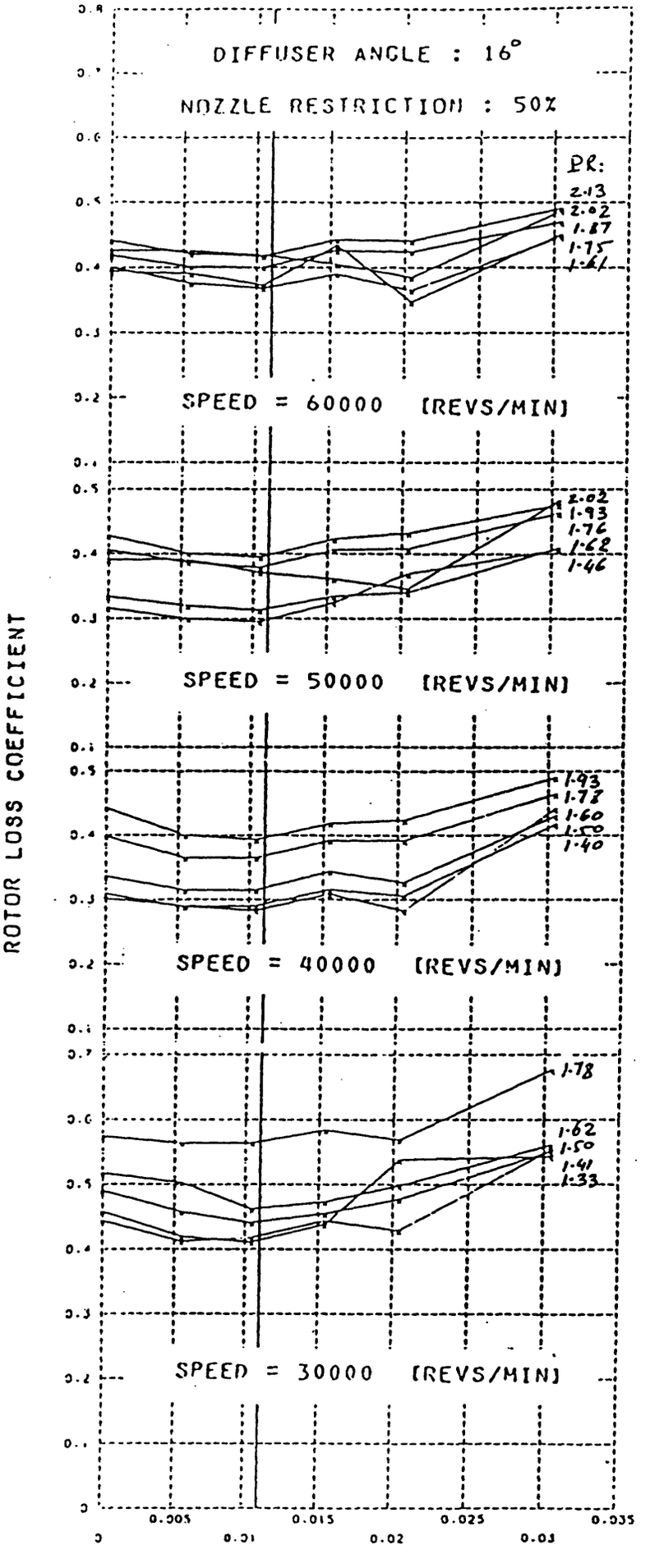

CHAPTER -V-

5. PRESENTATION AND DISCUSSION OF THEORETICAL RESULTS

5.1 Meridional Flow Analusis

The solution procedure applied to the rotor is shown in figure 5.1, while figures 5.2a,b show different typical mesh arrangements generated automatically by considering the hub and shroud curves to be represented by Lame' ovals, the derivation of which are described in references [22,27]. The computed streamlines contours are shown in figure 5.3.

Any computational techniques can be evaluated by comparing them with the results of other methods either exact or numerical or by comparison with experimental results. The results of the present analysis are compared to those from an existing streamline curvature method, see ref.[22]. The results of both methods, presented in terms of velocity contours over the mid stream surface, are shown in figures 5.4a,b. From the finite element results, figure 5.4a, it can be seen that the flow accelerates towards the exit having a peak value at the mid stream tube, and a smooth velocity distribution is predicted over the stream surface. The results of the streamline curvature method, figure 5.4b, show an uneven distribution of velocity and some fluctuation occur at inlet and exit

regions; a deceleration is predicted in the inlet passage.

The differences in the above results must be due to the theoretical techniques used. In the streamline curvature approach a first order ordinary differential equation describing the force balance in the direction of the normals to the streamlines was used. This equation was solved along the normals marching forward along the passage from inlet to exit, the continuity equation being satisfied at each normal. This approach involved first derivitives along the normal, while first and second order derivitives were used along the streamline, it was then necessary to apply curve fitting techniques to the computed streamlines. Two principal equations were used in the solution at far upstream and downstream, these were based upon the absolute velocities, while within the rotor the relative velocities were considered. This is believed to have affected the final results as clearly different initial values were applied for the solution domain.

In the finite element approach the solution is based upon a partial differential equation describing the steady, compressible and inviscid flow, and the flow field was divided into finite elements where the equation of motion was solved and assembled for the entire domain. The result was a system of linear equations which were then

solved for the nodal values of stream function. Only the relative velocities were applied at the boundaries, and a homogeneous velocity field resulted, figure 5.4a. Adding to this the economy in the computational time and the considerable space and storage savings the finite element results could be considered as more reliable than those of the streamline curvature method. However, as the two methods predict slightly different results it remains necessary to study the streamline curvature procedure in more detail before the precise cause of the differences can be identified.

5.2 The Isolated Aerofoil

The flow chart for the calculation procedure used to calculate the flow around the aerofoil is given in figure 5.5 ;figure 5.6 shows a typical mesh arrangement used. The computed potential function contours are shown in figure 5.7, and the predicted pressure distribution around the aerofoil is compared with that given in reference [57], figure 5.8. In the present analysis the circulation around the aerofoil was considered as a nodeless variable and was calculated from the first iteration values of the potential function on the either side of the splitting boundary. In the computational procedure the elementary matrices following the first iteration have not been

computed but were considered as identical to those of the previous iteration. By doing so the computational time was considerably reduced. Also relative to reference a coarse mesh was used, figure 5.6. Bearing in mind these differences the agreement shown between the two methods was considered satisfactory, figure 5.8

5.3 Volute Nozzle Assembly Investigation

The theory applied here is same as that used in the previous section, see figure 5.5, the only difference is in the mesh generation calculations. Figures 5.9a,b,c illustrate different mesh sizes used. Using the mesh arrangement of figure 5.9a the potential function contours, figure 5.10 were calculated.

The predicted blade pressure distribution are compared with those obtained experimentally in figures 5.11a,b,c. It is clear that the agreement between the measured and the predicted pressure distribution is not satisfactory. This discrepancy is due to (i) the lack of detailed pressure measurements over 60% of the chord length, and (ii) the various assumptions made in solving the flow equations which ignore the effects of compressibility and viscosity, and to the three dimensional nature of the flow. The the theoretical procedure clearly needs further development to accommodate these features. For the

experimental work it was not possible to place pressure tappings on the narrow trailing edge region of the blades.

In order to accurately predict the pressure distribution around the blades it is important to initially predict the correct inlet conditions to the blade row. Due to the narrow flow passages involved no attempt has been made to measure these inlet conditions. However, based upon the experimental measurements and assuming a free vortex flow to the blade leading edge, the flow angle at blade inlet has been calculated. This is shown in figures 5.12a,b and compared with that predicted with the finite element procedure. With the free vortex assumption it is only possible to calculate a single mean inlet angle whereas the finite element analysis yields a flow angle which varies with azimuth angle. Figures 5.12b shows that the free vortex analysis yields a mean flow angle which compares well with that predicted from the finite element method. However, the fluctuations about this mean are quite significant and improved experimental results are needed for comparison purposes.

FIG 5.1 FLOW CHART FOR THE HUB SHROUD ANALYSIS

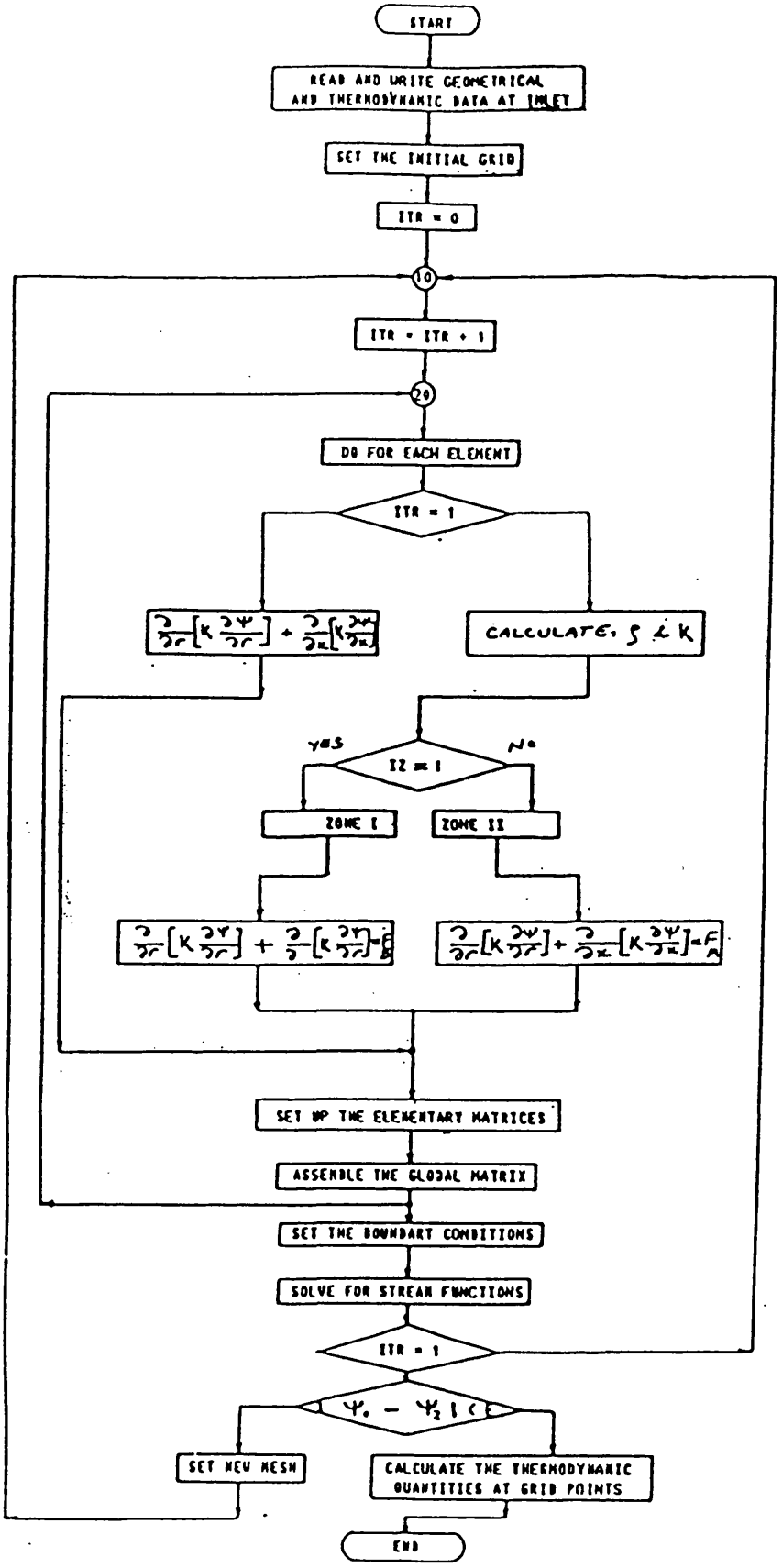

FIG 5.2a TYPICAL MESH USED IN THE HUB SHROUD ANALYSIS

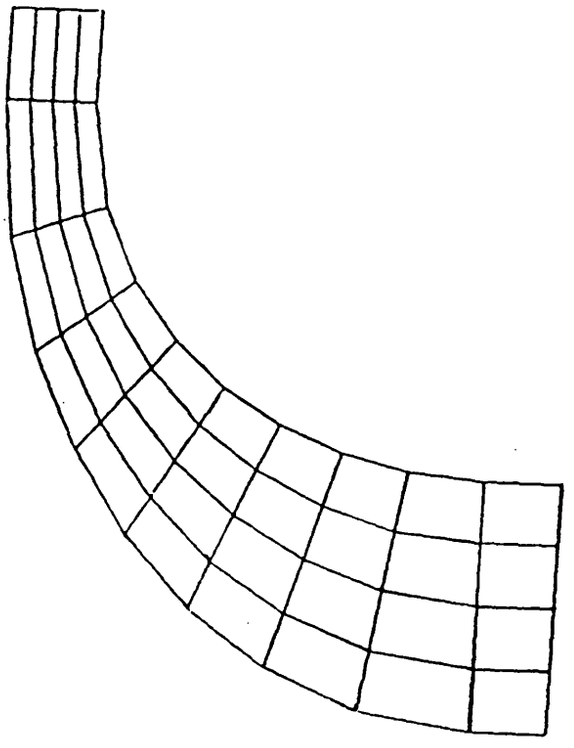

FIG 5.2b FINE MESH FOR THE HUB SHROUD ANALYSIS

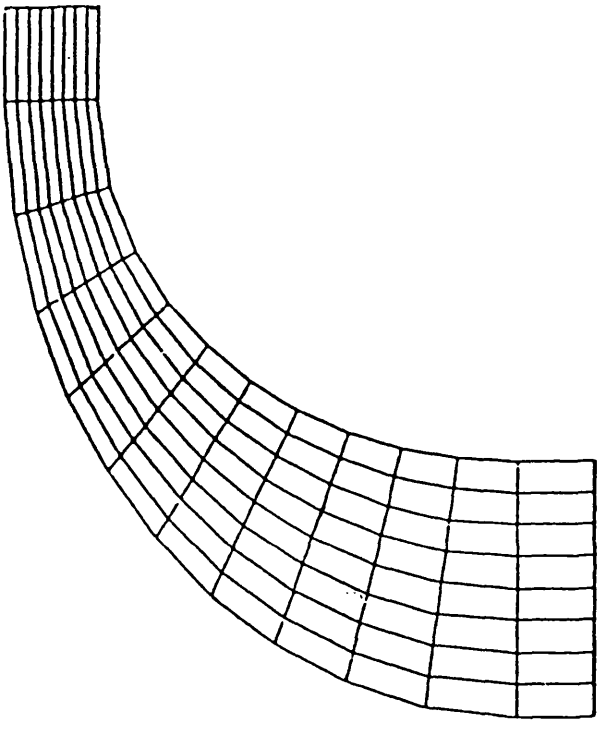

FIG 5.3 STREAMLINES CONTOURS OF THE HUB SHROUD ANALYSIS

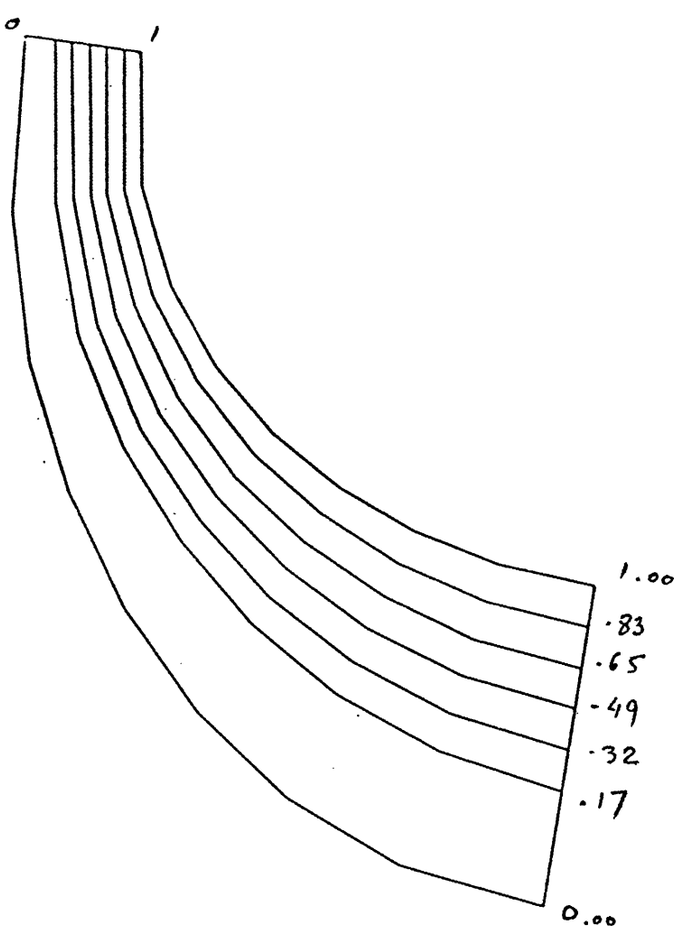

FIG 5.4a VELOCITY CONTOURS IN THE HUB SHROUD ANALYSIS

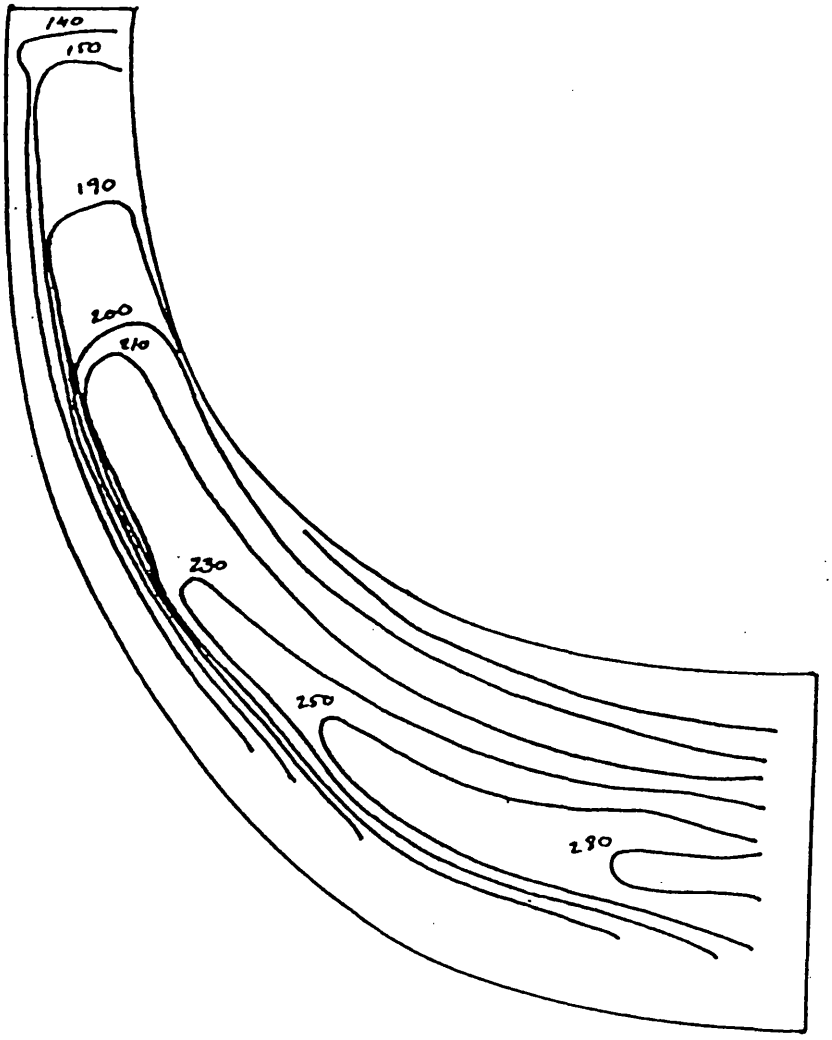

FIG 5.4b VELOCITY CONTOURS OF THE STREAMLINE CURVATURE ANALYSIS REF.[22]

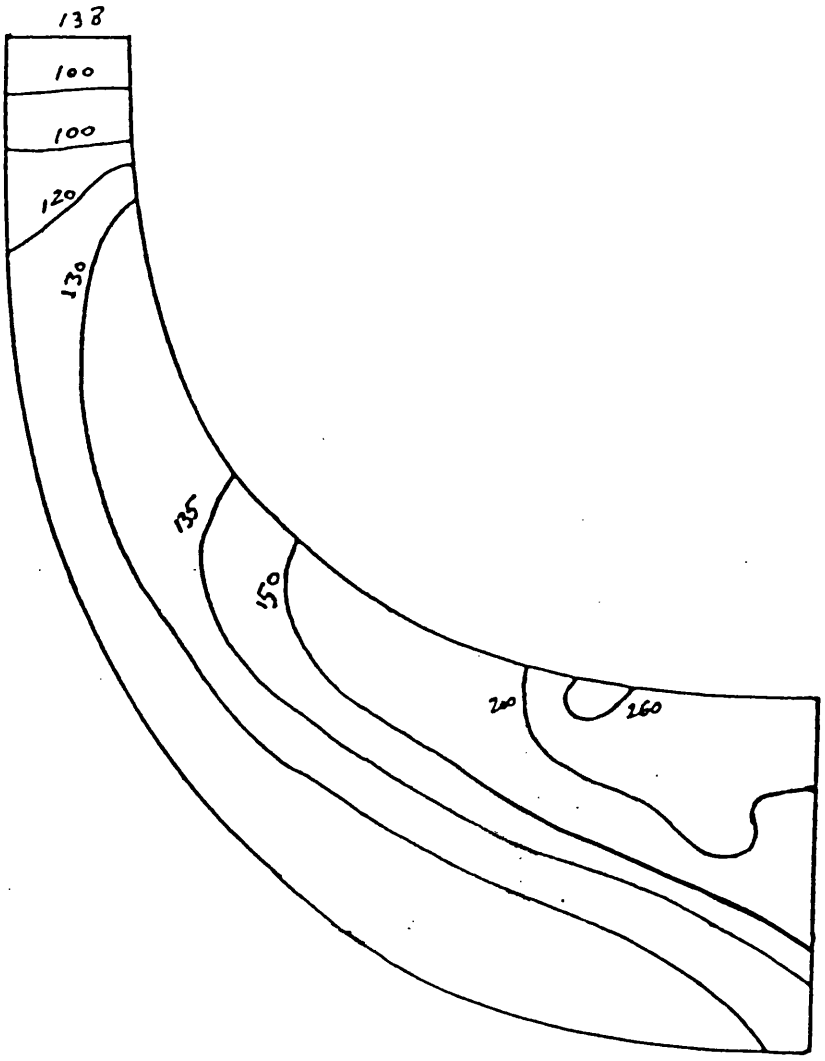

FIG 5.5 FLOW CHART FOR THE AEROFOIL ANALYSIS

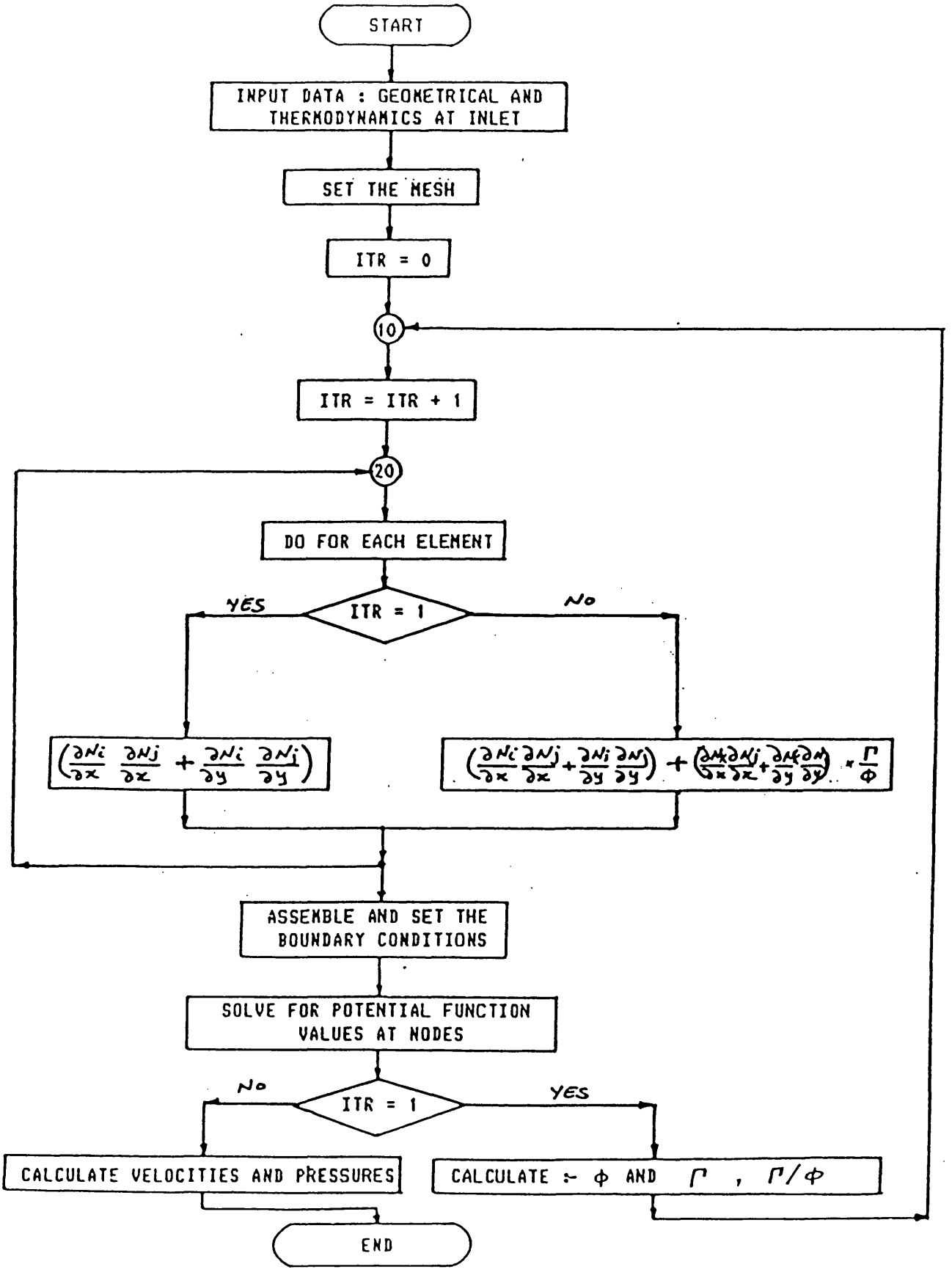

FIG 5.6 TYPICAL MESH USED IN THE ISOLATED AEROFOIL ANALYSIS

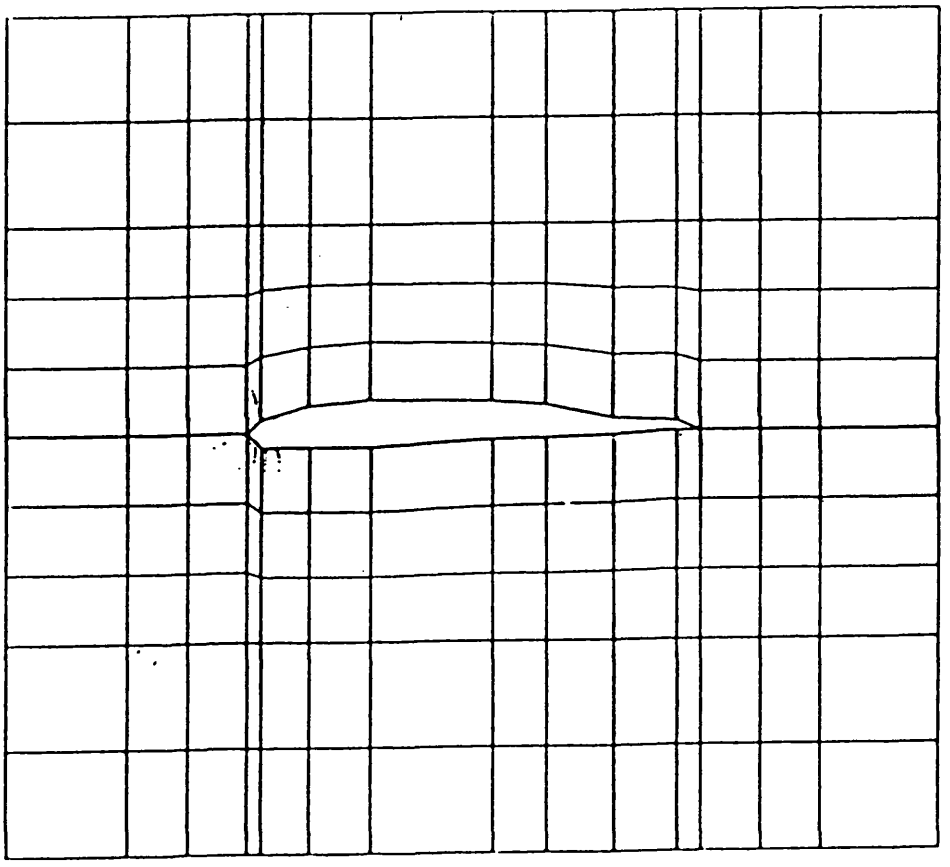

FIG 5.7 POTENTIAL FUNCTION CONTOURS OF THE ISOLATED AEROFOIL ANALYSIS

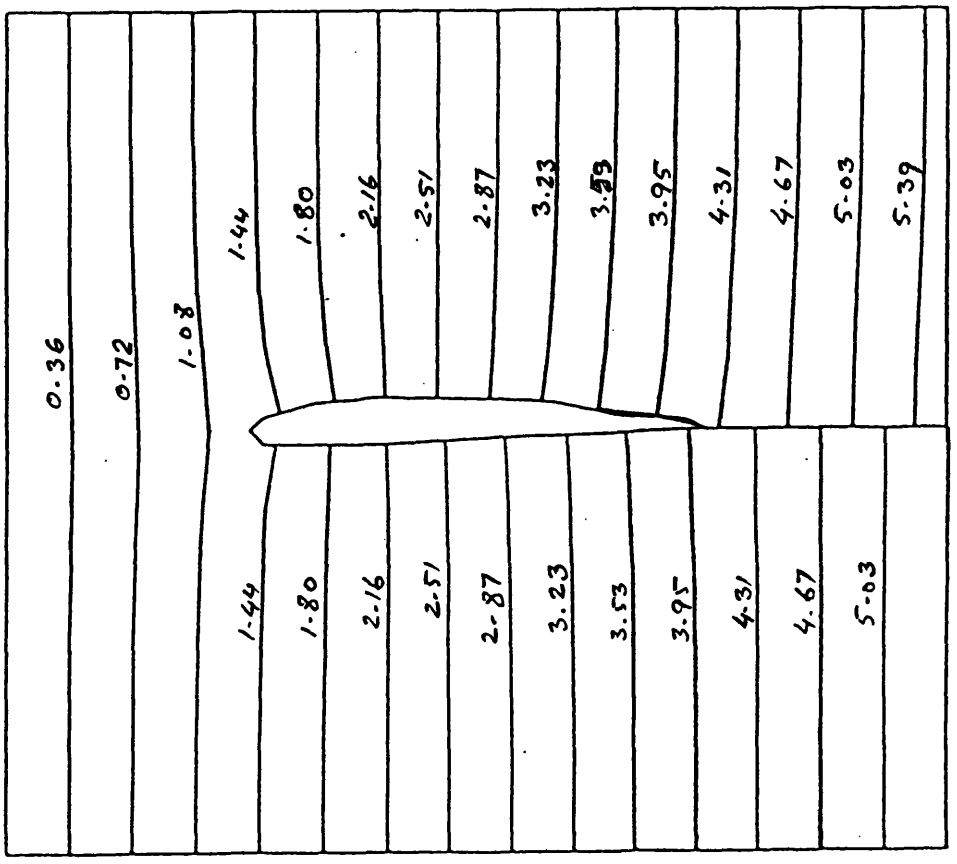

FIG 5.8 PRESSURE DISTRIBUTION ON THE AEROFOIL SURFACES

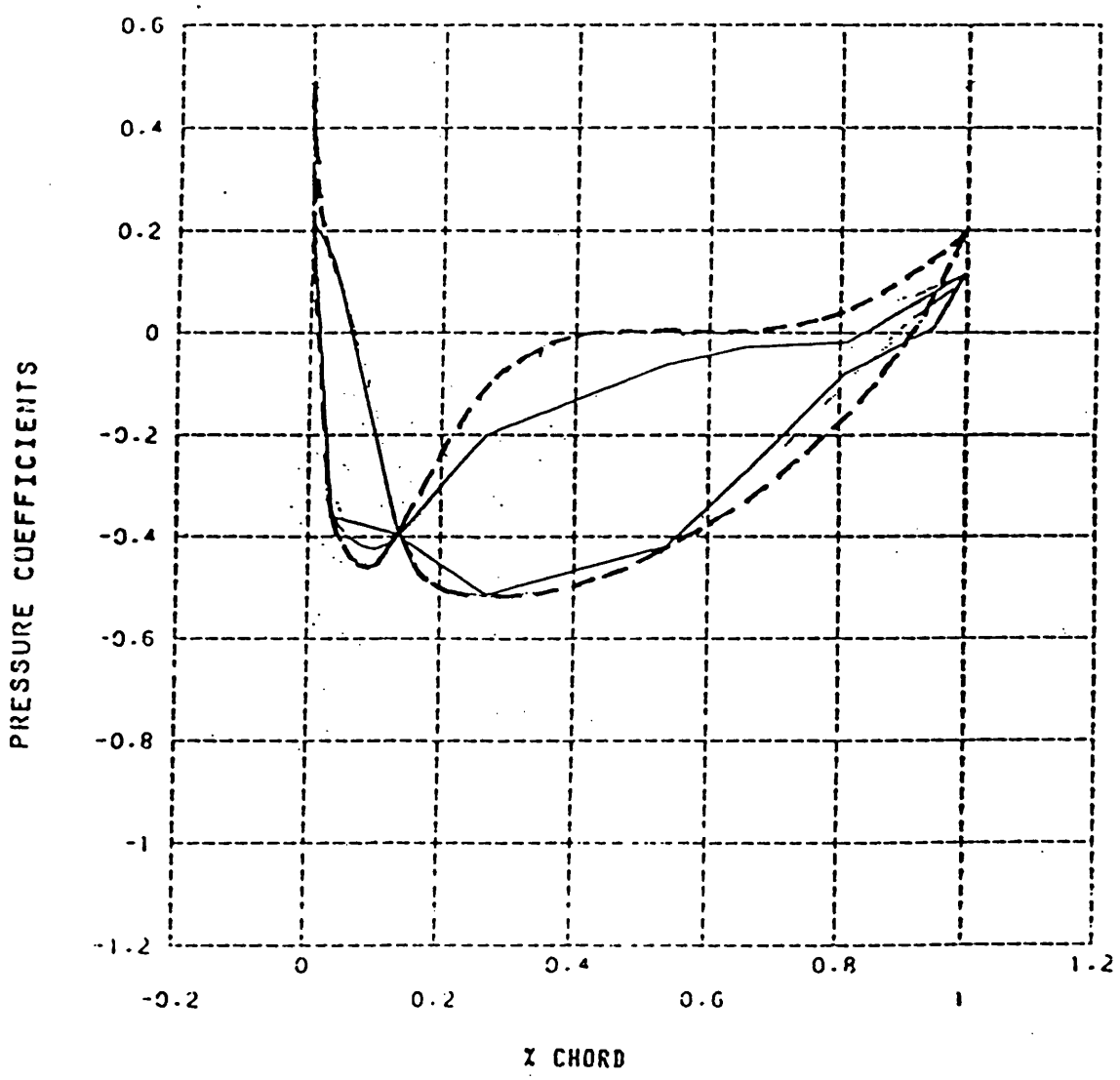

——————— PRESENT ANALYSIS

— — — — — — RESULTS OF REFERENCE [57]

FIG 5.9a TYPICAL MESH GENERATED IN THE VOLUTE NOZZLE ASSEMBLY ANALYSIS

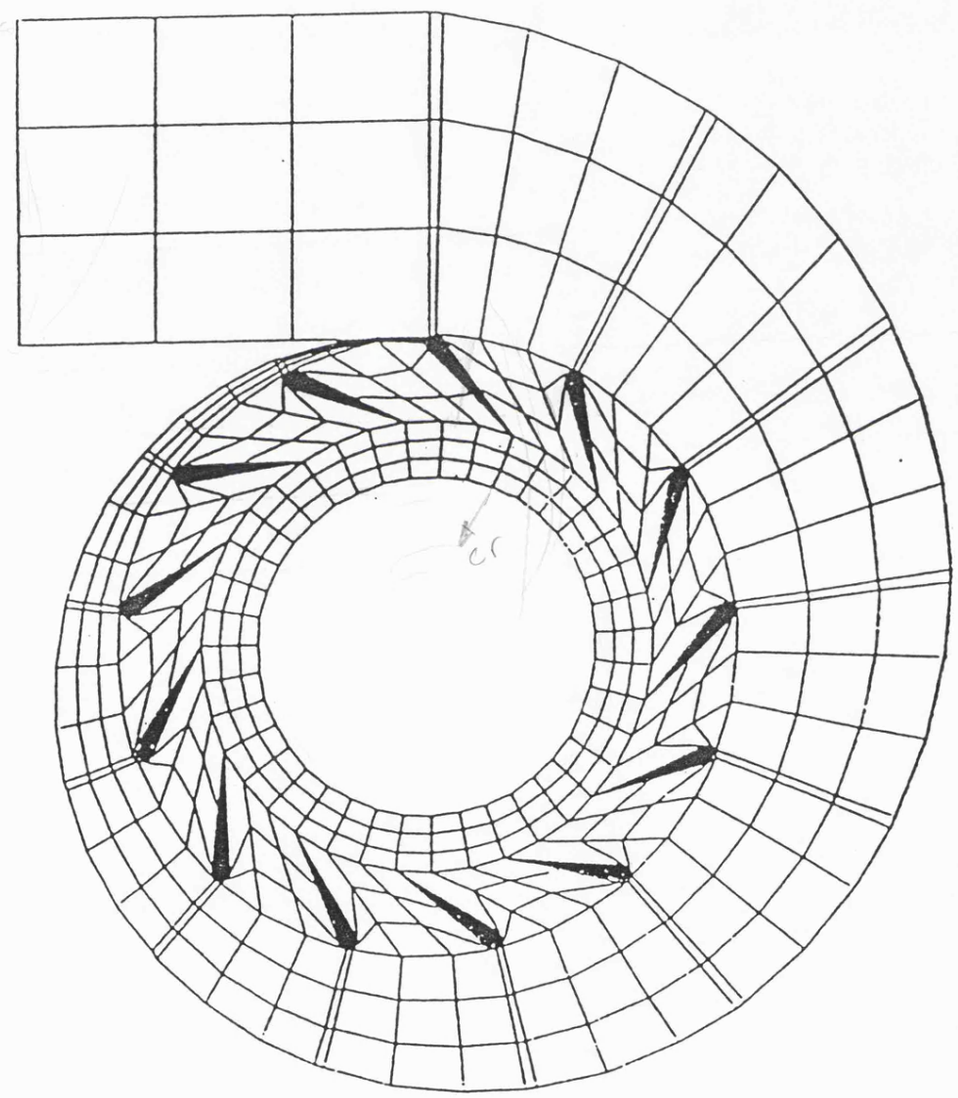

FIG 5.9b FINE MESH FOR THE VOLUTE NOZZLE ASSEMBLY ANALYSIS

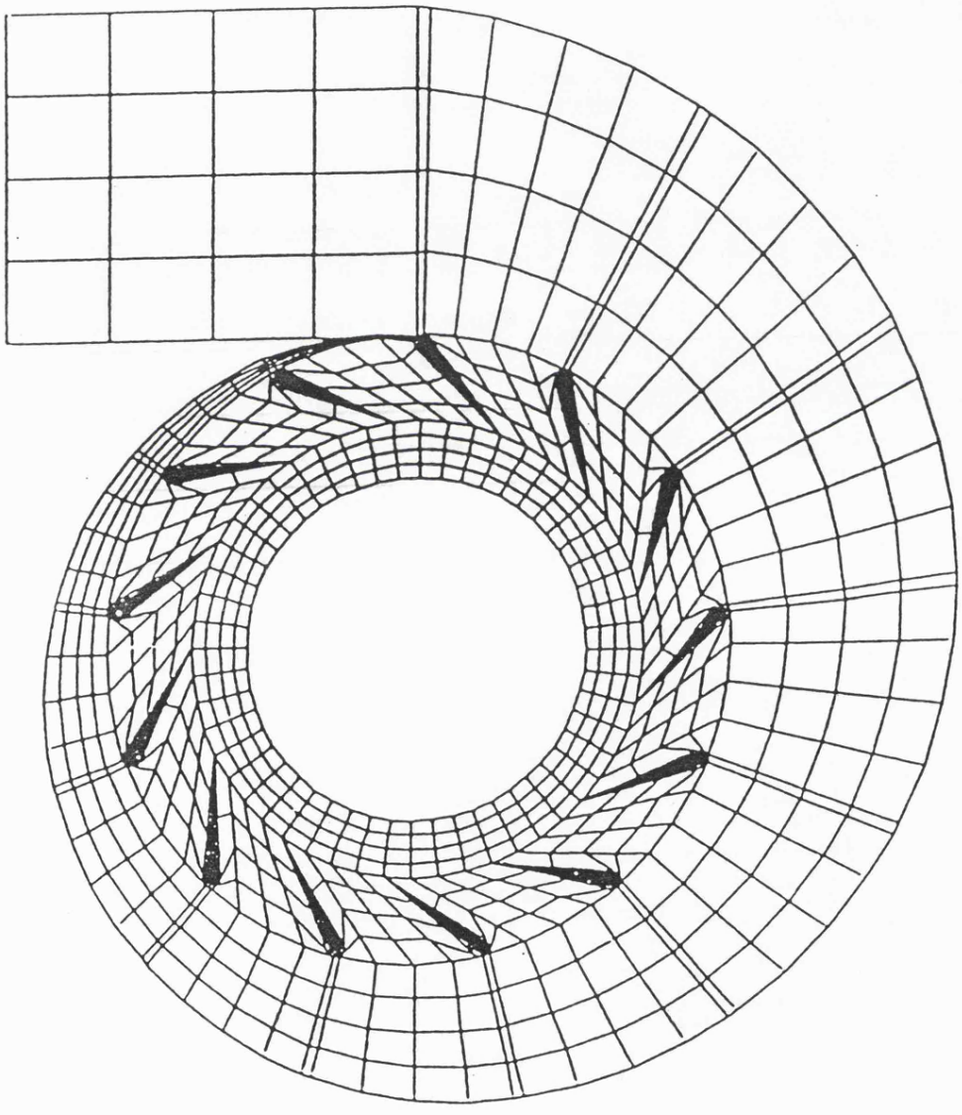

FIG 5.9c FINE MESH SIZE FOR THE VOLUTE NOZLE ASSEMBLY ANALYSIS

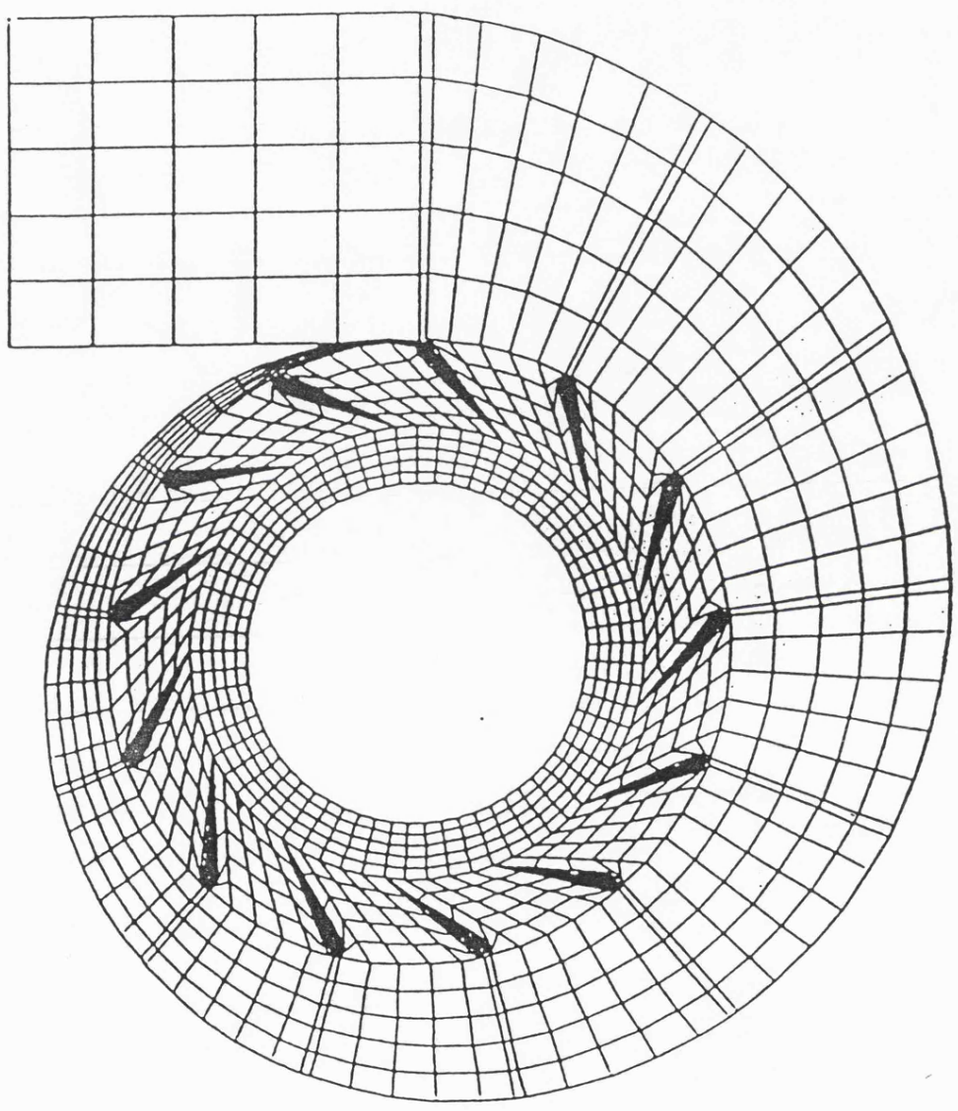

FIG 5.10 POTENTIAL FUNCTION CONTOURS FOR THE VOLUTE NOZZLE ASSEMBLY ANALYSIS

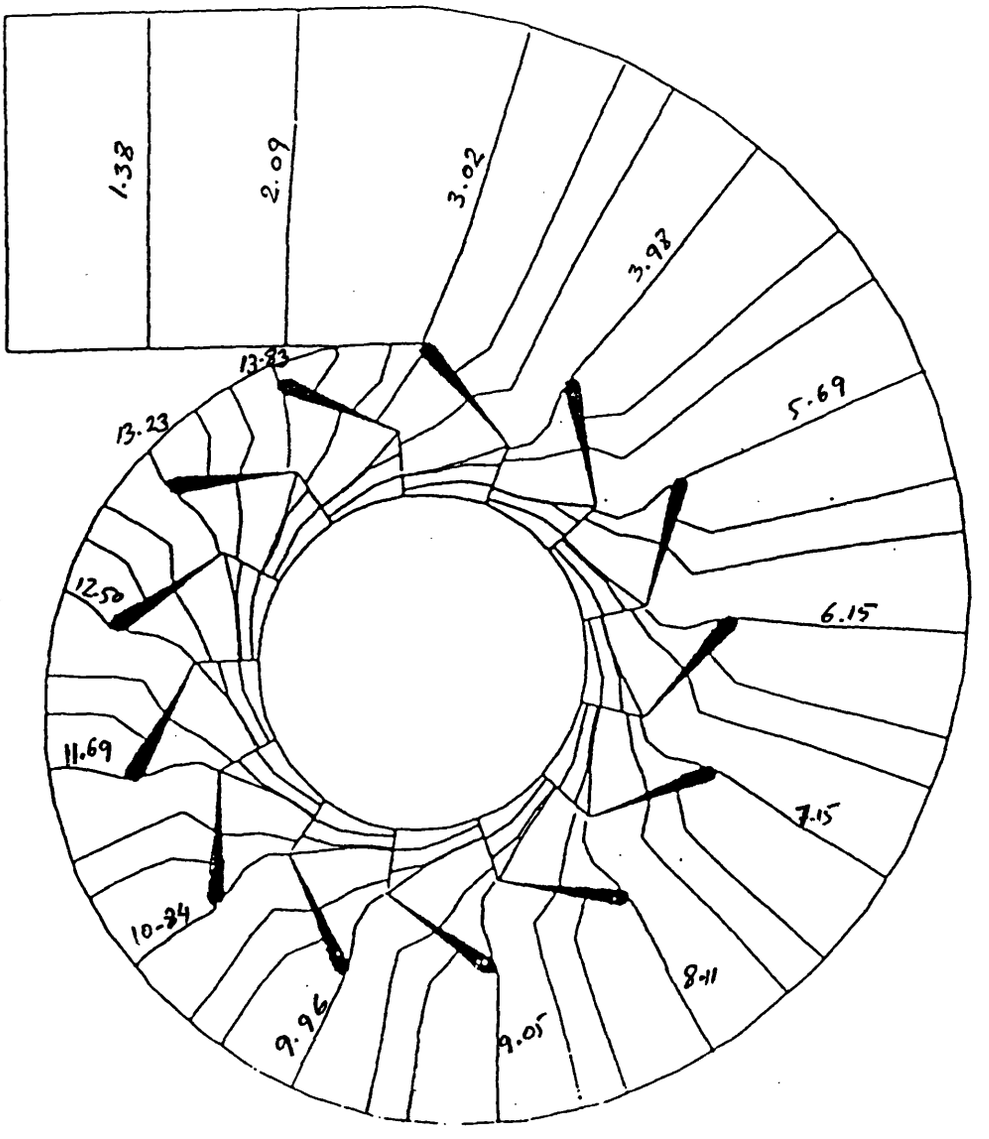

FIG 5.11a PRESSURE DISTRIBUTION ON THE NOZZLE BLADE SURFACES (AZIMUTH ANGLE-90 DEG.)

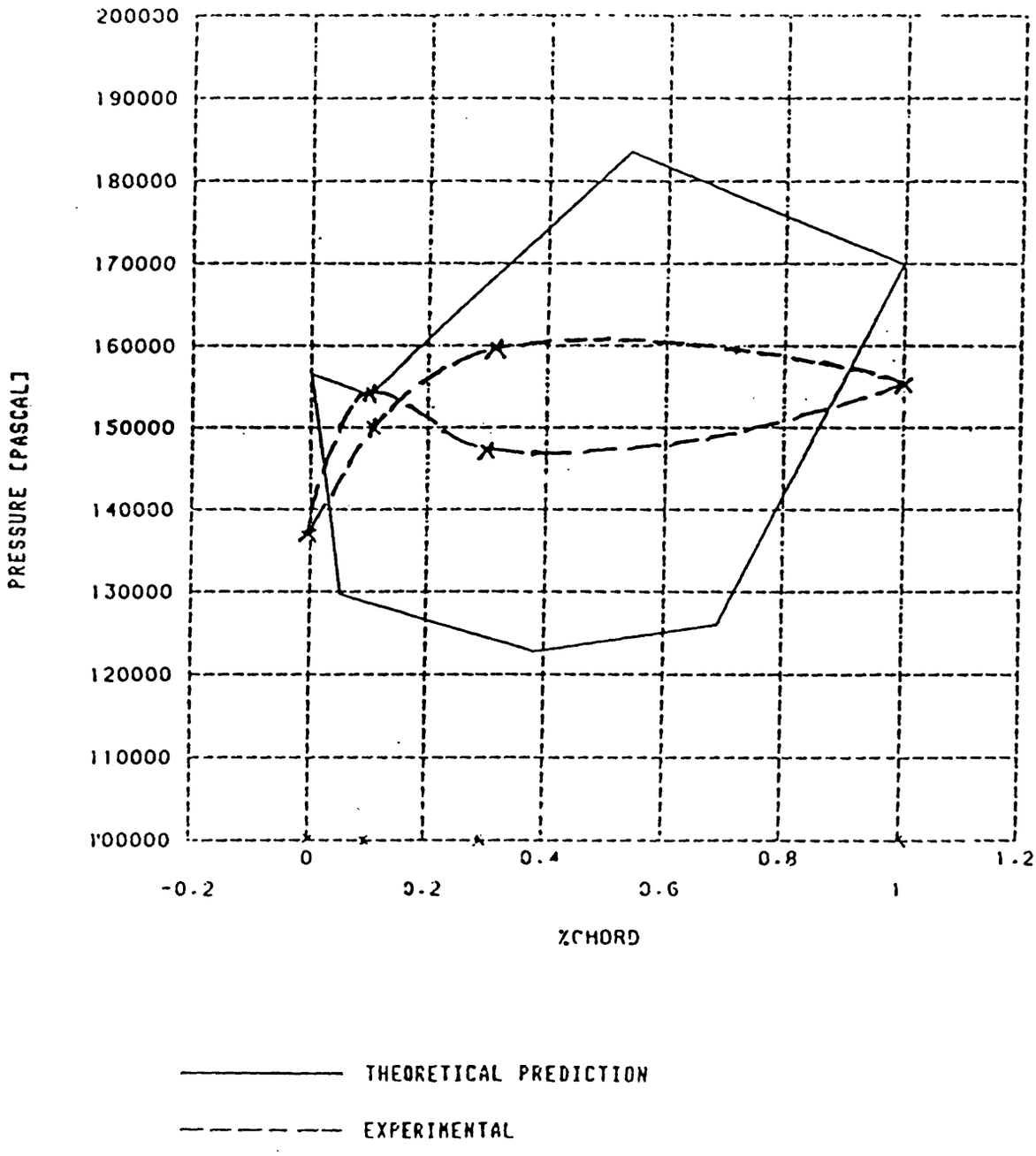

FIG 5.11b PRESSURE DISTRIBUTION ON THE NOZZLE BLADE SURFACES (AZIMUTH ANGLE-225 DEG.)

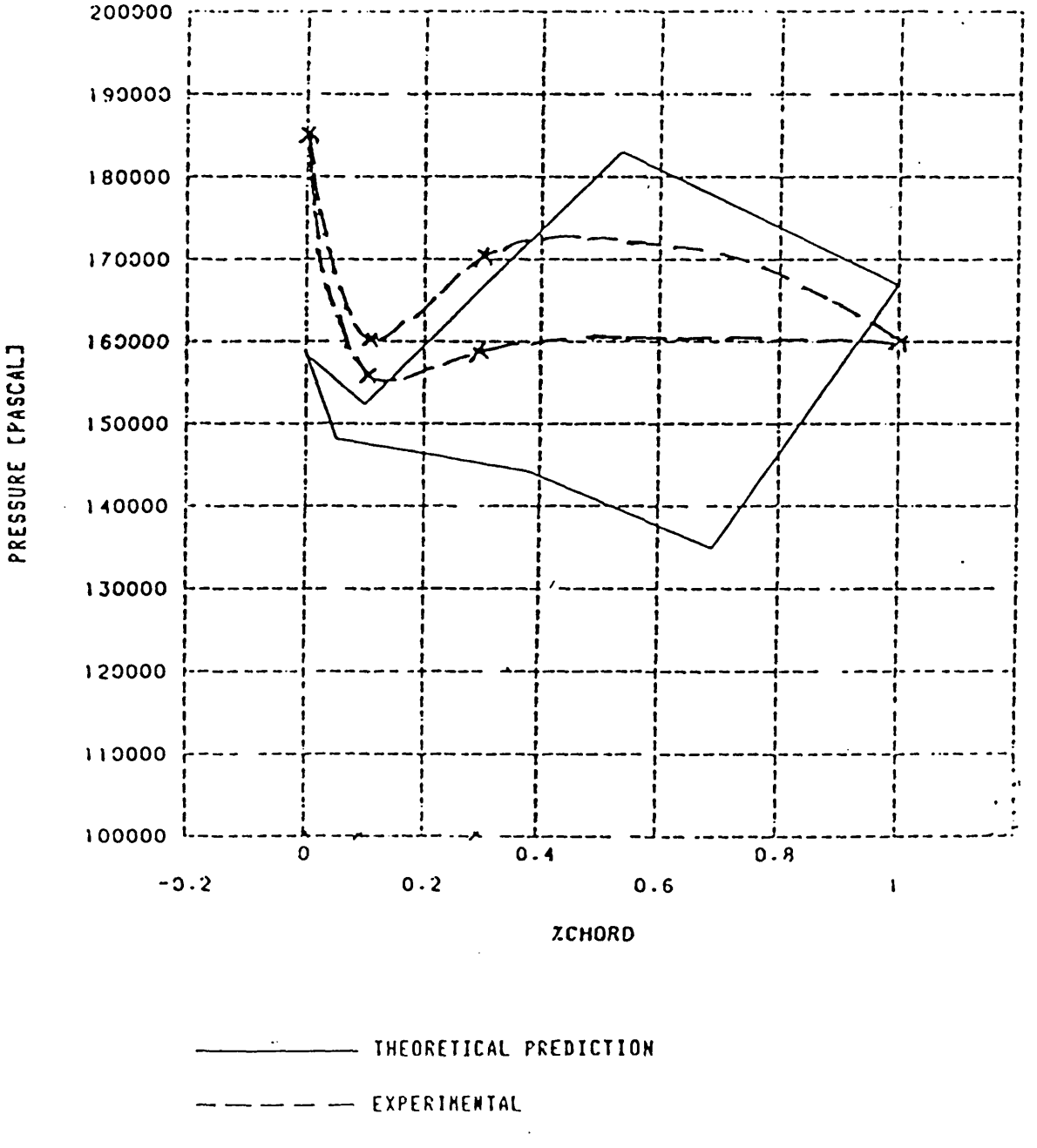

FIG 5.11c PRESSURE DISTRIBUTION ON THE NOZZLE BLADE SURFACES (AZIMUTH ANGLE-340 DEG.)

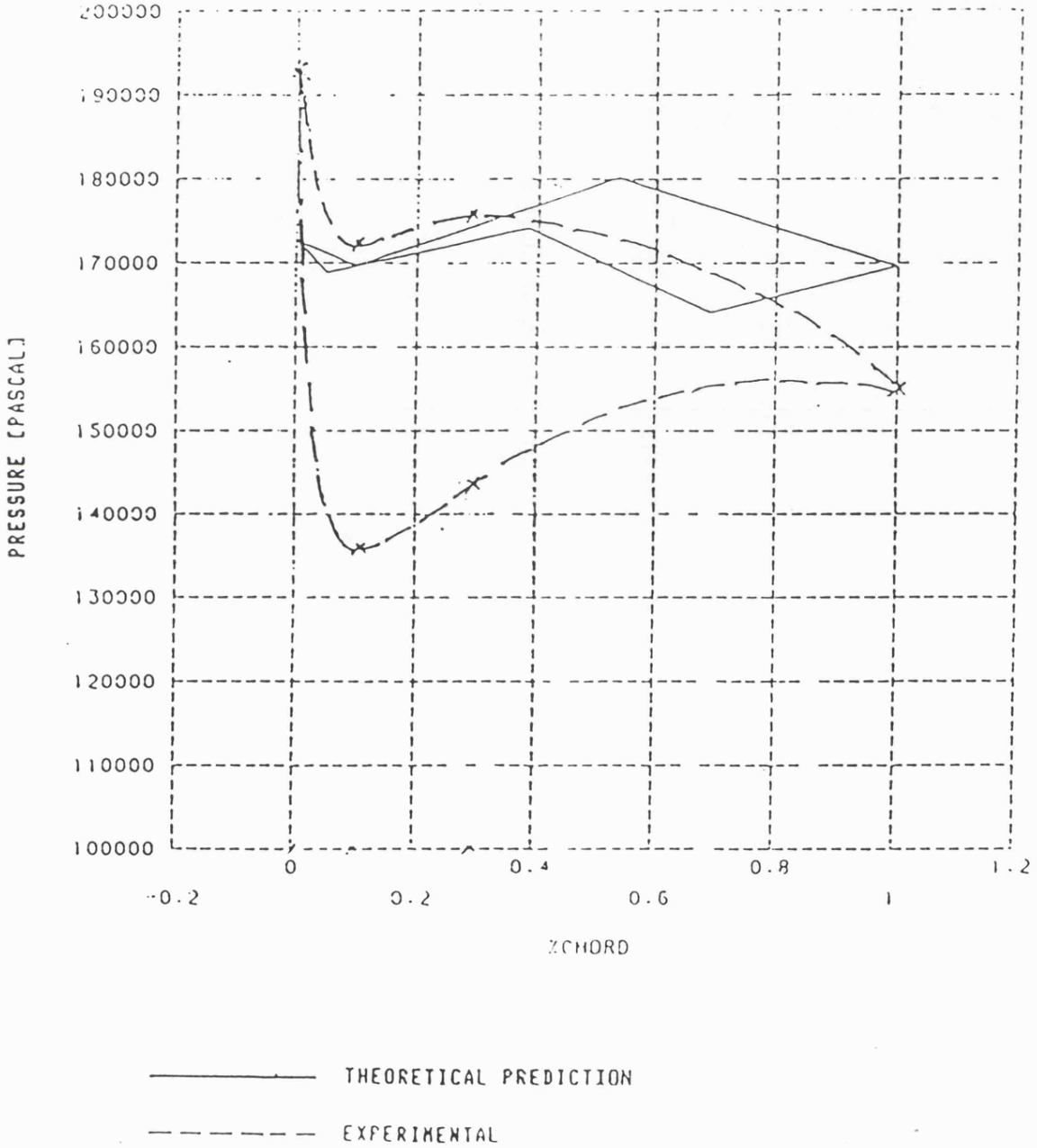

FIG 5.12a FLOW ANGLES AT NOZZLE BLADE INLET

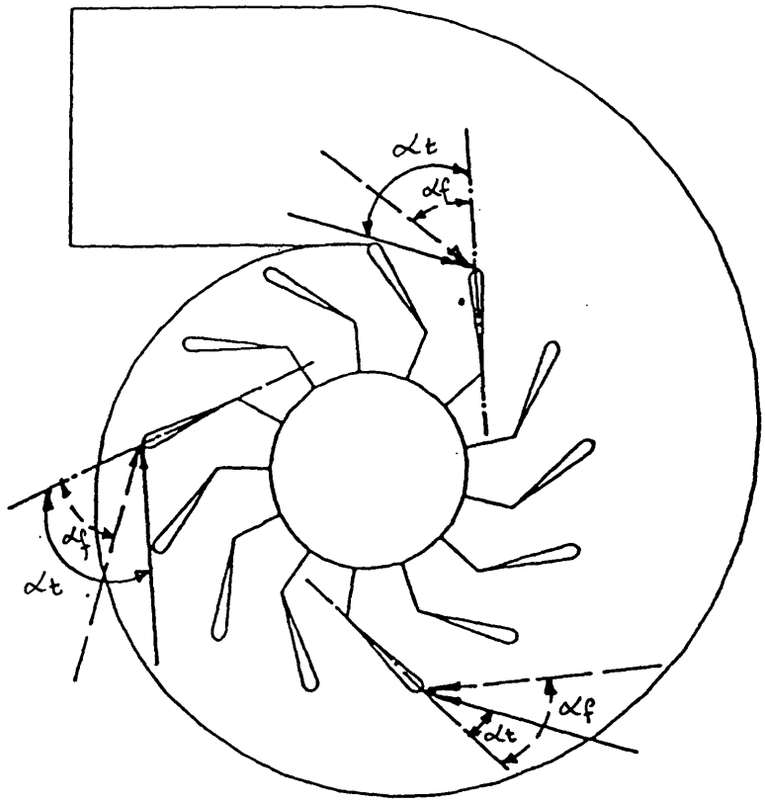

αt ——— THEORETICAL PREDICTION

——— αf ——— FREE VORTEX ASSUMPTIION

FIG 5.12b INLET FLOW ANGLE VARIATION WITH AZIMUTH ANGLE

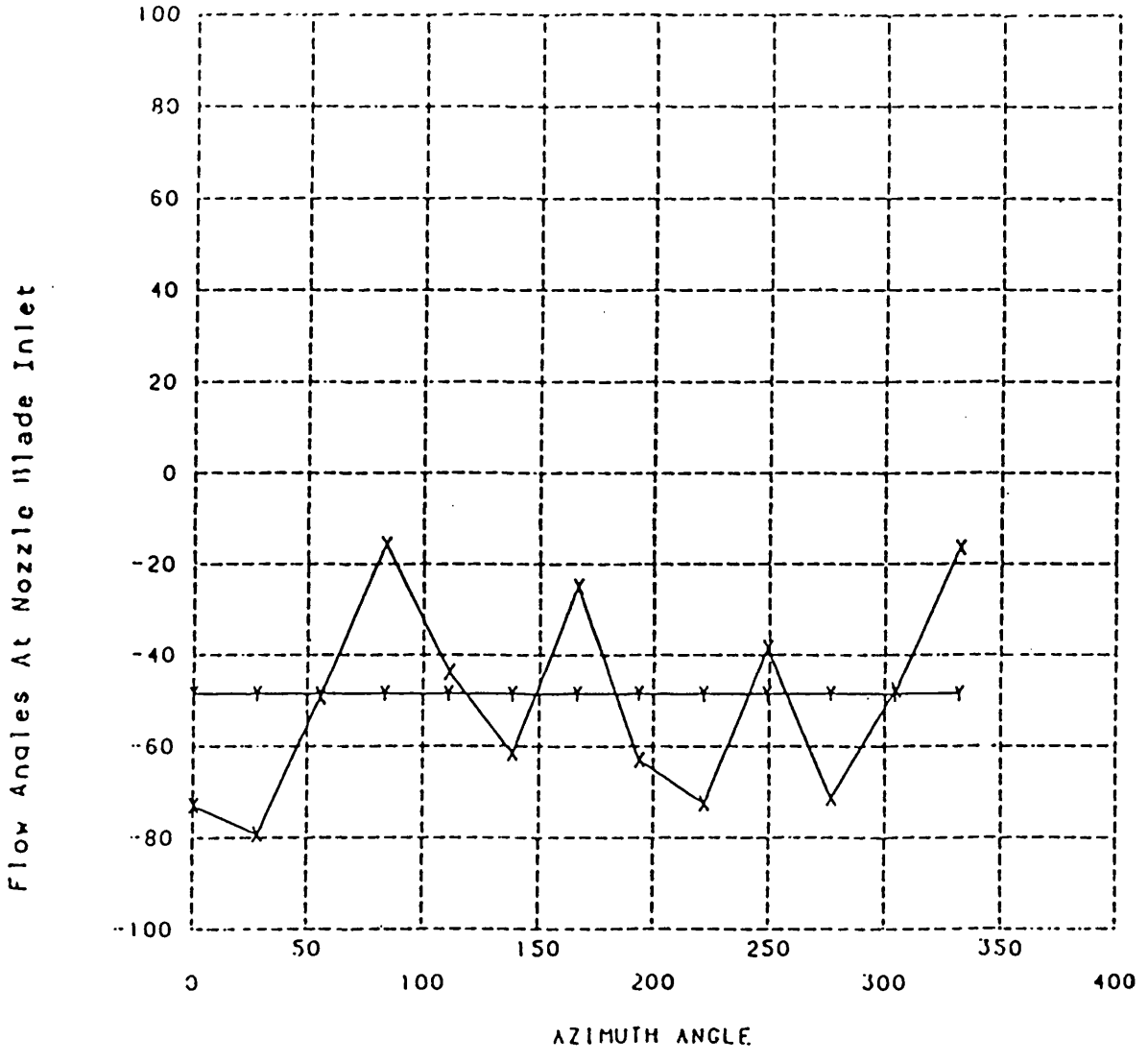

CHAPTER -VI-

---

6. CONCLUSIONS AND SUGGESTIONS FOR FURTHER WORK

6.1 Conclusions

In the theoretical part of this project the finite element method was applied to analyse the flow in the stator and rotor. This proved to be useful as it is easily applicable to any geometrical configurations however irregular, such as the volute-nozzle assembly. The finite element method requirement is such that the boundary conditions should be specified and these are derived as Dirichlet, Neuman or mixed type. The field variables employed are mainly the stream function or the potential function, both of these being easily applied to the finite element method. In comparison to previous streamline curvature analysis of flow in the rotor passage the finite element method is an order of magnitude faster although a detailed comparison of the computer requirements with respect to speed and space has not been carried out.

Experimentally, It can be concluded that the use of the restricted nozzle in the turbine gives a reduction in the performance parameters such as the non-dimensional mass flow and torque, whilst the efficiency is only slightly reduced except with the 20% restricted nozzle where an

increase in efficiency was noticed. The mass flow rate was choked at a pressure ratio of approximately 2.5.

From the pressure measurements on the nozzle blade surfaces it was observed that the blades are subject to non-uniform loadings with respect to the azimuth angle and this was accentuated with high restrictions i.e. 50% nozzle restriction.

From the calculated internal flow parameters in the nozzle exit - rotor inlet interspace, it was concluded that with the 20% nozzle restriction the rotor incidence and exit flow angles were minimum, and high turbine efficiencies resulted. However, with the 50% nozzle restriction zero rotor incidence and zero exit flow angles were not coincident, and high incidence occured with zero exit swirl. With zero restriction the matching of zero incidence with zero exit swirl was not as good as that obtained with the 20% restriction nozzle ring.

By introducing the exit diffuser; the efficiency was only slightly affected in general, and a slight increase was observed with the 16 deg. diffuser at high rotational speeds. No other major effect was apparent as a result of introducing the diffuser downstream of the turbine.

CHAPTER -VI-

The swirl at rotor exit has a generally positive effect upon the diffuser pressure recovery coefficient; optimally with moderate swirl, approximately 12%, with a diffuser angle of 29 deg. and with area ratio of 2.82. Without swirl poor performance would be expected as the diffuser design would fall in a stalled region.

6.2 Suggestions For Further Work

Theoretical Analysis

In the stator flow analysis the Kutta-Joukovski condition at the blade trailing edge has to be applied. In this investigation an infinitesimal width of splitting boundary was introduced extending radially from each trailing edge to the exit boundary. The difference in potential function on either side was considered equal to the circulation which was introduced in the solution as a nodeless variable. However, associated with this strategy (see flow chart, fig. 5.5) the elementary matrices should be recalculated once the circulation has been obtained from the first iteration ; this has not been done as the initial matrices were considered satisfactory to save computational time. The validity of this approximation needs further investigation. The finite element used in the calculations was four-noded, straight-sided

quadrilateral; a curved element could be applied which would improve the accuracy of the geometric description and the predicted results.

For the rotor, the flow analysis was restricted to the mid stream surface in the meridional plane, further development to include a blade-to-blade solution is the next step necessary for the development of a full three dimensional analysis.

The survey of losses at rotor exit could be used further to derive a total loss coefficients for the turbine. These experimentally based loss coefficients could be reintroduced in to both the one-dimensional analysis and any further development of the two- and three-dimensional procedures.

Experimental Procedure

All the experimental work was carried out on the turbine dynamometer rig which is designed mainly for the measurements of overall turbine characteristics. However, the rig was extended to accommodate the use of a diffuser downstream of the turbine and detailed nozzle measurements. Many problems arose during this adaptation such as the icing of particles in the flow at high pressure ratios which prevented proper measurements. When

the hot running procedure was used the heat resulted in an expansion which could have damaged the turbine wheel during the early stages. These difficulties were overcome by replacing the combustion chamber with an electric heater and allowing the diffuser flow to discharge directly to the atmosphere. This design could be improved by connecting the diffuser exit to the laboratory exhaust system in such a way as to prevent stresses on the rig and absorb any expansion at high loads and temperatures. Turbine operation at high temperatures would then be possible.

The sensitivity of the control of the turbine speed needs to be improved. This could be achieved by replacing the control valve on the main supply line by a better design with double acting piston, as this could eliminate the fluctuating pressure signal particularly at low pressure ratios.

The torque measurements were taken by a load cell, this had to be adjusted and recalibrated every time the pressure ratio changed because of the high hysteresis associated with it. This should be replaced by a better designed load cell for more accurate and easy measurements.

CHAPTER -VI-

The restricted nozzles used introduced a sudden contraction followed by a sudden enlargement. This clearly led to increased losses. These losses could be reduced at the expense of broad variable geometry by introducing thicker profiled blades over the initial design in order to increase the restriction. It ought to be possible to design for the addition of two further thickness of blade in a telescopic manner; no thought, however, has been given to the practical aspects of this suggestion.

The narrow passages in the nozzle exit-rotor inlet interspace and the space limitation at nozzle blades trailing edge made it difficult to take any experimental measurements in these places. Detailed velocity measurements can be evaluated by using a laser anemometery techniques in these places.

All diffuser tests were based on three conical diffusers of area ratio of 2.82. This could be extended to cover a wider range of geometrical configurations including an annular diffuser ; as this could be superior to the conical diffusers in the presence of the central wake at rotor exit.

APPENDIX -A-

DERIVATION OF GALERKIN EQUATION FOR QUADRILATERAL ELEMENT IN ISOPARAMETRIC COORDINATES

For a quadrilateral element, as shown in figure A.1, the isoparametric coordinates ξ , η , whose values range from 0 to ± 1 are established at the centroid of the element. By considering a polynomial expansion as the approximation for a variable; the reference coordinates x, r, and the dependent field variable are related to the local coordinates as

$$\begin{aligned} x &= \frac{1}{4}(a_1 + a_2\xi + a_3\eta + a_4\xi\eta) \\ r &= \frac{1}{4}(b_1 + b_2\xi + b_3\eta + b_4\xi\eta) \\ \psi &= \frac{1}{4}(c_1 + c_2\xi + c_3\eta + c_4\xi\eta) \end{aligned} \qquad \text{A.1}$$

To evaluate the constants a,b,c four equations in terms of the unknown values of the variable at each node are needed. Applying the stream function at nodes obtain

$$\begin{aligned} \psi_1 &= \frac{1}{4}(c_1 + c_2\xi_1 + c_3\eta_1 + c_4\xi_1\eta_1) \\ \psi_2 &= \frac{1}{4}(c_1 + c_2\xi_2 + c_3\eta_2 + c_4\xi_2\eta_2) \\ \psi_3 &= \frac{1}{4}(c_1 + c_2\xi_3 + c_3\eta_3 + c_4\xi_3\eta_3) \\ \psi_4 &= \frac{1}{4}(c_1 + c_2\xi_4 + c_3\eta_4 + c_4\xi_4\eta_4) \end{aligned} \qquad \text{A.2}$$

Solving for the unknowns c1,c2,c3,c4 yields

$$\begin{aligned} c_1 &= +\psi_1 + \psi_2 + \psi_3 + \psi_4 \\ c_2 &= -\psi_1 - \psi_2 + \psi_3 + \psi_4 \\ c_3 &= +\psi_1 - \psi_2 - \psi_3 + \psi_4 \\ c_4 &= -\psi_1 + \psi_2 - \psi_3 + \psi_4 \end{aligned} \qquad \text{A.3}$$

APPENDIX -A-

Introducing equation A.3 into the last equation of A.1 yields

$$\Psi = \frac{1}{4}\left[(1-\xi+\eta-\xi\eta)\,\Psi_1 + (1-\xi-\eta+\xi\eta)\,\Psi_2 + (1+\xi-\eta-\xi\eta)\,\Psi_3 + (1+\xi+\eta+\xi\eta)\,\Psi_4\right] \qquad \text{A.4}$$

The interpolation function is only dependent on the local coordinates and is

$$N_i = \frac{1}{4}\sum (1+\xi_i\xi)(1+\eta_i\eta) \qquad \text{A.5}$$

The local coordinates and the interpolation function are related to the original coordinates as

$$\xi = \xi(x,r)$$
$$\eta = \eta(x,r) \qquad \text{A.6}$$

$$N_i = F\left[\xi(x,r),\ \eta(x,r)\right] \qquad \text{A.7}$$

By differentiation equation A.7 with respect to the local coordinates gives

$$\frac{\partial N_i}{\partial \xi} = \frac{\partial N_i}{\partial x}\frac{\partial x}{\partial \xi} + \frac{\partial N_i}{\partial r}\frac{\partial r}{\partial \xi}$$

$$\frac{\partial N_i}{\partial \eta} = \frac{\partial N_i}{\partial x}\frac{\partial x}{\partial \eta} + \frac{\partial N_i}{\partial r}\frac{\partial r}{\partial \eta} \qquad \text{A.8}$$

APPENDIX -A-

Solving for the unknowns $\frac{\partial N_i}{\partial x}, \frac{\partial N_i}{\partial r}$

$$\begin{bmatrix} \frac{\partial x}{\partial \xi} & \frac{\partial r}{\partial \xi} \\ \frac{\partial x}{\partial \eta} & \frac{\partial r}{\partial \eta} \end{bmatrix} \times \begin{bmatrix} \frac{\partial N_i}{\partial x} \\ \frac{\partial N_i}{\partial r} \end{bmatrix} = \begin{bmatrix} \frac{\partial N_i}{\partial \xi} \\ \frac{\partial N_i}{\partial \eta} \end{bmatrix} \qquad \text{A.9}$$

The Jacobian determinant takes the form of

$$J = \frac{\partial x}{\partial \xi}\frac{\partial r}{\partial \eta} - \frac{\partial r}{\partial \xi}\frac{\partial x}{\partial \eta} \qquad \text{A.10}$$

Hence,

$$\frac{\partial N_i}{\partial x} = \frac{1}{J}\left(\frac{\partial N_i}{\partial \xi}\frac{\partial r}{\partial \eta} - \frac{\partial N_i}{\partial \eta}\frac{\partial r}{\partial \xi}\right)$$

$$\frac{\partial N_i}{\partial r} = \frac{1}{J}\left(\frac{\partial N_i}{\partial \eta}\frac{\partial x}{\partial \xi} - \frac{\partial N_i}{\partial \xi}\frac{\partial x}{\partial \eta}\right) \qquad \text{A.11}$$

By differentiating the first two equations of A.1 and A.5 with respect to ξ and η yields

$$\frac{\partial N_i}{\partial \eta} = \frac{1}{4}\left(\eta_i + \xi_i \eta_i \xi\right) \qquad \frac{\partial N}{\partial \xi} = \frac{1}{4}\left(\xi - \xi_i \eta_i \eta\right)$$

$$\frac{\partial x}{\partial \xi} = \frac{1}{4}\left(a_2 + a_4 \eta\right) \qquad \frac{\partial x}{\partial \eta} = \frac{1}{4}\left(a_3 - a_4 \xi\right) \qquad \text{A.12}$$

$$\frac{\partial r}{\partial \xi} = \frac{1}{4}\left(b_2 + b_4 \eta\right) \qquad \frac{\partial r}{\partial \eta} = \frac{1}{4}\left(b_3 - b_4 \xi\right)$$

APPENDIX -A-

And the following operators for the interpolation function can be deduced

$$\frac{\partial}{\partial x}=\frac{1}{4J}\left[\left(b_3+b_4\xi\right)\frac{\partial}{\partial \xi}-\left(b_2+b_4\eta\right)\frac{\partial}{\partial \eta}\right]$$
$$\frac{\partial}{\partial r}=\frac{1}{4J}\left[\left(a_2+a_4\eta\right)\frac{\partial}{\partial \eta}-\left(a_3+a_4\xi\right)\frac{\partial}{\partial \xi}\right] \qquad \text{A.13}$$

Which gives for Ni

$$\frac{\partial N_i}{\partial x}=\frac{1}{16J}\left(a_{xi}+b_{xi}\xi+c_{xi}\eta\right)$$
$$\frac{\partial N_i}{\partial r}=\frac{1}{16J}\left(a_{ri}+b_{ri}\xi+c_{xi}\eta\right) \qquad \text{A.14}$$

Where

$$a_{xi}=b_3\xi_i-b_2\eta_i \qquad a_{ri}=a_2\eta_i-a_3\xi_i$$
$$b_{xi}=b_4\xi_i-b_2\xi_i\eta_i \qquad b_{ri}=a_2\xi_i\eta_i-a_4\xi_i \qquad \text{A.15}$$
$$c_{xi}=b_3\xi_i\eta_i-b_4\eta_i \qquad c_{ri}=a_4\eta_i-a_3\xi\eta_i$$

In the same way the weight function takes the form

$$\frac{\partial N_j}{\partial x}=\frac{1}{16J}\left(a_{x_j}+b_{x_j}\xi+c_{x_j}\eta\right) \qquad \text{A.16}$$

$$\frac{\partial N_j}{\partial r}=\frac{1}{16J}\left(a_{r_j}+b_{r_j}\xi+c_{r_j}\eta\right)$$

APPENDIX -A-
---

where

$$a_{xj} = b_3 \xi_j - b_2 \eta_j \qquad a_{rj} = a_2 \eta_j - a_3 \xi_j$$

$$b_{xj} = b_4 \xi_j \eta_j - b_2 \xi_j \eta_j \qquad b_{rj} = a_2 \xi_j \eta_j - a_4 \xi_j \qquad \text{A.17}$$

$$c_{xj} = b_3 \xi_j - b_4 \eta_j \qquad c_{rj} = a_4 \eta_j - a_3 \xi_j \eta_j$$

The product of the interpolation and weight function resulting from the application of the divergence theorem to the Laplace equation leads to

$$\frac{\partial N_i}{\partial x}\frac{\partial N_j}{\partial x} = \left(\frac{1}{16J}\right)^2 \cdot \left[aa_x + bb_x \xi + cc_x \eta + dd_x \xi\eta + ee_x \xi^2 + ff_x \eta^2\right]$$

$$\frac{\partial N_i}{\partial r}\frac{\partial N_j}{\partial r} = \left(\frac{1}{16J}\right)^2 \cdot \left[aa_r + bb_r \xi + cc_r \eta + dd_r \xi\eta + ee_r \xi^2 + ff_r \eta^2\right] \qquad \text{A.18}$$

where

$$\begin{aligned} aa_x &= a_{xi}\, a_{xj} \\ bb_x &= a_{xi}\, b_{xj} + b_{xi}\, a_{xj} \\ cc_x &= a_{xi}\, c_{xj} + c_{xi}\, b_{xj} \\ dd_x &= b_{xi}\, c_{xj} + c_{xi}\, b_{xj} \\ ee_x &= b_{xi}\, b_{xj} \\ ff_x &= c_{xi}\, c_{xj} \end{aligned} \qquad \text{A.19}$$

And

$$\begin{aligned} aa_r &= a_{ri}\, a_{rj} \\ bb_r &= a_{ri}\, b_{rj} + b_{ri}\, a_{rj} \\ cc_r &= a_{ri}\, c_{rj} + c_{ri}\, b_{rj} \\ dd_r &= b_{ri}\, c_{rj} + c_{ri}\, b_{rj} \\ ee_r &= b_{ri}\, b_{rj} \\ ff_r &= c_{ri}\, c_{rj} \end{aligned} \qquad \text{A.20}$$

APPENDIX -A-

The Jacobian determinant is of the form

$$J = \frac{1}{16}\left[(aaa) + (bbb)\xi + (ccc)\eta\right] \qquad \text{A.21}$$

Where

$$\begin{aligned} aaa &= a_2 b_3 - a_3 b_2 \\ bbb &= a_2 b_4 - a_4 b_2 \\ ccc &= a_4 b_3 - a_3 b_4 \end{aligned} \qquad \text{A.22}$$

The integration over the domain referenced the original coordinates is changed to the isoparametric coordinates by

$$\iint b_z \, dx\,dr = \iint a_z |J| \, d\xi\, d\eta \qquad \text{A.23}$$

Where

$$a_z = \left(\frac{1}{16J}\right)^2 \left[a_{xr} + b_{xr}\xi + c_{xr}\eta + d_{xr}\xi\eta + e_{xr}\xi^2 + f_{xr}\eta^2\right]$$

$$\begin{aligned} a_{xr} &= aa_x + aa_r \\ b_{xr} &= bb_x + bb_r \\ c_{xr} &= cc_x + cc_r \\ d_{xr} &= dd_x + dd_r \\ e_{xr} &= ee_x + ee_r \\ f_{xr} &= ff_x + ff_r \end{aligned} \qquad \text{A.24}$$

APPENDIX -A-

After the calculation of the stream function at nodes the velocity for each element was obtained from equations A.4 and A.11 in the following manner

$$V_{xi} = k\frac{\partial \psi}{\partial r} = k\frac{\partial}{\partial r}\left[N_i \psi_i\right] = k\sum \frac{\partial N_i}{\partial r}\psi_i$$

$$V_{ri} = -k\frac{\partial \psi}{\partial x} = -k\frac{\partial}{\partial x}\left[N_i \psi_i\right] = -k\sum \frac{\partial N_i}{\partial x}\psi_i \qquad \text{A.25}$$

And an averaged velocity for each element was considered at the centroid

$$V_i = \sqrt{V_{xi}^2 + V_{ri}^2} \qquad \text{A.26}$$

$$V = \frac{1}{4}\sum_{i=1}^{4} V_i \qquad \text{A.27}$$

In the same way the velocity was derived when the potential function was used as the field variable.

FIG A.1 ISOPARAMETRIC ELEMENT FOR THE MERIDIONAL FLOW ANALYSIS

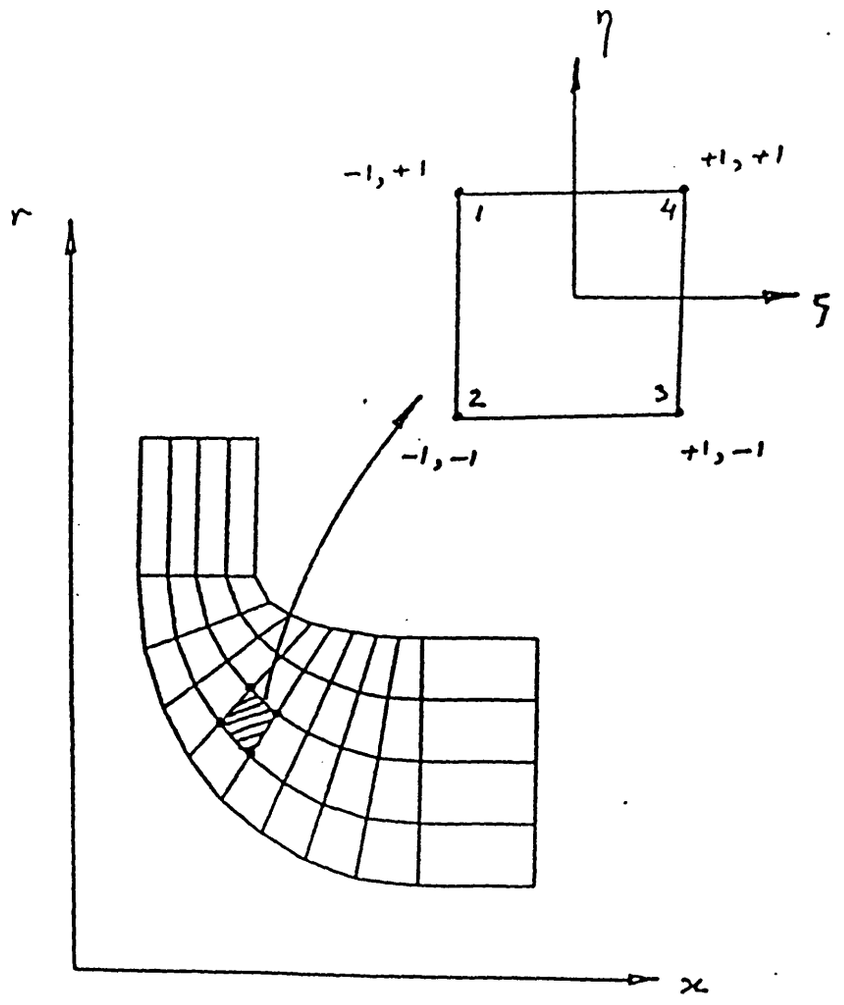

APPENDIX -B-

DERIVATION OF THE GALERKIN EQUATION FOR THE MERIDIONAL FLOW ANALYSIS

The flow equations have been derived previously, they take one of the following forms depending upon whether the predominant velocity is the radial or axial component

$$\frac{\partial}{\partial r}\left(k\frac{\partial \Psi}{\partial r}\right)+\frac{\partial}{\partial x}\left(k\frac{\partial \Psi}{\partial x}\right)=-F_r \qquad W_r \gg W_x$$

$$\frac{\partial}{\partial r}\left(k\frac{\partial \Psi}{\partial r}\right)+\frac{\partial}{\partial x}\left(k\frac{\partial \Psi}{\partial x}\right)=-F_x \qquad W_x \gg W_r \qquad \text{B.1}$$

Where, see figure B.1,

Fr :- is for region I

Fx :- is for region II

$$k=\frac{1}{\rho r b}$$

The tangential component of the absolute velocity is

$$C_\theta = W_\theta + \Omega r = \frac{W_\theta}{W_x} W_x + \Omega r =$$

$$= W_x \tan\phi + \Omega r = C_d r W_x + \Omega r \qquad \text{B.2}$$

And then

$$F_r = -\frac{W_\theta}{W_x}\frac{1}{r}\frac{\partial}{\partial r}(rC_\theta) =$$

$$= -C_{d1}^2\frac{\partial}{\partial r}\left(r^2 W_x\right) + 2\Omega r C_{d1} \qquad \text{B.3}$$

APPENDIX -B-

$$F_x = -\frac{W_\theta}{W_x}\frac{1}{r}\frac{\partial}{\partial x}(r C_\theta) =$$

$$= -\frac{C_{d_2}^{(2)}}{\tan\alpha}\frac{\partial}{\partial x}(r^2 W_x) \qquad \text{B.4}$$

Equations B.1 are both of the Poisson type

$$\frac{\partial}{\partial r}\left(k\frac{\partial \Psi}{\partial r}\right) + \frac{\partial}{\partial x}\left(k\frac{\partial \Psi}{\partial x}\right) + F = 0 \qquad \text{B.5}$$

By substituting for the variable Ψ by an approximate value $\tilde{\Psi}$, an error, or residual ϵ results

$$\frac{\partial}{\partial r}\left(k\frac{\partial \tilde{\Psi}}{\partial r}\right) + \frac{\partial}{\partial x}\left(k\frac{\partial \tilde{\Psi}}{\partial x}\right) + F = \varepsilon \qquad \text{B.6}$$

The orthogonal projection of this residual is forced to be zero over the domain of integration, therefore

$$\int \varepsilon \cdot N_j \, dV = 0 \qquad \text{B.7}$$

Where weight function is taken as the interpolation function itself; equation B.7 is written as

$$\iint \frac{\partial}{\partial r}\left(k\frac{\partial \Psi}{\partial r}\right) N_j \, dV + \iint \frac{\partial}{\partial x}\left(k\frac{\partial \Psi}{\partial x}\right) N_j \, dV + \iint F N_j \, dV = 0 \qquad \text{B.8}$$

APPENDIX -B-
---

where dv represent the volume element

Integrating equation B.8 by parts yields

$$\iint k\left(\frac{\partial \Psi}{\partial r}\frac{\partial N_j}{\partial r} + \frac{\partial \Psi}{\partial x}\frac{\partial N_j}{\partial x}\right) dr\,dx + \iint F N_j\, dr\,dx = \int k \frac{\partial \Psi}{\partial n} ds \qquad \text{B.9}$$

Substituting $\Psi = \sum N_i \Psi_i$

yields

$$\left[\iint k\left(\frac{\partial N_i}{\partial r}\frac{\partial N_j}{\partial r} + \frac{\partial N_i}{\partial x}\frac{\partial N_j}{\partial x}\right) dr\,dx\right] \Psi_i = \int k \frac{\partial \Psi}{\partial n} ds - \iint F N_j\, dr\,dx \qquad \text{B.10}$$

Which is the Galerkin equation to be solved.

The input vector : hj = $\int$ F.Nj.dr.dx is mainly dependent on the predominant relative velocity. When the radial velocity is the dominant component F = Fr, and if the axial component is predominant then : F = Fx

The Galerkin equation for one element is written as

$$\left[\iint k\left(\frac{\partial N_i}{\partial r}\frac{\partial N_j}{\partial r} + \frac{\partial N_i}{\partial x}\frac{\partial N_j}{\partial x}\right) dr\,dx\right]^e \Psi_i^e = \int k \frac{\partial \Psi^e}{\partial n} ds - \iint F N_j\, dr\,dx \qquad \text{B.11}$$

APPENDIX -B-

The RHS in the input vector is written in local coordinates as

$$h_j = F\iint N_j \left| J \right| d\xi\, d\eta \qquad \text{B.12}$$

The product of the interpolation function Nj and the Jacobian determinant as they are derived in appendix "A" is

$$\left[N_j J \right] = f_1 + f_2 \xi + f_3 \eta + f_4 \xi^2 + f_5 \eta^2 + f_6 \xi\eta + f_7 \xi^2\eta + f_8 \xi\eta^2 \qquad \text{B.13}$$

Where

$$f_1 = aaa \qquad f_5 = ccc\,\eta_j$$

$$f_2 = aaa\,\xi_i + bbb \qquad f_6 = aaa\,\xi_i\eta_i + bbb\,\eta_j + ccc\,\xi_j$$

$$f_3 = aaa\,\eta_i + ccc \qquad f_7 = bbb\,\xi_j\eta_j \qquad \text{B.14}$$

$$f_4 = bbb\,\xi_j \qquad f_8 = ccc\,\xi_j\eta_j$$

And the input vector can be computed as

$$h_j = F\iint \left[N_j J \right] d\xi\, d\eta =$$

$$= \frac{6}{64} F\left(f_1 + \frac{1}{3} f_4 + \frac{1}{3} f_3 \right) \qquad \text{B.15}$$

FIG B.1 MERIDIONAL PLAN VELOCITIES AND FLOW ANGLES

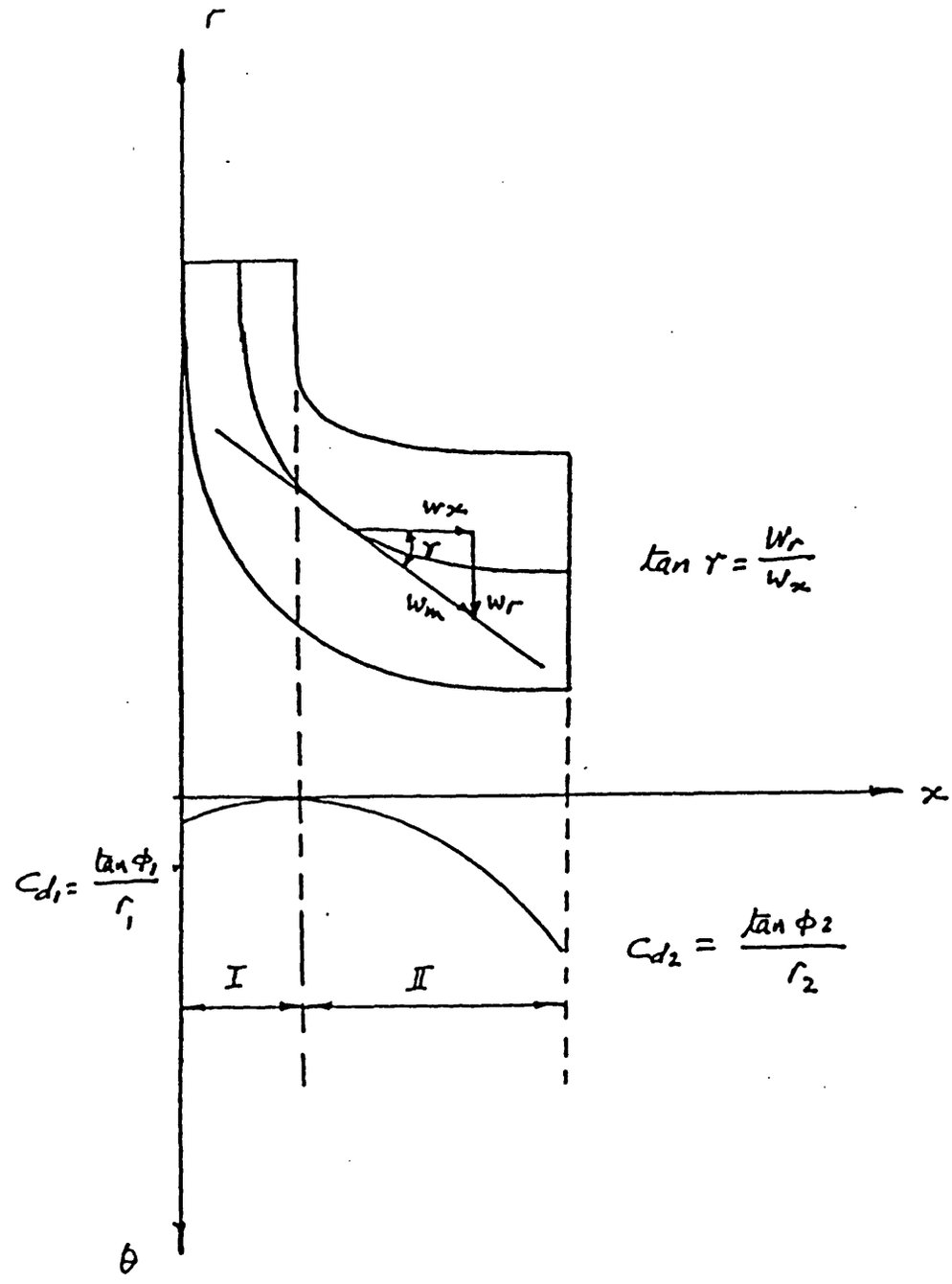

APPENDIX -C-

ASSEMBLING THE GLOBAL MATRIX

This has been done by nodes, Which has the advantage of transforming the large sparse matrix into a dense one. It also leads to a considerable space saving and excludes the need of the core storage during the computations.

After creating the elementary matrices,see fig. C.1, they are transformed into a one dimensional array and then the assembly is performed in the following sequence

(1) Specify the node for which the equation is to be assembled

(2) Find the number of elements associated with this node

(3) Find the local node number that coincides with the global node number

(4) Find the local matrix row that coresponds to the local node number

(5) Add the contribution of all elements to the node chosen and find the column identification for each element of the final equation.

For example, from figure C.1, two nodes have been chosen to illustrate this strategy

---
APPENDIX -C-

Node No. 2

Corresponding elements	a	b
Local Nodes	2	1

Local matrice's row

a_5	a_6	a_7	a_8	b_1	b_2	b_3	b_4

Global row

1	2	5	4	2	3	6	5

Final equation

1	2	3	4	5	6
a_5	a_6+b_1	b_2	a_8	a_7+b_4	b_3

Node No. 5

Coresponding Elements	a	b	c	d
Local Nodes	3	4	1	2

Local matrice's row

a_9	a_{10}	b_{13}	b_{14}	c_1	c_2	d_5	d_6
a_{11}	a_{12}	b_{15}	b_{16}	c_3	c_4	d_7	d_8

Global row

1	2	2	3	4	5	5	6
5	4	6	5	8	7	9	8

Final equation

1	2	3	4	5	6	7	8	9
a_9	$a_{10}+b_{13}$	b_{14}	$a_{12}+c_1$	a_4+b_6 c_2+d_5	$b_{15}+d_6$	c_4	c_3+d_8	d_7

FIG C.1 ASSEMBLING STRATEGY BY NODES FOR THE VOLUTE NOZLE ASSEMBLY ANALYSIS

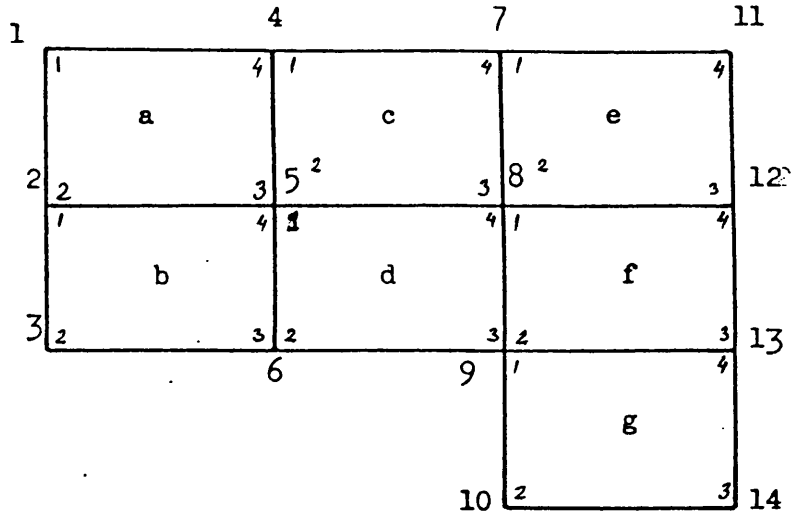

1,3,10, 11 , 1 4.	:	Corner Nodes With One Element
9	:	Corner Node With Three Elements
2,4,6,7,12,13	:	Line Nodes With Two Elements
5,8	:	Central Nodes With Four elements

$$[a]^{e} = \begin{bmatrix} a_1 & a_2 & a_3 & a_4 \\ a_5 & a_6 & a_7 & a_8 \\ a_9 & a_{10} & a_{11} & a_{12} \\ a_{13} & a_{14} & a_{15} & a_{16} \end{bmatrix}$$

Elementary matrix for element (a)

APPENDIX -D-

CALCULATION OF THE CIRCULATION AS A NODELESS VARIABLE

The potential function on one side of the splitting boundary differs from that on the opposite side by a value which is equal to the circulation around the blade. The elements on either side of this boundary will have a special form of interpolating function which includes the circulation in it. The circulation here is not connected to any node and is derived as follow

The approximation for the potential function is written in local coordinates as

$$\Phi = \frac{1}{4}\left(a_1 + a_2\xi + a_3\eta + a_4\xi\eta + \Gamma\xi^2\eta\right) \qquad \text{D.1}$$

The constants a1,a2,a3,a4 are to be determined by applying the equation to each node

$$\begin{aligned}
\Phi_1 &= \frac{1}{4}\left(a_1 - a_2 + a_3 - a_4 + \Gamma\right)\\
\Phi_2 &= \frac{1}{4}\left(a_1 - a_2 - a_3 + a_4 - \Gamma\right)\\
\Phi_3 &= \frac{1}{4}\left(a_1 + a_2 - a_3 - a_4 - \Gamma\right)\\
\Phi_4 &= \frac{1}{4}\left(a_1 + a_2 + a_3 + a_4 + \Gamma\right)
\end{aligned} \qquad \text{D.2}$$

And

$$\begin{aligned}
a_1 &= +\Phi_1 + \Phi_2 + \Phi_3 + \Phi_4\\
a_2 &= -\Phi_1 - \Phi_2 + \Phi_3 + \Phi_4\\
a_3 &= +\Phi_1 - \Phi_2 - \Phi_3 + \Phi_4 - \Gamma\\
a_4 &= -\Phi_1 + \Phi_2 - \Phi_3 + \Phi_4
\end{aligned} \qquad \text{D.3}$$

APPENDIX -D-

Introducing equation D.3 into D.1 and rearrange yields

$$\Phi = \sum_{i=1}^{4} \left[\frac{1}{4}\left(1+\xi_i\xi\right)\left(1+\eta_i\eta\right)\right]\cdot\Phi_i \quad +$$

$$+ \left[\frac{1}{4}\left(\xi^2\eta - \eta\right)\right]\cdot\Gamma = \sum_{i=1}^{4} N_i\Phi_i + N_k\Gamma \qquad \text{D.4}$$

The Galerkin equation for a Laplace differential equation is derived in appendix "B", and is of the form

$$\int\int\left(\frac{\partial\Phi}{\partial x}\frac{\partial N_j}{\partial x} + \frac{\partial\Phi}{\partial y}\frac{\partial N_j}{\partial y}\right)dx\,dy \quad =$$

$$= \int \frac{\partial\Phi}{\partial x} N_j\,dy + \int \frac{\partial\Phi}{\partial y} N_j\,dx \qquad \text{D.5}$$

By using the interpolation function D.4 yields

$$\frac{\partial\Phi}{\partial x} = \sum \frac{\partial N_i}{\partial x}\Phi_i + \frac{\partial N_k}{\partial x}\Gamma$$

$$\frac{\partial\Phi}{\partial y} = \sum \frac{\partial N_i}{\partial y}\Phi_i + \frac{\partial N_k}{\partial y}\Gamma \qquad \text{D.6}$$

Substituting into the main equation D.5, yields

$$\iint\left[\left(\frac{\partial N_i}{\partial x}\frac{\partial N_j}{\partial x} + \frac{\partial N_i}{\partial y}\frac{\partial N_j}{\partial y}\right) +\right.$$

$$\left. + \left(\frac{\partial N_k}{\partial x}\frac{\partial N_j}{\partial x} + \frac{\partial N_k}{\partial y}\frac{\partial N_j}{\partial y}\right)\frac{\Gamma}{\Phi_i}\right]\Phi_i = \int \frac{\partial\Phi}{\partial n} N_j\,dl \qquad \text{D.7}$$

APPENDIX -D-

Where the interpolating functions are written as

$$Nk = \frac{1}{4}\,\xi(\xi-1)(\eta-1)$$

$$Ni = \sum_{1}^{4}\frac{1}{4}(1+\xi_i\xi)(1+\eta_i\eta) \qquad \text{D.8}$$

$$Nj = \sum_{1}^{4}\frac{1}{4}(1+\xi_j\xi)(1+\eta_j\eta)$$

For the splitting boundary elements the term which includes the potential function and the circulation is

$$\iint\left(\frac{\partial N_k}{\partial x}\frac{\partial N_j}{\partial x}+\frac{\partial N_k}{\partial y}\frac{\partial N_j}{\partial y}\right)\bar{\Phi}_i\,dx\,dy=\int N_k\frac{\partial\Phi}{\partial n}\,dl$$

$$\bar{\Phi}_i=\frac{\Gamma}{\Phi_i} \qquad \text{D.9}$$

Here the input vector is to be determined from the previous iteration considering the opposite side value of the potential function. The calculation of the interpolation function then will be derived as follow

$$\frac{\partial N_k}{\partial\xi}=\frac{1}{4}(2\xi\eta)$$

$$\frac{\partial N_k}{\partial\eta}=\frac{1}{4}(\xi^2-1)$$

$$\frac{\partial N_k}{\partial x}=\frac{1}{16J}\left[2\xi\eta(b_3+b_4\xi)-(\xi^2-1)(b_2+b_4\eta)\right] \qquad \text{D.10}$$

$$\frac{\partial N_k}{\partial y}=\frac{1}{16J}\left[(\xi^2-1)(a_2+a_4\eta)-2\xi\eta(a_3+a_4\xi)\right]$$

APPENDIX -D-

And

$$\frac{\partial N_k}{\partial x}\frac{\partial N_j}{\partial x} = \frac{1}{16J}\left[(-b_2)\xi^2 + (b_4)\xi^2\eta + (2b_3)\xi\eta + \right.$$

$$\left. + (b_{xj})\xi + (c_{xj} + b_4)\eta + (a_{xj} + b_2)\right] \qquad \text{D.11}$$

$$\frac{\partial N_k}{\partial y}\frac{\partial N_j}{\partial y} = \frac{1}{16J}\left[(a_2)\xi^2 + (-a_4)\xi^2\eta + (-2a_3)\xi\eta + \right.$$

$$\left. + (b_{yj})\xi + (c_{yj} - a_4)\eta + (a_{yj} - a_2)\right] \qquad \text{D.12}$$

APPENDIX -E-

GENERAL DIFFUSER THEORY AND THE EFFECT OF SWIRL

A diffuser is a device to convert kinetic energy into pressure, therefore it produces both a reduction in the velocity level of the fluid stream and an increase in the static pressure. For an incompressibe and uniform flow

$$P_{o1} = P_1 + \frac{1}{2}\rho C_1^2$$

$$P_{o2} = P_2 + \frac{1}{2}\rho C_2^2$$

Then with Po1-Po2= ΔPo

$$\frac{P_2 - P_1}{\frac{1}{2}\rho C_1^2} = 1 - \left(\frac{C_2}{C_1}\right)^2 - \frac{\Delta P_o}{\frac{1}{2}\rho C_1^2} \qquad \text{E.1}$$

Where ΔPo is the stagnation pressure loss.

The pressure rise coefficient is normally defined as

$$C_p = \frac{P_2 - P_1}{\frac{1}{2}\rho C_1^2} \qquad \text{E.2}$$

and the ideal pressure rise coefficient is

$$C_{pi} = 1 - \left(\frac{C_2}{C_1}\right)^2 \qquad \text{E.3}$$

By combining the continuity equation and the above relations the ideal pressure rise coefficient can be

considered as a function of area ratio only

$$C_{pi} = 1 - \frac{1}{A_R^2} \qquad \text{E.4}$$

where the stagnation pressure loss coefficient is given by

$$\omega = \frac{\Delta P_o}{\frac{1}{2}\rho C_1^2} = \frac{P_{o1} - P_{o2}}{P_{o1} \quad P_1} \qquad \text{E.5}$$

In a real fluid with no slip condition on the walls the velocity varies from zero at the wall to some velocity greater than the mean velocity. The distortion of the velocity profile increases through the diffuser due to the pressure forces. The difference between the ideal and actual pressure recovery is due to both the high kinetic energy flux of the non uniform inlet velocity profile together with the frictional losses along the diffuser. Near the wall of the diffuser the velocity will fall to zero if the transfer of momentum to this near wall flow is no longer sufficient to move the flow against the pressure gradient and separation will take place and a stall region will occur. Separation is a function of the area ratio AR, diffuser length, and flow conditions at inlet. A variety of flow regimes associated with separation can exist in the diffusers. In two dimensional diffusers these flow regimes are related to the overall geometric characteristics of the diffuser.

APPENDIX -E-

The Effect Of Swirl

Diffusion in wide angle diffusers usually leads to separation and poor efficiency. Considerable efforts have been made to minimize this tendency to separation. Improvements in static pressure recovery has been found for diffusers with up to 30 deg. cone angle by imparting a moderate swirl at inlet [64]. Generally in cases of swirling flows the flow is pressed towards the wall by the centrifugal forces, and the wall boundary layer is less likely to separate even for large diffuser angles. The effect of swirl can be demonstrated by refering to the pressure recovery coefficient Cp, and the losses due to the stagnation pressure drop w in the following manner

If the swirl angle is α, then the continuity equation in one dimensional form and for incompressible flow is

$$A_1 C_1 \cos\alpha_1 = A_2 C_2 \cos\alpha_2 \qquad \text{E.6}$$

The velocity ratio can then be written as

$$\left(\frac{C_2}{C_1}\right)^2 = \left(\frac{A_1}{A_2}\right)^2 \left(\frac{\cos\alpha_1}{\cos\alpha_2}\right)^2 = \frac{\cos^2\alpha}{A_R^2} \cdot \frac{1}{\cos^2\alpha} \qquad \text{E.7}$$

The last term can be expanded as follows

$$\frac{1}{\cos^2\alpha_2} = \frac{C_{x2}^2 + C_{\theta 2}^2}{C_{x2}^2} = 1 + \left(\frac{C_{\theta 2}}{C_{x2}}\right)^2 = 1 + \left(\frac{C_{\theta 1} r_1}{C_{x2} r_2}\right)^2 \qquad \text{E.8}$$

APPENDIX -E-

Along a stream line the free vortex relationship has been considered as

$$C_{\theta 2} r_2 = C_{\theta} r_1 \qquad \text{E.9}$$

And from continuity

$$C_{x2} = C_{x1} \cdot \frac{A_1}{A_2} \qquad \text{E.10}$$

therefore

$$\frac{1}{\cos^2 \alpha_2} = 1 + \left(\frac{C_{\theta_1}}{C_{x1}} \frac{A_2}{A_1} \frac{r_1}{r_2}\right)^2 = 1 + \left(\tan \alpha_1 \frac{A_2}{A_1} \frac{r_1}{r_2}\right)^2 \qquad \text{E.11}$$

Then

$$\left(\frac{C_2}{C_1}\right)^2 = \frac{1}{A_R^2}\left(\frac{\cos \alpha_1}{\cos \alpha_2}\right)^2 = \frac{1}{A_R^2} \cos^2 \alpha_1 \left[1 + \tan^2 \alpha_1 A_R^2 \left(\frac{r_1}{r_2}\right)^2\right] \qquad \text{E.12}$$

For conical diffusers the area ratio is

$$A_R = \frac{A_2}{A_1} = \left(\frac{r_2}{r_1}\right)^2 \qquad \text{E.13}$$

And the ideal pressure recovery coefficient becomes

$$C_{pi} = \left(1 - \frac{1}{A_R}\right)\left(1 + \frac{1}{A_R} \cos^2 \alpha_1\right) \qquad \text{E.13}$$

It is clear that when the inlet swiri $\alpha 1$ is zero the equation above reduces to the non swirling ideal pressure recovery coefficient.

APPENDIX -E-

From the above it can be deduced that the ideal pressure recovery coefficient is a function of the area ratio and inlet swirl,while for non swirling flow it is a function of area ratio only. The effect of swirl is to reduce the pressure recovery coefficient ideally attainable.

In the above analysis it was assumed that the free vortex condition is valid along the stream line. This assumption is not valid for the central stream line when the radius approaches zero. An alternative approach for deriving the ideal pressure recovery can be based upon the following assumptions

(1) Uniform swirling flow at inlet (2) the free vortex condition to be applied at all stream lines except the central one where the tangential component of velocity is assumed to be constant (3) Meridional velocity is constant at exit (4) Tangential velocity varies linearly with radius at exit.

If the ideal pressure recovery is defined as

$$C_{pi} = \frac{Ke_1 - Ke_2}{Ke_1} \qquad \text{E.15}$$

The actual kinetic energy at exit is Ke2

$$Ke_2 = \int_o^{r_2} \frac{1}{2} C_2^2 \, dm = \frac{1}{2} \int_o^{r_2} \rho \, C_{m_2} C^2 \, dA =$$

$$= \pi \rho \, C_{m_2} \int_o^{r_2} r \left(C_\theta^2 + C_m^2 \right) dr \qquad \text{E.16}$$

APPENDIX -E-
---

with

$$C_{\theta 2} = C_{\theta 1}\left(\frac{r_1}{r_2}\right)$$

$$C_{\theta} = C_{\theta 1} - \left(C_{\theta 1} - C_{\theta 1}\frac{r_1}{r_2}\right)\frac{r}{r_2} \qquad \text{E.17}$$

And after some manipulations, the kinetic energy at exit is

$$Ke_2 = \frac{1}{2} m C_{\theta 1}^2 \left[\left(1 + \frac{1}{\tan^2\alpha_1}\frac{1}{A_R^2}\right) - \right.$$

$$\left. - \frac{4}{3}\left(1 - \frac{r_1}{r_2}\right) + \frac{1}{2}\left(1 - \frac{r_1}{r_2}\right)^2\right] \qquad \text{E.18}$$

And the ideal pressure recovery coefficient is

$$C_{pi} = 1 - \frac{C_{\theta 1}^2}{C_1^2}\left[\left(1 - \frac{1}{\tan^2\alpha_1}\frac{1}{A_R^2}\right) - \right.$$

$$\left. - \frac{4}{3}\left(1 - \frac{r_1}{r_2}\right) + \frac{1}{2}\left(1 - \frac{r_1}{r_2}\right)^2\right] \qquad \text{E.19}$$

Or

$$C_{pi} = \cos^2\alpha_1\left(1 - \frac{1}{A_R^2}\right) +$$

$$+ \sin^2\alpha_1\left[\frac{4}{3}\left(1 - \frac{r_1}{r_2}\right) - \frac{1}{2}\left(1 - \frac{r_1}{r_2}\right)^2\right] \qquad \text{E.20}$$

Equations E.14 and E.20 were plotted together with the experimental results of chapter 4 to analyse the effect of swirl on the pressure recovery coefficient

REFERENCES

[1] Wood, H. J."Current Technology Of Radial Inflow Turbines For Compressible Fluids", Trans. ASME, Jan. 1963, 62-CTP-9

[2] Wasserbauer, C. A., Kofski, M. G. And Nusbaum, W. J. "Cold Performance Evaluation Of A (4.59 in.) Radial Inflow Turbine Designed for a Bryton Cycle Space Power System", NASA TN D-3260 (1966)

[3] Kofski, M. G. And Wasserbauer, C. A."Experimental Performance Evaluation Of A Radial Inflow Turbine Over A Range Of Specific Speeds", NASA TN D-3742 (1966)

[4] Flaxington, D. And Szczupak, D. T. "Variable Area Radial Inflow Turbine", I Mech E Conference Publications 1982-3; Turbocharging And Turbochargers 1982"

[5] Balje, O. E. "Turbomachines, A Guide To Design Selection And Theory", Wiley-Interscience Publication, 1981

[6] Wallace F. J., Way, R. J. B. And Baghery, A. "Variable Geometry Turbocharging - The Realistic Way Forward", SAE, International Congress And Exposition, Detroit, Michigan 1981

REFERENCES

[7] Ziarati, M. R.,"Mathematical Modelling And Experimental Testing Of Variable Geometry Inward Radial Flow Turbines", PhD. Thesis , University Of Bath, School Of Engineering, 1979

[8] Wallace, F. J. "Theoretical Assessment Of The Performance Characteristics Of Inward Flow Radial Turbines", Proc. Instn. Mech. Engrs. 1958, 172,33

[9] Wilson, D. G. And Jansen, W. "The aerodynamic And Thermodynamic Design Of Cryogenic Radial-Inflow Expanders", ASME, No. 65-WA/PIA, 1964

[10] Futral, S. M. And Wasserbauer, C. A. "Off-Design Performance Prediction With Experimental Verification For A Radial Inflow Turbines", NASA TN D-2621 (1965)

[11] Benson, R. S. "An Analysis Of The Losses In A Radial Gas Turbine", Paper No. 16 , Thermodynamics And Fluid Mechanics Convention, Liverpool, 13-15 April,1966

REFERENCES

[12] Benson, R. S., Cartwright, W. G. And Das, S. K.
"An Investigation Of The Losses In The Rotor Of A Radial Flow Gas Turbine At Zero Incidence Under Conditions Of Steady Flow", Paper No. 23 , Thermodynamics And Fluid Mechanics Convention, Bristol, 27-29 March, 1968

[13] Jansen, W.
"A Method For Calculating The Flow In A Centrifugal Impeller When Entropy Gradients Are Present", Instn. Mech. Engrs., 1968

[14] Bridle, E. A. And Boulter, R. A.
"A Simple Theory For The Prediction Of Losses In The Rotors Of Inward Radial flow Turbines", Paper No. 42, Thermodynamics And Fluid Mechanics Convention, Bristol, 27-29 March, 1968

[15] Benson, R. S.
"A Revew Of Methods For Assessing Loss Coefficients In Radial Gas Turbines", Intrn. Jour. Mech. Sci., Vol. (12), 905-932, 1970

[16] Whitfield, A. And Wallace, F. J.
"Study Of Incidence Loss Models In Radial And Mixed Flow Turbomachinery", Paper C55/73, Instn. Mech. Engrs., 1973

REFERENCES

[17] Khalil, I. M., Tabakof, W. And Hamid, A.
"Losses In Radial Inflow Turbines", ASME, 76-FE-9 (1976)

[18] Rogers, C.
"Efficiency And Performance Characteristics Of Radial Turbines", SAE, (1966)

[19] Jansen, W. And Quale, E. B.
"A Rapid Method For Predicting The Off Design Performance Of Radial Inflow Turbines", ASME, 67-WA/GT-9, 1968

[20] Kastner, L. J. And Bhinder, F. S.
"A method For Predicting The Performance Of A Centripetal Gas Turbine Fitted With A Nozzleless Volute Casing", ASME, 75-GT-65, 1975

[21] Wallace, F. J., Baines, N. C. And Whitfield, A.
"A Unified Approach To The One Dimensional Analysis And Design Of Radial And Mixed Flow Turbines", ASME, 76-GT-100, 1976

[22] Baines, N.
"Computer Aided Design Of Radial And Mixed Flow Turbines", PhD. Thesis , University Of Bath, School Of Engineering, 1977

REFERENCES

[23] Wu, C. H.

"A General Theory Of Three Dimensional Flow In Subsonic And Supersonic Turbomachines Of Axial, Radial And Mixed Flow Types", NASA, Jan. , 1952, TN-2604

[24] Wallace, F. J.

"Introduction To Pseudo Three Dimensional Methods Of Flow Analysis In Radial And Mixed Flow Turbomachines", Queen's University, Departement Of Mech. Eng., August, 1971

[25] Tabakoff, W., Sheoran, Y. And Kroll, K.

"Flow Measurements In A Turbine Scrol", Trans ASME, Vol. 102, Sept., 1980

[26] Hamrick, J. T., Ginsburg, A. And Osborn, W. M.

"Method Of Analysis For Compressible Flow Through Mixed flow Centrifugal Impeller Of Arbitrary Design", NASA, Report 1082, 1952

[27] Atkey, R.

"Computer Aided Design Of Radial And Mixed Flow Compressor", Phd. Thesis , University Of Bath, School Of Engineering, 1976

[28] Katsanis, T.

"Use Of Arbitrary Quasi-Orthogonals For Calculating Flow Distribution In The meridional Plane Of A turbomachine", NASA, 1970

REFERENCES

[29] Bosman, C.
"An Analysis Of Three Dimensional Flow In Centrifugal Compressor Impeller", ASME, Jour. Of Eng. For Power, Vol. 102, July 1980

[30] Khalil, I., Tabakoff, W. And Hamid, A.
"Viscous Flow Analysis In Mixed Flow Rotors", ASME, 78-WA/GT-3, 1978

[31] Schmid, G.
"Incompressible Flow In Multiply Connected Regions", Finite Elements In Flow Problems", Int. Symp. On F.E.M In Flow Problems, Swansea UK 1974

[32] Bratanow, T. And Ecer, A.
"Analysis Of Moving Body Problems In Aerodynamics", Int. Symp. On F.E.M. In Flow Problems, Swansea UK, 1974

[33] Vooren, J. V. D. And Labrujere, Th. E.
"Finite Element Solution Of The Incompressible Flow Over An Aerofoil In A Non Uniform Stream", Int. Symp. On F.E.M. In Flow Problems, Swansea UK , 1974

[34] Hughes, T. J. R., Taylor, R. L. And Levy, J. F.
"High Reynolds Number, Steady, Incompressible Flows By A Finite Element Method", Int. Symp. On F.E.M. In Flow Problems, Swansea UK, 1974

REFERENCES

[35] "Design And Fabrication Of The Bryton Cycle High Performance Turbine Research Package", NASA, CR-72478 APS-5281-R, 1968

[36] Thompson, D. S.
"Finite Element Analysis Of The Flow Through A Cascade Of Aerofoils", University Of Cambridge, CUED/A, Turbo/TR, 45 (1973)

[37] Habashi, W. G.
"Compressible Potential Flows By The F.E.M.", Second Int. Symp. On F.E.M. In Flow Problems, Italy, June 1976

[38] Worster, D. M.
"The Calculation of Fully Three Dimensional Flows In Impellers Using The Finite Element Method", Heriot-Watt University, Edinburough, 1973

[39] Laskaris, T. E.
"Finite Element Analysis Of Three Dimensional Potential Flow In Turbomachines", AIAA Jour., Vol. 16, No. 7, July 1978

[40] Hirsch, Ch. And Warzee, G.
"An Integral Quasi Three Dimensional Finite Element Calculation Program For Turbomachinary Flows", ASME, Journal Of Engineering For Power Vol. 101, Jan. 1979

REFERENCES

[41] Runstadler, P. W., Dolan, F. X. And Dean, R. C. "Diffuser Data Book", Creare, TN-186, May 1975

[42] Kline, S. J., Abbotte, D. E. And Fox, R. W. "Optimum Design Of Straight Walled Diffusers", ASME, Jour. Of Basic Eng. Sept. 1959

[43] Howard, J. H. G. And Thornton-Trump, A. B. "Performance And Flow Regimes For Annular Diffusers", ASME, 67-WA/FE-21 , 1968

[44] Kwan, L. So. "Vortex Phenomenon In A Conical Diffusers", AIAA, Vol. 5, No. 6, 1966

[45] Sovran, G. And Klomp, E. D. "Experimentally Determinrd Optimum Geometries For Rectilinear Diffusers With Rectangular, Conical Or Annular Crossection", Elsurier Publishing Co. 1967

[46] Mohanty, A. K. "Performance Of Conical Diffusers With Non Uniform Inlet Velocity Profile"

[47] Mohanty, A. K. And Asthana, S. B. L. "Laminar Flow In The Entrance Region Of A Smooth Pipe" Jour. Of Fluid Mech., Vol. 90, Part 3, PP 433-447, 1979

REFERENCES
---

[48] Kaiser, K. F. And McDonald, A. T.
"Effect Of Wake Type Non Uniform Inlet Velocity Profiles On First Appreciable Stall In Plane Wall Diffusers", ASME, Jour. Of Fluid Eng., Vol. 102, sept. 1980

[49] McDonald, A. T. And Fox, R. W.
"Effects Of Swirling Inlet Flow On Pressure Recovery In Conical Diffusers", AIAA, Vol. 9, No. 10, 1971

[50] Senoo, Y., Kawaguchi, N. And Nagata, T.
"Swirl Flow In Conical Diffusers", JSME, Vol. 21, No. 151, Jan. 1978

[51] Coladiperto, R., Schneider, J. H. And Sridhar, K.
"Effects Of Inlet Flow Conditions On The Performance Of Echiangular Annular Diffusers", C SME Paper No. 73-CSME-84 (1974)

[52] Sakai, T., Sanbe, M. And Nakayama, T.
"Experimental Study On Diffusers For Mixed Flow Machines", ASME 78-GT-120 (1978)

[53] Wallace, F. J. And Whitfield, A.
"Experimental And Theoretical Evaluation Of Flow Patterns In Curved Annular Diffusers"

[54] Rayle, R. E.
"Influence Of Orifice Geometry On Static Pressure Measurements", ASME , 59-A-234, 1960

[55] Dixon, L. S.

REFERENCES

"Fluid Mechanics, Thermodynamics Of Turbomachinary", Pregmon Press 1978

[56] Whitfield, A.
"One Dimensional Prediction Program For Radial And Mixed Flow Turbines", Internal Report, University Of Bath, School Of Engineering, 1980

[57] Baskharone, E. And Hamed, A.
"A New Approach To Cascade Flow Analysis Using The Finite Element Method", AIAA-80-0389, Pasadina, California, Jan. 14-16 / 1980

[58] Hamed, A. And Baskharone, E.
"Analysis Of The Three Dimensional Flow In A Turbine Scroll", ASME, Jour. , Of Fluid Engineering, Vol. 102, Sept. 1980

[59] Vries, G. And Norrie, D. H.
"The Application Of The Finite Element Technique To Potential Flow Problems", Trans. ASME, Dec. 1971

[60] Irons, B. M.
"A Frontal Solution Program For Finite Element Analysis", Intr. Jour. Num. Meth. In Eng., Vol. 2, 5-32 (1970)

REFERENCES

[61] Hood, P.

"Frontal Solution Program For Unsymetric Matrices", Intr. Jour. Num. Meth. In Eng., Vol. 10, 379-399 (1976)

[62] Carnahan, B. Luther, H. A. And Wilkes, J. O.

"Applied Numerical Methods", J. Wiley, 1969

[63] Kupta, S. K. And Tanji, K. K.

"Computer Program For Solution Of Large Sparse Unsymetric Systems Of Linear Equations", Int. J. Num. Meth. Eng., Vol. 11, No. 8, 1977, pp 1251-1259

[64] Neve, R. S. And Wirasinghe, N. E. A.

"Changes In Conical Diffuser Performance By Swirl Addition", Aeronautical Quarterly Vol. 19, August, 1978.

[65] Bereny, S. G. And Raffa, C. J.

"Variable Area Turbocharger For High Output Diesel Engines", Paper 79006 of SAE Special Publications, Turbocharging And Turbocharged Engines, 1979.